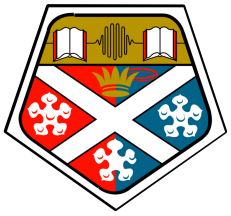
Low-Noise, Narrow-Linewidth Optical Parametric Oscillator Intracavity-Pumped by a Continuous-Wave VECSEL



University of Strathclyde Glasgow

A thesis presented in fulfilment of the
requirements for the degree of

Doctor of Philosophy

by

Steven Anderson

Institute of Photonics, Department of Physics
University of Strathclyde

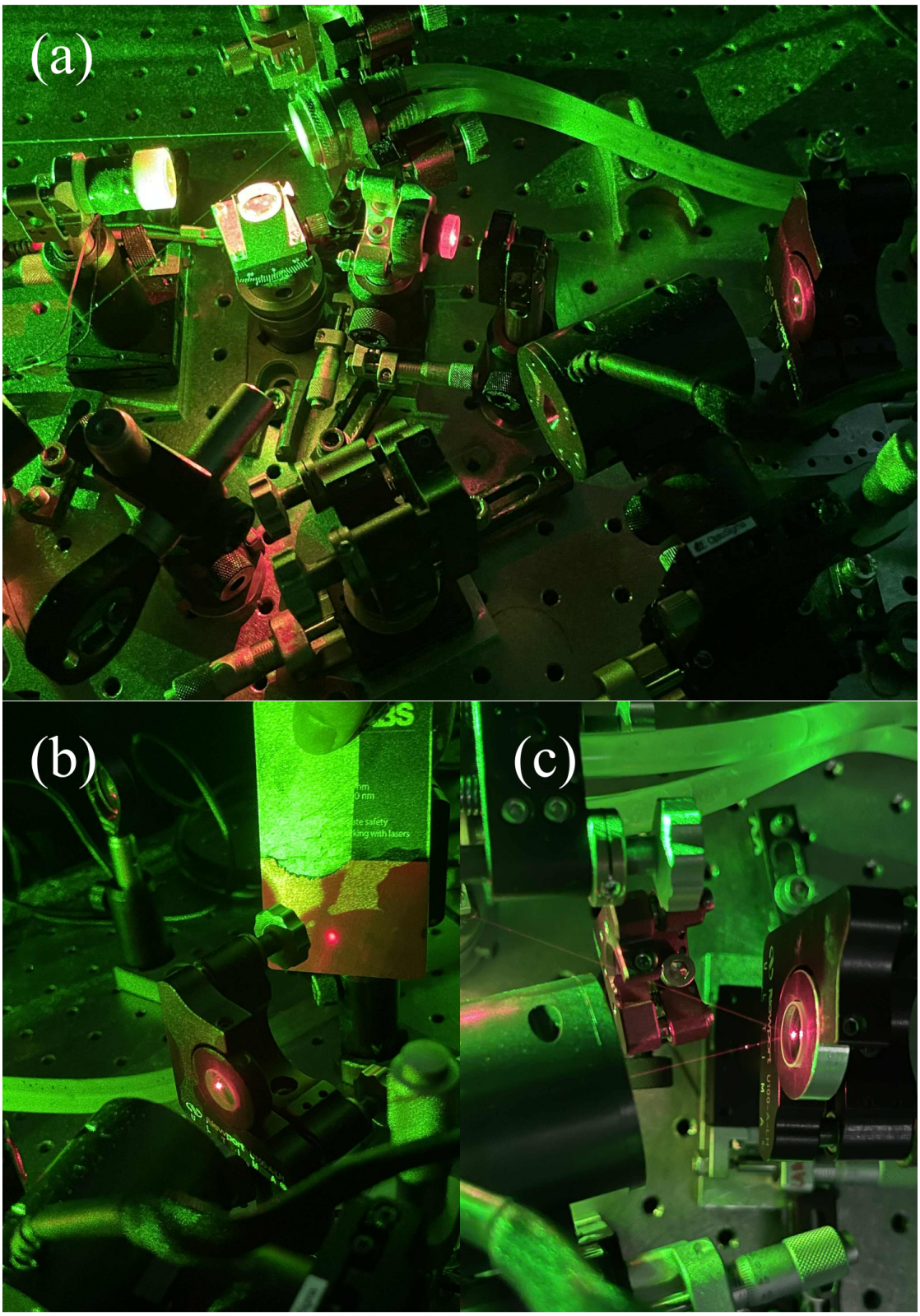
2026

This thesis is the result of the author's original research. It has been composed by the author and has not been previously submitted for examination which has led to the award of a degree.

The copyright of this thesis belongs to the author under the terms of the United Kingdom Copyright Acts as qualified by University of Strathclyde Regulation 3.50. Due acknowledgement must always be made of the use of any material contained in, or derived from, this thesis.

Signed: Steven Anderson

Date: 1st May 2026



Photographs of the first visible VECSEL-pumped OPO laser system. (a) Operational singly-resonant OPO pumped intracavity by an AlGaInP-based red VECSEL. (b) Detection of infrared emission from the OPO cavity, verifying above-threshold OPO operation. (c) Observation of the bright intracavity VECSEL pump beam, confirming above-threshold VECSEL performance.

Acknowledgements

I would like to express my sincere gratitude to the following people for their invaluable support and guidance throughout my PhD:

First and foremost, my supervisor, Prof. Jennifer Hastie, for her guidance and support throughout my time as a PhD student. Her approachable and encouraging supervision enhanced both my professional and personal development, and her confidence in my abilities was instrumental in the successful realisation of the first visible VECSEL-pumped OPO system. I am also deeply appreciative of her support during my postdoctoral research, and for facilitating the procurement of new dielectric mirror coatings after the initial batch proved unsuccessful.

To Dr. Lucia Caspani, my secondary supervisor, for her valuable insights and thoughtful discussions, particularly regarding the theoretical background of nonlinear optics and quantum optics.

To Prof. Loyd McKnight of the Fraunhofer Centre of Applied Photonics and Institute of Photonics at the University of Strathclyde, for supplying the infrared FPI, used for locking the resonant idler wave to the OPO cavity.

To Dr Paulo Hisao Moriya, senior postdoctoral researcher in the "High Brightness Semiconductor Lasers Group," for his technical guidance throughout my doctoral studies. His support was instrumental in developing my skills and understanding of electronic systems for active stabilisation, particularly the implementation of the Pound–Drever–Hall and side-of-fringe techniques.

To Sharon Kelly and Lorraine Annand for their continual assistance and support with administrative tasks, especially in coordinating international travel for conference visits.

To the rest of my colleagues and members of staff at the Institute of Photonics, not mentioned by name, for contributing to such a welcoming and supportive environment.

Additionally, to the UK Engineering and Physical Sciences Research Council (EPSRC) under the:

- National Quantum Technology Hub for Sensors and Metrology (EP/M013294/1),
- National Quantum Technology Hub in Sensing and Timing (EP/T001046/1),
- EPSRC Training Grant (EP/R513167/1; studentship 2419856),
- New Investigator Award (EP/R513167/1), and
- ERC Consolidator Grant (G.A. 101125923).

Finally, I would like to thank my girlfriend, Rachel, for her constant support, patience, and encouragement throughout my PhD studies. I am also grateful to my close friends and family for helping me maintain a healthy work-life balance along the way.

Abstract

This thesis demonstrates a unique type of continuous-wave (CW) optical parametric oscillator (OPO), called an intracavity singly resonant OPO (ICSRO). This configuration exploits the high circulating optical field within a laser cavity to efficiently overcome the otherwise high oscillation threshold associated with externally-pumped SROs. The fundamental nonlinear process associated with OPOs is optical parametric down-conversion (PDC), which results in the simultaneous creation of two distinguishable photons from a single higher-energy pump photon. The parametrically generated signal and idler photon pairs are intrinsically correlated in energy, momentum, and polarization and, in the ideal lossless case, exhibit complete suppression of intensity-difference noise.

An ICSRO based on 5%-mol magnesium-oxide-doped periodically-poled $LiNbO_3$ (5%-MgO:PPLN) was implemented and fully characterised. The nonlinear crystal was integrated within a four-mirror, optically-pumped, vertical-external-cavity surface emitting laser (VECSEL). Optimised for low-oscillation threshold and in the absence of output coupling (OC), the system exhibited a SRO threshold at an input external pump power of 1.78 W, delivering 14.2 mW (one-way) of extractable non-resonant signal power at 2.96 W of input pump power, corresponding to a total down-conversion efficiency of 72.1%. With the introduction of a 1.7% OC at the resonant idler wavelength, the SRO produced 26.2 mW of signal and 5.6 mW of one-way idler output power. This corresponds to a down-conversion efficiency of 70.2% and an extraction efficiency of 43%. Thermal tuning of the 5%-MgO:PPLN crystal enabled continuous wavelength tuning over 1155–1300 nm (for the signal) and 1474–1718 nm (for the idler), limited solely by

the bandwidth of the dielectric mirror coatings. For quantum applications, where balanced photodetectors exhibit high quantum efficiency at telecom wavelengths, emission was targeted near the telecom O-band (1.3 µm) and C-band (1.55 µm), achieved with a fixed VECSEL fundamental wavelength of 690.6 nm, a 5%-MgO:PPLN grating period of 14.55 µm, and a stabilised crystal temperature of 114°C.

Furthermore, the short-term power stability of the VECSEL fundamental was characterised both above and below the SRO threshold, demonstrating high amplitude stability in both regimes, in agreement with the Class-A dynamics of the VECSEL. Long-term RMS stability was also measured, yielding 0.4%, 1.8%, and 2.3% for the VECSEL fundamental, signal, and idler, respectively, with all three interacting waves oscillating in a single longitudinal mode.

Due to the stable, single-frequency operation of the ICSRO VECSEL, further development of the system was demonstrated through the implementation of active stabilisation schemes. Under dual-locking conditions, where the VECSEL fundamental and the intracavity resonant idler were stabilised using Pound–Drever–Hall (PDH) and side-of-fringe (SOF) locking, respectively, relative intensity noise (RIN) was reduced by more than 20 dB for each interacting wave at low Fourier frequencies (∼10 Hz). Narrow integrated linewidths of 6.21(1) kHz for the VECSEL fundamental and 151(1) Hz for the resonant idler were achieved over integration times as long as 4s, illustrating the transfer of noise from the VECSEL fundamental to the OPO non-resonant signal. Even under PDH-locking alone, the non-resonant signal linewidth remained narrow at 3.48(1) kHz.

In conclusion, the superior noise performance – particularly in terms of both intensity and frequency noise – demonstrates that the dual-locked ICSRO VECSEL system is a promising high-quality coherent light source for future quantum technologies, especially in quantum optics experiments and the generation of squeezed states of light. Future work may focus on achieving further noise reduction through additional active and passive stabilisation techniques, as well as exploring more complex OPO architectures.

Contents

Acknowledgements **iii**

Abstract **v**

List of Figures **xiv**

List of Tables **xv**

List of Acronyms **xvi**

List of Symbols **xxi**

1 Introduction **1**

1.1 Introduction 1

1.2 The continuous-wave optical parametric oscillator (CW OPO) 2

1.3 Vertical-external-cavity surface-emitting lasers (VECSELs) 7

1.4 Quasi-phase matching (QPM) 10

1.5 Periodically-poled $LiNbO_3$ (PPLN) 11

1.6 Historical review of CW OPOs and ICSROs 12

1.7 Motivation for investigating VECSEL-pumped OPOs for quantum optical applications 14

1.7.1 Intensity-difference squeezing 15

1.7.2 Proposed advantages of VECSEL pumping for intensity–difference squeezing . . . 17
1.7.3 Proposed advantages of VECSEL pumping for continuous–variable (CV) quantum optics . . . 18
1.8 Thesis overview . . . 19

2 Theoretical Background **23**
2.1 Introduction . . . 23
2.2 Nonlinear optics . . . 24
2.2.1 The origins of nonlinear optics . . . 24
2.3 The theory of nonlinear optics . . . 26
2.3.1 Crystal symmetry and the nonlinearity coefficients . . . 27
2.3.2 Frequency conversion through the $\chi^{(2)}$ susceptibility . . . 30
2.4 Optical parametric down-conversion (PDC) . . . 32
2.5 Quasi-phase matching (QPM) . . . 34
2.5.1 QPM domain-reversal theory . . . 38
2.5.2 QPM acceptance parameters . . . 41
2.5.3 QPM tuning ranges . . . 46
2.6 ICSRO steady-state threshold power analysis . . . 47
2.6.1 ICSRO steady-state power characteristics . . . 48
2.6.2 ICSRO steady-state power optimisation . . . 51
2.7 Stothard model . . . 55
2.8 Conclusion . . . 57

3 Design considerations for a CW ICSRO **59**
3.1 Introduction . . . 59
3.2 Vertical-external-cavity surface-emitting laser (VECSEL) . . . 59
3.2.1 VECSEL design and operational principles . . . 60
3.2.2 Optical pumping . . . 62

3.2.3 Thermal management . . . 64
3.2.4 Wavelength coverage . . . 66
3.2.5 VECSEL applications . . . 69
3.2.6 Transient dynamics above the SRO threshold . . . 71
3.3 OPO nonlinear χ^2 crystal: 5%-MgO:PPLN . . . 75
3.3.1 $LiNbO_3$ structure . . . 75
3.3.2 Optical properties of $LiNbO_3$ . . . 77
3.4 ICSRO resonator design requirements . . . 79
3.5 Cavity modelling and the final ICSRO design . . . 84
3.5.1 Stability analysis . . . 85
3.5.2 Beam waists . . . 90
3.6 Modelling of the ICSRO oscillation threshold . . . 92
3.7 Conclusion . . . 95

4 Single-frequency CW visible VECSEL-pumped OPO 97
4.1 Introduction . . . 97
4.2 AlGaInP-based VECSEL gain structure . . . 98
4.3 VECSEL pump source: Coherent Verdi V5 laser . . . 99
4.4 VECSEL cavity design and characterisation . . . 101
4.4.1 Power transfer . . . 102
4.4.2 Caird analysis . . . 104
4.4.3 Spectral performance . . . 106
4.5 ICSRO VECSEL cavity design and characterisation . . . 110
4.5.1 Alignment procedure . . . 111
4.5.2 Spectral performance . . . 114
4.5.3 VECSEL beam quality . . . 115
4.5.4 HR-idler ICSRO power and efficiency performance . . . 118
4.5.5 OC-idler ICSRO power and efficiency performance . . . 125

4.5.6 Passive power stability characteristics of the SRO pumped in a multi-longitudinal-mode VECSEL . . . 131
4.6 Single-frequency ICSRO VECSEL . . . 134
4.6.1 Confocal Fabry–Pérot interferometer . . . 134
4.6.2 The Fabry–Pérot etalon effect . . . 137
4.6.3 Experimental configuration . . . 140
4.6.4 Spectral characteristics . . . 140
4.6.5 Passive power stability characteristics . . . 147
4.7 Conclusion . . . 149

5 Sub-kHz linewidth intracavity VECSEL-pumped OPO 152
5.1 Introduction . . . 152
5.2 Noise and coherence properties of lasers . . . 153
5.2.1 Schawlow-Townes-Henry (STH) linewidth . . . 155
5.2.2 Intensity noise: Class-A dynamics . . . 156
5.2.3 Photon and electron shot-noise . . . 158
5.2.4 Relative intensity noise (RIN) . . . 159
5.2.5 Phase noise . . . 159
5.3 Noise properties of VECSELs: Myara model . . . 162
5.4 Frequency stabilisation . . . 164
5.5 Pound-Drever-Hall (PDH) stabilisation: theory and implementation . . . 166
5.5.1 PDH error signal . . . 167
5.5.2 Proportional-integral-derivative (PID) controller . . . 171
5.6 Noise dynamics in a dual-locked ICSRO VECSEL . . . 174
5.6.1 Motivation . . . 175
5.6.2 Experimental configuration . . . 176
5.7 Lock acquisition and operating conditions . . . 178
5.8 Relative intensity noise characteristics of the ICSRO VECSEL . . . 181
5.8.1 VECSEL fundamental . . . 182

5.8.2 OPO non-resonant signal . . . 184
5.8.3 OPO resonant idler . . . 185
5.9 Frequency noise characteristics of the ICSRO VECSEL . . . 187
5.9.1 Free-running regime . . . 188
5.9.2 PDH-lock-only regime . . . 189
5.9.3 Dual-lock regime . . . 190
5.10 Spectral linewidth characteristics of the ICSRO VECSEL . . . 193
5.10.1 Free-running regime . . . 193
5.10.2 PDH-lock-only regime . . . 197
5.10.3 Dual-lock regime . . . 198
5.10.4 Comparative analysis of frequency stability with externally-pumped OPOs . . . 200
5.11 Conclusion . . . 201

6 Conclusions **204**
6.1 Introduction . . . 204
6.2 Summary of experimental results and conclusions . . . 205
6.3 Future work . . . 210
6.4 Conclusion . . . 215

Bibliography **216**

List of Publications **240**

Appendix A: Python Script for Calculating RIN PSD **242**

Appendix B: Python script for calculating frequency noise PSD **249**

List of Figures

1.1 Virtual energy-level diagram of PDC 3
1.2 CW OPO cavity configurations 5
1.3 Schematic illustration of PDC in a periodically-poled nonlinear material . 11
1.4 Intensity-difference noise spectrum 16

2.1 First direct evidence of nonlinear optics via SHG 25
2.2 Energy and momentum conservation in PDC 33
2.3 Second harmonic intensity for different phase matching techniques 36
2.4 Nonlinear coefficient ratio versus duty cycle for QPM interactions 40
2.5 Phase matching acceptance bandwidths for type-0 QPM PDC 44
2.6 QPM tuning curves for PDC 47
2.7 Photon flow characteristics of an ICSRO 51
2.8 Power and efficiency characteristics of an ICSRO 54

3.1 Operating principles of an AlGaInP-based red-VECSEL 62
3.2 Thermal management approaches for VECSELs 65
3.3 VECSEL wavelength coverage 67
3.4 Transient dynamics of an ICSRO 74
3.5 Crystal structure of $LiNbO_3$ 76
3.6 Schematic of the 5% MgO:PPLN crystal 78
3.7 Gaussian beam parameters 81
3.8 HR-idler VECSEL-pumped ICSRO experimental configuration 85

3.9 Stability analysis of the AlGaInP-based VECSEL cavity 86
3.10 Stability analysis of the OPO resonant idler cavity 87
3.11 ICSRO oscillation threshold versus 5%-MgO:PPLN crystal length 94

4.1 External Verdi pump laser setup 99
4.2 Calibration of VECSEL pump power 100
4.3 Free-running VECSEL experimental configuration 102
4.4 Free-running VECSEL power transfer characteristics 103
4.5 Caird analysis 106
4.6 Spectral shift characteristics of the free-running VECSEL 107
4.7 Spectral performance of the free-running VECSEL 109
4.8 Free-running VECSEL emission spectra for different BRF thicknesses . . 110
4.9 OC-idler VECSEL-pumped ICSRO experimental setup 112
4.10 VECSEL spectral performance with all OPO components introduced . . . 113
4.11 Spectral characteristics and temperature tuning of the ICSRO 114
4.12 Beam quality of the AlGaInP-based VECSEL 116
4.13 Intracavity VECSEL power in the HR-idler ICSRO regime 119
4.14 Non-resonant signal power in the HR-idler ICSRO regime 120
4.15 Optimum VECSEL output power with PDC suppressed. 121
4.16 Power characteristics of the ICSRO VECSEL in the HR-idler regime . . . 123
4.17 Efficiency characteristics of the ICSRO VECSEL in the HR-idler regime . 124
4.18 Intracavity VECSEL power in the OC-idler regime 126
4.19 Power characteristics of the ICSRO VECSEL in the OC-idler regime . . . 127
4.20 Efficiency characteristics of the ICSRO VECSEL in the OC-idler regime . 129
4.21 Power stability of the OC-idler ICSRO pumped by a multimode VECSEL 133
4.22 Schematic of a scanning confocal Fabry–P'erot interferometer 136
4.23 Single-frequency mode selection using intracavity etalons 139
4.24 Single-frequency VECSEL-pumped ICSRO experimental configuration . . 141
4.25 FPI transmission trace of the multimode VECSEL 142

4.26 FPI transmission trace of the resonant idler 143
4.27 FPI transmission trace of the single-frequency VECSEL 145
4.28 FPI transmission trace of the non-resonant signal 146
4.29 Single-frequency ICSRO power stability 148

5.1 Photon lifetimes of various laser technologies 156
5.2 Theoretical noise model of an optically-pumped VECSEL 163
5.3 Side-of-fringe laser stabilisation 165
5.4 Theoretical PDH error signal as a function of frequency detuning 172
5.5 Comparison of P, PI, and PID control responses 174
5.6 Dual-locked VECSEL-pumped ICSRO experimental setup 177
5.7 ICSRO VECSEL error signals under active frequency stabilisation 180
5.8 VECSEL RIN under active frequency stabilisation 183
5.9 OPO signal RIN under active frequency stabilisation 185
5.10 OPO idler RIN under active frequency stabilisation 186
5.11 Free-running ICSRO VECSEL frequency noise PSD 189
5.12 PDH-locked ICSRO VECSEL frequency noise PSD 190
5.13 Dual-locked ICSRO VECSEL frequency noise PSD 191
5.14 ICSRO VECSEL frequency noise PSD in unlocked and locked regimes . . 192
5.15 ICSRO VECSEL spectral linewidth under free-running conditions 194
5.16 ICSRO VECSEL spectral linewidth under PDH-locking conditions 197
5.17 ICSRO VECSEL spectral linewidth under dual-locking conditions 199

6.1 Dual-cavity VECSEL-pumped ICDRO experimental configuration 213
6.2 Degree of intensity-difference squeezing versus detection efficiency 214

List of Tables

2.1 Measured nonlinear coefficients of $LiNbO_3$ 29

3.1 Characteristics of Class-A, Class-B, and Class-C laser dynamics. 72
3.2 Predicted beam waist diameters at minimum ICSRO threshold 83
3.3 Elements used in the VECSEL cavity design 88
3.4 Elements used in the OPO cavity design 90
3.5 HR-idler ICSRO system parameters 93

4.1 Optical power and efficiency of the ICSRO VECSEL 130

5.1 Dynamical classification and noise limits of different laser architectures . . 162
5.2 Experimental conditions for frequency locking 180
5.3 Experimental conditions for shot-noise calculation 182
5.4 Comparison of frequency-stabilised OPO systems 201

List of Acronyms

AC	alternating current
AlGaAs	aluminium gallium arsenide
AlGaInP	aluminium gallium indium phosphide
AR	anti-reflective
BPM	birefringent phase matching
BRF	birefringent filter
CV	continuous-variable
CW	continuous-wave
DBR	distributed Bragg reflector
DC	direct current
DFB	distributed feedback
DFG	difference-frequency generation
DHS	diamond heat spreader
DM	dichroic mirror
DPSSL	diode-pumped solid-state laser
DRO	doubly-resonant optical parametric oscillator
ECDL	external-cavity diode laser

List of Acronyms

ECOPO	externally-pumped optical parametric oscillator
EM	electromagnetic
EOM	electro-optic modulator
FNPSD	frequency noise power spectral density
FP	Fabry–Pérot
FPI	Fabry–Pérot interferometer
FSR	free spectral range
FWHM	full-width at half-maximum
GaAs	gallium arsenide
GaInP	gallium indium phosphide
GaSb	gallium antimonide
HR	highly-reflective
HVA	high-voltage amplifier
HVC	high-voltage controller
HWP	half-wave plate
ICDRO	intracavity doubly-resonant optical parametric oscillator
ICSRO	intracavity singly-resonant optical parametric oscillator
InGaAs	indium gallium arsenide
IR	infrared
KTA	potassium titanyl arsenate
$KTiOPO_4$	potassium titanyl phosphate
KTP	potassium titanyl phosphate
$LiNbO_3$	lithium niobate

List of Acronyms

$LiTaO_3$	lithium tantalate
LO	local oscillator
MgO	magnesium oxide
MgO:PPLN	magnesium oxide-doped periodically-poled lithium niobate
MgO:PPSLT	magnesium oxide-doped periodically-poled stoichiometric lithium tantalate
MOCVD	metal-organic chemical-vapour deposition
MQW	multiple quantum well
Nd:YAG	neodymium-doped yttrium aluminium garnet
Nd:YVO_4	neodymium-doped yttrium orthovanadate
NPM	non-phase matched
NR	non-resonant
OC	output-coupler
OP-ECL	optically-pumped external-cavity laser
OPA	optical parametric amplifier
OPO	optical parametric oscillator
OPSL	optically-pumped semiconductor laser
OR	optical rectification
OSA	optical spectrum analyser
PBS	polarizing beam splitter
PDC	parametric down-conversion
PDH	Pound-Drever-Hall
PE-OPO	pump-enhanced optical parametric oscillator
PID	proportional-integral-derivative
Pk-pk	peak-to-peak

POF	peak-of-fringe
PP	periodically-poled
PPLN	periodically-poled lithium niobate
PPM	perfectly-phase matched
PSD	power spectral density
PZT	piezoelectric transducer
QD	quantum dot
QPM	quasi-phase matching
QW	quantum well
QWP	quarter-wave plate
R	resonant
RIN	relative intensity noise
RIN$_{\text{shot}}$	Shot-noise-limited relative intensity noise
RMS	root mean square
RPG	resonant periodic gain
RTA	rubidium titanyl arsenate
S	sagittal
SDL	semiconductor disk laser
SFG	sum-frequency generation
SHG	second-harmonic generation
Si	silicon
SMSR	side-mode suppression-ratio
SNLO	Select Nonlinear Optics
SOF	side-of-fringe
Sr	strontium
SRO	singly-resonant optical parametric oscillator

SRS	stimulated Raman scattering
STH	Schawlow-Townes-Henry
SWaP-C	size, weight, power and cost
T	tangential
TE	transverse-electric
TPA	two-photon absorption
TRO	triply-resonant optical parametric oscillator
UV	ultraviolet
VCSEL	vertical-cavity surface-emitting laser
VECSEL	vertical-external-cavity surface-emitting laser
YAG	yttrium aluminium garnet
Yb	ytterbium
Yb:KYW	ytterbium-doped potassium yttrium tungstate

List of Symbols

α_{RT}	Round-trip loss of the optical resonator
$(\xi_i)_{\mathrm{out}}$	Output idler photon flux
α_p	Round-trip loss of the fundamental pump-laser cavity
α_s	Round-trip loss of the resonant signal cavity
α_{par}	Cavity parasitic loss
α_{tr}	Cavity transmission loss
α_{H}	Henry linewidth enhancement factor
β	Phase-modulation depth
$\chi^{(1)}$	First-order linear susceptibility
$\chi^{(2)}$	Second-order nonlinear susceptibility
$\chi^{(3)}$	Third-order nonlinear susceptibility
$\Delta\nu_{\mathrm{FWHM}}$	FWHM linewidth of the cavity resonance
$\delta f(t)$	Instantaneous frequency fluctuation
Δk	Wavevector mismatch
Δt_{FWHM}	Temporal FWHM of the cavity resonance

List of Symbols

$\delta\lambda$	Spectral acceptance bandwidth
$\Delta\lambda_{\mathrm{FSR}}^{\mathrm{E}}$	Etalon free spectral range in wavelength
$\Delta\lambda_{\mathrm{FWHM}}$	FWHM spectral linewidth of the cavity resonance
$\Delta\nu_{\mathrm{FSR}}^{\mathrm{cav}}$	Cavity free spectral range
$\Delta\nu_{\mathrm{FSR}}^{\mathrm{E}}$	Etalon free spectral range
$\Delta\nu_{\mathrm{FSR}}^{\mathrm{FPI}}$	Fabry–Pérot interferometer free spectral range
$\Delta\nu_{\mathrm{FSR}}^{\mathrm{PDH}}$	PDH reference cavity free spectral range
$\Delta\nu_{\mathrm{cold}}$	Cold-cavity linewidth
$\Delta\nu_{\mathrm{det}}$	Frequency detuning from the cavity resonance
$\Delta\nu_{\mathrm{RMS}}$	Root-mean-square linewidth
$\Delta\nu_{\mathrm{STH}}$	Quantum-limited Schawlow–Townes–Henry linewidth
ϵ	Pound–Drever–Hall error signal
ϵ_0	Permittivity of free space
$\eta_{\mathrm{in}}^{\mathrm{ext}}$	External pump coupling efficiency
η_0	Slope efficiency in the absence of cavity losses
η_{abs}	Absorbed fraction of external pump power
$\eta_{\mathrm{conv,max}}$	Maximum pump-to-laser conversion efficiency
η_{det}	Detection efficiency
η_{eff}	Effective slope efficiency
η_{int}	Internal conversion efficiency
η_{quant}	Quantum efficiency

List of Symbols

η_{sig}	Signal field coupling efficiency
γ	Effective damping constant
Γ_{NL}	Nonlinear coupling coefficient
Γ_{par}	Parametric gain factor
λ	Optical wavelength
λ_{in}^{p}	External pump wavelength
λ_L	Fundamental pump laser wavelength
λ_{fund}	Fundamental pump laser wavelength
λ_{id}	OPO idler wavelength
λ_{lock}	Locked wavelength
λ_{sig}	OPO signal wavelength
Λ_{QPM}	Quasi-phase-matched grating period
$\mathcal{F}$	Cavity finesse
$\mathcal{L}$	Cavity loss
ν	Optical frequency
ν_e	Cyclic carrier frequency
Ω	Phase-modulated angular frequency
ω	Angular frequency
ω_e	Optical carrier angular frequency
ω_n	n^{th} angular frequency
ω_{RO}	Relaxation oscillation angular frequency

List of Symbols

$\phi(t)$	Instantaneous phase fluctuation of the optical field
$\phi_E(\lambda)$	Etalon round-trip phase
ϕ_{Gouy}	Gouy phase shift
Φ_{RT}	Round-trip optical phase
σ	Normalised external pump parameter
σ_{th}^{L}	Photon flow threshold of the fundamental laser
$\sigma_{\text{th}}^{\text{SRO}}$	Photon flow threshold of the SRO
τ	Time delay
$\tau_{\perp}$	Polarization dephasing time
τ_c	Cavity photon lifetime
τ_p	Photon lifetime of the intracavity pump field
τ_s	Photon lifetime of the OPO signal field
τ_u	Upper-state population lifetime
τ_{SRO}	Photon lifetime of the SRO field
θ	Beam divergence angle
θ_E	Etalon internal refraction angle
θ_{inc}	Angle of incidence relative to the optical axis
ξ_s	Intracavity signal photon flux
ξ_{foc}	Focussing parameter
ξ_{max}	Maximum slope efficiency of the fundamental pump laser
ξ_{sat}	Saturated intracavity signal photon flux

List of Symbols

ξ_{sp}	Spontaneous-emission contribution to the laser mode
B	Spatial walk-off parameter
b	Confocal parameter
c	Speed of light in vacuum
D	Duty cycle
d_{eff}	Effective nonlinear coefficient
d_{il}	Nonlinear coefficient of a single-domain bulk material
e	Elementary charge
$E(t)$	Complex optical electric field
$e(t)$	Control error signal
E_2^{out}	Output second-harmonic electric-field amplitude
E_0	Unmodulated electric-field amplitude
E_{inc}	Incident electric-field
E_{ref}	Reflected electric-field
$F(\omega_e)$	Complex cavity reflection coefficient
f_c^{laser}	Laser cavity cutoff frequency
$f_{\mathrm{cutoff}}^{\mathrm{OPO}}$	OPO cavity cutoff frequency
$f_{\mathrm{cutoff}}^{\mathrm{VECSEL}}$	VECSEL cavity cutoff frequency
f_c^{th}	Thermal cutoff frequency
$f_{\mathrm{cutoff,3dB}}$	3-dB cavity cutoff frequency
G_m	Fourier coefficient of the m^{th} grating harmonic

List of Symbols

G_{cw}	Parametric gain of the ICSRO in the CW regime
h	Plank's constant
h_m	Boyd–Kleinman focussing function of order m
I	Photocurrent
I_p	Intensity of the fundamental pump laser
k	Wavevector magnitude
k_d	Derivative gain
k_i	Integral gain
k_m	Fourier wavevector of the QPM grating
k_p	Proportional gain
l	Total crystal length
l_c	Coherence length
l_d	Microscopic domain length
L_E	Etalon thickness
L_{cav}	Cavity length
M^2	Beam propagation ratio
M_{OC}	Output-coupling mirror
N	Saturated laser gain
n	Refractive index
n_E	Etalon refractive index
P_{th}^L	External pump power at the fundamental laser threshold

List of Symbols

$P_{\text{th}}^{\text{SRO}}$	External pump power at the SRO threshold
P_c^{PDH}	Optical power in the PDH carrier
P_s^{PDH}	Optical power in the PDH sideband
P_{out}^{L}	Output power of the fundamental pump laser
P_p	Fundamental pump power used in the coupled-wave equations
P_s	OPO signal power used in the coupled-wave equations
P_{DC}	Total down-converted power
P_{id}	OPO idler output power
P_{intra}	Intracavity pump power
P_{in}	Input pump power of the external pump laser
P_{out}	Laser output power
P_{ref}	Reflected power
P_{sig}	OPO signal output power
$P_{\text{th}}^{\text{SRO,intra}}$	Intracavity pump power at the SRO threshold
q	Complex beam parameter
R	Radius of curvature of a wavefront
r	Radius of curvature of a mirror
R_E	Etalon surface reflectivity
$R_E(\tau)$	Temporal autocorrelation function
R_M	Mirror reflectivity
r_m	Amplitude reflection coefficient

List of Symbols

R_T	Product of cavity mirror reflectivities
R_{DM}	Dichroic mirror reflectivity
R_{id}	Mirror reflectivity at the idler wavelength
R_{PD}	Photodiode responsivity
R_{sig}	Mirror reflectivity at the signal wavelength
S_0	Shot-noise-limit
$S_I(\omega)$	Intensity-difference noise spectrum
$S_I(f)$	Current power spectral density
$S_\beta(f)$	β-separation line for frequency noise analysis
$S_{\mathrm{SN}}(f)$	Shot-noise power spectral density
$S_\nu(f)$	Frequency noise power spectral density
$S_\phi(f)$	Phase noise power spectral density
T_E	Etalon single-pass transmission
$T_E(\lambda)$	Etalon wavelength-dependent transmission
T_{crystal}	Nonlinear crystal temperature
T_{NC}	Single-pass transmission of the nonlinear crystal
T_{OC}	Output coupler transmission
$u(t)$	PID controller output
V	Variance of the squeezed state after optical loss
V_0	Variance of the squeezed state before optical loss
w	Gaussian beam radius

List of Symbols

w_0	Gaussian beam waist radius
x	Intracavity saturation parameter
y_{pv}	Measured process variable
y_{sp}	Setpoint of the control system
z_0	Beam waist position
z_R	Rayleigh range

Chapter 1

Introduction

1.1 Introduction

Continuous-wave (CW) (optical parametric oscillators (OPOs)) constitute a significant class of coherent light sources, notable for their exceptionally broad spectral coverage and high degree of tunability. These characteristics have positioned CW OPOs as essential tools across both fundamental scientific research and a wide range of industrial sectors. In particular, their versatility enables advanced capabilities in ultra-sensitive trace-gas detection [1], [2], where precise, stable, and spectrally agile light sources are critical. An especially compelling attribute of CW OPOs is their inherent suitability for quantum optics experiments and emerging quantum information processing platforms and protocols. Through the generation of highly-correlated signal and idler fields, CW OPOs offer an efficient and well-suited platform for the implementation of entanglement-based protocols [3], [4], [5] and for the potential generation of squeezed states of light [6], [7], [8].

The strong correlations between signal and idler photons in CW OPOs arise from a simple and well-established nonlinear optical interaction. Within a nonlinear $\chi^{(2)}$ medium, parametric down-conversion (PDC) can result in the simultaneous creation of two photons from a single higher-energy pump photon. The parametrically generated signal and idler photon pairs are intrinsically correlated in energy, momentum, and

polarization and, in the ideal lossless case, exhibit complete suppression of intensity-difference noise at zero analysis frequency [9].

In this investigation, we undertake a comprehensive approach to the design, characterisation and development of a compact, low-noise laser system tailored for high-precision applications, where stringent requirements on phase and intensity noise are critical. The focus of this work is the realisation of an actively-stabilised, dual-locked CW singly-resonant optical parametric oscillator (SRO), pumped internally to an AlGaInP based vertical-external-cavity surface-emitting laser (VECSEL).

The following introductory chapter provides a concise overview of the fundamental concepts underlying CW OPOs, including phase matching principles and periodically-poled lithium niobate (PPLN) technology, as well as a historical perspective on the development of CW OPO systems. The role of VECSELs as compact, high-power, and low-noise pump sources for CW OPOs is also briefly reviewed, together with an explanation of why VECSELs are well-suited to act as the pump source for OPOs in future quantum experiments, particularly in the generation of intensity-difference squeezing. Finally, the chapter concludes with an outline of the thesis, highlighting the design and implementation of a compact, low-noise laser system tailored for integration into next-generation quantum optical platforms.

1.2 The continuous-wave optical parametric oscillator (CW OPO)

The optical parametric oscillator, referred to as an OPO, is the laser source of choice if high-conversion efficiency, broad spectral tunability, and/or highly-correlated photon-pair generation is required. The CW OPO is a nonlinear (coherent) frequency converter. It operates by converting monochromatic pump laser light into a tunable optical output through a second-order nonlinear interaction known as three-wave mixing. At the heart of an OPO lies a nonlinear optical medium. While OPOs can, in principle, be realised in both $\chi^{(2)}$ and $\chi^{(3)}$ media, the former is by far the most commonly employed, particularly

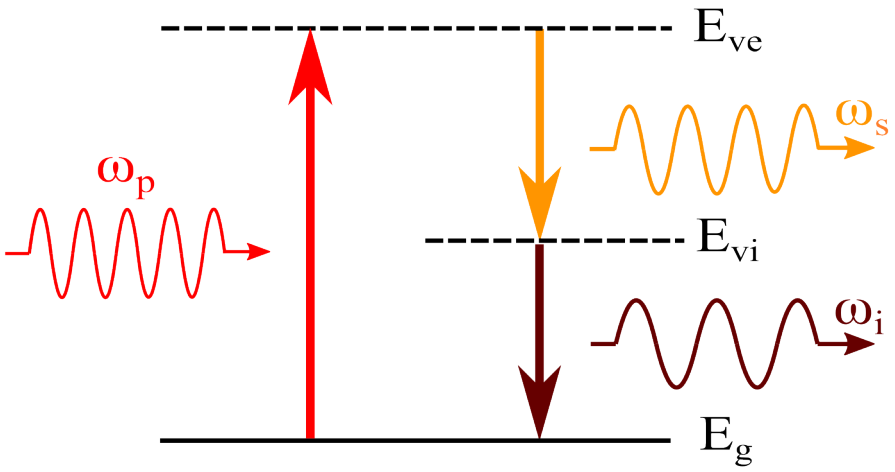


Figure 1.1: Virtual energy-level diagram of parametric down-conversion (PDC) in a $\chi^{(2)}$ nonlinear medium, where a pump photon at frequency ω_p is converted into signal (ω_s) and idler (ω_i) photons via a virtual state, satisfying $\omega_p = \omega_s + \omega_i$. E_g: ground-state energy; E_{vi}: intermediate virtual-state energy; E_{ve}: excited virtual-state energy.

in bulk-optics. In the $\chi^{(2)}$ case, a non-centrosymmetric crystal is typically used and is characterised by an effective nonlinearity coefficient d_{eff} which governs the strength of the parametric interaction. Within this medium, PDC occurs as a nonlinear optical process in which a pump photon ω_p is converted into two lower-energy photons, referred to as the signal ω_s and idler ω_i. The interaction proceeds via a virtual energy state and conserves energy such that $\omega_p = \omega_s + \omega_i$, reflecting the underlying coherent three-wave mixing process (see Fig. 1.1). Due to energy conservation in the parametric interaction, the sum of the energies of the down-converted photons equals the energy of the pump photon.

Likewise, the signal and idler are also governed by momentum conservation, a phenomenon commonly referred to as phase matching. Phase matching is the condition where the phase velocities (or wave vectors) of all the interacting waves are matched so that the generated wave builds up coherently along the propagation direction. Due to its instantaneous nature and independence from vibrational or electronic transitions, PDC readily satisfies phase matching conditions across a broad range of signal–idler

wavelength combinations. Therefore, the tuning range of an OPO can span over the entire transparency range of the nonlinear medium. To enhance the efficiency of the parametric process and reduce the otherwise high oscillation threshold, the OPO is constructed by placing the nonlinear medium inside an optical cavity (see Fig. 1.2). This cavity provides selective feedback at the signal, idler, or both wavelengths, effectively compensating for the low parametric gain of the nonlinear process.

Among the key trends in the literature on CW OPOs, a significant focus is the threshold characteristics of different resonance schemes. The five main configurations of CW OPOs are presented in Fig. 1.2, each offering distinct trade-offs in terms of complexity, stability and performance. Of these, the externally-pumped SRO [10], depicted at the top of Fig. 1.2, is widely regarded as the most practically robust and structurally simple configuration. However, this simplicity comes at a cost. Even with the use of advanced, periodically-poled (PP) nonlinear materials, the typical threshold pump power required to initiate oscillation in such systems remains on the order of a few Watts [11]. When employing more conventional birefringent nonlinear materials or PP arsenate or phosphate crystals – such as potassium titanyl phosphate (KTP), rubidium titanyl arsenate (RTA) or potassium titanyl arsenate (KTA) – the thresholds are often significantly higher, frequently exceeding tens of watts. This imposes stringent performance demands on the pump laser, often negating the low-scale engineering aims of pursuing such a simple OPO configuration.

To address the high-threshold power requirements of CW SROs, several alternative configurations have been explored. As illustrated in Fig. 1.2, these include the doubly-resonant OPO (DRO), the pump-enhanced OPO (PE-OPO), and the triply-resonant OPO (TRO). Among these, the TRO configuration remains largely impractical – despite offering the lowest oscillation thresholds – due to the considerable complexity involved in maintaining the simultaneous resonance of the pump, signal, and idler waves within a single optical cavity [12]. In addition, TROs typically operate with minimal output power extraction, further limiting its utility in real-world applications. However, it is

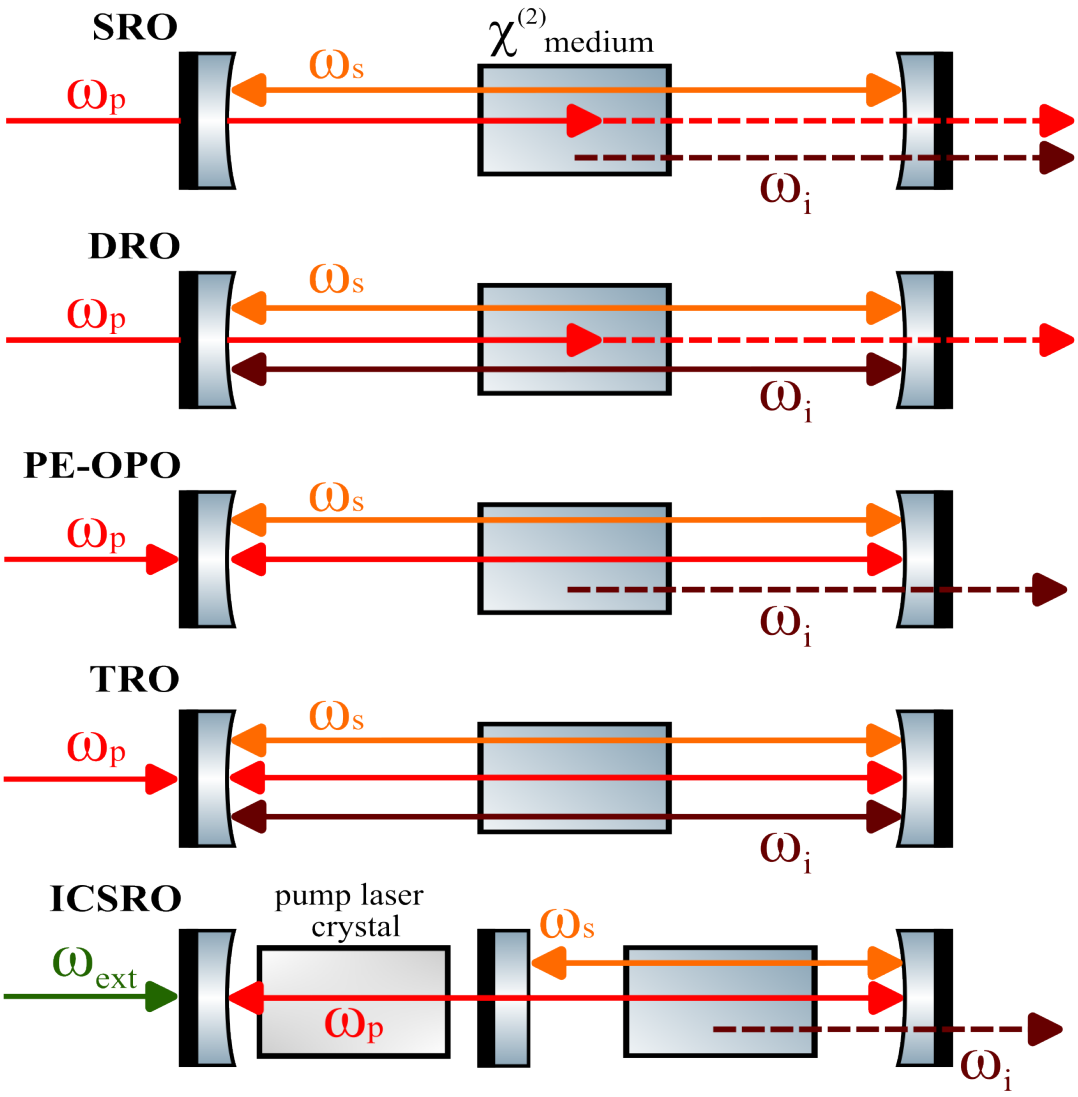


Figure 1.2: CW OPO cavity configurations. **SRO**: externally-pumped singly-resonant OPO with resonant signal field. **DRO**: doubly-resonant OPO with both signal and idler fields resonated. **PE-OPO**: pump-enhanced OPO with resonant signal and enhanced pump field. **TRO**: triply-resonant OPO with resonant signal, idler, and pump fields. **ICSRO**: intracavity pumped singly-resonant OPO with resonant signal field. ω_{ext}, ω_p, ω_s, and ω_i denote the external pump, OPO pump, signal, and idler angular frequencies, respectively. To note, each configuration is implemented using different mirror coatings (broadband or dielectric) to achieve the desired resonances.

worth noting that such a configuration can become more feasible in integrated photonic platforms, where phase matching and cavity constraints can be more readily engineered.

Similarly, the DRO architecture offers a substantial reduction in oscillation threshold compared to the SRO – often down to the several tens of milliwatt level – because it resonates both the signal and idler waves. The DRO was in fact the basis for the first experimental demonstration of a CW OPO [13]. Despite its favorable threshold characteristics, it has not been considered a widespread choice in practical systems primarily because of the stringent stability requirements of its optical cavity. Maintaining simultaneous resonance of both signal and idler fields requires stabilisation of the cavity length to within $\sim 1\,\text{nm}$ [14], [15].

A hybrid solution that seeks to combine the low-threshold advantage of the DRO with the spectral tunability of the SRO is found in the PE-OPO design [16]. In this configuration, the pump field is resonant in the cavity along with one of the parametrically generated waves (either the signal or the idler), thereby relaxing the dual-resonance constraint of the DRO and enabling broader wavelength tunability. However, this advantage is still accompanied by increased system complexity, in comparison to the SRO configuration, as stable operation typically requires active stabilisation of the enhancement cavity to maintain pump resonance.

To realise a practical, field-deployable OPO system with robust temporal and amplitude stability, it is essential to eliminate the stringent stability demands imposed by the DRO resonance condition – without the corresponding increase in oscillation threshold. The ideal configuration would be to combine the passive stability inherent to SROs with the threshold powers comparable to those of PE-OPOs and DROs. These advantageous characteristics are embodied in the intracavity singly-resonant OPO (ICSRO) configuration, as illustrated at the bottom of Fig. 1.2. In this architecture, an SRO is embedded within the resonator of a high-finesse pump laser, enabling it to benefit from the intense intracavity pump field and, as a result, substantially reduce the threshold values typically associated with externally-pumped SROs. Moreover, since the pump field is not resonant within the OPO cavity, the system does not require a single-frequency pump laser; any multimode structure in the pump is transferred directly to the non-resonant output field of the OPO, rather than being constrained by resonance conditions. In the

ICSRO scheme, the pump wave and the resonant parametric wave (signal; see Fig. 1.2) propagate through a shared arm of the laser cavity. A key design element is the mirror that is highly reflective at both the pump and resonant OPO wavelength, forming one end of the OPO resonator. A dichroic beam splitter mirror is also incorporated into the cavity to distinguish between the pump and resonant parametric wave. This beam splitter is antireflection coated for the pump wavelength – allowing it to pass through with minimal loss – while being highly reflective at the wavelength of the resonant OPO wave, thus maintaining effective feedback for the OPO. The ICSRO cavity is completed by a third mirror, forming a compact and efficient intracavity resonator.

In this work, particular emphasis is placed on ICSRO systems in which the OPO is internally pumped by a VECSEL, motivated by their intrinsically low-noise characteristics and their suitability for high-precision, low-noise applications. Since VECSELs constitute a central element of the present study, the following section provides a brief overview of the VECSEL technology.

1.3 Vertical-external-cavity surface-emitting lasers (VECSELs)

Vertical-external-cavity surface-emitting lasers (VECSELs), also known as semiconductor disk lasers (SDLs), have emerged as versatile laser sources, particularly in applications where high brightness and spectral flexibility are required. These devices represent a hybrid class of laser sources that effectively merge the advantageous characteristics of both solid-state and semiconductor laser technologies, while mitigating many of their respective limitations.

A typical VECSEL comprises a semiconductor gain chip incorporating multiple quantum wells (MQWs) and an integrated distributed Bragg reflector (DBR), together with an external optical cavity containing the output coupler (OC) and, where required, additional intracavity optical elements. The DBR provides high reflectivity at the semiconductor end of the resonator, while the OC couples a fraction of the intracavity field

out as the laser output. Unlike conventional edge-emitting semiconductor lasers, where emission occurs along the plane of the wafer, the VECSEL cavity emits light perpendicular to the chip surface. Moreover, the gain chip is predominantly optically pumped – typically at an angle relative to its surface – with the pump radiation absorbed primarily in the barrier regions surrounding the MQWs. The resulting photogenerated carriers then relax into the quantum wells to generate the required population inversion, enabling lasing once the round-trip optical gain compensates the total cavity losses. By spatially separating the semiconductor gain structure from most of the cavity optics, this external-cavity configuration permits wavelength-selective, polarization-control, mode-control, and nonlinear optical elements to be incorporated within the resonator, providing substantial flexibility in tailoring the spectral, polarization, modal, and nonlinear characteristics of the laser output.

Among these capabilities, wavelength-selective elements within the external cavity enable precise control over the laser's emission spectrum. For example, the insertion of a birefringent filter enables continuous wavelength tuning over spectral ranges spanning tens of nanometers, depending on the gain bandwidth, while also narrowing the emission linewidth [17], [18]. Further spectral refinement can be achieved through the addition of one or more intracavity etalon or Lyot filters, allowing the laser to operate in a single longitudinal mode, as demonstrated by the GaAs-AlGaAs VECSEL reported by Holm *et al.* [19], which operated near 870 nm. In addition to intracavity spectral control, the emission wavelength of VECSELs can be tailored through bandgap and cavity engineering. This provides broad wavelength flexibility, with VECSEL-based sources demonstrated from the deep ultraviolet via harmonic generation [20] to the mid-infrared [21].

Beyond spectral control, the external cavity architecture permits integration of nonlinear optical crystals, exploiting the high intracavity power to enable processes such as second-harmonic generation (SHG) [22] and stimulated Raman scattering (SRS) [23], [24]. This capability also underpins the intracavity OPO concept, in which the OPO crystal is placed directly within the high-finesse cavity of the pump laser, leading to substantially reduced oscillation thresholds compared with externally-pumped OPO sys-

tems. In this context, the high mechanical stability requirements associated with DROs, TROs, and PE-OPOs [25] can be avoided by designing the OPO to operate where only one of the down-converted fields is made resonant (SRO). Although this configuration has a higher oscillation threshold, the high intracavity power available from the VECSEL makes this threshold readily accessible and, in addition, the alignment and tunability of the SRO will be far more straightforward in comparison to DRO, TRO, and PE-OPO systems. The first demonstration of a VECSEL-pumped OPO was carried out by Stothard *et al.* [26], delivering a total down-conversion efficiency (down-converted power) of 83.3% (1.25 W) by pumping the OPO with a 1060 nm InGaAs-based VECSEL system to reach the mid-infrared. A few years later, Hempler *et al.* [27] reported up to 250 mW of narrow-linewidth idler output at 3.3 µm. To date, this remains the only study suggesting that 'frequency pulling' may influence the stability of such systems operating under high nonlinear frequency conversion. Despite this phenomenon, the spectral bandwidth of the OPO output was measured to be <0.14 nm through careful and laborious alignment. More recently, Tsai *et al.* [28] demonstrated a dual-wavelength InGaAs-based VECSEL-pumped OPO system, enabling dual-wavelength idler generation in the mid-infrared. At a maximum diode pump power of 13.6 W, a combined dual-wavelength idler output power of 153 mW was obtained, corresponding to a conversion efficiency of 1.13% and an extraction efficiency of 2.26%.

Another important advantage of VECSELs is their potential for low intensity noise, which is associated with their Class-A dynamical regime. This regime arises when the upper-state carrier lifetime is short relative to the cavity photon lifetime, allowing the population inversion to respond rapidly to fluctuations in the intracavity field. Consequently, the carrier dynamics can be adiabatically eliminated, resulting in an effective first-order model of the intracavity field and avoiding the relaxation-oscillation dynamics that are characteristic of Class-B operation. Therefore, when combined with their high brightness and broad spectral flexibility, these low-noise characteristics make VECSELs attractive pump sources for OPOs and promising candidates for applications in next-generation quantum technologies.

The fundamental operating characteristics of VECSELs have been introduced here to establish their relevance to the present work, while a detailed review of the VECSEL technology and its properties relevant to VECSEL-pumped OPOs is presented in Chapter 3.

1.4 Quasi-phase matching (QPM)

Phase matching, otherwise referred to as momentum conservation, ensures that the interacting and generated waves remain in phase as they propagate through a nonlinear crystal. In nonlinear optics, phase matching is typically achieved via birefringent phase matching (BPM), where the birefringence of suitable nonlinear crystals is exploited. In a birefringent crystal, the refractive index depends on both wavelength and polarization relative to the crystal axes. Therefore, by choosing appropriate polarizations and directions for each of the interacting waves, BPM ensures that their wave vectors are matched, corresponding to equal phase velocities [29]. This allows the generated waves to build up coherently along the crystal, thus maximising the efficiency of the nonlinear interaction.

An alternative approach, known as quasi-phase matching (QPM), eliminates the need for BPM to satisfy the phase matching condition ($\Delta k = 0$). QPM is realised via ferroelectric domain engineering, in which the sign of the crystal's nonlinear coefficient is periodically inverted after each coherence length (see Fig. 1.3; first-order QPM). Each domain reversal effectively resets the phase mismatch, enabling constructive interference to be maintained throughout the entire interaction length of the crystal.

QPM offers several key advantages over conventional BPM techniques. Unlike BPM schemes, QPM can be achieved for an arbitrary range of operating temperatures, meaning non-critical phase matching is possible at any wavelength throughout the transparency range of the nonlinear material. In addition, QPM allows the nonlinear interaction to be engineered to exploit the largest component of the material's second-order nonlinear susceptibility tensor. This is particularly effective in ICSRO research, as the

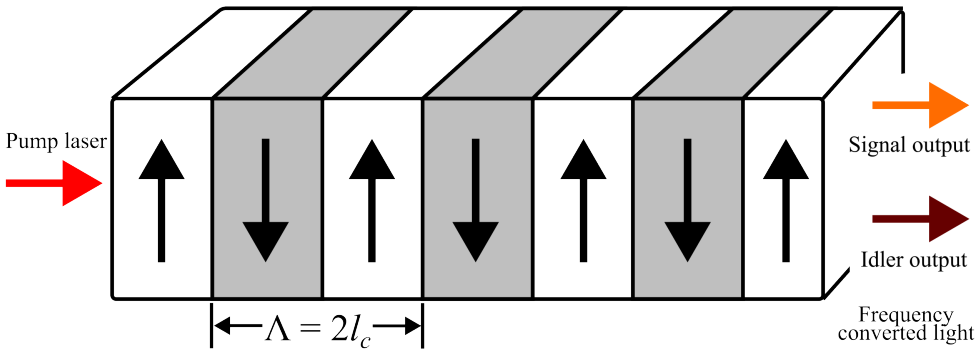


Figure 1.3: Schematic illustration of PDC in a periodically-poled nonlinear material. The sign of the nonlinear coefficient is inverted periodically (after every coherence length, l_c; first-order QPM) to compensate for phase mismatch and enable constructive interference throughout the material's interaction length.

SRO threshold condition scales inversely with the square of the effective nonlinearity coefficient [30]. Therefore, QPM is promising for reducing the pump power required to reach oscillation threshold in ICSRO systems. In many cases, QPM allows all interacting waves to be polarized along the same direction – a configuration that is incompatible with BPM. Consequently, QPM not only enhances the efficiency of nonlinear optical processes but also extends the range of usable materials to include non-birefringent and optically isotropic crystals, such as GaAs, InP, and ZnSe. A more complete description and theoretical treatment of QPM appears in Chapter 2.

1.5 Periodically-poled $LiNbO_3$ (PPLN)

The majority of CW OPOs developed to date have been based on periodically-poled $LiNbO_3$ (PPLN) [25]. This is in no small part down to the high nonlinearity of the material ($d_{\text{eff}} \sim 17$ pm/V) and the long (commercially-available) interaction lengths, both of which significantly reduce the threshold power required for OPO oscillation. Consequently, PPLN-based ICSROs have achieved operation well within the capabilities of commercially-available CW pump lasers. Therefore, the use of PPLN, especially for SRO and ICSRO configurations, has enabled remarkably low threshold levels to be obtained,

along with high down-conversion efficiencies and broad spectral tunability. However, to mitigate the risk of photorefractive damage – a known issue in undoped congruent $LiNbO_3$ – the PPLN crystal is typically doped with a small amount of magnesium oxide (MgO). The resulting material, referred to as MgO:PPLN, combines high nonlinear performance with enhanced photostability, making it a material of choice in many modern CW ICSRO systems. A more comprehensive review of PPLN and MgO:PPLN is provided in Chapter 3.

1.6 Historical review of CW OPOs and ICSROs

In 1965, Giordmaine and Miller [31] provided the first experimental demonstration of OPOs, utilising high peak power pulsed lasers as the pump source. While this milestone marked a significant advancement in nonlinear optics, the limitations of pulsed systems – particularly with respect to spectral linewidth and frequency stability – motivated a shift in research focus towards the development of CW OPOs.

The first CW OPO was demonstrated by Smith *et al.* [13], who developed a CW DRO pumped by a frequency-doubled Nd:YAG laser. Despite its significance, the CW DRO system suffered from severe limitations in both spectral and amplitude stability. These shortcomings ultimately hindered their practical use, especially after the advent of dye lasers in the early 1970s, which offered superior tunability and spectral performance [32]. In the years that followed, Smith [33] contributed significantly to diagnosing and addressing these limitations, thereby renewing interest in CW OPOs more broadly. The potential of these devices was further realised with the introduction of stable, single-frequency, actively-stabilised pump lasers (isolated from detrimental back-reflections) which, in turn, enabled the demonstration of a CW DRO operating with amplitude-stable, single-frequency output over an acquisition time of several seconds [33].

It was not until the late 1980s that CW OPOs emerged as viable sources of highly stable and tunable radiation for high-precision applications. The devices developed during this time period primarily employed monolithic CW DROs in ring-cavity ge-

ometries, which offered unidirectional operation and enhanced stability. These systems were typically pumped by single-frequency diode-pumped solid-state lasers (DPSSLs), frequency-doubled to the green spectral region, with frequency precision at the kHz-level [34], [35].

Subsequent advances in nonlinear crystal technology greatly improved both the practicality and versatility of CW OPO systems. While early implementations predominantly relied on BPM crystals, the mid-1990s marked a pivotal shift in direction with the widespread adoption of QPM techniques. Originally proposed by Armstrong *et al.* [36] in the early 1960s, QPM revolutionised the field and led to substantial reductions in the oscillation threshold for SRO devices, which are now driven by readily available CW pump lasers [10], [11].

The development of periodically-poled materials not only broadened the spectral accessibility of CW OPOs but it also inspired novel cavity configurations. One such configuration involved placing the CW SRO within the resonator of the pump laser itself, thereby exploiting the high circulating pump intensities. This architecture, known as the CW ICSRO, was first reported by Colville *et al.* [37] in 1997. This system employed a KTP crystal positioned at the intracavity focus of a Ti:sapphire laser, generating an output power of 400 mW with an amplitude-stability of $\pm 8\%$ over a 50s measurement interval. A detailed insight into the steady-state and transient power characteristics of CW ICSROs can be found in Refs. [30], [38].

Considerable progress in the development of CW ICSROs was achieved through integration of well-established DPSSLs, particularly those employing Neodymium-doped crystal hosts such as Nd:YAG [39] and Nd:YVO_4 [40], [41]. Thanks to their ability of being efficiently pumped by compact, high-brightness laser diodes, these systems offer significantly higher wall-plug efficiency compared to Ti:sapphire-based counterparts, which depend on bulky and energy-inefficient pump sources like argon-ion lasers. Despite these advantages, the applicability of DPSSL-based ICSROs – especially for quantum optics experiments and squeezed light generation – has been constrained by their Class-B dynamical behaviour. This regime, in which the upper-state population lifetime of

the gain medium exceeds the cavity photon lifetime, is inherently prone to such prolonged bursts of relaxation oscillations occurring above the SRO oscillation threshold. As a result, the coupling between the pump-wave relaxation oscillation and the OPO resonant-wave depletion, results in a so-called self-pulsing effect.

Recent work has demonstrated effective methods for suppressing self-pulsing in solid-state-pumped ICSROs. One approach employs a SHG crystal inside the pump resonator, where the quadratic pump depletion introduced by SHG provides a stabilising mechanism that counteracts the linearly driven instability associated with the resonant signal (or idler) field. This passive stabilisation has minimal impact on the non-resonant idler (or signal) wave, with reported power reductions below 3% [42]. Building on this concept, Cho and Chen [43] demonstrated suppression of self-pulsing in a CW Nd:YVO_4 ICSRO using Raman-based damping, eliminating the need for an additional SHG crystal. In this scheme, self-stimulated Raman scattering in the Nd:YVO_4 crystal introduces a higher-order depletion of the pump field through appropriate resonator coating design, analogous to SHG-based stabilisation, while similarly limiting the reduction in non-resonant idler power to $\sim$3%.

Having reviewed the historical development of CW OPO and ICSRO platforms, the following section introduces the concept of intensity–difference squeezing and examines how the favourable characteristics of the VECSEL technology position it as an ideal pump source for OPO systems. Particular emphasis is placed on the suitability of VECSEL-pumped architectures for integration into high-precision applications, including quantum optics experiments and squeezed states of light, where low-noise performance is essential.

1.7 Motivation for investigating VECSEL-pumped OPOs for quantum optical applications

The generation of non-classical states of light with ultra-low technical noise and long-term stability is a central requirement in modern quantum optics experiments and under-

pins a wide range of continuous-variable (CV) quantum technologies [8]. In this context, OPOs operating in the CW regime have emerged as a leading platform for producing squeezed and entangled optical fields. However, the performance of such systems is fundamentally constrained by the noise and stability characteristics of the pump source, which ultimately limits the degree of squeezing attainable in practice.

The following subsections outline the principles of intensity-difference squeezing and evaluate the advantages of utilising a VECSEL-pumped OPO system rather than a conventional DPSSL-pumped OPO system for quantum optical applications.

1.7.1 Intensity-difference squeezing

The reduction of noise in the intensity-difference between the signal and idler fields can be understood through a simple physical argument. In the process of PDC, each annihilated pump photon gives rise to the simultaneous emission of a photon pair at frequencies ω_1 and ω_2. This pairwise generation mechanism produces so-called 'twin beams' whose photon-number fluctuations are intrinsically correlated, resulting in identical photon statistics and, in the ideal lossless case, complete noise suppression in the intensity difference. In an OPO, the presence of a resonant cavity surrounding the nonlinear crystal introduces partial temporal decorrelation between the two fields due to the finite cavity storage time. Consequently, the photon numbers in the signal and idler output beams are expected to be nearly equal only within a time interval equivalent to the OPO cavity storage time.

Several factors limit the achievable degree of intensity-difference squeezing in an OPO system. Of these factors, limitations arising from photodetector quantum efficiency are negligible due to the current availability of high-efficiency balanced detectors, while excess pump intensity noise is not expected to be restrictive when employing a VECSEL pump source, as discussed in Section 1.7.2. Photocurrent imbalance between the signal and idler fields can also reduce the observed squeezing; however, this effect can be mitigated through appropriate cavity design, as detailed in Chapter 6. For context, this photocurrent imbalance disrupts the ideal cancellation of correlated noise between the

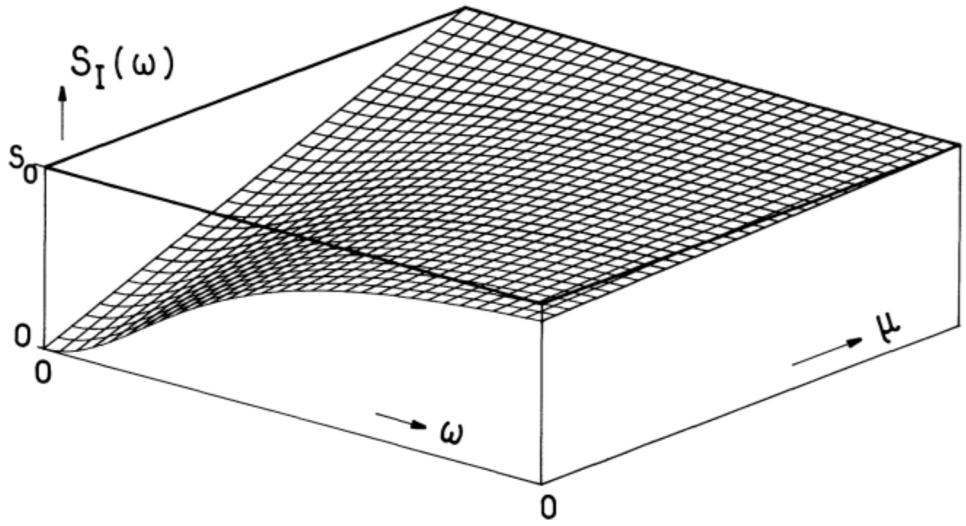


Figure 1.4: Intensity-difference $(I_1 - I_2)$ noise spectrum $S_I(\omega)$ as a function of intracavity loss μ and angular frequency ω. The reference level S_0 represents the standard quantum (shot) noise for a beam with total intensity $I_1 + I_2$, where I_1 and I_2 are the intensities of the signal and idler. Figure reproduced from Ref. [9].

signal and idler fields, thereby allowing pump-induced fluctuations to partially leak into the measured intensity noise. However, when the pump source exhibits intrinsically low noise – as is the case for VECSEL-based systems – the impact of this residual noise coupling is expected to be significantly reduced compared with DPSSL-based OPO systems. Therefore, the dominant limitation in a VECSEL-pumped OPO system arises from intracavity losses, which introduce uncorrelated vacuum fluctuations that degrade the attainable squeezing level. This behaviour is illustrated in Fig. 1.4, where the intensity-difference noise spectrum $S_I(\omega)$ – under conditions of perfect photocurrent balance – is reduced below the shot-noise-level S_0, with complete noise suppression at zero frequency in the absence of internal loss.

1.7.2 Proposed advantages of VECSEL pumping for intensity–difference squeezing

The generation of non-classical states of light has traditionally followed a "top-down" approach, in which quantum light sources are developed to operate with commercially available laser systems treated as fixed external components. While this strategy has proven effective for proof-of-principle demonstrations, it inherently limits both performance optimisation and scalability, since the pump laser is not designed as an integral part of the quantum system. This limitation is particularly evident in DPSSL-based OPOs, where imperfections such as prolonged bursts of relaxation oscillations can prevent complete cancellation of correlated noise between the signal and idler channels, especially at low Fourier frequencies. This sensitivity underscores the importance of pump sources with intrinsically low noise characteristics in order to suppress the transfer of technical noise into the quantum noise spectrum.

In contrast to conventional solid-state laser systems, which often require additional nonlinear stabilisation mechanisms to mitigate self-pulsing behaviour above OPO threshold [42], [43], VECSELs intrinsically avoid such instabilities due to their aforementioned Class-A gain dynamics, operating free from relaxation oscillations even above OPO threshold [26]. This intrinsically low-noise behaviour, together with their natural compatibility with intracavity integration, makes VECSELs particularly well-suited for applications in quantum optics. In this intracavity configuration, the nonlinear interaction benefits from a high effective pump intensity while simultaneously reducing the influence of technical pump noise, resulting in lower oscillation thresholds and improved noise performance compared with DPSSL-based OPO architectures.

Although the transient dynamics of ICSRO VECSEL systems have been studied both theoretically [44] and experimentally [26], their frequency and phase stability remain largely unexplored. In particular, neither the transfer of noise between the signal and idler waves under active stabilisation nor a quantitative analysis of linewidth and frequency noise has been reported. Apart from an isolated observation suggesting 'frequency-pulling' effects may influence the stability of such systems where nonlinear

frequency conversion is high [27], a systematic characterisation of noise properties in such systems is still lacking.

From an intensity-noise perspective, a more detailed discussion of VECSEL noise dynamics is provided via the model outlined by Myara *et al.* [45] in Section 5.3, where Class-A behaviour and the influence of technical noise sources are reviewed. In particular, superior low intensity noise performance of the ICSRO VECSEL system is experimentally investigated in Section 5.8, highlighting its relevance for applications in, for example, quantum-enhanced sensing [46], [47] or high-sensitivity spectroscopy [48], [49].

1.7.3 Proposed advantages of VECSEL pumping for continuous–variable (CV) quantum optics

A further potential advantage of ICSRO VECSEL systems is the ease of implementing active frequency stabilisation, enabled by the open high-finesse external cavity geometry of the VECSEL. In this work, we will show that this architecture permits simultaneous stabilisation of both the pump and resonant OPO waves, enabling the potential for all three ICSRO interacting fields to operate with low phase noise and narrow integrated linewidths. For example, previous studies of the noise dynamics of stabilised AlGaInP-based red-VECSEL systems have been demonstrated without the intracavity OPO, where integrated linewidths of 11.4 kHz [50] and 25 kHz [51] have been observed in extended three- and four-mirror VECSEL configurations, respectively. These results indicate that comparable frequency stability should be achievable for both the pump and non-resonant parametric waves in ICSRO VECSEL systems which, in turn, would represent a significant improvement over actively stabilised externally-pumped SRO architectures, for which MHz-level linewidths have typically been reported for the non-stabilised wave [52], [53]. While amplitude squeezing is relatively insensitive to pump phase noise, the simultaneous suppression of amplitude and phase fluctuations on both down-converted waves, rather than only one, is therefore crucial for advanced quantum technologies, including CV entanglement [3], [4], [5], and quantum computing [54], communication [55], [56], and imaging [57].

1.8 Thesis overview

This section provides an overview of the structure and content of the thesis, outlining the focus of each chapter and the progression of the research presented. It must also be stated that certain parts of this thesis are based on work published in peer-reviewed journals. For example, Chapter 4 is based on the work outlined in Ref. [58], while Chapter 5 is based on the work reported in Ref. [59]. In both of these publications, the candidate was the lead contributor to the research, responsible for data curation, formal analysis, investigation, methodology, software development, and preparation of the original manuscript, with equal contribution to conceptualisation and manuscript review and editing.

The second author contributed in a supporting capacity to data curation, formal analysis, investigation, and methodology development, and contributed equally to conceptualisation and manuscript review and editing. The third author contributed in a supporting capacity to formal analysis, funding acquisition, project administration, and supervision, with equal contribution to conceptualisation and manuscript review and editing. The fourth author was responsible for funding acquisition, project administration, provision of resources, and supervision, while also contributing equally to conceptualisation, formal analysis, and manuscript review and editing.

To the best of the authors' knowledge, the work presented in these publications includes, for the first time, the demonstration of an OPO pumped by a visible VECSEL system. The VECSEL gain structure is based on an AlGaInP semiconductor material platform. A key advantage of operating an OPO with a pump source in the visible spectral region lies in the ease with which the signal and idler wavelengths can be engineered to coincide with the telecommunications O- and C-bandwidths (centred at 1.3 µm and 1.55 µm, respectively), which are otherwise difficult to achieve or impossible to obtain with infrared pump sources. In addition, the ICSRO VECSEL demonstrates excellent frequency stability over extended time intervals. Based on these promising results, it was proposed that further improvements in system performance, particularly

in terms of laser stability and system noise, could be achieved through implementation of active stabilisation techniques. Building on this, Ref. [59] reports the first realisation of an actively-stabilised, dual-locked ICSRO VECSEL system. Furthermore, Ref. [59] presents the first comprehensive characterisation of the noise dynamics, including intensity and frequency noise, in a VECSEL-pumped OPO system in general. The work presented in this thesis therefore demonstrates a compact, low-noise laser system, ideally suited for future integration into quantum-based experiments and applications.

Chapter 2 provides the theoretical background for the research presented in this thesis. The chapter begins with a brief overview of the origins and development of nonlinear optics, followed by an introduction into the second-order nonlinear susceptibility tensor which governs all the second-order nonlinear frequency-mixing processes. Optical PDC is then reviewed in detail, with a focus on phase matching conditions and acceptance bandwidths. Given the central role of QPM to the design and operation of our ICSRO VECSEL system, the principles, implementation, and critical parameters of QPM techniques are then explored in detail. The chapter concludes with a review of the steady-state power characteristics of CW ICSROs, followed by a derivation of the threshold condition, based on a model outlined by Stothard [60], for ICSRO systems based on Gaussian beam profiles.

Chapter 3 provides a detailed overview of the key design considerations involved in generating efficient nonlinear frequency conversion in a VECSEL-pumped OPO system. The chapter begins with a comprehensive literature review on VECSELs, highlighting their suitability to operate as the pump source for OPOs. Following this, the selection of MgO:PPLN as the nonlinear medium is justified, based on its high effective nonlinearity, broad transparency range, and resistance to photorefractive damage. To conclude the chapter, we extended Stothard's model [60] to estimate the intracavity pump power required to reach oscillation threshold for our ICSRO VECSEL design parameters.

Chapter 4 describes the experimental investigation of achieving efficient mid-infrared generation in a CW ICSRO VECSEL system. Operating near 690 nm, the VECSEL, together with a 5%-MgO:PPLN crystal placed at the secondary intracavity focus of

a four-mirror resonator, generates CW output across the 1155–1718 nm wavelength range, with efficient PDC achieved under optimised phase matching conditions. Through careful optimisation and fine-tuning of the cavity parameters, long-term single-frequency operation was achieved for both the non-resonant signal and resonant idler waves near the telecommunications O- and C-bandwidths (1.3 µm and 1.55 µm, respectively). A full characterisation of the ICSRO VECSEL performance, including results on power scaling, output power stability, frequency stability, beam quality, spectral tunability, and overall conversion efficiency, are also presented in Chapter 4.

Chapter 5 details, for the first time, the implementation of active frequency stabilisation within an ICSRO VECSEL system. This chapter begins with a review of optical noise dynamics in optically-pumped external-cavity lasers, followed by a discussion of the dominant noise contributions specific to VECSELs, as described by the model of Myara [45]. It then introduces the principles of active frequency stabilisation, covering both Pound-Drever-Hall (PDH) and side-of-fringe (SOF) techniques, and presents a theoretical derivation of the PDH error signal. Building upon the single-frequency ICSRO VECSEL system developed in Chapter 4, this chapter details the implementation of both active-stabilisation schemes applied simultaneously to both the VECSEL fundamental wave (serving as the ICSRO pump) and the resonant idler wave of the OPO. This dual-locking approach, employing PDH locking for the pump and SOF locking for the idler, achieves sub-10 kHz integrated linewidths for the VECSEL fundamental and non-resonant signal waves and, notably, sub-kHz linewidth for the resonant idler wave. Furthermore, relative intensity noise (RIN) suppression exceeding 20 dB is achieved for all three ICSRO interacting waves at low Fourier frequencies relative to the free-running regime, while each wave exhibits a RIN below -120 dBc/Hz at frequencies above 1 kHz.

Finally, Chapter 6 provides a comprehensive summary of the work presented throughout this thesis, consolidating the key findings and contributions. In addition, the chapter outlines prospective directions for future research aimed at enhancing system performance, with particular emphasis on strategies for further noise reduction, including the implementation of additional passive and active stabilisation techniques. This chapter

also introduces a novel concept: the dual-cavity intracavity DRO (ICDRO) architecture, proposed as a potential platform for achieving high levels of quantum noise suppression. Owing to its decoupled resonance control, this configuration is expected to offer significant advantages for intensity-difference squeezing experiments. The final part of the chapter presents a numerical simulation showing that intracavity losses directly limit the achievable intensity-difference squeezing level, highlighting the critical importance of minimising losses in both the down-converted signal and idler beams.

Chapter 2

Theoretical Background

2.1 Introduction

In this chapter, there will be an extensive theoretical review of the fundamental components associated with intracavity singly-resonant optical parametric oscillators (ICSROs) and a concise overview of the frequency conversion processes inherent within $\chi^{(2)}$ optical media. The primary focus will be on optical parametric down-conversion (PDC), as this is the nonlinear process inherent to optical parametric oscillator (OPO) devices. A detailed analysis of quasi-phase matching (QPM) is also undertaken to underpin the essential acceptance parameters for efficient PDC generation. This includes the pump spectral bandwidth, which determines the maximum bandwidth over which the OPO pump can operate before portions of the pump power no longer contribute effectively to the PDC interaction. Furthermore, this chapter presents the theoretical analysis of power scaling and optimisation in continuous-wave (CW) ICSROs, highlighting the pump 'clamping' effect above the OPO threshold and identifying the conditions under which optimal pump depletion can be achieved. A derivation of the ICSRO threshold using the Stothard model [60] is then presented for a CW Gaussian pump field matched to our experimental configuration, identifying the key parameters that must be optimised to operate the ICSRO at a minimum oscillation threshold, given the limited external pump power available.

2.2 Nonlinear optics

Advances in technology and optical materials have propelled nonlinear optics into a rapidly expanding scientific research field over the past few decades. Nonlinear optics investigates the interactions between light and matter, with a particular focus on the nonlinear response of the atoms. In the following sub-chapter, we provide an overview of nonlinear optics and introduce the fundamental physical principles that govern nonlinear optical interactions. Particular emphasis is placed on second-order nonlinear interactions, with a focus on the underlying frequency-mixing processes that underpin such phenomena.

2.2.1 The origins of nonlinear optics

While most investigations into nonlinear optical phenomena rely on lasers, the theory of nonlinear optics predates the invention of the laser. This theory was initially proposed based on the electro-optic effects observed by German physicist Freidrich Pockels and Scottish physicist John Kerr [61], [62]. However, it was only with the advent of the laser – capable of generating incredibly high light intensities – that researchers were able to conduct systematic investigations into optical nonlinearities and observe remarkable nonlinear optical phenomena.

In 1961, the pioneering work of Franken *et al.* [63] marked the first practical application of nonlinear optics during the laser era. Using a pulsed ruby-optical maser, they generated a high-intensity fundamental beam at 694.3 nm, leading to the initial observation of second-harmonic generation (SHG) at 347.2 nm upon propagation through a crystalline quartz material. The resulting second harmonic signal appeared only as a very small spot on the photographic plate. This subtle feature was unfortunately misinterpreted by the lithographers at *Physical Review Letters* as a speck of dust rather than a genuine signal, and was subsequently removed from the final published version of the paper (see Fig. 2.1). Despite a relatively low conversion efficiency of $\sim 10^{-8}$,

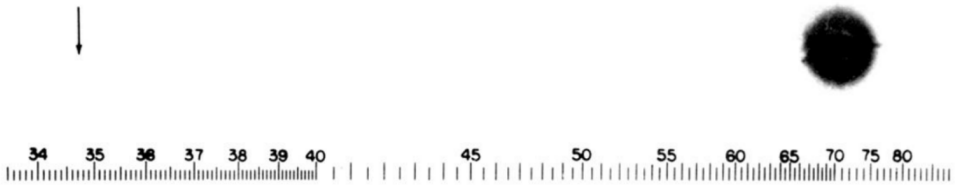


Figure 2.1: The first direct evidence of nonlinear optics within the laser era, demonstrating light at the second harmonic frequency. The wavelength scale is in units of 100 Å. It is noted that the evidence beneath the arrow is absent from the published version. Figure reproduced from Ref. [63].

this ground-breaking experiment laid the foundation for significant advancements with second-harmonic conversion efficiencies reaching $\sim$20% by early 1963 [64].

Nonlinear optical materials are commonly classified according to the order n of the nonlinear susceptibility tensor $\chi^{(n)}$ derived from a Taylor series expansion of the induced optical polarization in powers of the applied electric field [65]. In this description, the polarization is expressed as a power series, where the lowest-order terms are typically the most significant. The first term, associated with $\chi^{(1)}$, describes linear optical behaviour, while higher-order terms account for nonlinear effects. The leading nonlinear contribution is generally given by $\chi^{(2)}$, followed by $\chi^{(3)}$, with progressively smaller contributions at higher orders. However, in materials possessing inversion symmetry, the second-order susceptibility vanishes due to symmetry constraints, such that the dominant nonlinear response is governed by $\chi^{(3)}$.

Building on this classification, the order of the nonlinear susceptibility directly determines the physical processes that can occur within a given material. Second-order nonlinear optical processes include phenomena such as SHG [63], [66], [67], sum-frequency generation (SFG) [68], [69], difference-frequency generation (DFG) [36], [70], optical parametric amplification (OPA) and oscillation (OPO) [31], [71], [72], and optical rectification (OR) [73], [74]. By contrast, the third-order nonlinear susceptibility $\chi^{(3)}$ underpins a range of alternative nonlinear optical phenomena, including the Kerr effect [62], [75] and Raman scattering [76]. In this work, we restrict our attention to second-order

$\chi^{(2)}$ nonlinear interactions as these are the most relevant to bulk OPO systems. It is worth noting that the primary objective of such frequency-mixing processes is to generate light at new wavelengths that are otherwise difficult to achieve or inaccessible using conventional laser sources.

2.3 The theory of nonlinear optics

A material will become polarized when an electromagnetic (EM) wave propagates through a dielectric medium. The polarization that arises is determined by both the strength of the dielectric susceptibility and the magnitude of the electric field. Prior to the invention of the laser, the applied electric field E was generally much weaker than the inter-atomic field. Hence, the resulting polarization P was limited to a linear response described by the following expression:

$$P = \varepsilon_0 \chi^{(1)} E, \tag{2.1}$$

where ε_0 is the permittivity of free space and $\chi^{(1)}$ represents the linear electrical susceptibility. When the electric field strength of the EM wave is comparable to the inter-atomic field, as facilitated by the intense fields of focussed laser beams, the atomic response to this field enters the nonlinear regime. Consequently, the linear relationship expressed in Eq. (2.1) is no longer valid for describing the atomic response. Within the nonlinear regime, the polarization is now expressed as a power series expansion in terms of the electric field strength:

$$P = \varepsilon_0 \chi^{(1)} E + \varepsilon_0 \chi^{(2)} E^2 + \varepsilon_0 \chi^{(3)} E^3 + \cdots, \tag{2.2}$$

where $\chi^{(2)}$ and $\chi^{(3)}$ are the 2^{nd}– and 3^{rd}–order nonlinear susceptibilities, respectively.

The remainder of this sub-chapter will adopt a theoretical approach that builds upon the findings of Kleinman [77] and Boyd [65]. The focus will be exclusively on materials that exhibit a $\chi^{(2)}$ nonlinear susceptibility. This is because, in this work, optical PDC

is treated as the nonlinear process responsible for frequency conversion in the OPO, originating from second-order $\chi^{(2)}$ nonlinear interactions.

2.3.1 Crystal symmetry and the nonlinearity coefficients

The susceptibility tensors describe the relationship between the induced polarization vector and the applied electric field vector in a dielectric medium. Specifically, the second-order nonlinear susceptibility, denoted as $\chi^{(2)}_{ijk}$, is a third-rank tensor comprising 3 x 3 x 3 = 27 components. Each index $i, j, k \in \{x, y, z\}$ corresponds to one of the principal crystallographic axes of the crystal. These components collectively determine the efficiency and directionality of second-order nonlinear optical processes within the material. The tensor $\chi^{(2)}_{ijk}$ can be written as:

$$\chi^{(2)}_{ijk} = \begin{bmatrix} \chi^{(2)}_{xxx} & \chi^{(2)}_{xxy} & \chi^{(2)}_{xxz} \\ \chi^{(2)}_{xyx} & \chi^{(2)}_{xyy} & \chi^{(2)}_{xyz} \\ \chi^{(2)}_{xzx} & \chi^{(2)}_{xzy} & \chi^{(2)}_{xzz} \end{bmatrix}, \quad \begin{bmatrix} \chi^{(2)}_{yxx} & \chi^{(2)}_{yxy} & \chi^{(2)}_{yxz} \\ \chi^{(2)}_{yyx} & \chi^{(2)}_{yyy} & \chi^{(2)}_{yyz} \\ \chi^{(2)}_{yzx} & \chi^{(2)}_{yzy} & \chi^{(2)}_{yzz} \end{bmatrix}, \quad \begin{bmatrix} \chi^{(2)}_{zxx} & \chi^{(2)}_{zxy} & \chi^{(2)}_{zxz} \\ \chi^{(2)}_{zyx} & \chi^{(2)}_{zyy} & \chi^{(2)}_{zyz} \\ \chi^{(2)}_{zzx} & \chi^{(2)}_{zzy} & \chi^{(2)}_{zzz} \end{bmatrix}. \tag{2.3}$$

At this point, it is useful to introduce a widely adopted notation in the field of second-order nonlinear optics. Indeed, the susceptibility tensor $\chi^{(2)}_{ijk}$ is commonly expressed in terms of the so-called d-coefficient, where d is a tensor given by:

$$d_{ijk} = \frac{1}{2}\chi^{(2)}_{ijk}. \tag{2.4}$$

In nonlinear optics, the nonlinear polarization depends on products of electric field components and is invariant under permutation of the last two field indices. This property, known as intrinsic permutation symmetry, allows the contraction of the last two indices of the second-order nonlinear susceptibility tensor. As a result, the third-rank tensor d_{ijk} can be expressed in the contracted form d_{il}, where the combined index l represents the symmetric pair of the original indices j and k. Under this representation,

where $i = 1$ corresponds to x, $i = 2$ corresponds to y, and $i = 3$ corresponds to z, l takes on the following values:

$$\begin{array}{cccccc} xx & yy & zz & yz = zy & xz = zx & xy = yx \\ 1 & 2 & 3 & 4 & 5 & 6 \end{array} . \tag{2.5}$$

Therefore, from Eq. (2.5), $d_{xyz} = d_{xzy} = d_{14}$, $d_{zxx} = d_{31}$, and so on. This notation allows the d-coefficients to be conveniently represented as elements of a 3 x 6 matrix, rather than as a full 3 x 3 x 3 tensor (see Eq. (2.3)):

$$d_{il} = \begin{bmatrix} d_{11} & d_{12} & d_{13} & d_{14} & d_{15} & d_{16} \\ d_{21} & d_{22} & d_{23} & d_{24} & d_{25} & d_{26} \\ d_{31} & d_{32} & d_{33} & d_{34} & d_{35} & d_{36} \end{bmatrix} . \tag{2.6}$$

Another fundamental symmetry, known as Kleinman symmetry [77], applies to materials with a non-dispersive nonlinear response, in which the refractive index is effectively constant across the interacting frequencies. This symmetry states that all indices of the nonlinear susceptibility tensor can be interchanged without changing its value. Under this condition, the nonlinear polarization of the medium is invariant under any permutation of the tensor indices. Therefore, when applied to the contracted tensor d_{il}, not all of the 18 tensor elements are independent (e.g., $d_{12} = d_{26}$, $d_{14} = d_{25}$, etc.). Hence, the contracted tensor d_{il} reduces to 10 independent components:

$$d_{il} = \begin{bmatrix} \mathbf{d_{11}} & \mathbf{d_{12}} & \mathbf{d_{13}} & \mathbf{d_{14}} & \mathbf{d_{15}} & \mathbf{d_{16}} \\ d_{16} & \mathbf{d_{22}} & \mathbf{d_{23}} & \mathbf{d_{24}} & d_{14} & d_{12} \\ d_{15} & d_{24} & \mathbf{d_{33}} & d_{23} & d_{13} & d_{14} \end{bmatrix} . \tag{2.7}$$

Let us take, for example, the d_{il} coefficient for lithium niobate ($LiNbO_3$) as it is the nonlinear material utilised in this investigation. $LiNbO_3$ is a ferroelectric material that falls under the point group 3m, meaning it is a uniaxial crystal with a 3-fold rotational symmetry around the z-axis [78]. Further discussion will be given in Chapter 3. In

Table 2.1: Experimentally measured d_{il} coefficients for undoped and MgO-doped $LiNbO_3$. Each coefficient is measured in units of pm/V. Data taken from Ref. [80].

Crystal sample	**Nonlinear coefficient**	**Wavelength**	
		1064 nm	**852 nm**
Congruent undoped $LiNbO_3$	d_{31}	4.6	4.8
	d_{33}	25.2	25.7
1%-MgO:$LiNbO_3$	d_{31}	4.6	4.8
	d_{33}	24.9	27.5
5%-MgO:$LiNbO_3$	d_{31}	4.4	4.9
	d_{33}	25.0	28.4

addition, $LiNbO_3$ possesses only four independent nonlinear tensor components, all of which are outlined below [79]:

$$d_{il} = \begin{bmatrix} 0 & 0 & 0 & 0 & d_{15} & -2d_{22} \\ -d_{22} & d_{22} & 0 & d_{15} & 0 & 0 \\ d_{31} & d_{31} & d_{33} & 0 & 0 & 0 \end{bmatrix}. \tag{2.8}$$

Here, the rotational symmetry and vertical mirror planes of the 3m point group enforce that many tensor elements vanish or are equal to one another (e.g., $d_{15} = d_{24}$, $d_{22} = -d_{21} = (-d_{16}/2)$, and $d_{31} = d_{32}$), reflecting the intrinsic symmetry constraints of the $LiNbO_3$ crystal. The negative sign of the d_{22} component indicates that the induced nonlinear polarization is oriented antiparallel to the applied electric field. Table 2.1 presents measured values of the d_{31} and d_{33} coefficients for three different types of $LiNbO_3$ crystals, as taken from Ref. [80]. These include congruent undoped $LiNbO_3$, $LiNbO_3$ doped with 1% magnesium oxide (MgO), and $LiNbO_3$ doped with 5% MgO. The measurements were taken at 1064 nm and 852 nm. Furthermore, due to its comparatively low second-order nonlinearity, the d_{22} coefficient is rarely utilised; experimental measurements report a value of 2.1 pm/V in congruent, undoped $LiNbO_3$ at 1064 nm [81].

2.3.2 Frequency conversion through the $\chi^{(2)}$ susceptibility

The second-order susceptibility $\chi^{(2)}$ characterises the material's response to the electric field in second-order nonlinear optical processes. This phenomenon is observed in systems lacking an inversion symmetry. In the following theoretical treatment, we assume an instantaneous nonlinear response which constitutes a valid approximation for the system under consideration. Under this assumption, the second-order term of Eq. (2.2) can be expressed in the time domain as:

$$P_i^{(2)}(t) = \varepsilon_0 \chi_{ijk}^{(2)} E_j(t) E_k(t). \tag{2.9}$$

For the parametric down-conversion process considered in this work, a type-0 configuration is employed, such that the fundamental pump, signal, and idler fields share the same polarization state. In the nonlinear medium considered here, this common polarization is oriented along the z-direction. Accordingly, only the z-component of the electric field and the resulting nonlinear polarization need be considered. The general tensor expression in Eq. (2.9) therefore reduces to:

$$P_z^{(2)}(t) = \varepsilon_0 \chi_{zzz}^{(2)} E_z^2(t), \tag{2.10}$$

where $\chi_{zzz}^{(2)}$ is the relevant component of the second-order nonlinear susceptibility tensor for the z-polarized interaction.

Let us also consider the propagation of two plane waves at frequencies ω_1 and ω_2 through a nonlinear medium, with complex field amplitudes $E_z(\omega_1)$ and $E_z(\omega_2)$, respectively. Assuming ω_1 is the larger of the two frequencies, the resulting amplitude of the electric field is described by the following expression [65]:

$$E_z(t) = E_z(\omega_1) e^{-i\omega_1 t} + E_z(\omega_2) e^{-i\omega_2 t} + \text{c.c.}. \tag{2.11}$$

By substituting Eq.(2.11) into Eq.(2.10), the explicit form of the second-order nonlinear polarization is obtained:

$$\begin{aligned} P_z^{(2)}(t) = \varepsilon_0 \chi_{zzz}^{(2)} \Big[& E_z^2(\omega_1) e^{-2i\omega_1 t} + E_z^2(\omega_2) e^{-2i\omega_2 t} \\ & + 2E_z(\omega_1) E_z(\omega_2) e^{-i(\omega_1+\omega_2)t} \\ & + 2E_z(\omega_1) E_z^*(\omega_2) e^{-i(\omega_1-\omega_2)t} + \text{c.c.} \\ & + 2\big(E_z(\omega_1) E_z^*(\omega_1) + E_z(\omega_2) E_z^*(\omega_2)\big) \Big]. \end{aligned} \tag{2.12}$$

Re-writing Eq. (2.12) in terms of its individual frequency components gives:

$$P_z^{(2)}(t) = \sum_n P_z^{(2)}(\omega_n) e^{-i\omega_n t}, \tag{2.13}$$

where the summation extends over positive and negative frequencies, and $P_z^{(2)}(\omega_n)$ is the complex amplitude of the second-order nonlinear polarization at frequency ω_n. By grouping the terms in Eq. (2.12) by their oscillating frequencies, we obtain the nonlinear polarization components for the corresponding $\chi^{(2)}$ processes:

$$P_z^{(2)}(2\omega_1) = \varepsilon_0 \chi_{zzz}^{(2)} E_z^2(\omega_1) \tag{2.14a}$$

$$P_z^{(2)}(2\omega_2) = \varepsilon_0 \chi_{zzz}^{(2)} E_z^2(\omega_2) \tag{2.14b}$$

$$P_z^{(2)}(\omega_1 + \omega_2) = 2\varepsilon_0 \chi_{zzz}^{(2)} E_z(\omega_1) E_z(\omega_2) \tag{2.14c}$$

$$P_z^{(2)}(\omega_1 - \omega_2) = 2\varepsilon_0 \chi_{zzz}^{(2)} E_z(\omega_1) E_z^*(\omega_2) \tag{2.14d}$$

$$P_z^{(2)}(0) = 2\varepsilon_0 \chi_{zzz}^{(2)} \big[|E_z(\omega_1)|^2 + |E_z(\omega_2)|^2 \big]. \tag{2.14e}$$

From Eq. (2.14) above, it is evident that the first two terms correspond to the phenomenon known as SHG. This process involves the mixing of two identical photons of the same frequency within a nonlinear medium, resulting in the generation of a new output photon with twice the energy of the incident photons [63], [66], [67]. Equation (2.14c) corresponds to SFG. In this process, two photons at different frequencies interact in a nonlinear medium to create a single photon. The frequency and energy of the result-

ing photon is equal to the sum of the two incident photons [68], [69]. In contrast, the fourth term describes DFG (see Eq. 2.14d), where two input photons with different energies interact to generate a new photon, whose energy equals the difference between the two incoming energies. The concluding term in Eq. (2.14) is indicative of OR (see Eq. (2.14e)), where a quasi-DC nonlinear polarization is generated by an intense optical field [73], [74].

When designing a system that incorporates one of the second-order nonlinear processes outlined in Eq. (2.14), it is essential to satisfy two fundamental conditions. The first condition is to ensure that the frequencies of interest lie within the transparency range of the chosen $\chi^{(2)}$ nonlinear medium. The second involves selecting the most suitable nonlinear process for the intended application. This is accomplished through suitable 'phase matching', a method that will be further explored and examined later on in this chapter. It is worth noting that, in practice, only a single process described by Eq. (2.14) is typically efficiently realised, as efficient nonlinear interaction requires fulfilment of the phase matching condition, which is generally satisfied for at most one interaction in a given configuration.

2.4 Optical parametric down-conversion (PDC)

In OPO devices, optical parametric down-conversion (PDC) constitutes the fundamental nonlinear process. PDC can be viewed as a form of DFG, in which a pump field at frequency ω_p amplifies an externally injected signal at ω_s while simultaneously generating an idler at the difference frequency ω_i. However, for PDC, the seed is provided by the vacuum fluctuations of the EM field. This three-wave mixing mechanism also underlies OPA, where a strong pump field transfers energy coherently into the signal field, increasing its intensity while producing a phase-correlated idler. This parametric interaction forms the basis of OPO operation, where placing the nonlinear medium inside a resonant cavity allows the generated field (or fields) to circulate, undergo repeated amplification, and reach a self-sustained oscillation once the parametric gain exceeds the

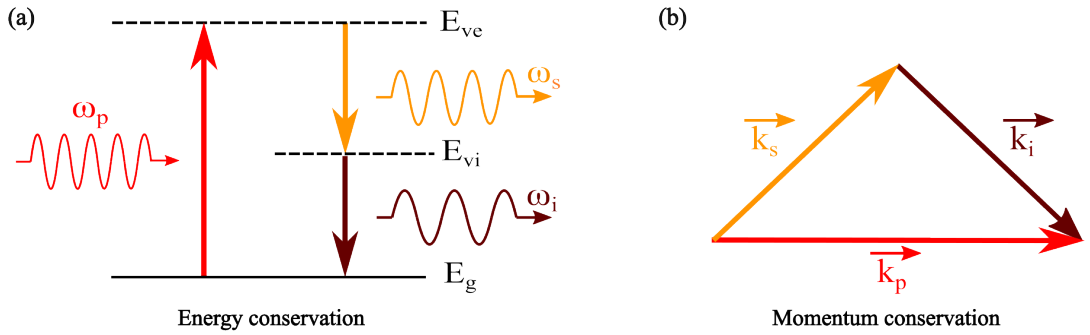


Figure 2.2: Schematic illustrations of the **(a)** energy and **(b)** momentum conservation laws associated with PDC. E_g: ground-state energy; E_{vi}: intermediate virtual-state energy; E_{ve}: excited virtual-state energy; $\omega_{p,s,i}$: angular frequencies of the pump, signal, and idler; $k_{p,s,i}$: wave vectors of the pump, signal, and idler. Panel (a) is adapted from Fig. 1.1.

cavity losses. Energy conservation, which underpins the PDC process, requires that the pump frequency is equal to the sum of the signal and idler frequencies. Thus, the frequencies satisfy the relation:

$$\omega_p = \omega_s + \omega_i, \tag{2.15}$$

where ω_p, ω_s, and ω_i denote the pump, signal, and idler angular frequencies, respectively.

Equation (2.15) explains how PDC can be perceived as the splitting of a high-energy pump photon into two down-converted signal and idler photons of lower frequency. The total combined energy of the signal and idler photons is thus equivalent to the energy of the pump photon. In terms of atomic transitions, the absorption of a pump photon leads to the excitation of an electron within the nonlinear medium to a higher energy 'virtual' level. As illustrated in Fig. 2.2a, the electron in the excited 'virtual' level will undergo a fast decay down to an intermediate 'virtual' level, resulting in the emission of a coherent signal photon at a frequency ω_s. Concomitant with the emission of the signal photon, there will be another fast decay down to the ground-state, leading to the coherent emission of an idler photon at a frequency ω_i.

Different combinations of signal and idler wavelengths can be selected for a specific pump frequency, provided the energy conservation relation in Eq. (2.15) is met. Nev-

ertheless, the exact wavelengths of the signal and idler are determined by the phase matching condition mentioned earlier, which is characterised by the wave-vector mismatch (see Fig. 2.2b, example of non-collinear phase matching). The fundamental principles of phase matching, particularly in relation to OPO research, are discussed in the next section.

2.5 Quasi-phase matching (QPM)

Efficient nonlinear gain requires precise phase matching to enable net energy transfer from the pump to the signal and idler frequencies. For collinear interactions, phase matching in PDC is achieved when the wave-vector mismatch along the propagation (longitudinal) direction vanishes. In this case, the mismatch parameter Δk is defined as:

$$\Delta k = k_p - k_s - k_i = \frac{1}{c}\left(n_p\omega_p - n_s\omega_s - n_i\omega_i\right), \tag{2.16}$$

where $k_{p,s,i}$ denote the wave-vector magnitudes of the pump, signal, and idler fields, respectively, along the propagation (longitudinal) direction, and $n_{p,s,i}$ represent their corresponding refractive indices. According to Eq. (2.16), achieving perfect phase matching ($\Delta k = 0$) requires the refractive indices of the interacting waves to satisfy a specific relationship. However, since each wave operates at a different wavelength (for the non-degenerate case), the refractive indices generally differ due to material dispersion, causing each field to experience a different phase velocity.

Two widely used techniques have been developed to compensate for material dispersion in nonlinear interactions: birefringent phase matching (BPM) and quasi-phase matching (QPM). BPM exploits the intrinsic birefringence of the crystal to satisfy the phase matching condition by appropriately selecting the polarization and propagation directions of the interacting waves (see Eq. (2.16)). In contrast, QPM provides an alternative to BPM by enabling net energy transfer from the pump to the down-converted signal and idler fields through fabrication of a periodically-poled domain structure within the nonlinear medium. Although QPM was first proposed by Armstrong *et al.* [36] in

1962, practical implementation was not realised until the mid-1990s, largely due to technological limitations in domain fabrication. The present investigation focuses exclusively on QPM devices and, therefore, all subsequent discussions will be confined to this phase matching approach. For a more detailed understanding of the BPM scheme, see Refs. [82], [83].

QPM is particularly advantageous in situations where BPM is impractical, especially for exploiting the largest nonlinear coefficient, such as d_{33} in $LiNbO_3$ (see Table 2.1). BPM cannot access this nonlinear coefficient because collinear phase matching requires different polarization states when using crystal anisotropy. In contrast, QPM enables full utilisation of the d_{33} coefficient, making the previously prohibitive oscillation thresholds of SROs achievable with commercial laser sources [10], [11], since the SRO threshold scales inversely with the square of the effective nonlinearity coefficient [60]. Similarly, for materials lacking natural birefringence, such as GaAs, phase mismatch can only be compensated through the introduction of a periodic grating [65].

Figure 2.3 presents a comparison between QPM, perfect phase matching, and the absence of phase matching. For clarity, we model the second-harmonic intensities for each phase matching scheme, as they effectively replicate the characteristic intensity behavior observed in PDC under ideal phase matching conditions. Both processes exhibit the same increase in intensity because their phase matching behaviour is governed by the same sinc^2 dependence. In the absence of phase matching, as shown by the black curve in Fig. 2.3, the relative intensity of the up-converted field peaks after one coherence length, beyond which destructive interference limits further growth. The coherence length l_c is defined as the propagation distance over which the phase mismatch between the interacting waves accumulates to π, leading to the first maximum in conversion efficiency. Beyond this point, the faster phase velocity of the pump field causes the generated second-harmonic wave to fall out of phase, resulting in reduced energy transfer. The QPM technique, illustrated by the purple curve in Fig. 2.3, suppresses destructive interference by periodically reversing the sign of the nonlinearity coefficient, thereby resetting the accumulated phase mismatch and enabling efficient frequency con-

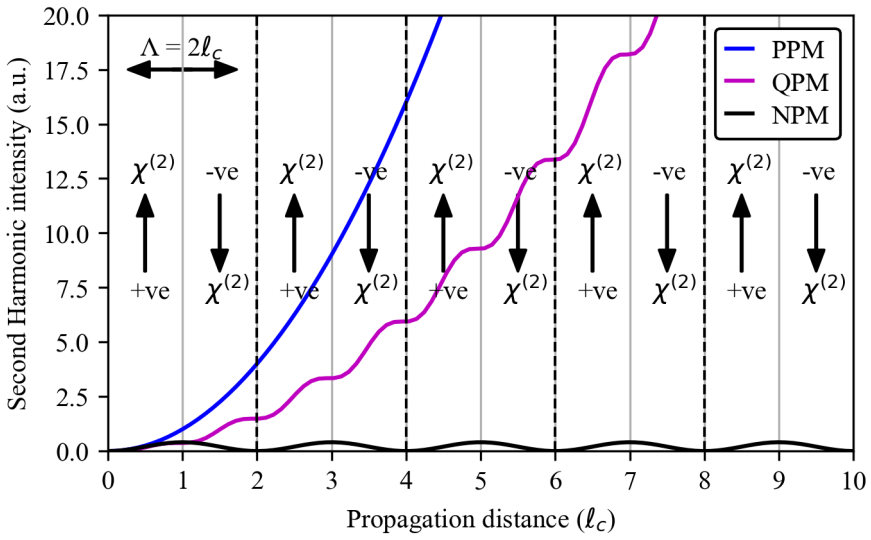


Figure 2.3: Comparison of the second harmonic intensities versus propagation distance for different phase matching techniques. The black curve corresponds to a non-phase matched (NPM) interaction, exhibiting intensity oscillations with a period of $2l_c$. The blue curve shows a perfectly-phase matched (PPM) interaction, characterised by a quadratic increase in intensity. The purple curve illustrates domain-reversal QPM, where the relative intensity grows stepwise after each coherence length, l_c.

version over extended interaction lengths. Under perfect phase matching conditions (see Fig. 2.3, blue curve), the intensity of the up-converted field increases quadratically with propagation distance, reflecting ideal phase coherence and energy transfer.

Domain-reversal QPM is the most commonly used QPM technique and was first demonstrated by Yamada *et al.* [84]. It is implemented through ferroelectric domain engineering, in which a strong electric field is applied to periodically invert the domain orientation of a nonlinear ferroelectric crystal. This periodic inversion causes the sign of the nonlinear coefficient d_{il} to alternate every coherence length (for a first-order QPM interaction). As a result, the accumulated phase mismatch between the interacting waves is repeatedly reset, allowing constructive interference to be maintained. This process enables continuous amplification of the generated fields, as illustrated by the purple curve in Fig. 2.3. Common materials used for domain-reversed QPM include

periodically-poled $LiNbO_3$ (PPLN), $LiTaO_3$ (PPLT), and $KTiOPO_4$ (PPKTP) along with their isomorphs [85].

The experiments presented in this investigation employ a PPLN crystal to achieve QPM and enable efficient PDC. As a result, a user-engineered grating vector term k_m is introduced into Eq. (2.16). By substituting the angular frequency terms ($\omega_{p,s,i}$) with their corresponding frequency terms ($\nu_{p,s,i}$), the wave-vector mismatch for PDC can now be expressed in the following form:

$$\Delta k_{\mathrm{QPM}} = k_p - k_s - k_i - k_m = \frac{2\pi}{c}\left(n_p\nu_p - n_s\nu_s - n_i\nu_i\right) - \frac{2\pi}{\Lambda_{\mathrm{QPM}}} = 0. \tag{2.17}$$

Here, Λ_{QPM} denotes the poling period of the periodically-poled nonlinear medium. For first-order QPM, the required poling period is determined by the magnitude of the phase mismatch according to:

$$\Lambda_{\mathrm{QPM}} = \frac{2\pi}{|k_p - k_s - k_i|}. \tag{2.18}$$

Using $k_j = 2\pi n_j\nu_j/c$, where $j = p, s, i$ denotes the pump, signal, and idler fields, respectively, this can equivalently be expressed in terms of the refractive indices and optical frequencies as:

$$\Lambda_{\mathrm{QPM}} = \frac{c}{|n_p\nu_p - n_s\nu_s - n_i\nu_i|}. \tag{2.19}$$

The terms enclosed in the parenthesis of Eq. (2.17), and the denominator of Eq. (2.19), represent the conventional phase matching condition, which can typically be adjusted using standard techniques such as temperature or angular tuning of the nonlinear crystal. The inclusion of the grating term introduces a tunable modification to the phase matching condition without altering the intrinsic properties of the nonlinear material. This term is primarily responsible for the significantly broader tuning ranges that can be achievable in QPM compared to BPM.

2.5.1 QPM domain-reversal theory

Fejer *et al.* [86] provide an outline of the domain-reversal QPM theory, focussing on the simplest case of SHG. In the case of imperfect phase matching ($\Delta k_{\mathrm{QPM}} \neq 0$), the QPM condition is satisfied through the following relationship:

$$\Delta k_{\mathrm{QPM}} = k_{2\omega} - 2k_{\omega} - k_m. \tag{2.20}$$

A Fourier analysis of the periodic nonlinear susceptibility was used to derive the expression for k_m. The underlying principle of this approach is that the amplitude of the frequency components generated through a nonlinear interaction over a distance l can be determined by integrating the appropriate coupled amplitude equations. Under the slowly-varying-envelope approximation, the following equation governs the growth of the second-harmonic field:

$$\frac{dE_2}{dz} = \Gamma_{\mathrm{NL}} d(z) e^{-i\Delta kz}, \tag{2.21}$$

and, therefore, by integrating Eq. (2.21) over the propagation length of the nonlinear medium l, we obtain:

$$E_2^{\mathrm{out}} = \Gamma_{\mathrm{NL}} \int_0^l d(z)\, e^{-i\Delta kz}\, dz. \tag{2.22}$$

In Eq. (2.21), Γ_{NL} denotes a nonlinear coupling coefficient containing the relevant frequency, refractive index, and field-normalization factors that determine the strength of the generated second-harmonic field, while $d(z)$ represents the periodically-poled effective nonlinear coefficient. Under Fourier analysis, $d(z)$ can be expanded to the following series:

$$d(z) = d_{il} \sum_{m=-\infty}^{\infty} G_m e^{ik_m z}, \tag{2.23}$$

where d_{il} is the nonlinear coefficient of a single-domain bulk material, while G_m represents the Fourier coefficient corresponding to the m^{th} harmonic. Thus, $d(z)$ represents the spatially modulated nonlinear coefficient produced by periodic poling, with

d_{il} providing the corresponding bulk nonlinear coefficient. The periodicity of $d(z)$ is characterised by the QPM grating period Λ_{QPM}, giving the m^{th}-order grating vector as:

$$k_m = \frac{2\pi m}{\Lambda_{\mathrm{QPM}}}. \tag{2.24}$$

Equations (2.23) and (2.24) clarify the role of the integer m in determining the order of the QPM interaction defined in Eq. (2.20). A closer examination reveals that the m^{th}-order interaction dominates when $\Delta k \approx k_m$. Under this condition, the relation $d_{\mathrm{eff}} = d_{il}\, G_m$ applies, and the Fourier component in Eq. (2.23) can be evaluated using a standard transform pair, yielding:

$$G_m = \frac{2}{\pi m} \sin(\pi m D). \tag{2.25}$$

In this context, the parameter D represents the duty cycle, defined as the fraction of the QPM grating period Λ_{QPM} over which the nonlinear coefficient remains positive before inversion, relative to the microscopic domain length l_d, as given by:

$$D = \frac{l_d}{\Lambda_{\mathrm{QPM}}}. \tag{2.26}$$

To achieve an efficient first-order ($m = 1$) QPM domain inversion scheme, as illustrated by the red curve in Fig. 2.4, the duty cycle must be configured such that each domain inverts precisely at every coherence length. This corresponds to a grating period of $\Lambda_{\mathrm{QPM}} = 2l = 2l_c$. Under this condition, the effective QPM nonlinear coefficient d_{eff} can be directly related to the intrinsic nonlinear coefficient d_{il} of the material. Therefore, for the m^{th}-order process, we have:

$$d_{\mathrm{eff}} = \frac{2}{\pi m} d_{il}. \tag{2.27}$$

According to Eq. (2.27) and the graphical representation in Fig. 2.4, the optimal duty cycle varies depending on the specific order of the QPM interaction. For instance, in a

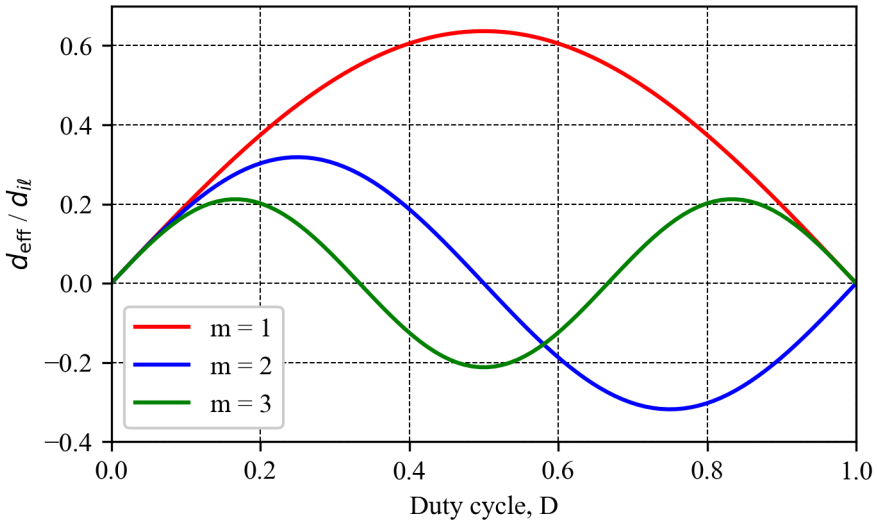


Figure 2.4: Ratio d_{eff}/d_{il} versus duty cycle D for QPM interactions.

first-order QPM interaction ($m = 1$), the optimal duty cycle is 50%. In contrast, for a second-order interaction ($m = 2$), the optimal duty cycles are 25% and 75%, while for a third-order interaction ($m = 3$), the optimal values are approximately 17.5% and 82.5%. Higher-order QPM interactions simplify the fabrication process, particularly when the interaction involves short coherence lengths, though, as indicated by Eq. (2.27), this comes at the cost of a reduced effective nonlinearity coefficient.

In practice, first-order QPM is typically preferred, as it enables the highest effective nonlinearity coefficient to be accessed for the material of interest. Although a penalty factor of $2/\pi$ is incurred, as described in Eq. (2.27), this configuration still achieves close to two-thirds of the effective nonlinearity attainable in perfectly phase matched interactions. Its effectiveness lies in allowing the interacting waves to maintain a polarization configuration that accesses a large, and potentially the largest, nonlinear tensor component of the material – for example, $d_{il} = d_{33}$ in $LiNbO_3$. In most cases, the $2/\pi$ penalty is more than compensated by this advantage, enabling d_{eff} to surpass any of the d_{il} coefficients obtainable via BPM.

Beyond enhanced nonlinearity, QPM offers other significant practical advantages. For example, by judiciously selecting the poling period, it is possible to theoretically phase

match any wavelength combination within the transparency window of the nonlinear material via non-critical phase matching. This approach ensures momentum conservation is maintained over a broad range of stabilised operating temperatures and eliminates spatial walk-off. Spatial walk-off is a phenomenon that arises in birefringent crystals when extraordinarily polarized beams experience a deviation between the direction of energy flow and the wave-vector due to angular dispersion. In QPM systems, phase matching is achieved without angular tuning, allowing all interacting waves to propagate collinearly along a principal crystal axis and thereby avoid such walk-off effects.

Section 2.5.2 provides a detailed analysis of the pump wavelength and temperature acceptance bandwidths for a first-order QPM PDC interaction in a PPLN crystal doped with 5%-MgO.

2.5.2 QPM acceptance parameters

The conversion efficiency of a nonlinear optical process depends on the wavelengths, polarizations, and propagation directions of all interacting waves. In practice, the phase matching condition not only dictates the efficiency but also defines the spectral bandwidth over which constructive interference can occur between the interacting fields. A critical requirement is that the magnitude of the phase mismatch remains below π/l; exceeding this limit suppresses full constructive interference and reduces conversion efficiency [87]. This behaviour arises from the sinc^2 dependence of the conversion efficiency, where the interaction is regarded as inefficient once the function falls below half of its peak value. Consequently, expressions for the acceptance parameters of a given nonlinear process can be derived, with each expression depending on the phase matching scheme used.

Following the analysis of Barnes and Corcoran [87], we theoretically evaluate the spectral bandwidth acceptance parameters for QPM devices. Consider a collinear BPM

interaction evaluated near the perfect phase matching condition ($\Delta k = 0$). The wave vector mismatch Δk can be expanded in a Taylor series up to second order:

$$\Delta k = \Delta k_0 + \frac{\partial \Delta k}{\partial X}\,\Delta X + \frac{1}{2}\frac{\partial^2 \Delta k}{\partial X^2}\,(\Delta X)^2. \tag{2.28}$$

The perfect phase matching condition is satisfied when $\Delta k_0 = 0$, and the parameter of interest varies by a maximum amount ΔX. As described in the previous paragraph, one criterion for acceptable phase mismatch is that its modulus must remain below π/l. By setting $\Delta k_0 = 0$, $\Delta k = \pm\,\pi/l$, and $X = \lambda_x$, Eq. (2.28) can be rewritten as:

$$\frac{\partial \Delta k}{\partial \lambda_x}\,\Delta\lambda_x + \frac{1}{2}\frac{\partial^2 \Delta k}{\partial \lambda_x^2}\,(\Delta\lambda_x)^2 = \left|\frac{\pi}{l}\right|. \tag{2.29}$$

The complete expression for the wave vector mismatch in the BPM case is provided in Eq. (2.16). However, Eq. (2.17) is employed in the subsequent analysis as the current investigation undergoes a QPM interaction. To evaluate the spectral acceptance bandwidth, Eq. (2.17) is reformulated to express the phase mismatch in terms of the interacting wavelengths. Accordingly, the wave-vector mismatch for the QPM case is given by:

$$\Delta k_{\mathrm{QPM}} = k_p - k_s - k_i - k_m = 2\pi\left[\frac{n_p(\lambda_p)}{\lambda_p} - \frac{n_s(\lambda_s)}{\lambda_s} - \frac{n_i(\lambda_i)}{\lambda_i} - \frac{1}{\Lambda_{\mathrm{QPM}}}\right], \tag{2.30}$$

where the refractive indices are now explicitly dependent on their respective wavelengths. By expressing the full spectral bandwidth $\delta\lambda_x$ in the following form:

$$\delta\lambda_x = 2\Delta\lambda_x, \tag{2.31}$$

and invoking the energy conservation relation in PDC:

$$\frac{1}{\lambda_p} = \frac{1}{\lambda_s} + \frac{1}{\lambda_i}, \tag{2.32}$$

the first derivative of the Taylor series expansion in Eq. (2.29) with respect to the pump wavelength is given by:

$$\frac{\partial \Delta k_{\mathrm{QPM}}}{\partial \lambda_p} = 2\pi \left[\frac{\partial n_p(\lambda_p)}{\partial \lambda_p} \frac{1}{\lambda_p} - \frac{n_p(\lambda_p)}{\lambda_p^2} - \frac{\partial n_s(\lambda_s)}{\partial \lambda_s} \frac{\lambda_s}{\lambda_p^2} + \frac{n_s(\lambda_s)}{\lambda_p^2} \right], \tag{2.33}$$

where the additional engineered grating wave vector term in Eq. (2.30) vanishes upon differentiation, since it is independent of wavelength. Typically, the first derivative of Eq. (2.29) dominates the acceptance bandwidth in the overwhelming number of cases. Therefore, we omit the theoretical derivation of $\frac{\partial^2 \Delta k}{\partial \lambda_p^2}$. The acceptance bandwidth of the pump wavelength in PDC is then determined by substituting Eqs. (2.29) and (2.31) into Eq. (2.33), yielding:

$$\delta\lambda_p = \frac{1}{L} \left[\frac{\partial n_p(\lambda_p)}{\partial \lambda_p} \frac{1}{\lambda_p} - \frac{n_p(\lambda_p)}{\lambda_p^2} - \frac{\partial n_s(\lambda_s)}{\partial \lambda_s} \frac{\lambda_s}{\lambda_p^2} + \frac{n_s(\lambda_s)}{\lambda_p^2} \right]^{-1}. \tag{2.34}$$

The experiments presented in Chapters 4 and 5 employ a 5%-MgO:PPLN crystal to enable efficient PDC. Accurate determination of the wave vectors and frequencies involved in this process requires precise knowledge of the crystal's refractive indices. These can be obtained from the phenomenological Sellmeier equations, which describe the dispersion properties for both the ordinary and extraordinary polarizations of 5%-MgO:PPLN at a given temperature. As an example, consider a 5%-MgO:PPLN crystal stabilised at 114°C; the Sellmeier equations for the extraordinary and ordinary refractive indices at this temperature are given by [88]:

$$n_e(\lambda) = \sqrt{5.9313 + \frac{198.7130\,\lambda^2 - 24.2644}{\lambda^4 - 156.7927\,\lambda^2 + 6.6305} - 0.0132\,\lambda^2}, \tag{2.35a}$$

$$n_o(\lambda) = \sqrt{5.7017 + \frac{89.5963\,\lambda^2 - 18.0752}{\lambda^4 - 117.7661\,\lambda^2 + 5.1337} - 0.0197\,\lambda^2}, \tag{2.35b}$$

where λ is expressed in µm. Throughout this investigation, the extraordinary refractive index n_{e} is used for all interacting wavelengths in order to exploit the largest nonlinear

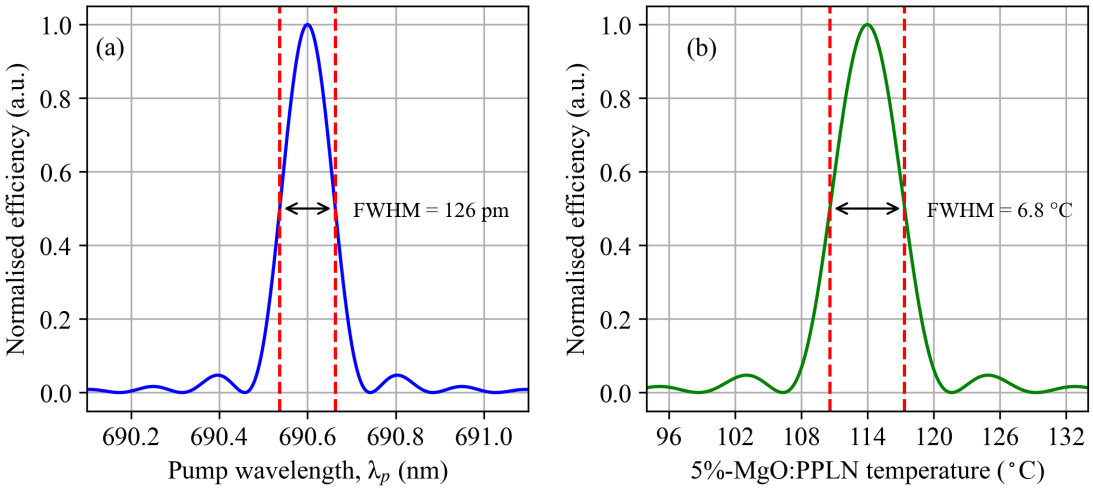


Figure 2.5: Theoretical phase matching acceptance bandwidths of a type-0 QPM PDC interaction in a 5%-MgO:PPLN crystal pumped at 690.6 nm. **(a)** Pump wavelength acceptance bandwidth, and **(b)** temperature acceptance bandwidth for a crystal temperature of 114°C.

tensor coefficient (d_{33}; see Table 2.1) under collinear pumping along the crystal's x-axis. By applying Eqs. (2.32) and (2.35a), the polarization states are chosen to be aligned with the crystal's z-axis, and the corresponding wavelength parameters are calculated under the condition of perfect phase matching ($\Delta k = 0$).

Using this approach, the poling period and operating temperature of the 5%-MgO:PPLN crystal are chosen to realise phase matching for signal and idler wavelengths near 1.24 µm and 1.55 µm, respectively. For a pump wavelength of 690.6 nm, this corresponds to a poling period of $\Lambda_{\mathrm{QPM}} = 14.55$ µm and a stabilised crystal temperature of 114°C. The corresponding pump acceptance bandwidth is illustrated in Fig. 2.5a, which shows the dependence of the wavelength tolerance for a 40-mm-long 5%-MgO:PPLN crystal maintained at this temperature. The shape of this curve arises from the underlying sinc^2 dependence of the conversion efficiency on phase mismatch, as discussed at the beginning of this section. Using Eqs. (2.34) and (2.35a), the acceptance bandwidth at a pump wavelength of 690.6 nm is calculated to be 126 pm for the chosen grating period of 14.55 µm. This value represents the maximum bandwidth of an input pump beam that

will contribute constructively to the nonlinear interaction within the phase mismatch range $\Delta k \leq \frac{\pi}{l}$.

To determine the temperature acceptance bandwidth of the 5%-MgO:PPLN crystal, a similar theoretical approach is employed. In this case, however, the refractive indices explicitly depend on the crystal temperature. Additionally, unlike the analysis performed for the pump wavelength, the thermal expansion of the crystal's poling period directly affects the acceptance bandwidth. To account for this effect, an additional term is introduced to incorporate the temperature-induced variation of the grating period. As a result, and in analogy to Eq. (2.34), the temperature acceptance bandwidth can be expressed as [89]:

$$\delta T = \frac{1}{L}\left[\frac{1}{\lambda_p}\left(\frac{\partial n_p}{\partial T}\right)\Big|_T - \frac{1}{\lambda_s}\left(\frac{\partial n_s}{\partial T}\right)\Big|_T - \frac{1}{\lambda_i}\left(\frac{\partial n_i}{\partial T}\right)\Big|_T - \frac{\partial \alpha(T)}{\partial T}\left(\frac{1}{\Lambda}\right)\right]^{-1}, \tag{2.36}$$

where the additional term [90]:

$$\frac{\partial \alpha(T)}{\partial T} = -2.6 + 22.4 \times 10^{-3}\, T \quad \left(10^{-5}\,\mathrm{K}^{-1}\right), \tag{2.37}$$

accounts for the thermo-optic coefficient of $LiNbO_3$ for the extraordinary refractive index n_e over the temperature range of 47–242°C. Although Eq. (2.37) was originally derived for a wavelength of 0.632 µm, it remains valid for application in Eq. (2.36) for the present analysis, as the pump wavelength employed here, 690.6 nm, lies sufficiently close. By substituting Eq. (2.37) into Eq. (2.36) and employing the same interacting wavelengths as in the pump analysis ($\lambda_s = 1.24$ µm, $\lambda_i = 1.55$ µm), the temperature acceptance bandwidth of a 5%-MgO:PPLN crystal is calculated to be 6.8°C. This calculation assumes a crystal length of 40 mm, a grating period of 14.55 µm, and a crystal temperature at 114°C, as illustrated in Fig. 2.5b.

2.5.3 QPM tuning ranges

The benefits of QPM for enhancing optical amplification in OPO devices are well established, as illustrated by the purple curve in Fig. 2.3. Beyond photon amplification, QPM also provides a versatile mechanism for tuning the OPO output. In practice, this tunability can be achieved by adjusting the temperature of the 5%-MgO:PPLN crystal, varying the pump wavelength, or employing a crystal with multiple poling periods. To model the theoretical wavelength tuning ranges of the OPO, two scenarios were analysed: one using the temperature-dependent Sellmeier equations from Gayer *et al.* [88], and the other using the Select Nonlinear Optics (SNLO) software [91].

Figure 2.6a presents the theoretically calculated QPM temperature tuning curves for the down-converted signal and idler wavelengths as a function of the 5%-MgO:PPLN crystal temperature, assuming a fixed OPO pump wavelength of 0.689 µm. This pump wavelength corresponds to the design wavelength of the AlGaInP-based VECSEL employed experimentally. It differs from the wavelength used in the spectral acceptance bandwidth analysis (see Section 2.5.2), as the QPM tuning curves were computed prior to experimental characterisation of the pump, whereas the acceptance bandwidth was subsequently evaluated using the measured OPO pump spectrum. Due to the limited operating range of the OPO crystal oven (30–200°C), not all of the fabricated poling periods are experimentally accessible. Nonetheless, by employing the 14.55 µm and 15.10 µm poling periods, the OPO can, in practice, be tuned across a broad wavelength range of 1.03 µm to 2.09 µm [88].

Figure 2.6b shows the theoretical signal and idler wavelengths as a function of the OPO pump wavelength for 5%-MgO:PPLN crystal temperatures of 50°C and 200°C, with a fixed grating period of 14.55 µm. For a tunable pump spanning 0.62–0.70 µm, the OPO can, in principle, access a signal-idler range of 0.74–3.72 µm at 200°C [88] (see red data points in Fig. 2.6b).

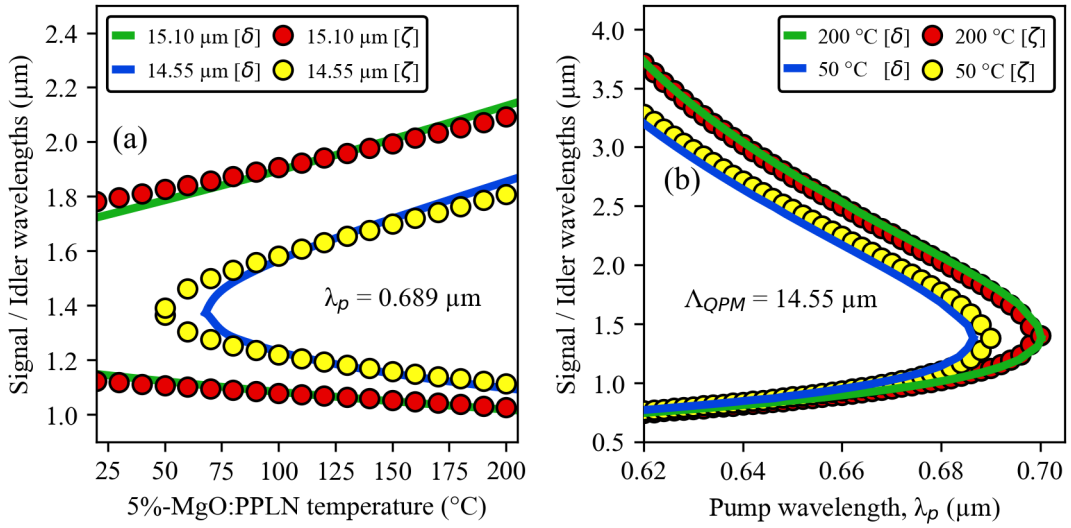


Figure 2.6: QPM tuning curves for a type-0 QPM PDC interaction based on a 5%-MgO:PPLN crystal. **(a)** Temperature tuning curves calculated for poling periods of 14.55 µm and 15.10 µm, using a fixed pump wavelength of 0.689 µm. **(b)** Pump wavelength tuning curves calculated using a fixed poling period of 14.55 µm, for crystal temperatures of 50°C and 200°C. δ : signal/idler wavelengths computed using SNLO software [91]; ζ : signal/idler wavelengths calculated from the Sellmeier equations reported by Gayer *et al.* [88].

2.6 ICSRO steady-state threshold power analysis

This section introduces the steady-state power characteristics of an ICSRO and derives the corresponding optimisation conditions. Following theoretical analysis, we derive an analytical expression that allows us to determine the precise input external pump power needed to maximise the total down-converted output. It is important to note that transient dynamics are excluded from this theoretical framework. This is justified by the nature of the pump source used in this investigation: a vertical-external-cavity surface-emitting laser (VECSEL), which exhibits Class-A dynamical behaviour and, as a result, operates free from relaxation oscillations above the OPO threshold [26]. For more information as to how relaxation oscillations influence the transient dynamics of ICSROs more broadly, see Refs. [38], [42].

2.6.1 ICSRO steady-state power characteristics

In 1998, Turnbull *et al.* [30] extended the theoretical model originally developed by Debuisschert *et al.* [92] to examine the power dynamics of ICSROs. Their work introduced a comprehensive model capable of describing systems pumped by CW lasers, thereby significantly extending the scope of earlier theoretical treatments. As the core of this investigation is experimental in nature, a complete theoretical treatment of ICSRO operation is outwith the scope of this research. Readers seeking a detailed theoretical analysis of CW ICSROs are referred to the following Refs. [30], [89], [93], [94].

The steady-state analysis presented here thus follows the framework established by Turnbull *et al.* [30] and is included to provide contextual completeness for the subsequent discussion. In later chapters, the predictions of this theoretical analysis are directly compared with the experimentally measured power characteristics of the ICSRO, thereby establishing a clear link between the steady-state model and the practical device performance.

The steady-state power characteristics of an ICSRO are examined across all operating regimes under the assumption of a CW pump laser operating on a single longitudinal mode, consistent with the operating conditions of the VECSEL pump source employed in the current experimental investigation. Furthermore, the analysis assumes that only the signal field of the OPO is resonant, corresponding to the singly resonant configuration considered throughout this work. In practice, the idler field can be selected as the resonant wave instead, in which case all parameters carrying the subscript 's' are replaced by 'i'. Consequently, for a single-frequency pump laser, the rate equations governing the dynamics of the ICSRO are given by [30], [92]:

$$\tau_p \frac{\partial P_p}{\partial t} = P_p \left(N - 1 - F P_s\right), \tag{2.38a}$$

$$\tau_u \frac{\partial N}{\partial t} = \sigma - N \left(1 + x P_p\right), \tag{2.38b}$$

$$\tau_s \frac{\partial P_s}{\partial t} = P_s \left(P_p - 1\right). \tag{2.38c}$$

Here, Eqs. (2.38a)–(2.38c) represent the coupled rate equations governing the fundamental pump power P_p, the saturated laser gain N, and the OPO resonant signal power P_s, respectively. The parameters τ_p and τ_s denote the photon lifetimes of the intracavity pump and signal fields, respectively, while the parameter F represents the ratio of the finesse of the fundamental pump-laser cavity to that of the signal cavity. The parameter σ denotes the normalised pump parameter of the single-frequency laser mode, τ_u denotes the upper-state lifetime of the fundamental pump laser, and x is the saturation parameter. By setting the time derivatives of Eqs. (2.38a)–(2.38c) to zero, the corresponding steady-state solutions can be obtained. For the first operating regime, namely, operation below the pump-laser threshold, the general steady-state solutions are given by:

$$P_p^0 = 0, \tag{2.39a}$$

$$N^0 = \sigma, \tag{2.39b}$$

$$P_s^0 = 0, \tag{2.39c}$$

where P_p^0, N^0, and P_s^0 represent the zeroth-order, time-independent values for the fundamental pump power, normalised pump gain, and OPO resonant signal power, respectively. In this regime, an increase in normalised pumping rate σ leads to a proportional rise in the pump laser gain (see Fig. 2.7, Region I). Once the laser surpasses its threshold, but before sufficient intracavity power is available to reach the SRO threshold – that is, for $\sigma_{\text{th}}^L \leq \sigma \leq \sigma_{\text{th}}^{\text{SRO}}$ – the system's steady-state solutions begin to evolve accordingly:

$$P_p^0 = \frac{\sigma - 1}{x}, \tag{2.40a}$$

$$N^0 = 1, \tag{2.40b}$$

$$P_s^0 = 0, \tag{2.40c}$$

The solutions to Eqs. (2.40a)–(2.40c), depicted in region II of Fig. 2.7, describe the operational behavior of a conventional single-frequency laser operating with its gain clamped at the laser threshold. Within this regime, two significant characteristics emerge. First, the SRO remains below its threshold and primarily contributes as an additional linear loss mechanism within the pump laser cavity. Second, the laser exhibits a linear response to increasing pump levels, similar to the laser gain observed in region I. As the pumping rate σ is increased beyond the point at which the intracavity field is sufficient to sustain efficient PDC, specifically for $\sigma_{\text{th}}^{\text{SRO}} \leq \sigma$, the steady-state solutions in the regime above the SRO threshold are given by:

$$P_p^0 = 1, \tag{2.41a}$$

$$N^0 = \frac{\sigma}{1+x}, \tag{2.41b}$$

$$P_s^0 = \frac{N^0 - 1}{F}. \tag{2.41c}$$

The final steady-state solutions described by Eqs. (2.41a)–(2.41c) are depicted in Region III of Fig. 2.7. Equation (2.41a) demonstrates that the intracavity pump power becomes clamped at its SRO threshold value, consistent with Siegman's nonlinear power-limiting concept [95], while further increases in the pump rate σ lead to a linear rise in laser gain and, via the nonlinear interaction, a corresponding linear growth of the signal and idler photon flows. Furthermore, the photon-flow thresholds σ_{th}^{L} and $\sigma_{\text{th}}^{\text{SRO}}$ are reformulated in terms of the corresponding pump power thresholds P_{th}^{L} and $P_{\text{th}}^{\text{SRO}}$, thereby recasting the model in experimentally accessible power units that directly reflect the operating characteristics of the ICSRO, as shown in Fig. 2.7. It is worth pointing out that, in Fig. 2.7, the down-converted (and intracavity) photon flow is evaluated as a function of the input power from the external pump laser, P_{in}.

Although the analysis presented here is purely theoretical, the predicted power scaling and operating-regime behavior play a central role in interpreting the experimental results discussed in later chapters. In particular, the regime transitions and intracavity field clamping behaviour predicted by the steady-state model are directly compared with

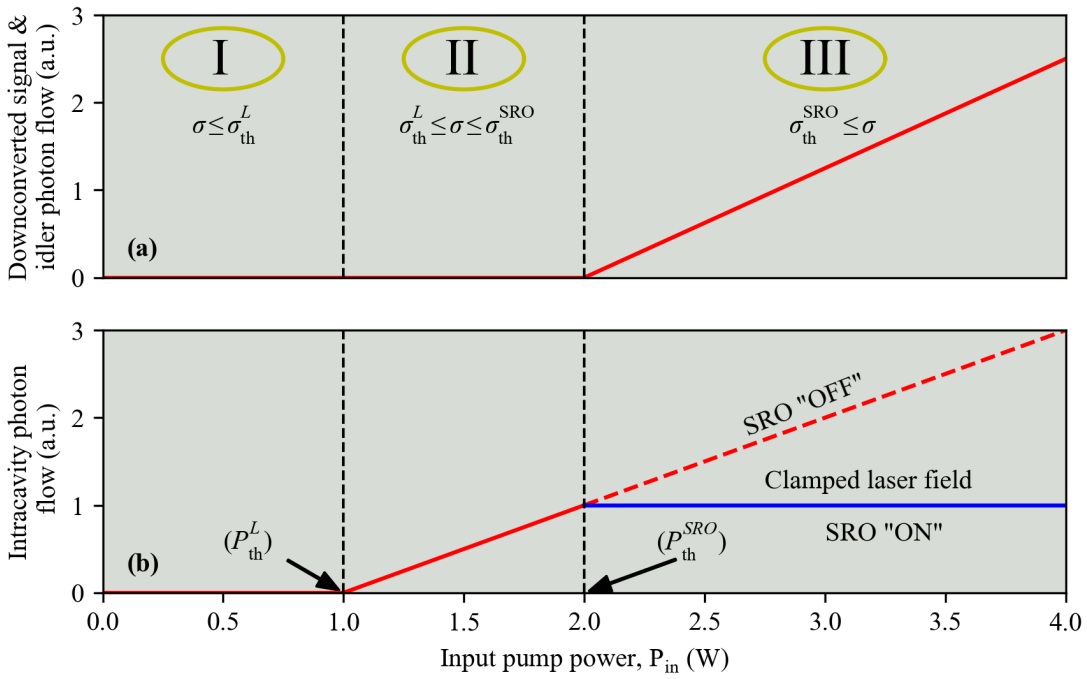


Figure 2.7: **(a)** Down-converted photon flow characteristics of an ICSRO, with laser threshold $P_{\text{th}}^{L} = 1.0$ W and SRO threshold $P_{\text{th}}^{\text{SRO}} = 2.0$ W. Regions I, II, and III correspond to the solution sets of Eqs. (2.39a)–(2.39c), (2.40a)–(2.40c), and (2.41a)–(2.41c), respectively. **(b)** Intracavity laser photon flow in each operating region. Note the clamping effect in Region III for input pump powers exceeding $P_{\text{th}}^{\text{SRO}}$. These theoretical trends provide a framework for interpreting the experimentally measured power characteristics presented in Figs. 4.13 and 4.18.

the experimentally measured ICSRO power characteristics presented in Chapter 4 (see Figs. 4.13 and 4.18).

The role of the ICSRO as a nonlinear output coupler is evident from Fig. 2.7 and Eqs. (2.39)–(2.41). If this scenario holds, an optimal ratio between output coupling and the input pumping rate will exist. This concept is addressed in Section 2.6.2.

2.6.2 ICSRO steady-state power optimisation

Optimisation of the down-converted power in the ICSRO was first addressed by Tran-Ba-Chu and Broyer [96]. They demonstrated that, under optimal nonlinear coupling conditions, it is possible to down-convert 100% of the potentially extractable laser power.

Again, for a single-frequency pump laser, the expression for the signal photon-flow inside the OPO cavity is given by [30]:

$$\xi_s = \xi_{\text{sat}} \, \frac{\alpha_p}{\alpha_s} \left(\sigma - \sigma_{\text{th}}^{\text{SRO}}\right) \left(1 - \frac{\sigma_{\text{th}}^{L}}{\sigma_{\text{th}}^{\text{SRO}}}\right), \tag{2.42}$$

where α_s and α_p represent the round-trip losses of the resonant signal cavity and the fundamental pump-laser cavity, respectively. Equating the round-trip losses of the signal and idler fields under steady-state conditions yields an idler output of:

$$(\xi_i)_{\text{out}} = \xi_{\text{sat}} \, \alpha_p \left(\sigma - \sigma_{\text{th}}^{\text{SRO}}\right) \left(1 - \frac{\sigma_{\text{th}}^{L}}{\sigma_{\text{th}}^{\text{SRO}}}\right). \tag{2.43}$$

At this stage, it is advantageous to combine the equations describing the signal and idler photon flows into a single expression that incorporates both the input laser power and the threshold parameters. Accordingly, the expression for the total down-converted power P_{DC} is obtained by combining Eqs. (2.42) and (2.43):

$$P_{\text{DC}} = \xi_{\text{max}} \left(P_{\text{in}} - P_{\text{th}}^{\text{SRO}}\right) \left(1 - \frac{P_{\text{th}}^{L}}{P_{\text{th}}^{\text{SRO}}}\right). \tag{2.44}$$

Here, P_{in} denotes the external input pump power, P_{th}^{L} represents the external pump power at the threshold of the fundamental laser, and $P_{\text{th}}^{\text{SRO}}$ denotes the external pump power at the threshold of the SRO. Moreover, ξ_{max} denotes the maximum slope efficiency of the fundamental pump laser, and is given by the following expression:

$$\xi_{\text{max}} = \eta_{\text{in}}^{\text{ext}} \, \eta_{\text{abs}} \, \frac{\lambda_{\text{in}}^{p}}{\lambda_L}, \tag{2.45}$$

where $\eta_{\text{in}}^{\text{ext}}$ denotes the optical coupling efficiency of the external pump laser at λ_{in}^{p}, while η_{abs} represents the fraction of external pump power usefully absorbed by the gain medium of the fundamental pump laser. The quantities λ_{in}^{p} and λ_L correspond to the wavelengths of the external pump laser and the fundamental pump laser, respectively.

Optimisation of Eq. (2.44) for a given external pump power P_{in} is achieved by solving the following first-order partial differential equation [30]:

$$\frac{\partial P_{\text{DC}}}{\partial P_{\text{th}}^{\text{SRO}}} = 0. \tag{2.46}$$

The above differential equation defines the SRO threshold, which maximises the total down-converted power for a given input pump power P_{in} and pump-laser threshold P_{th}^{L}, expressed as:

$$P_{\text{th}}^{\text{SRO}} = \sqrt{P_{\text{th}}^{L}\, P_{\text{in}}}. \tag{2.47}$$

This expression can be used to determine the maximum down-converted power achievable for a given fundamental laser threshold power and external input pump power under optimal conditions, which is:

$$(P_{\text{DC}})_{\text{max}} = \xi_{\text{max}} \left(\sqrt{P_{\text{in}}} - \sqrt{P_{\text{th}}^{L}} \right)^2. \tag{2.48}$$

Equation (2.48) coincides with the maximum power attainable from the fundamental pump laser when SRO operation is ceased, which is:

$$\left(P_{\text{out}}^{L}\right)_{\text{max}} = \xi_{\text{max}} \left(\sqrt{P_{\text{in}}} - \sqrt{P_{\text{th}}^{L}} \right)^2. \tag{2.49}$$

Thus, under optimal conditions, Eqs. (2.44) and (2.49) combine to yield:

$$\xi_{\text{max}} \left(P_{\text{in}} - P_{\text{th}}^{\text{SRO}} \right) \left(1 - \frac{P_{\text{th}}^{L}}{P_{\text{th}}^{\text{SRO}}} \right) = \xi_{\text{max}} \left(\sqrt{P_{\text{in}}} - \sqrt{P_{\text{th}}^{L}} \right)^2, \tag{2.50}$$

where

$$P_{\text{in}} = \frac{\left(P_{\text{th}}^{\text{SRO}}\right)^2}{P_{\text{th}}^{L}}. \tag{2.51}$$

These optimisation conditions can be illustrated graphically by plotting the corresponding functions for the optimum down-converted power and fundamental laser output power over a range of external input pump powers, as shown in Fig. 2.8.

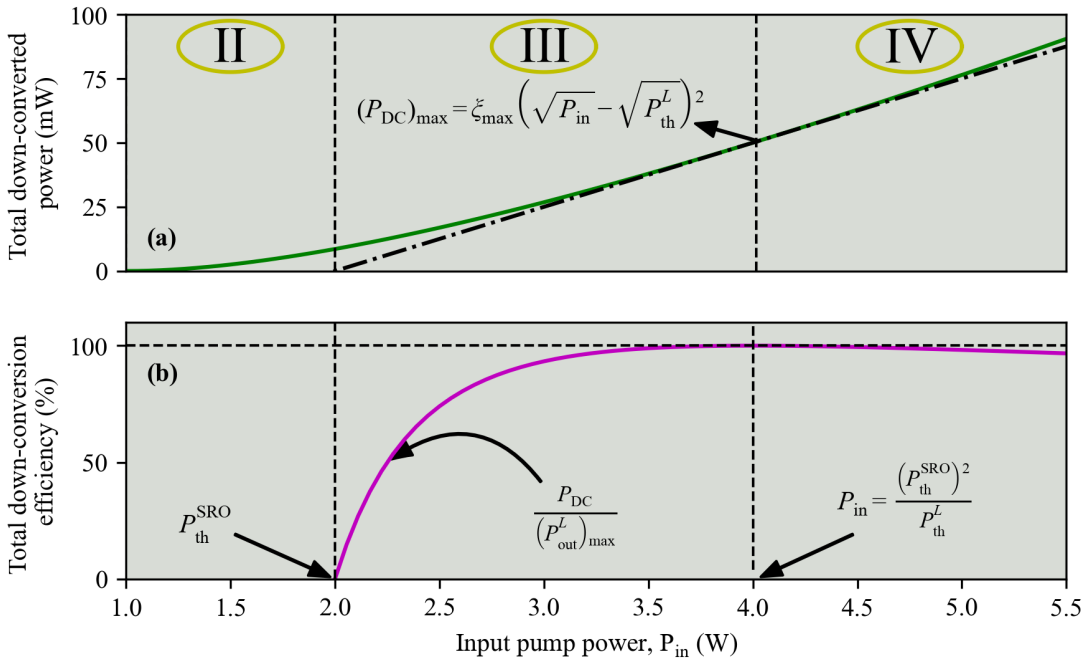


Figure 2.8: Total down-converted **(a)** power and **(b)** efficiency characteristics of an ICSRO $\left(P_{\text{th}}^{L} = 1.0\,\text{W};\ P_{\text{th}}^{\text{SRO}} = 2.0\,\text{W};\ \xi_{\text{max}} = 0.05\right)$. Regions II and III correspond to those illustrated in Fig. 2.7. Note the "over-coupling" regime in Region IV, which occurs for input pump powers exceeding $(P_{\text{DC}})_{\text{max}}$. The behaviour predicted by this steady-state optimisation analysis provides a theoretical basis for the experimentally observed power and efficiency trends presented in Chapter 4 (see Figs. 4.16 and 4.17).

Figure 2.8 illustrates the operational characteristics of the ICSRO. Above threshold, the SRO rapidly approaches 100% efficiency under the optimal relationship between the fundamental laser and SRO threshold conditions, as given by Eq. (2.51). It is worth noting that this optimal operating point corresponds to complete conversion of the theoretically extractable fundamental laser power into useful OPO output power, which is subsequently extracted through an optimised output coupler. To maximise the non-resonant idler output for a given external pump power and fundamental laser threshold power, the optimal relationship between the SRO and fundamental laser thresholds is given by Eq. (2.51). Operating regions II and III correspond to those shown in Fig. 2.7. The maximum fundamental laser output $(P_{\text{out}}^{\text{L}})_{\text{max}}$ is also indicated in Fig. 2.8 to highlight the optimum down-conversion condition. Under ideal operating conditions, the

SRO cavity outputs power solely via the down-converted signal and idler fields, with no such output coupling at the pump wavelength. However, output coupling at the pump wavelength can still occur within the pump branch of the ICSRO resonator.

The steady-state optimisation analysis presented here establishes the expected limits on down-converted power and efficiency in a CW ICSRO, and serves as a guide for interpreting the experimentally measured performance of the system in later chapters. In particular, the experimentally measured power and efficiency characteristics are directly compared with the above theoretical predictions in Chapter 4 (see Figs. 4.16 and 4.17).

In Section 2.7, a simplified threshold model for a CW Gaussian-beam-pumped ICSRO is presented, based on the theoretical model developed by Stothard [60].

2.7 Stothard model

David J. M. Stothard proposed a theoretical model in 2010 describing the behavior of a CW ICSRO laser system. This model provided an expression for the threshold pump level, identified the primary physical parameters influencing it, and introduced strategies for its minimisation [60].

Before proceeding with the theoretical analysis, it is assumed that, for the SRO to exhibit gain across its phase matched bandwidth, the pump laser must be highly coherent and spectrally monochromatic. Additionally, it is assumed that both the fundamental pump and resonant signal fields propagate uniformly and are confocally focussed at the centre of the OPO crystal. Under these assumptions, the parametric gain of the ICSRO can be expressed as follows:

$$G = \frac{P_{\text{out}}}{P_{\text{in}}} - 1 = \sinh^2(\Gamma_{\text{par}} l), \tag{2.52}$$

where l represents the total length of the OPO crystal, and Γ_{par} denotes the parametric gain factor, given by:

$$\Gamma_{\text{par}}^2 = \left(\frac{d_{\text{eff}}^2}{n_p n_s n_i} \right) \frac{2\omega_s \omega_i I_p}{\varepsilon_0 c^3}. \tag{2.53}$$

In the above equation, I_p denotes the intensity of the fundamental pump laser as it propagates through the OPO crystal; d_{eff} is the effective nonlinearity coefficient of the crystal under QPM conditions; ω_s and ω_i represent the angular frequencies of the down-converted signal and idler fields, respectively; and $n_{p,s,i}$ denotes the refractive indices of the OPO crystal at the pump, signal, and idler wavelengths, respectively. In the low-gain regime, where $\Gamma_{\text{par}} l \leq 1$, as is typical in CW operation, Eq. (2.52) simplifies to:

$$G_{\text{cw}} \approx \Gamma_{\text{par}}^2 l^2. \tag{2.54}$$

Therefore, when properly phase matched, the single-pass gain exhibits a quadratic dependence on the product $\Gamma_{\text{par}} l$. When the OPO is placed within the same cavity as the fundamental pump laser, the parametric gain as a function of the intracavity circulating power P_{intra} can be fully described by the following expression:

$$G_{\text{cw}} = \left(\frac{d_{\text{eff}}^2}{n_p n_s n_i} \right) \frac{4\,\omega_s\,\omega_i\,l^2\,P_{\text{intra}}}{\varepsilon_0\,c^3\,\pi\left(w_p^2 + w_s^2\right)}, \tag{2.55}$$

where the radii of the confocally focussed pump and signal beams are given by w_p and w_s, respectively. The waist radius is expressed as:

$$w_\lambda = \sqrt{\frac{\lambda l}{2\pi n}}. \tag{2.56}$$

It is important to note the two-fold increase in Eq. (2.55) relative to Eq. (2.53). This increase arises because the signal field experiences gain on each pass of the pumping field, which is of course travelling in both directions through the nonlinear crystal on each round-trip of the fundamental pump cavity. Therefore, the SRO threshold is surpassed when the intracavity pump field becomes sufficiently strong for the parametric gain to overcome the round-trip loss experienced by the resonant signal field:

$$G_{\text{cw}} \geq \alpha_{\text{tr}} + \alpha_{\text{par}}, \tag{2.57}$$

where α_{par} represents the cumulative parasitic losses associated with the resonant signal field, and α_{tr} denotes the total transmission loss of the resonant signal field through the OPO cavity mirrors. Ultimately, P_{th} can be defined as the intracavity circulating power required for the SRO system to reach its threshold. This is achieved by rearranging Eq. (2.55), and setting $P_{\text{intra}} = P_{\text{th}}^{\text{SRO,intra}}$ to give:

$$P_{\text{th}}^{\text{SRO,intra}} = \frac{n_p n_s n_i \, \varepsilon_0 c^3 \pi (w_p^2 + w_s^2)}{4 \, \omega_s \omega_i l^2 d_{\text{eff}}^2} \left(\alpha_{\text{tr}} + \alpha_{\text{par}}\right). \tag{2.58}$$

Equation (2.58) identifies the key parameters that enable the SRO threshold to be achieved with low intracavity pump power and, consequently, low external pump power. These parameters include the intrinsic nonlinear coefficient of the OPO material d_{il}, and the order of the QPM interaction, both of which directly affect the effective QPM nonlinear coefficient d_{eff} (see Eq. (2.27)). Additionally, the total length of the OPO crystal l, and the transmission loss of the resonant signal field within the OPO cavity α_{tr}, also play a crucial role. Given experimental limitations in external pump power, and thus intracavity circulating power, the choice of OPO crystal is thus pivotal to minimising the denominator in Eq. (2.58). Moreover, highly reflective dielectric-coated mirror substrates at the resonant signal wavelength are also essential for minimising signal-field transmission losses and reaching the SRO threshold when the pump power is limited.

2.8 Conclusion

In conclusion, this chapter has established the mathematical foundation and theoretical principles governing ICSRO operation and the relevant underpinning nonlinear optics. Specifically, we have defined the CW ICSRO steady-state power characteristics, derived the optimisation parameters that dictate ICSRO performance, and extended the theoretical model of Stothard [60], which identifies the key design criteria for minimising the SRO threshold in practical experimental configurations. When external pump power is limited, reducing the SRO threshold is critical; this can be accomplished by selecting an

OPO crystal with a long effective interaction length and a large nonlinear coefficient, and by employing cavity mirrors with high reflectivity at the resonant OPO wavelength.

Furthermore, the exploitation of the second-order nonlinear susceptibility tensor $\chi^{(2)}$ enables a range of second-order nonlinear processes in non-centrosymmetric media, including SHG and PDC. For a PDC interaction, efficient energy transfer from the pump to the signal and idler fields require satisfaction of the momentum conservation condition, commonly referred to as phase matching. In this investigation, the domain-reversal QPM technique was analysed, and the corresponding acceptance parameters of the 5%-MgO:PPLN crystal were modelled under our experimental parameters ($T_{\text{crystal}} = 114°\text{C}$, $\lambda_p = 690.6$ nm, $\Lambda_{\text{QPM}} = 14.55$ µm). Simulations indicate that efficient pump-to-signal conversion requires an intracavity pump laser bandwidth below 126 pm, while the crystal exhibits a temperature acceptance bandwidth of 6.8°C. Theoretical QPM tuning curves further demonstrate the ICSRO's broad spectral tunability: poling periods of 14.55 µm and 15.10 µm enable operation from 1.03 µm to 2.09 µm for temperatures between 30°C and 200°C, assuming a pump wavelength of 0.689 µm and using the Sellmeier equations of Gayer *et al.* [88].

The following chapter addresses the theoretical design of the ICSRO system, which is, of course, intracavity-pumped by a VECSEL in this investigation. It begins with a concise review of the VECSEL technology, followed by an overview of the nonlinear properties of the 5%-MgO:PPLN crystal employed for generating efficient PDC. The chapter concludes with an estimation of the intracavity circulating pump power required to reach the SRO threshold, based on the experimental parameters implemented in this work.

Chapter 3

Design considerations for a CW ICSRO

3.1 Introduction

This chapter presents the key design considerations for a continuous-wave (CW) intracavity singly resonant OPO (ICSRO), focussing on an optical resonator optimised for minimum oscillation threshold when pumped by a vertical-external-cavity surface-emitting laser (VECSEL). A comprehensive review of the VECSEL technology is presented, followed by a detailed overview of the 5%-MgO:PPLN crystal selected for achieving efficient parametric down-conversion (PDC) in this work. The chapter concludes with a quantitative analysis, based on the model developed by Stothard [60], to accurately determine the intracavity VECSEL power required to reach oscillation threshold in our designed ICSRO VECSEL system.

3.2 Vertical-external-cavity surface-emitting laser (VECSEL)

Vertical-external-cavity surface-emitting lasers (VECSELs), also referred to as semiconductor disk lasers (SDLs), or optically-pumped semiconductor lasers (OPSLs), emerged

in the 1990s as a significant advancement in laser photonics, driven by improvements in semiconductor epitaxial growth techniques. These lasers were developed to overcome the limitations of conventional edge-emitting semiconductor lasers and vertical-cavity surface-emitting lasers (VCSELs). While traditional semiconductor lasers typically achieve either high optical powers or high-quality output beams, VECSELs can simultaneously maintain the fundamental transverse TEM_{00} mode for circular beam operation and scale the mode size to increase optical power [97]. This unique combination of high output power and excellent beam quality has made VECSELs highly desirable in a wide range of scientific and commercial applications [98].

The following section provides a detailed overview of state-of-the-art VECSEL devices, including their operational principles, thermal management strategies, extensive wavelength coverage, and diverse applications. Furthermore, an analysis of the transient dynamics of VECSELs is presented to emphasise their Class-A dynamical behaviour, which permits relaxation-oscillation-free operation above the SRO oscillation threshold.

3.2.1 VECSEL design and operational principles

The structural design of VECSELs was first pioneered by Jiang and co-workers in 1991 [99], and subsequently developed further by Kuznetsov *et al.* [100], [101]. Their work demonstrated the remarkable potential of multiple quantum well (MQW) semiconductor gain structures vertically integrated within external laser cavities to achieve high output power. A typical VECSEL chip consists of two main components: a distributed Bragg reflector (DBR) and a MQW gain region.

The DBR is fabricated from N pairs of semiconductor layers with a high refractive index contrast, carefully chosen to be transparent at the VECSEL design wavelength. A high refractive index contrast is desirable for achieving high reflectivity and a broad spectral bandwidth [102]. To satisfy the Bragg condition [103], each layer is deposited with a quarter-wavelength optical thickness.

The active gain region, epitaxially grown atop the DBR, typically comprises MQWs or layers of quantum dots (QDs) separated by pump-absorbing barrier layers. In QW-

based gain structures, the composition and thickness of each QW is carefully optimised using transition energy calculations derived from the time-independent Schrödinger equation for a finite square well [104]. This enables precise tailoring of the material composition to achieve the desired emission and absorption at the operating wavelength. The QWs are also strategically positioned at the antinodes of the optical field standing wave in a process known as resonant periodic gain (RPG) [105]. RPG provides several benefits: it suppresses spatial hole-burning, reduces spectral broadening, and enhances the efficiency of the gain medium.

Owing to the intrinsic structural design of the VECSEL chip, a Fabry–Pérot (FP) etalon is inherently formed between the semiconductor–air interface and the DBR. This FP sub-cavity can be deliberately engineered to function in either a resonant or anti-resonant configuration. In the resonant case, an antinode of the standing-wave field is located at the semiconductor surface, maximising the optical confinement factor and thereby enhancing the modal gain while reducing the lasing threshold. Conversely, in the anti-resonant configuration, the field node is positioned at the semiconductor surface, leading to a reduced confinement factor. This configuration favours a broader gain bandwidth and enhanced wavelength tunability, albeit at the expense of reduced gain and an increased threshold relative to the resonant design [106].

For the current research investigation, an AlGaInP-based red-VECSEL is employed, and is schematically shown in Fig. 3.1. The resonant VECSEL gain structure comprises multiple AlGaInP QWs grown on an AlGaAs DBR, and is engineered for optical pumping at green wavelengths with laser emission centred near 689 nm. The QWs are strategically positioned at the antinodes of the intracavity optical field in order to maximise RPG. In addition, tensile-strained compensation layers are incorporated to ensure a zero net in-plane strain across the heterostructure, thereby preserving structural integrity and crystalline quality [107]. Finally, a lattice-matched GaInP cap layer is deposited to passivate the surface, providing protection against oxidation associated with the high aluminium content of the compensation layers.

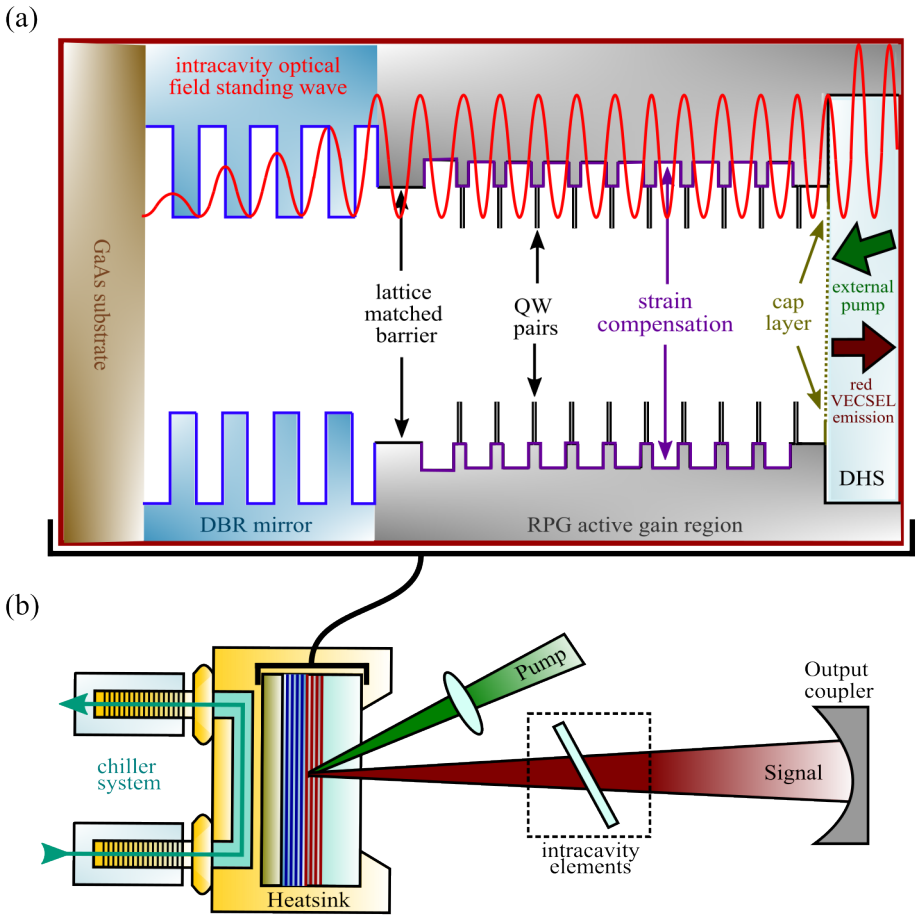


Figure 3.1: Schematic illustration (not to scale) of the operating principles of an AlGaInP-based red-VECSEL device. **(a)** Semiconductor bandgap structure of the DBR, active gain region, compensation layers, and cap layer. **(b)** Typical two-mirror standing-wave laser cavity incorporating a VECSEL gain mirror as the optically pumped end mirror, thermally managed via a diamond heat spreader (DHS), with intracavity elements included for wavelength tuning. DBR: distributed Bragg reflector.

3.2.2 Optical pumping

Optical pumping constitutes the dominant method for achieving population inversion in VECSELs, with high-power CW laser diodes widely regarded as the most practical and efficient pump sources. Electrically pumped counterparts of VECSELs, known as NECSELs, also exist, with the nomenclature originating from their initial development and commercialisation by Novalux Inc. [108]. The NECSEL architecture employs both

p-doped and n-doped DBR mirrors, in a manner analogous to a VCSEL, while an additional external mirror completes a coupled external cavity. As the present investigation exclusively considers optically pumped VECSEL architectures, this pumping scheme is adopted throughout the remainder of this thesis. For a more comprehensive discussion of NECSEL devices, the reader is referred to Refs. [97], [109].

Optical pumping is preferred over electrical injection for VECSEL operation, as it offers several distinct advantages that outweigh the limitations of the electrically driven approach. Foremost, optical pumping facilitates uniform transverse carrier excitation across large emission apertures. Secondly, the elimination of wafer doping not only simplifies the epitaxial growth process but also reduces parasitic free-carrier absorption, thus improving device efficiency. Another critical advantage is scalability: multiple pump lasers can be employed simultaneously, provided that all pump beams are focussed onto the same region of the gain chip. This flexibility is particularly advantageous in high-power applications where increased external pump power is required. Moreover, owing to the relatively short absorption length of the active region – typically limited to 1–2 µm – the output beam quality remains largely insensitive to the spatial characteristics of the external pump source, as the VECSEL inherently operates as a mode converter. As a result, cost-effective diode lasers are highly suitable pump sources, with mode-matching conditions satisfied simply by focussing the external pump beam into a circular spot within a single transverse plane.

Optically pumped VECSELs are implemented using two primary schemes: in-well pumping [110] and barrier pumping [111]. In-well pumping involves direct absorption within the QWs; however, this absorption is typically weak due to the thin QWs in the active region. This limitation can be mitigated either by increasing the number of pump passes through the gain region using external pump recycling optics, or by engineering the epitaxial structure to enhance absorption [112]. In particular, in-well pumped devices can be designed to incorporate a sub-cavity resonant at both the pump and signal wavelengths. This approach requires a broadband or dual-band DBR, resulting in a doubly resonant cavity architecture.

By contrast, barrier-pumping ensures that most of the pump light is absorbed within a single pass of the active region. Following absorption, excited carriers are promoted to higher-lying energy levels in the conduction band before diffusing into the QWs. Once population inversion is reached, the carriers undergo stimulated or spontaneous emission, after which non-radiative decay processes return them to the QW ground state. Finally, optical gain occurs when the stimulated emission rate surpasses the absorption rate.

The fundamental limiting factor in optical pumping is the 'quantum defect', defined as the energy difference between the absorbed pump photons and the emitted signal photons from the QWs. This energy disparity primarily manifests as heat, arising from non-radiative vibrational relaxation of carriers as they relax from the barrier region into the QWs.

3.2.3 Thermal management

Semiconductor light-emitting devices achieve higher efficiency at lower temperatures due to reduced carrier leakage [113]. Surface-emitting lasers, in particular, exhibit a strong temperature-dependent gain arising from their complex multilayer structure, leading to the phenomenon known as 'thermal rollover' [114]. Under these conditions, the output power initially increases with pump power, reaches a maximum, and subsequently decreases rapidly, ultimately leading to the termination of laser oscillation. Therefore, the implementation of robust and effective thermal management strategies is a critical requirement for extending the thermal rollover point to higher pump powers [101].

Although VECSELs benefit from an external cavity that enables efficient beam shaping and power scaling, thermal effects associated with the alignment between the gain spectrum and the FP resonance remain comparable to those observed in VCSELs. In practice, optical pumping induces a temperature rise, resulting in redshifts of both the QW gain peak and sub-cavity resonance, albeit at different rates. For the VECSEL investigated in this work, comprising GaInP QWs separated by AlGaInP barriers, the QW gain peak typically redshifts at $\sim 0.3\ \mathrm{nm \cdot K^{-1}}$, while the sub-cavity resonance exhibits a slower redshift of $\sim 0.1\ \mathrm{nm \cdot K^{-1}}$ [115].

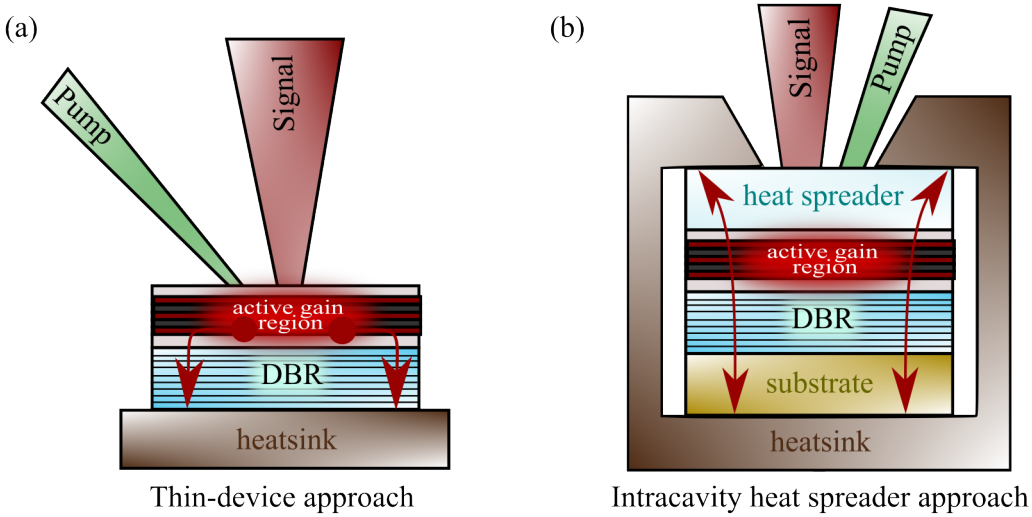


Figure 3.2: Schematic of the **(a)** thin-device and **(b)** intracavity heat-spreader thermal management approaches employed in VECSELs.

Beyond mounting the VECSEL chip on a temperature-stabilised (or water-cooled) heatsink, typically fabricated from brass or copper, more advanced thermal management techniques can be employed. These include the 'thin-device' approach (see Fig. 3.2a) and the 'intracavity heat spreader' approach (see Fig. 3.2b), both of which are designed to enhance heat extraction from the active region [101], [116].

In the thin-device scheme, the semiconductor substrate is removed through a combination of mechanical and chemical etching, after which the epitaxially grown semiconductor gain mirror is soldered directly onto a heatsink. Owing to the large difference in thickness between the optically pumped region and the overall semiconductor structure, the heat flow in this configuration is predominantly one-dimensional. The thin-device approach has demonstrated effectiveness in extracting heat from the gain region of InGaAs/(Al)GaAs-based VECSELs operating near 1 µm [117].

Despite its success in achieving high output powers, the thin-device approach exhibits a significant drawback: its strong dependence on the thermal conductivity of the DBR structure. Therefore, devices operating in the visible wavelength band require alternative thermal management solutions. In this spectral range, DBR materials typically exhibit

lower thermal conductivity, while the reduced refractive index contrast also necessitates a larger number of DBR layers to achieve high reflectivity. In such cases, the incorporation of an intracavity heat spreader has proven highly effective in enhancing heat extraction from the active region. As illustrated in Fig. 3.2b, this technique involves bonding a highly thermally conductive, optically transparent crystalline disk directly to the top surface of the wafer. The bonding is achieved via liquid-assisted optical contacting, thus avoiding the use of adhesives that could otherwise impair thermal conductivity. Unlike the thin-device approach, this scheme does not necessitate removal of the semiconductor substrate. Instead, heat is efficiently extracted from the gain region and transferred directly to the intracavity heat spreader in close proximity to the optically pumped region.

Several materials have been widely employed as heat spreaders in VECSEL systems, among which diamond is generally considered the most effective due to its exceptionally high thermal conductivity of $\sim 2200\ \mathrm{W\,m^{-1}\,K^{-1}}$ [118], surpassing that of all other available crystalline materials. Other commonly employed heat spreaders include silicon carbide ($\sim 490\ \mathrm{W\,m^{-1}\,K^{-1}}$) [119] and sapphire ($\sim 30\ \mathrm{W\,m^{-1}\,K^{-1}}$) [120].

3.2.4 Wavelength coverage

The wavelength versatility inherent to the VECSEL technology represents a considerable advantage, particularly due to its ability to tailor the emission wavelength according to specific design parameters. Variations in fundamental emission wavelength arise from the diverse bandgap energies exhibited by compound semiconductor materials. Additionally, the transition energy of the VECSEL gain medium is strongly influenced by several factors, including temperature, strain level, and QW thickness. Therefore, the emission wavelength can be precisely controlled through careful structural design. While the subcavity resonance is responsible for determining the fundamental emission wavelength, the achievable output power is contingent upon a broad range of external considerations. These include thermal management, epitaxial growth quality, available pump power, output coupling efficiency, mode-matching, and laboratory conditions. As illustrated in

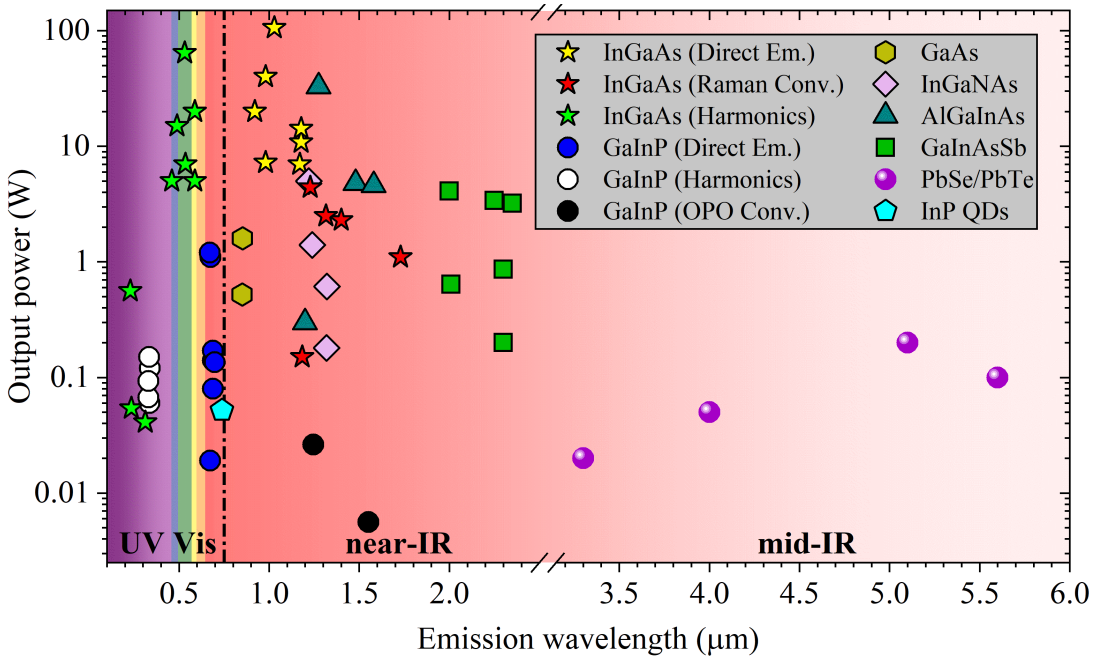


Figure 3.3: State-of-the-art continuous-wave VECSEL output power as a function of emission wavelength across various semiconductor gain media and frequency conversion schemes. Plotted literature results encompass: **InGaAs-based** architectures including *direct fundamental emission* [121], [122], [123], [124], [125], *harmonic generation* [121], [126], [127], [128], [129], [130], and *Raman frequency conversion* [23], [24], [131], [132], [133]; **GaInP-based** architectures including *direct fundamental emission* [22], [134], [135], [136], [137], [138] and *harmonic generation* [22], [139], [140], [141]; and other active region materials such as **GaAs** [17], [110], dilute-nitride **InGaNAs** [142], [143], [144], [145], **AlGaInAs** structures [146], [147], [148], [149], **InP QDs** [150], mid-IR **GaInAsSb** alloys [151], [152], [153], [154], and IV-VI lead-salt **PbSe/PbTe** chalcogenides [21], [155], [156]. For clarity, the experimental results of the ICSRO VECSEL obtained in the current investigation are indicated by the black circles.

Fig. 3.3, VECSELs have demonstrated operation across an exceptionally wide spectral range, extending from ∼225 nm in the deep-UV [20] – via a combination of semiconductor bandgap engineering and intracavity nonlinear frequency conversion – to ∼5.6 µm in the mid-IR [21].

Here, emphasis is placed on the red (visible) spectral region and the near-IR telecommunications wavelength bands, as these constitute the operational regimes explored in the present investigation.

Direct emission in the visible spectral region is commonly realised using GaInP QWs, lattice-matched to a GaAs substrate and embedded within AlGaInP barrier layers. This epitaxial material configuration has been shown to support efficient high-power operation throughout the red spectral range, typically spanning ∼650–700 nm. To achieve the required transverse-electric (TE) polarized optical gain, compressively strained QWs are generally incorporated within the active region. Optical excitation is typically provided by commercially available green laser sources operating at 532 nm. The first demonstration of a CW green-pumped red-VECSEL was reported by Hastie *et al.* [18] at the Institute of Photonics, University of Strathclyde. Later, output power of > 1 W was achieved, corresponding to a slope efficiency of 20%, at an emission wavelength of 675 nm [22]. The laser exhibited excellent beam quality, with a measured beam propagation ratio of $M^2 < 1.05$. Moreover, wavelength tunability was demonstrated through the insertion of a birefringent filter (BRF) positioned at Brewster's angle, with tuning achieved by rotation of the filter about an axis perpendicular to the optical axis. From this rotation, a continuous tuning range of ~ 5 nm, centred around 674 nm was achieved, while maintaining an output power of > 100 mW. More recently, the same research group has reported significant advances in terms of high-power operation and reduced noise performance of AlGaInP-based VECSELs. In particular, by implementing Pound–Drever–Hall (PDH) stabilisation, linewidth narrowing to the sub-kilohertz level was obtained in a conventional two-mirror resonator. Under these conditions, single-frequency output powers exceeding 130 mW were realised at emission wavelengths of 689 nm [135] and 698 nm [137], respectively, for application in laser cooling and spectroscopy of neutral strontium atoms.

The fundamental wavelength range spanning ∼1.2–1.6 µm, which is of particular importance for fibre-optic communication applications, can be accessed using the AlGaInAs/InP material system via the technique of 'wafer fusion'. Since such heterostructures cannot be grown monolithically due to lattice mismatch, wafer fusion provides a means of integrating dissimilar materials into a single semiconductor device design. Significant research at the Optoelectronics Research Centre, Tampere, has demonstrated the

effectiveness of this approach, where wafer-fused structures employing GaAs-substrate-based mirrors yielded output powers of more than 4.5 W [147], [148], [149]. These devices operated across spectral ranges extending from 1.2 µm [146] to 1.58 µm [148].

3.2.5 VECSEL applications

VECSELs possess a remarkable amalgamation of high-brightness output, broad wavelength coverage, excellent beam quality, low noise, ultra-narrow linewidths, and single-frequency operation. As a result, they have found widespread application across a wide range of scientific and technological fields. One of the most prominent areas of application is spectroscopy, in particular intracavity laser absorption spectroscopy, or ICLAS. First demonstrated in a VECSEL by Garnache *et al.* [157], ICLAS is an extremely sensitive technique capable of detecting absorption lines as weak as 10^{-10}–$10^{-11}\,\mathrm{cm}^{-1}$. Traditional implementations rely on complex and cumbersome laser systems with broad emission spectra, such as cryogenically cooled colour-centre lasers. In contrast, VECSELs can effectively suppress amplified spontaneous emission, serving as compact and cost-effective sources for ICLAS, particularly in the near-IR spectral regions. Several studies, including those by Bertseva *et al.* [158] and Naumenko *et al.* [159], have successfully demonstrated VECSEL-based near-IR ICLAS systems.

In medical applications, photodynamic therapy can be enhanced through the use of multi-Watt red lasers emitting within the spectral range of $\sim$630–690 nm. Light in this wavelength range penetrates tissue to depths 50–200% greater than that of blue light (400–500 nm), while providing optimal absorption for commercially available photosensitisers, which are critical for the treatment of malignant tumors [160]. A distinctive advantage of VECSELs is their ability to directly emit high-power red light that can be conveniently coupled into optical fibres with high efficiency, making them a superior alternative to traditional argon lasers in photodynamic therapy.

In ophthalmology, high-brightness yellow VECSELs have been developed for photocoagulation treatments to seal retinal blood vessels [161], as well as for dermatological applications, such as the treatment of cutaneous vascular lesions like telangiectasia [162].

Yellow-emitting sources outperform green-emitting sources in these applications due to their spectral alignment with the absorption peak of oxygenated hemoglobin. Consequently, VECSELs, with their compact design, simplicity, and ability to generate yellow wavelengths efficiently via nonlinear frequency conversion, are ideally suited to replace diode-pumped solid-state lasers (DPSSLs).

Another prominent application of yellow-emitting laser sources occurs at 589 nm, namely in sodium guide star systems for astronomical adaptive optics. Ground-based telescopes are fundamentally limited in angular resolution by atmospheric turbulence, arising from spatial and temporal variations in the refractive index of the atmosphere. Adaptive optics systems mitigate these distortions in real time; however, they require a bright artificial reference source in the sky. This is provided by a laser guide star, generated via resonance fluorescence of mesospheric sodium atoms at the 589 nm D2 transition. Recently, a VECSEL-based sodium guide star laser system has been demonstrated on-sky for the first time [163], delivering up to 12 W of single longitudinal mode output at 589 nm with tunability around the sodium D2 resonance, thereby demonstrating the capability of the VECSEL technology to deliver high-power emission at challenging yellow wavelengths for astronomical applications.

Finally, the development of multi-Watt portable green laser sources has also become increasingly important, particularly for forensic applications in the detection of bodily fluids and fingerprints under ambient illumination. Historically, coherent green emission has been realised using frequency-doubled neodymium-doped yttrium aluminium garnet (Nd:YAG) lasers operating at 532 nm. Although such systems can achieve high CW output powers, they generally suffer from limited wavelength tunability. VECSELs present a compelling alternative, offering power scalability, wavelength flexibility, single-frequency and low-noise operation, together with an open-cavity architecture that enables efficient intracavity frequency doubling. This advantage is exemplified by commercial OPSL platforms, such as the Verdi series from Coherent Inc. [164], which evolved from conventional DPSSLs to mitigate “green noise” and thermal lensing, as discussed in

Ref. [165]. These systems operate at 532 nm and deliver intracavity frequency-doubled output powers ranging from 2 W (Verdi G2) to 18 W (Verdi C18).

The following section examines the transient dynamics of VECSELs, with particular emphasis on their operation as pump sources for ICSROs. It is shown that the intrinsic gain dynamics of VECSELs enable relaxation-oscillation-free behaviour even when operating above the SRO oscillation threshold.

3.2.6 Transient dynamics above the SRO threshold

The transient dynamics of a laser are governed by the coupled evolution of the electromagnetic field and the material variables responsible for optical gain. Laser dynamical classes are distinguished by the relative characteristic relaxation times of these variables, particularly the intracavity photon lifetime τ_c, the upper-state lifetime τ_u, and, where relevant, the polarization dephasing time $\tau_\perp$ [166]. On this basis, laser systems are conventionally classified as Class-A, Class-B, or Class-C.

In a Class-A laser, the upper-state population relaxes much faster than the intracavity field, such that $\tau_u \ll \tau_c$. The population inversion therefore follows changes in the optical field adiabatically and can be eliminated from the dynamical equations, leaving the optical field as the principal dynamical variable. Consequently, the conventional relaxation oscillation response associated with the coupled field-inversion dynamics is suppressed.

In a Class-B laser, the upper-state population evolves much more slowly than the intracavity field, such that $\tau_u \gg \tau_c$. The population inversion must therefore be retained as an independent dynamical variable alongside the optical field. The resulting coupled field-inversion dynamics give rise to relaxation oscillations following perturbations, with their frequency and damping determined by the characteristic timescales and coupling between the two variables.

Class-C lasers additionally require the material polarization to be treated as an independent dynamical variable. This occurs when the polarization cannot be assumed to follow the optical field adiabatically, such that its dephasing dynamics must be re-

Table 3.1: Characteristics of Class-A, Class-B, and Class-C laser dynamics.

	Class-A	**Class-B**	**Class-C**
Timescale relation	$\tau_u \ll \tau_c$	$\tau_u \gg \tau_c$	$\tau_\perp \sim \tau_c, \tau_u$
Inversion dynamics	Adiabatic	Dynamical	Dynamical
Polarization dynamics	Adiabatic	Adiabatic	Dynamical
Relaxation oscillations	Suppressed	Present	Present

tained. The laser dynamics can therefore be described by a set of coupled Maxwell–Bloch equations governing the optical field, population inversion, and material polarization.

The laser classification thus reflects both the hierarchy of relaxation timescales and the number of independent dynamical variables required to describe the laser response. The distinction between Class-A and Class-B dynamics is particularly relevant to the present work, as the relative upper-state and cavity photon lifetimes determine the transient response, relaxation oscillation damping, and intensity-noise characteristics of the OPO pump source. The principal characteristics of the three dynamical classes are summarised in Table 3.1.

These dynamical considerations are particularly important for an ICSRO pump source, where fluctuations in the intracavity pump field can be transferred to the down-converted signal and idler fields. This has direct consequences for the generation of squeezed states of light. As shown theoretically by White *et al.* [167], intensity-difference squeezing is significantly degraded when the intracavity pump field exhibits pronounced relaxation oscillations, owing to the transfer of fundamental pump fluctuations to the down-converted fields. For a shot-noise-limited pump, the intensity-difference squeezing is predicted to be greatest at zero frequency, with a Lorentzian-like roll-off at higher detection frequencies [9]. Consequently, excess pump noise, particularly in the vicinity of relaxation oscillations, can increase the intensity-difference fluctuations above the standard quantum limit. Suppression of relaxation oscillations and minimisation of intracavity pump intensity noise are therefore important requirements for achieving high levels of squeezing.

Furthermore. the importance of the laser dynamical class can be illustrated by comparing the transient response of ICSROs pumped by different laser sources. Building on the analysis of Stothard *et al.* [26], the relaxation oscillation behaviour of an ICSRO pumped by a VECSEL is compared with that obtained using a neodymium-based solid-state laser. For the ICSRO, the angular frequency of the relaxation oscillations ω_{RO}, is determined by the photon lifetimes of the intracavity pump and SRO cavities according to:

$$\omega_{\mathrm{RO}} \approx \sqrt{\frac{X-1}{\tau_p \tau_{\mathrm{SRO}}}}, \tag{3.1}$$

where τ_p and τ_{SRO} denote the photon lifetimes of the intracavity pump and SRO cavities, respectively, and X represents the pump level relative to the SRO threshold.

In addition to the oscillation frequency, the effective damping constant γ determines the temporal stability and decay of the relaxation oscillation response. For an ICSRO operated above the SRO threshold, the effective damping constant is given by [26]:

$$\gamma_{\mathrm{ICSRO}} \approx \frac{(X-1)\left(\sqrt{\tau_p \tau_{\mathrm{SRO}}}/\tau_u\right)}{\tau_u}, \tag{3.2}$$

where τ_u denotes the upper-state lifetime of the fundamental pump laser. For comparison, the corresponding damping constant for a basic laser is approximately [26]:

$$\gamma_B \approx \frac{X}{2\tau_u}. \tag{3.3}$$

The contrasting transient behaviour of the two fundamental pump sources can therefore be understood in terms of their respective dynamical classes. For neodymium-based solid-state lasers, experimentally measured upper-state lifetimes are typically on the order of 100 µs [168], substantially exceeding the relevant cavity photon lifetimes, such that $\tau_u \gg \tau_p, \tau_{\mathrm{SRO}}$. The fundamental pump therefore exhibits Class-B dynamics, with the population inversion acting as a slowly evolving dynamical variable. The relatively weak damping of the resulting relaxation oscillations permits quasi-continuous bursts of

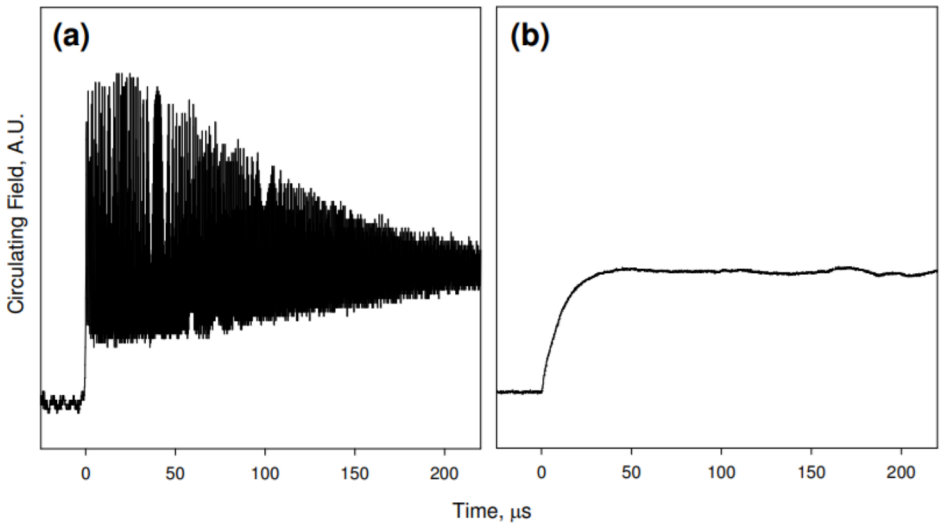


Figure 3.4: Transient dynamics of an ICSRO in the steady-state regime, as reported by Stothard *et al.* [26], for an SRO pumped internally by **(a)** a neodymium-doped yttrium orthovanadate (Nd:YVO_4) laser and **(b)** a VECSEL.

amplitude fluctuations to be triggered by perturbations occurring on timescales shorter than the damping time, as shown in Fig. 3.4a.

In contrast, the VECSEL possesses an upper-state lifetime of $\sim$ 1–10 ns [98], more than five orders of magnitude shorter than that of neodymium-based sources. Since the photon lifetimes of the VECSEL pump cavity and SRO cavity are substantially longer than the VECSEL upper-state lifetime, such that $\tau_u \ll \tau_p, \tau_{\mathrm{SRO}}$, the VECSEL operates in the Class-A regime. The population inversion can therefore respond rapidly to fluctuations in the intracavity field, suppressing the sustained relaxation oscillation bursts observed for the Class-B pump source, as illustrated in Fig. 3.4b. This reduced tendency towards relaxation oscillations, together with the associated reduction in excess intensity noise, makes the VECSEL particularly attractive as an ICSRO pump source for applications requiring low-noise operation, including squeezed-light generation.

The preceding discussion establishes the importance of the pump-laser dynamics to the performance of an ICSRO. The next consideration is the nonlinear medium responsible for parametric down-conversion (PDC), which must be established before considering the design of the ICSRO cavity. The following section introduces the structure and rel-

evant optical and physical properties of the MgO:PPLN crystal selected for this work, including its suitability for efficient PDC and its practical availability as an off-the-shelf nonlinear component.

3.3 OPO nonlinear χ^2 crystal: 5%-MgO:PPLN

As outlined in Chapter 2, the nonlinear crystal must be non-centrosymmetric, possess a high damage threshold, and exhibit a large effective nonlinearity coefficient. As a consequence, the most rational options for this investigation are either a conventional lithium niobate crystal ($LiNbO_3$) or a periodically-poled lithium niobate (PPLN) crystal. Furthermore, a decision must be made regarding whether to dope the nonlinear crystal with a small concentration of magnesium oxide (MgO).

Here, the structure of $LiNbO_3$ will be examined alongside its optical and physical properties. In addition, the phase matching conditions – modelled to the specific parameters of our ICSRO system – will be presented. Finally, a detailed justification will be provided for the selection of a 5%-MgO:PPLN crystal as the nonlinear medium of choice for our ICSRO system.

3.3.1 $LiNbO_3$ structure

Lithium niobate ($LiNbO_3$) was first grown in 1965 using the Czochralski method [169]. It is a negative uniaxial crystal belonging to the space group $R3c$. In this crystal structure, oxygen ions are arranged in hexagonally close-packed planar sheets. Moreover, $LiNbO_3$ belongs to the crystallographic point group 3m, exhibiting a three-fold rotational symmetry along the c-axis, together with mirror symmetry about three planes separated by 60°, as illustrated in Fig. 3.5. Figure 3.5 also provides a visual representation of the stacking sequence of Li and Nb ions along the positive c-axis within the oxygen octahedral sites. The ion sequence can be described as: Nb, vacancy, Li, Nb, vacancy, Li, and so on. In this structure, the octahedral interstices are composed of one-third vacancies, one-third Li atoms, and one-third Nb atoms.

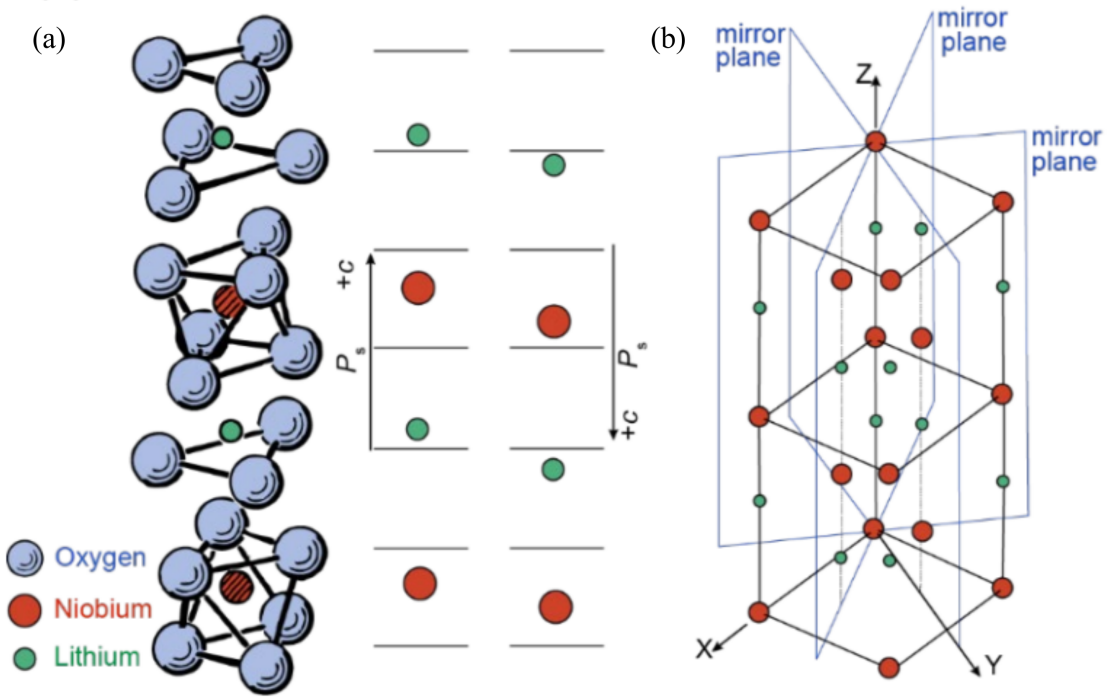


Figure 3.5: Crystal structure of $LiNbO_3$. (a) Positions of the Li and Nb atoms with respect to the oxygen octahedra in the ferroelectric domain. (b) Standard representation of the X, Y, and Z axes, with the Y-axis aligned to a mirror plane. Figure reproduced from Ref. [170].

A unique feature of $LiNbO_3$ is its ferroelectric nature, which makes it particularly valuable for applications requiring ferroelectric domain engineering [84]. This engineering technique, known as periodic domain reversal, involves modifying the polarity of neighboring ferroelectric domains by applying a sufficiently strong external poling field. The widespread use of $LiNbO_3$ can be attributed, in part, to its ability to undergo such domain engineering. Under a strong external poling field, the Nb ions are displaced within the oxygen octahedra, while the Li ions not only shift to the opposite side of the nearest oxygen triangle but can also migrate into the adjacent vacancies. This process, illustrated in Fig. 3.5, leads to a periodic reversal of the ferroelectric domains and constitutes the underlying mechanism for quasi-phase matching (QPM).

3.3.2 Optical properties of $LiNbO_3$

The key optical properties that make $LiNbO_3$ attractive for ICSRO research include its broad optical transparency, high second-order nonlinearity, versatile phase matching capability, enhanced photorefractive resistance when MgO-doped, and commercial availability in long interaction lengths. Bulk $LiNbO_3$ exhibits a wide transparency range from 0.35–5 µm, covering the visible, near-IR, and mid-IR spectral regions. There is also a secondary transparency window that exists between 6.3–7.5 µm [171], in which the extraordinary crystal axis provides broader transmission compared to the ordinary axis.

Regarding optical nonlinearity, $LiNbO_3$ and PPLN differ due to their respective phase matching capabilities. Bulk $LiNbO_3$ is restricted to birefringent phase matching (BPM), whereas PPLN allows QPM to take place. As shown in Table 2.1, the largest nonlinear coefficient accessible with congruent, undoped $LiNbO_3$ is $d_{31} = 4.8$ pm/V [80]. In contrast, QPM in PPLN ensures that all three interacting fields share the same polarization state, enabling the use of the largest tensor element which, for 5%-MgO:PPLN, is $d_{33} = 28.4$ pm/V [80], thus maximising the nonlinear response. Therefore, even considering the QPM penalty (see Section 2.5.1), PPLN has the potential to reduce the ICSRO threshold by over an order of magnitude relative to congruent, undoped $LiNbO_3$, consistent with the inverse-square dependence of the ICSRO threshold on the nonlinear coefficient (see Eq. 2.58).

Photorefractive damage is another critical consideration when selecting a suitable crystal for ICSRO applications. The photorefractive effect, which alters the refractive index under light exposure, poses a significant challenge for generating short wavelengths at high optical powers. To mitigate photorefractive damage in $LiNbO_3$, particularly in the visible spectrum, operation above 150°C is required. Hence, a temperature-controlled oven is necessary to house the crystal. According to the phase matching analysis in Chapter 2, achieving efficient PDC under the ICSRO experimental parameters (i.e., targeting signal and idler wavelengths near 1.24 µm and 1.55 µm, respectively) requires a theoretical crystal temperature of 114°C [88]. While both $LiNbO_3$ and PPLN can individually

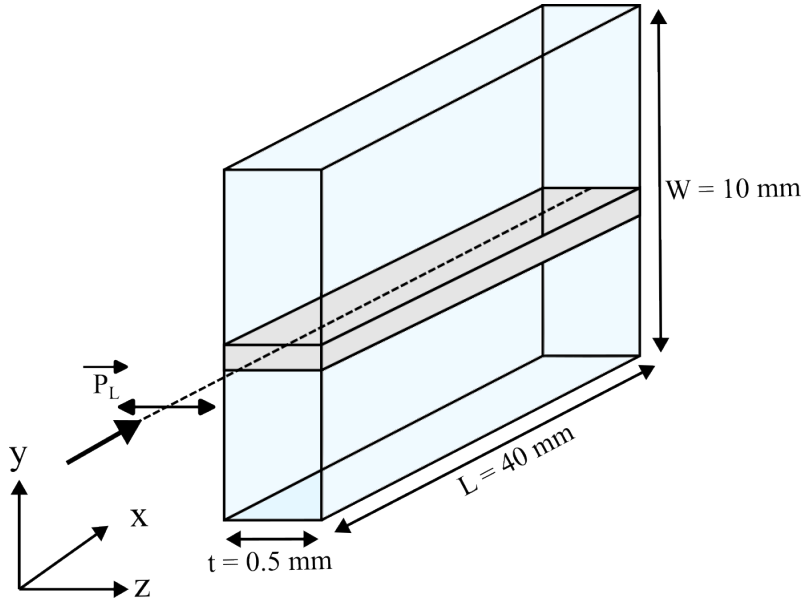


Figure 3.6: Schematic illustration of the 5%-MgO:PPLN crystal, oriented perpendicular to the incident pump polarization, $\vec{P}_L$, which is applied along the crystal's z-axis. The crystal dimensions along the x, y, and z crystallographic directions are $L = 40$ mm, $W = 10$ mm, and $t = 0.5$ mm, respectively. Nine periodically-poled grating periods, ranging from 13.83 to 17.10 µm, are fabricated along the crystal's x-axis, each separated by 0.5 mm along the y-axis. Only the target 14.55 µm poling period is shown and is highlighted in grey. L: length; W: width; t: thickness.

achieve either efficient PDC or photorefractive resistance, neither can accomplish both simultaneously for targeting the telecom O- and C- bands. The incorporation of a small concentration of MgO into the crystal addresses this limitation. MgO-doped PPLN or $LiNbO_3$ exhibits negligible photorefractive damage and can operate at room temperature without altering the refractive index. Moreover, MgO doping preserves the high nonlinear coefficient while enhancing the crystal's optical and photorefractive robustness, making it ideally suited for ICSRO applications.

Following a comparative analysis of the optical properties of $LiNbO_3$ and PPLN, MgO:PPLN was identified as the most suitable nonlinear crystal for this investigation. This choice is motivated by the crystal's ability to maintain a temperature conducive to efficient QPM while mitigating photorefractive damage, thereby enabling type-0 QPM to exploit the material's largest optical nonlinearity coefficient.

The 5%-MgO:PPLN crystal employed in this investigation was fabricated by Covesion Ltd., a research, development, and manufacturing company located in Southampton, England. Details including the crystal dimensions, MgO doping concentration, and orientation relative to the incident pump polarization are provided in the caption of Fig. 3.6. The grating period of interest, $\Lambda_{\mathrm{QPM}} = 14.55$ µm, was carefully selected to achieve non-critical QPM for a non-degenerate PDC interaction between an SRO pump wavelength near 689 nm and a resonant idler wavelength near 1550 nm. A visible-wavelength pump laser is employed in this investigation as it enables the generation of signal and idler wavelengths near the desired 1.3 µm and 1.55 µm, corresponding to the telecom O- and C-bands, respectively. Operation in these spectral regions permits low-loss photon transmission in silica optical fibres, with attenuation coefficients of $0.28\,\mathrm{dB\,km^{-1}}$ at 1.3 µm and $0.14\,\mathrm{dB\,km^{-1}}$ at 1.55 µm [172]. This makes such sources particularly well suited to long-distance quantum communication applications, including a future quantum internet [173]. For this investigation, it must be noted that our VECSEL system is specifically optimised for operation at 689 nm. This focus stems from the previous work of our research group at the Institute of Photonics, University of Strathclyde, where Moriya *et al.* [135], [174] demonstrated sub-kHz linewidths and ultra-low noise performance necessary for addressing the second-stage cooling transition in neutral strontium (Sr) atoms.

With the OPO crystal selected, the design and modelling of the ICSRO optical resonator could proceed. This provides the foundation for the following section, in which the ICSRO is optimised for low-threshold operation to accommodate the constraints imposed by the available external pump power.

3.4 ICSRO resonator design requirements

Designing an ICSRO is inherently challenging due to the presence of two distinct cavities within the system; however, the negligible thermal lensing in the VECSEL active region – achieved through efficient thermal management techniques – simplifies the pro-

cess. Accordingly, the realisation of a stable, efficient, and low-threshold ICSRO optical resonator requires the following considerations:

Key ICSRO Design Requirements

1. Efficient mode matching between the intracavity VECSEL mode and the external pump laser incident on the VECSEL chip.
2. Confocal focussing of both the intracavity VECSEL and resonant idler modes, ensuring spatial overlap at the centre of the 5%-MgO:PPLN crystal.
3. Selection of the ICSRO resonator configuration: either a standing-wave linear cavity or a travelling-wave ring resonator.

The realisation of high brightness and efficiency in VECSEL devices is strongly contingent upon maximising the spatial overlap between the external pump beam incident on the semiconductor wafer and the intracavity VECSEL mode. Precise mode-matching between these two fields ensures high-quality laser beam output and high conversion efficiency. Exceeding the SRO threshold depends on maximising the intracavity VECSEL power, therefore efficient mode-matching is essential. In this investigation, an AlGaInP-based red-VECSEL structure is employed, where a focussed pump spot of ~ 90 µm in diameter is selected as an optimal starting point based on similar VECSEL structures reported in the literature [50], [135]. In addition, the VECSEL is specifically engineered for optical pumping at 532 nm, while the desired 90 µm spot size is achieved simply by focussing the external pump beam through an appropriately chosen lens.

Satisfying the second condition requires careful consideration of the physical size and shape of both the VECSEL and resonant idler beams within their respective resonators. Firstly, the ICSRO system must be stable, meaning that the intracavity field must reproduce itself after each cavity round trip. Therefore, the intracavity field can be described by two key parameters: the beam radius perpendicular to the resonator axis w and the radius of curvature of the wavefront R [175]. For CW ICSROs, achieving low oscillation thresholds (or high down-conversion efficiencies) typically requires aligning the beam waist of the intracavity field to coincide with the centre of the OPO crystal.

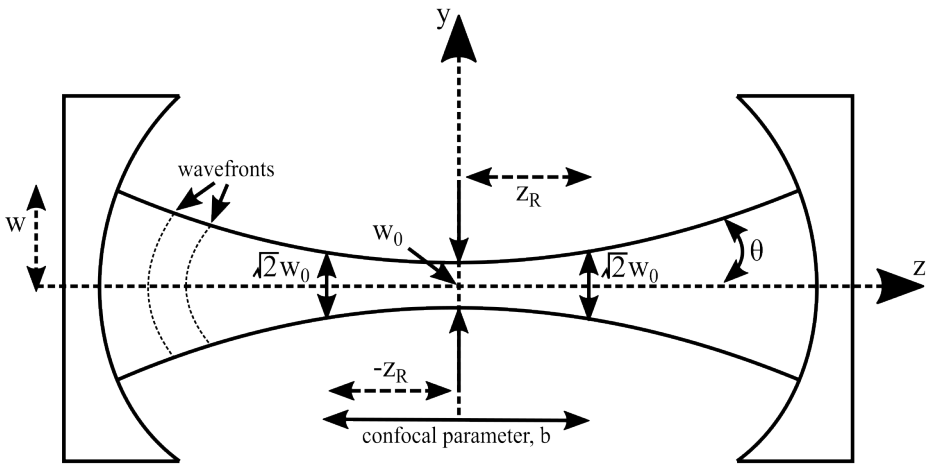


Figure 3.7: Schematic representation of a Gaussian beam, characterised by its beam waist w_0, Rayleigh range z_R, and divergence angle θ.

As illustrated in Fig. 3.7, the beam waist w_0 represents the minimum beam radius and corresponds to the location of maximum beam irradiance.

Secondly, this investigation focuses on optimising the ICSRO for a minimum oscillation threshold rather than for a maximum down-conversion efficiency. This design choice is necessitated by the limited output power available from the external pump laser. A critical factor in achieving this low-threshold operation is the optimisation of the beam waist at the centre of the 5%-MgO:PPLN crystal. The ideal focus required to reach this threshold can be estimated theoretically. For instance, a seminal study by Boyd and Kleinman [176] provided a detailed analysis of threshold minimisation in second-harmonic generation (SHG) and doubly-resonant OPO (DRO) systems employing focussed Gaussian beams. For the case of a DRO, their model assumes that all interacting fields share identical confocal parameters. As illustrated in Fig. 3.7, the confocal parameter b is related to the Rayleigh range z_R by:

$$b = 2z_R, \tag{3.4}$$

which may be expressed explicitly as:

$$b = \frac{2\pi n w_0^2}{\lambda}, \tag{3.5}$$

where n is the refractive index of the OPO crystal, w_0 is the beam waist radius, and λ is the incident wavelength.

The threshold for parametric oscillation in a DRO system is governed by the dimensionless Boyd–Kleinman focussing function $h_m(B, \xi_{\text{foc}})$, where B denotes the spatial walk-off parameter and ξ_{foc} is the focussing parameter. The quantity $h_m(B, \xi_{\text{foc}})$ represents the maximum value of the Boyd–Kleinman interaction function with respect to the phase-mismatch parameter, and therefore describes the efficiency of the nonlinear interaction for a given spatial walk-off and focussing condition. In the case of non-critical phase matching, the walk-off is negligible ($B = 0$). Under these conditions, the minimum threshold is obtained when [176]:

$$h_m(0, \xi_{\text{foc}}) = 1.068 \quad \text{at} \quad \xi_{\text{foc}} = 2.84.$$

The focussing parameter ξ_{foc} is defined as the ratio between the total crystal length l and the confocal parameter:

$$\xi_{\text{foc}} = \frac{l}{b}. \tag{3.6}$$

Therefore, by substituting Eq. (3.5) into Eq. (3.6), and rearranging for the beam waist, the optimal waist for a DRO system is found to be:

$$w_0^{\text{DRO}} = \sqrt{\frac{\lambda l}{5.68\pi n}}. \tag{3.7}$$

Building upon this analysis, Guha *et al.* [177], [178] extended the treatment to SROs. Unlike Boyd and Kleinman, their model makes no *a priori* assumption as to the relative beam sizes for the pump and resonant fields, but instead numerically evaluates the efficiency and threshold over a range of focussing conditions. They demonstrated that

Table 3.2: Theoretically predicted beam waist diameters corresponding to the minimum ICSRO threshold condition.

ICSRO beam	**Beam waist**	
	SRO ($\xi_{\text{foc}} = 1$)	**DRO** ($\xi_{\text{foc}} = 2.84$)
Pump ($\lambda = 0.689$ µm)	89.2 µm	53.0 µm
Signal ($\lambda = 1.240$ µm)	121.0 µm	71.8 µm
Idler ($\lambda = 1.550$ µm)	135.6 µm	80.4 µm

the threshold is minimised under confocal focussing, i.e., when $\xi_{\text{foc}}^{p} = \xi_{\text{foc}}^{i} = 1$, where the superscripts denote the pump and resonant idler beams, respectively. Under these conditions, the re-arranged Eq. (3.5) yields:

$$w_0^{\text{SRO}} = \sqrt{\frac{\lambda l}{2\pi n}}. \tag{3.8}$$

Equation (3.8) therefore serves as a convenient starting point for estimating the beam waist parameters required to minimise the oscillation threshold in the ICSRO. Table 3.2 summarises the theoretically predicted beam waist diameters for the VECSEL fundamental and resonant idler fields in a 40-mm-long, 5%-MgO:PPLN crystal, assuming confocal focussing of Gaussian beams. For these calculations, the extraordinary refractive index at each of the interacting wavelengths was calculated using Eq. (2.35a), giving values of 2.2017, 2.1589, and 2.1488 for the VECSEL fundamental, signal, and idler fields, respectively. At the centre of the 5%-MgO:PPLN crystal, the calculated beam waist diameters are 89.2 µm for the VECSEL fundamental and 135.6 µm for the resonant idler.

Having established the beam waist requirements necessary for efficient mode matching at the VECSEL chip surface and for achieving operation at the minimum oscillation threshold in the ICSRO, the focus now shifts to the selection of an appropriate resonator geometry. Two configurations are commonly considered: the standing-wave linear cavity and the travelling-wave ring resonator. The linear cavity offers a substantial practical advantage in terms of alignment simplicity, as it avoids the pronounced astigmatic aberrations that are commonly encountered in ring resonator geometries. By contrast,

the ring resonator is widely recognised for its ability to support stable single-frequency operation. This behaviour stems from its intrinsically unidirectional operation, which suppresses spatial hole burning [179].

For this investigation, it is essential that the intracavity VECSEL field operates on a single longitudinal mode. This requirement is motivated by two key factors: first, it ensures that the non-resonant signal field is also constrained to a single longitudinal mode; second, it enables the implementation of efficeint active stabilisation within the ICSRO system. On this basis, a ring cavity might initially appear to be the most suitable resonator configuration. However, the specific design of the VECSEL obviates the necessity for a ring geometry. Owing to the RPG QW arrangement [105], spatial hole burning is inherently suppressed, thereby enabling stable, low-noise, single-frequency operation within a linear standing-wave resonator. Consistent with this, numerous demonstrations reported in the literature confirm that VECSELs can reliably achieve single-frequency operation in linear cavity geometries [50], [135], [136]. For these reasons, a standing-wave linear cavity is adopted as the resonator configuration for the ICSRO in this work, combining practical simplicity in alignment with a proven capability for achieving the required single-frequency performance.

3.5 Cavity modelling and the final ICSRO design

The preceding section identified the linear standing-wave cavity as the optimal configuration for the ICSRO VECSEL. To accommodate two distinct beam waists at the centre of the 5%-MgO:PPLN crystal, a modified split-cavity architecture is required. This is implemented through the inclusion of a dichroic mirror (DM), allowing independent control of the intracavity VECSEL and resonant idler modes.

In practice, this geometry necessitates a larger folding angle within the SRO cavity than is typical for conventional VECSEL resonators. This adjustment provides sufficient clearance for the temperature-stabilised oven enclosing the 5%-MgO:PPLN crystal.

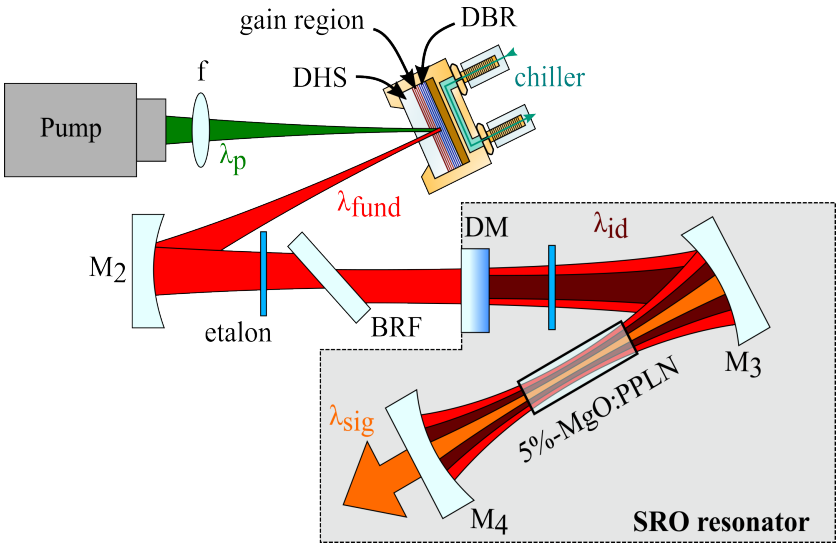


Figure 3.8: Schematic illustration (not to scale) of the four-mirror VECSEL-pumped ICSRO experimental setup. In this configuration, there is no output coupler at the resonant idler wavelength. The optical elements are indicated as follows: f: lens; DBR: distributed Bragg reflector; DHS: diamond heat spreader; M_x (x = 2, 3, 4): cavity mirrors; DM: dichroic mirror; BRF: birefringent filter; λ_p, λ_{fund}, λ_{sig}, λ_{id}: VECSEL pump, VECSEL fundamental, signal, and idler wavelengths at 532 nm, 690.6 nm, 1245.2 nm, and 1550.8 nm, respectively.

Consequently, a wide-angled, four-mirror VECSEL-pumped ICSRO design is adopted, as schematically illustrated in Fig. 3.8.

To enable tunability and ensure single-frequency operation, spectral filtering elements were incorporated into both cavity branches. A 4-mm-thick BRF was inserted into the VECSEL branch for wavelength tuning, while two fused silica etalon filters were employed: 300 µm-thick etalon in the VECSEL branch and 200 µm-thick etalon in the SRO branch. The inclusion of these etalon filters ensures that the spectral bandwidth of the VECSEL fundamental remains well within the ICSRO pump acceptance bandwidth.

3.5.1 Stability analysis

The design of the ICSRO VECSEL system shown in Fig. 3.8 was carried out computationally using 'Rezonator', a software that uses the ABCD-matrix formalism for evaluating resonator stability and for characterising the Gaussian properties of the lowest-order

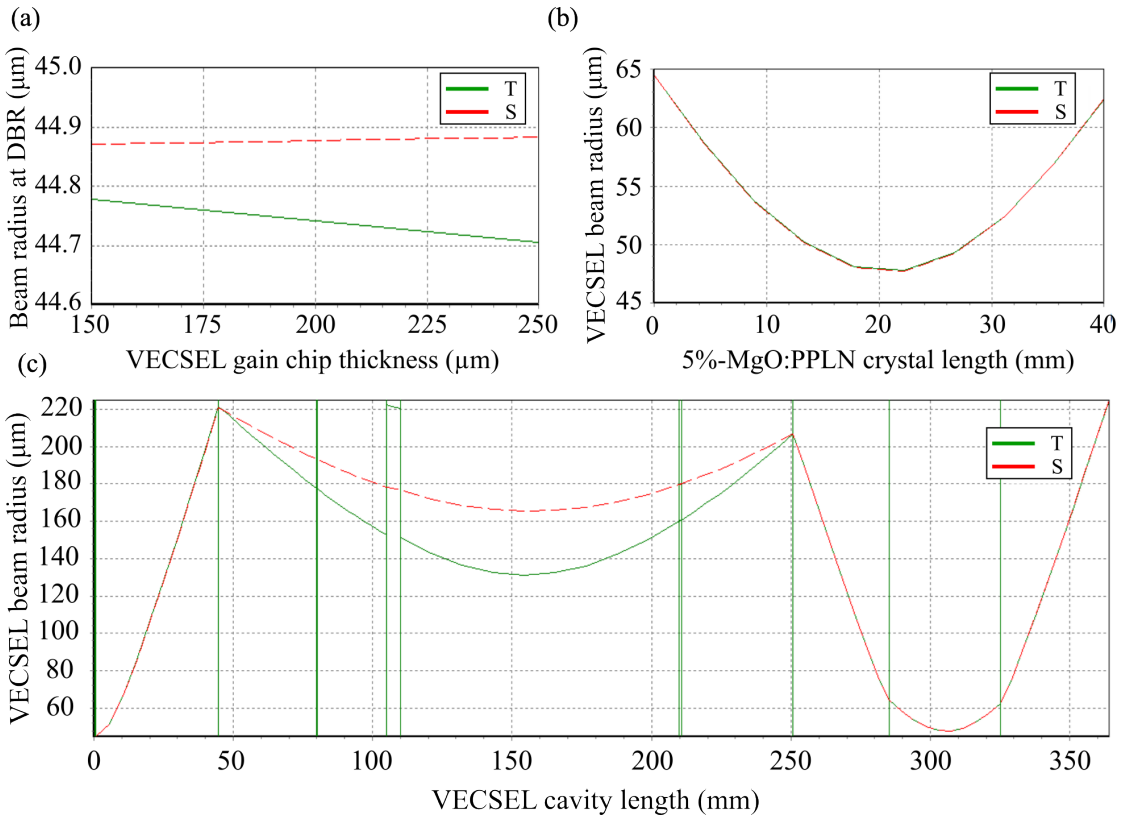


Figure 3.9: Stability analysis of the designed AlGaInP-based VECSEL cavity. **(a)** VECSEL beam radius at the DBR mirror as a function of increasing VECSEL gain chip thickness. **(b)** VECSEL beam radius versus 5%-MgO:PPLN crystal length. **(c)** VECSEL beam radius along the full VECSEL cavity length. In all plots, the green and red curves correspond to the tangential and sagittal planes of the VECSEL beam, respectively.

Hermite-Gaussian modes [175], [180], [181]. Figures 3.9 and 3.10 present the stability analysis of the VECSEL and SRO cavities in the tangential and sagittal planes, respectively. Additionally, the optical elements employed in the design of the VECSEL and SRO cavities are summarised in Tables 3.3 and 3.4, respectively.

To validate the stability of both the VECSEL and SRO resonators shown in Figs. 3.9 and 3.10, Sylvester's theorem [175] is employed. This theorem defines an angle θ through the relation:

$$\begin{bmatrix} A & B \\ C & D \end{bmatrix}^m = \frac{1}{\sin\theta} \begin{bmatrix} A\sin(m\theta) - \sin((m-1)\theta) & B\sin(m\theta) \\ C\sin(m\theta) & D\sin(m\theta) - \sin((m-1)\theta) \end{bmatrix}, \quad (3.9)$$

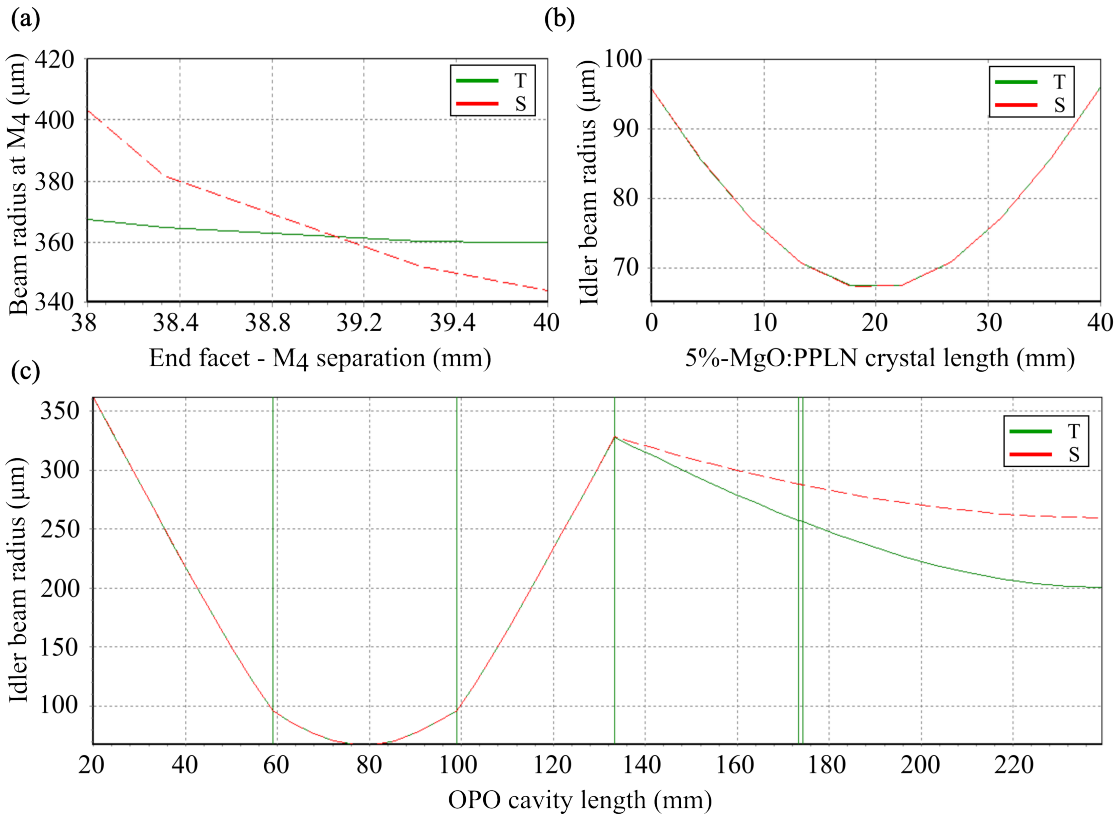


Figure 3.10: Stability analysis of the designed OPO resonant idler cavity. **(a)** Resonant idler beam radius at the cavity end mirror M_4 as a function of the distance between the end facet of the 5%-MgO:PPLN crystal and M_4. **(b)** Resonant idler beam radius versus the 5%-MgO:PPLN crystal length. **(c)** Resonant idler beam radius along the full OPO cavity length. In all plots, the green and red curves correspond to the tangential and sagittal planes of the resonant idler beam, respectively.

where

$$\cos\theta = \frac{A+D}{2}. \tag{3.10}$$

Here, m represents the number of consecutive optical elements traversed by the beam, while A–D denote the ray matrix coefficients of each element. For a resonator to remain stable, Eq. (3.9) must remain finite, ensuring that the light ray does not diverge catastrophically from the resonator axis. Because the sine function is bounded, the arguments of Eq. (3.9) are constrained within $[-1, 1]$. If θ becomes imaginary, however,

Table 3.3: Elements used in the design of the VECSEL cavity. The DM is omitted from the analysis as its normal incidence orientation, high transmittance at the VECSEL wavelength, and reduced thickness compared to the main cavity mirrors result in no significant effect on the calculated resonator beam parameters. $\mathcal{R}$: radius of curvature; α: angle; L: length (or thickness); n: refractive index. To note, the value $\mathcal{R} = 1.50\,\mathrm{m}$ represents a flat-plane mirror substrate, approximating an infinite radius of curvature.

Element	**Transfer Matrix**		**Properties**
	Tangential	**Sagittal**	
DBR Mirror	$\begin{bmatrix} 1 & 0 \\ -2/(\mathcal{R}\cos(\alpha)) & 1 \end{bmatrix}$	$\begin{bmatrix} 1 & 0 \\ -(2\cos(\alpha))/\mathcal{R} & 1 \end{bmatrix}$	$\mathcal{R} = 1.50$ m $\alpha = 0°$
AlGaInP VECSEL wafer	$\begin{bmatrix} 1 & L/n \\ 0 & 1 \end{bmatrix}$	$\begin{bmatrix} 1 & L/n \\ 0 & 1 \end{bmatrix}$	$L = 200$ µm $n \approx 3.2$
Diamond heat spreader	$\begin{bmatrix} 1 & L/n \\ 0 & 1 \end{bmatrix}$	$\begin{bmatrix} 1 & L/n \\ 0 & 1 \end{bmatrix}$	$L = 500$ µm $n \approx 2.4$
Displacement, d_1	$\begin{bmatrix} 1 & L/n \\ 0 & 1 \end{bmatrix}$	$\begin{bmatrix} 1 & L/n \\ 0 & 1 \end{bmatrix}$	$L = 44$ mm $n = 1.0$
Mirror, M_2	$\begin{bmatrix} 1 & 0 \\ -2/(\mathcal{R}\cos(\alpha)) & 1 \end{bmatrix}$	$\begin{bmatrix} 1 & 0 \\ -(2\cos(\alpha))/\mathcal{R} & 1 \end{bmatrix}$	$\mathcal{R} = 75$ mm $\alpha = 16°$
Displacement, d_2	$\begin{bmatrix} 1 & L/n \\ 0 & 1 \end{bmatrix}$	$\begin{bmatrix} 1 & L/n \\ 0 & 1 \end{bmatrix}$	$L = 35$ mm $n = 1.0$
Fused-silica etalon	$\begin{bmatrix} 1 & \frac{n^2 L(1-\sin^2(\alpha))}{\sqrt{(n^2-\sin^2(\alpha))^3}} \\ 0 & 1 \end{bmatrix}$	$\begin{bmatrix} 1 & L/\sqrt{n^2-\sin^2(\alpha)} \\ 0 & 1 \end{bmatrix}$	$L = 300$ µm $n = 1.456$ $\alpha \approx 0.1°$
Displacement, d_3	$\begin{bmatrix} 1 & L/n \\ 0 & 1 \end{bmatrix}$	$\begin{bmatrix} 1 & L/n \\ 0 & 1 \end{bmatrix}$	$L = 25$ mm $n = 1.0$
Birefringent filter, BRF	$\begin{bmatrix} 1 & L\sqrt{n^2+1}/n^4 \\ 0 & 1 \end{bmatrix}$	$\begin{bmatrix} 1 & L\sqrt{n^2+1}/n^2 \\ 0 & 1 \end{bmatrix}$	$L = 4$ mm $n = 1.456$
Displacement, d_4	$\begin{bmatrix} 1 & L/n \\ 0 & 1 \end{bmatrix}$	$\begin{bmatrix} 1 & L/n \\ 0 & 1 \end{bmatrix}$	$L = 100$ mm $n = 1.0$
Fused silica etalon	$\begin{bmatrix} 1 & \frac{n^2 L(1-\sin^2(\alpha))}{\sqrt{(n^2-\sin^2(\alpha))^3}} \\ 0 & 1 \end{bmatrix}$	$\begin{bmatrix} 1 & L/\sqrt{n^2-\sin^2(\alpha)} \\ 0 & 1 \end{bmatrix}$	$L = 200$ µm $n = 1.8$ $\alpha \approx 0.1°$
Displacement, d_5	$\begin{bmatrix} 1 & L/n \\ 0 & 1 \end{bmatrix}$	$\begin{bmatrix} 1 & L/n \\ 0 & 1 \end{bmatrix}$	$L = 40$ mm $n = 1.0$
Mirror, M_3	$\begin{bmatrix} 1 & 0 \\ -2/(\mathcal{R}\cos(\alpha)) & 1 \end{bmatrix}$	$\begin{bmatrix} 1 & 0 \\ -(2\cos(\alpha))/\mathcal{R} & 1 \end{bmatrix}$	$\mathcal{R} = 75$ mm $\alpha = 17°$
Displacement, d_6	$\begin{bmatrix} 1 & L/n \\ 0 & 1 \end{bmatrix}$	$\begin{bmatrix} 1 & L/n \\ 0 & 1 \end{bmatrix}$	$L = 34.3$ mm $n = 1.0$
5%-MgO:PPLN crystal	$\begin{bmatrix} 1 & L/n \\ 0 & 1 \end{bmatrix}$	$\begin{bmatrix} 1 & L/n \\ 0 & 1 \end{bmatrix}$	$L = 40$ mm $n = 2.2017$
Displacement, d_7	$\begin{bmatrix} 1 & L/n \\ 0 & 1 \end{bmatrix}$	$\begin{bmatrix} 1 & L/n \\ 0 & 1 \end{bmatrix}$	$L = 39$ mm $n = 1.0$
Mirror, M_4	$\begin{bmatrix} 1 & 0 \\ -2/(\mathcal{R}\cos(\alpha)) & 1 \end{bmatrix}$	$\begin{bmatrix} 1 & 0 \\ -(2\cos(\alpha))/\mathcal{R} & 1 \end{bmatrix}$	$\mathcal{R} = 50$ mm $\alpha = 0°$

accurate evaluation of cavity stability becomes problematic. Therefore, assuming θ is real, a laser cavity is stable if and only if:

$$-1 < \frac{A+D}{2} < 1. \tag{3.11}$$

Equation (3.11) establishes the general stability criterion, which is critical when it comes to designing both VECSEL and SRO cavities. Therefore, to evaluate the stability of the designed ICSRO system, the round-trip matrices for the tangential (T) and sagittal (S) planes are calculated by multiplying the individual ray matrices corresponding to all optical elements in the cavity. Using the data from Tables 3.3 and 3.4, the resulting round-trip matrices are:

$$\begin{bmatrix} A & B \\ C & D \end{bmatrix}_T^{\text{VECSEL}} = \begin{bmatrix} 0.693 & -6.582 \\ 0.079 & 0.693 \end{bmatrix}, \tag{3.12a}$$

$$\begin{bmatrix} A & B \\ C & D \end{bmatrix}_S^{\text{VECSEL}} = \begin{bmatrix} -0.135 & -9.098 \\ 0.108 & -0.135 \end{bmatrix}, \tag{3.12b}$$

$$\begin{bmatrix} A & B \\ C & D \end{bmatrix}_T^{\text{SRO}} = \begin{bmatrix} 5.075 & 228.423 \\ -0.095 & -4.062 \end{bmatrix}, \tag{3.12c}$$

$$\begin{bmatrix} A & B \\ C & D \end{bmatrix}_S^{\text{SRO}} = \begin{bmatrix} 3.547 & 134.245 \\ -0.056 & -1.822 \end{bmatrix}. \tag{3.12d}$$

Substituting the appropriate coefficients from Eqs. (3.12a)–(3.12d) into Eq. (3.11) yields the stability parameters for each resonator:

$$\frac{A+D}{2}\Big|_T^{\text{VECSEL}} = 0.693, \tag{3.13a}$$

$$\frac{A+D}{2}\Big|_S^{\text{VECSEL}} = -0.135, \tag{3.13b}$$

$$\frac{A+D}{2}\Big|_T^{\text{SRO}} = 0.507, \tag{3.13c}$$

$$\frac{A+D}{2}\Big|_S^{\text{SRO}} = 0.862. \tag{3.13d}$$

Table 3.4: Elements used in the design of the OPO cavity. $\mathcal{R}$: radius of curvature; α: angle; L: length (or thickness); n: refractive index. To note, the value $\mathcal{R} = 1.50\,\mathrm{m}$ represents a flat-plane mirror substrate, approximating an infinite radius of curvature.

Element	**Transfer Matrix**		**Properties**
	Tangential	**Sagittal**	
Mirror, M_4	$\begin{bmatrix} 1 & 0 \\ -2/(\mathcal{R}\cos(\alpha)) & 1 \end{bmatrix}$	$\begin{bmatrix} 1 & 0 \\ -(2\cos(\alpha))/\mathcal{R} & 1 \end{bmatrix}$	$\mathcal{R} = 50$ mm $\alpha = 0°$
Displacement, d_7	$\begin{bmatrix} 1 & L/n \\ 0 & 1 \end{bmatrix}$	$\begin{bmatrix} 1 & L/n \\ 0 & 1 \end{bmatrix}$	$L = 39$ mm $n = 1.0$
5%-MgO:PPLN crystal	$\begin{bmatrix} 1 & L/n \\ 0 & 1 \end{bmatrix}$	$\begin{bmatrix} 1 & L/n \\ 0 & 1 \end{bmatrix}$	$L = 40$ mm $n = 2.1488$
Displacement, d_6	$\begin{bmatrix} 1 & L/n \\ 0 & 1 \end{bmatrix}$	$\begin{bmatrix} 1 & L/n \\ 0 & 1 \end{bmatrix}$	$L = 34.3$ mm $n = 1.0$
Mirror, M_3	$\begin{bmatrix} 1 & 0 \\ -2/(\mathcal{R}\cos(\alpha)) & 1 \end{bmatrix}$	$\begin{bmatrix} 1 & 0 \\ -(2\cos(\alpha))/\mathcal{R} & 1 \end{bmatrix}$	$\mathcal{R} = 75$ mm $\alpha = 17°$
Displacement, d_5	$\begin{bmatrix} 1 & L/n \\ 0 & 1 \end{bmatrix}$	$\begin{bmatrix} 1 & L/n \\ 0 & 1 \end{bmatrix}$	$L = 40$ mm $n = 1.0$
Fused silica etalon filter	$\begin{bmatrix} 1 & \frac{n^2 L(1-\sin^2(\alpha))}{\sqrt{(n^2-\sin^2(\alpha))^3}} \\ 0 & 1 \end{bmatrix}$	$\begin{bmatrix} 1 & L/\sqrt{n^2-\sin^2(\alpha)} \\ 0 & 1 \end{bmatrix}$	$L = 200\,\mu$m $n = 1.8$ $\alpha \sim 0.1°$
Displacement, d_4	$\begin{bmatrix} 1 & L/n \\ 0 & 1 \end{bmatrix}$	$\begin{bmatrix} 1 & L/n \\ 0 & 1 \end{bmatrix}$	$L = 65$ mm $n = 1.0$
Dichroic beam splitter mirror, DM	$\begin{bmatrix} 1 & 0 \\ -2/(\mathcal{R}\cos(\alpha)) & 1 \end{bmatrix}$	$\begin{bmatrix} 1 & 0 \\ -(2\cos(\alpha))/\mathcal{R} & 1 \end{bmatrix}$	$\mathcal{R} = 1.50$ m $\alpha = 0°$

Finally, since all values lie within the stability bounds of $[-1, 1]$, this confirms that both the VECSEL and SRO resonators are stable in both tangential and sagittal planes.

3.5.2 Beam waists

The Rezonator software was also employed to calculate the beam spot sizes within the designed ICSRO VECSEL system. The theoretical framework and practical determination of beam sizes and positions in optical resonators have been extensively documented [180], [181], [182]. Here, the analysis adopts the theoretical framework of Kogelnik and Li [175]. For example, the system matrix of a general resonator is obtained by multiplying the individual ray matrices of all optical elements traversed by the beam during a single round-trip. A reference plane must be defined to compute the beam radius w and the

radius of curvature R at each optical element, provided the resonator satisfies the stability condition given in Eq. (3.11). For a stable resonator, the complex beam parameter:

$$q = \left(\frac{1}{R} - j\frac{\lambda}{\pi w^2}\right)^2, \tag{3.14}$$

reproduces itself after a complete round-trip. The propagation of the fundamental TEM_{00} mode can be described via the ABCD-law for Gaussian beams. Consequently, for a single optical element, the Hermite-Gaussian mode is given by:

$$u(x, y, z) = \frac{1}{A + B/q_1} \exp\left[-jk\frac{x^2 + y^2}{2q}\right], \tag{3.15}$$

where the complex beam parameter q is related to the incident parameter q_1 through the standard ABCD transformation:

$$q = \frac{Aq_1 + B}{Cq_1 + D}. \tag{3.16}$$

Once the system matrix is determined, the beam waist w_0 and radius of curvature R at any point in the cavity can be computed. In particular, at a distance z from the beam waist:

$$w^2(z) = w_0^2\left[1 + \left(\frac{z}{z_R}\right)^2\right], \tag{3.17}$$

$$R(z) = z\left[1 + \left(\frac{z_R}{z}\right)^2\right], \tag{3.18}$$

where the Rayleigh range is defined as:

$$z_R = \frac{\pi n w_0^2}{\lambda}. \tag{3.19}$$

Rezonator also accounts for astigmatism, allowing independent calculation of beam waists in the tangential and sagittal planes. As shown in Figs. 3.9b and 3.10b, for a 40-mm-long, 5%-MgO:PPLN crystal, the beam waist radii at the crystal centre are

$w_0^{\mathrm{VECSEL}} = 48.7$ µm and $w_0^{\mathrm{SRO}} = 67.0$ µm for the VECSEL fundamental and resonant idler, respectively. These values correspond to confocal parameters of $\xi_{\mathrm{foc}}^{p} = 1.09$ and $\xi_{\mathrm{foc}}^{i} = 0.99$ which, according to Guha *et al.* [177], [178] (see Eq. 3.8), are close to the minimum oscillation threshold condition.

Finally, to ensure efficient mode-matching between the external pump laser and the intracavity VECSEL mode, the beam waist at the DBR mirror must be considered. Rezonator calculations yield a VECSEL beam radius of $w_0^{\mathrm{VECSEL}} = 44.8\,\mu\mathrm{m}$ at the DBR mirror (see Fig. 3.9a), in close agreement with the target beam diameter of $\sim 90\,\mu\mathrm{m}$. Therefore, the ICSRO VECSEL configuration shown in Fig. 3.8 serves as a robust starting point for building the system experimentally. In practice, however, small adjustments to the cavity length were required to optimise performance and minimise the oscillation threshold.

With the design of the ICSRO VECSEL system established, the focus now shifts to estimating the intracavity power required to reach the SRO oscillation threshold. This analysis follows the theoretical analysis presented by Stothard [60] in Section 2.7, which assumes an undepleted pump and an ideal type-0 QPM interaction. The final section of this chapter also considers the case where there is no output coupling present for the resonant idler field, consistent with the design illustrated in Fig. 3.8.

3.6 Modelling of the ICSRO oscillation threshold

A key factor in determining the oscillation threshold is the round-trip cavity loss experienced by the resonant idler field. Following the work outlined by Svelto [181], the round-trip loss of the optical resonator can be expressed as:

$$\alpha_{\mathrm{RT}} = \underbrace{1 - [R_T(1 - T_{\mathrm{NC}})^2(1 - T_E)^2]}_{\text{cavity transmission losses}} + \underbrace{\alpha_{\mathrm{par}}}_{\text{cavity parasitic losses}}, \tag{3.20}$$

where R_T represents the product of the SRO cavity mirror reflectivities at the idler wavelength, $(1 - T_{\mathrm{NC}})^2$ and $(1 - T_E)^2$ denote the double-pass fractional transmission

Table 3.5: HR-idler ICSRO system parameters used to solve the SRO oscillation threshold condition of Eq. (3.21). The symbols R_{DM}, R_{M3}, and R_{M4} denote the reflectivities of the DM, cavity mirror M_3 and cavity mirror M_4, respectively.

Parameter	**Value**	**Units**
n_p	2.2017	-
n_s	2.1589	-
n_i	2.1488	-
ϵ_0	8.85×10^{-12}	$\mathrm{m^{-3}\ kg^{-1}\ s^4\ A^2}$
c	3×10^8	$\mathrm{m\ s^{-1}}$
w_p	48.7	µm
w_i	67.0	µm
ω_s	1.52×10^{15}	$\mathrm{rad\ s^{-1}}$
ω_i	1.22×10^{15}	$\mathrm{rad\ s^{-1}}$
l	40	mm
d_{eff}	~ 14	$\mathrm{pm\ V^{-1}}$
R_{DM}	> 99.99	%
R_{M3}	> 99.9	%
R_{M4}	> 99.9	%
T_{NC}	(2.1 ± 0.1)	%
T_E	(0.15 ± 0.02)	%
α_{par}	~ 2	%

losses through the 5%-MgO:PPLN crystal and the fused silica etalon filter (within the SRO branch), respectively, and α_{par} accounts for parasitic losses such as scattering and absorption within the SRO resonator.

Substituting Eq. (3.20) into Eq. (2.58) yields the theoretical expression for the intracavity VECSEL power required to reach SRO oscillation threshold:

$$P_{\mathrm{th}}^{\mathrm{SRO,intra}} = \frac{n_p n_s n_i\, \varepsilon_0 c^3 \pi (w_p^2 + w_i^2)}{4\, \omega_s \omega_i l^2 d_{\mathrm{eff}}^2} \alpha_{\mathrm{RT}}, \tag{3.21}$$

where n_p, n_s, and n_i denote the refractive indices of the VECSEL fundamental, signal, and idler, respectively; w_p and w_i represent the corresponding beam radii of the VECSEL

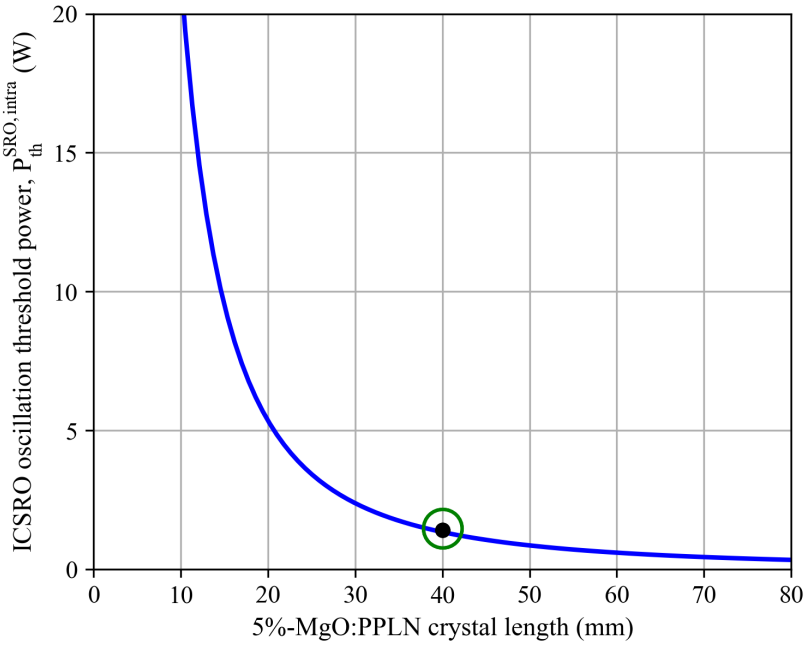


Figure 3.11: Theoretical ICSRO oscillation threshold as a function of 5%-MgO:PPLN crystal length, calculated using Eq. (3.21). The highlighted marker indicates that an intracavity VECSEL power of 1.54 W is required to reach the SRO oscillation threshold (for the HR-idler regime) for a 40-mm-long 5%-MgO:PPLN crystal.

fundamental and resonant idler at the centre of the 5%-MgO:PPLN crystal, respectively; ω_s and ω_i are the angular frequencies of the signal and idler, respectively; l denotes the total length of the 5%-MgO:PPLN crystal; and d_{eff} is the effective nonlinearity coefficient.

Table 3.5 provides the parameters required for modelling $P_{\text{th}}^{\text{SRO,intra}}$, including the anti-reflective (AR) coatings of the 5%-MgO:PPLN crystal facets and the cavity mirror reflectivity coefficients as specified by the manufacturer. Using the data provided in Table 3.5, and substituting the parameters into Eq. (3.21), the theoretical intracavity VECSEL power required to reach oscillation threshold (for the highly-reflective (HR)-idler ICSRO regime) is calculated to be 1.54 W. Figure 3.11 illustrates the dependence of the ICSRO threshold on the 5%-MgO:PPLN crystal length.

3.7 Conclusion

In conclusion, the key considerations for designing an ICSRO system have been outlined, and a VECSEL-pumped ICSRO resonator design has been developed and optimised to achieve the minimum oscillation threshold. The design process began with the selection of MgO:PPLN as the nonlinear crystal, owing to its ability to support type-0 QPM, which enables the strongest nonlinear interaction. MgO:PPLN also enables non-critical phase matching to take place, thereby avoiding spatial walk-off, and is commercially available with high-quality AR coatings on both crystal facets. Incorporation of 5%-mol MgO enhances the crystal's optical and photorefractive resistance, allowing operation at lower temperatures. This is critical for stabilising the crystal at 114°C [88], corresponding to the target telecommunications wavelength of 1.55 µm for the resonant idler, given a VECSEL fundamental wavelength of 690.6 nm and a periodic grating period of 14.55 µm.

The resonator design was guided by the temporal and spatial characteristics of the intracavity VECSEL and resonant idler fields within the ICSRO VECSEL system. In particular, optimising the beam waist at the centre of the 5%-MgO:PPLN crystal was critical for both fields. Using the optimal focussing condition described by Guha *et al.* [177], [178], the theoretical VECSEL fundamental and resonant idler beam waists were calculated to be 44.6 µm and 67.8 µm in radius, respectively. For the final design, the confocally focussed VECSEL fundamental and resonant idler beam waists at the centre of the 40-mm-long, 5%-MgO:PPLN crystal are weakly astigmatic, measuring 48.7 µm and 67.0 µm in radius, corresponding to focussing parameters of $\xi^{p}_{\mathrm{foc}} = 1.09$ and $\xi^{i}_{\mathrm{foc}} = 0.99$, respectively.

Additional design requirements for the resonator include high stability and efficient mode-matching between the intracavity VECSEL mode at the DBR mirror and the external pump laser incident on the VECSEL chip surface. Our design achieves a beam waist diameter of ~ 90 µm at the DBR mirror, closely matching the target value and thereby enabling efficient mode-matching through an appropriately chosen focussing lens

for the external pump. Stability analysis also confirms that the entire ICSRO VECSEL system is highly stable in both tangential and sagittal planes.

Furthermore, the intracavity VECSEL power required to reach the SRO oscillation threshold was theoretically evaluated following the model outlined by Stothard [60] in Section 2.7. Threshold reduction is primarily influenced by maximising the effective nonlinearity coefficient and minimising the round-trip cavity loss of the resonant idler field. For the final ICSRO design, which incorporates a 40-mm-long 5%-MgO:PPLN crystal, an estimated parasitic loss of $\sim 2\%$, and customised mirror coatings from external suppliers, the intracavity VECSEL power required to reach SRO threshold is calculated to be 1.54 W; well within experimentally achievable levels. For example, in a comparable three-mirror AlGaInP-based VECSEL operating near 689 nm [50], 80 mW of output was obtained using a 1.8% output-coupler (OC). For a 3 W external pump laser operating at 532 nm, this corresponded to an intracavity VECSEL power of $\sim$ 5.5 W. This demonstrates that practical operation of the ICSRO is feasible using the available pump source, a Coherent Verdi V5 laser, capable of delivering up to 5.5 W at 532 nm.

The next chapter presents the full characterisation of the first visible VECSEL-pumped ICSRO system, optimised for low SRO oscillation threshold and evaluated under both HR-idler and OC-idler operating regimes.

Chapter 4

Single-frequency CW visible VECSEL-pumped OPO

4.1 Introduction

The work presented in this chapter has been published in the peer-reviewed journal Optics Express (Optica Publishing Group) under Ref. [58]. In this publication, the candidate was the lead contributor to the research, responsible for experimental design, implementation, data acquisition, analysis, software development, validation, visualisation, and preparation of the original manuscript. Co-authors contributed in supporting and supervisory capacities, as detailed in the *Thesis Overview* section of Chapter 1.

This chapter provides a detailed account of the experimental characterisation and systematic development that led to the successful realisation of the first intracavity singly-resonant optical parametric oscillator (ICSRO) pumped internally by a visible vertical-external-cavity surface-emitting laser (VECSEL). The ICSRO VECSEL development commenced with the design, implementation, and optimisation of a free-running, four-mirror red-VECSEL based on an AlGaInP semiconductor gain structure. A critical aspect of this optimisation involved the introduction of intracavity spectral filtering, which enabled deliberate control of the VECSEL emission spectrum. As a result, the

intrinsic gain bandwidth of the VECSEL was spectrally confined to lie well within the calculated acceptance bandwidth of the SRO.

The integration of a 40-mm-long, 5%-mol MgO-doped periodically-poled $LiNbO_3$ (5%-MgO:PPLN) crystal, together with a dichroic mirror (DM), enabled efficient parametric down-conversion (PDC) across a broad spectral range spanning 1155–1718 nm. Under ideal operating conditions: that is, when the down-converted signal and idler wavelengths are operating around 1.24 µm and 1.55 µm, respectively, a comprehensive characterisation of the ICSRO system is presented, addressing output power, conversion efficiency, wavelength tunability, and spectral performance. This characterisation is performed both with and without output-coupling of the resonant idler wave, referred to as the OC-idler and HR-idler configurations, respectively.

The chapter concludes with experimental results demonstrating single-frequency operation of a VECSEL-pumped ICSRO across all three interacting waves. In addition, the passive stability of the ICSRO is examined for two operating regimes: when the VECSEL is oscillating on multiple longitudinal modes or on a single-mode. Achieving stable, single-frequency operation enhances the overall performance of the ICSRO and enables the future implementation of active stabilisation techniques required for further noise suppression and integration into next-generation quantum technologies.

4.2 AlGaInP-based VECSEL gain structure

The AlGaInP-based VECSEL gain structure employed in this investigation was grown by Dr. Andrey Krysa at the III-V National Epitaxy Facility, University of Sheffield. Fabricated on a 2-inch GaAs substrate using metal-organic chemical-vapour deposition (MOCVD), the structure was engineered for optical pumping at green wavelengths. As shown in Fig. 3.1, the active region consists of pairs of compressively strained GaInP quantum wells (QWs) located at the anti-nodes of the optical field standing wave in a process known as resonant periodic gain (RPG) [105]. Lattice-matched AlGaInP barrier layers and tensile-strained compensation layers are positioned at the field nodes to

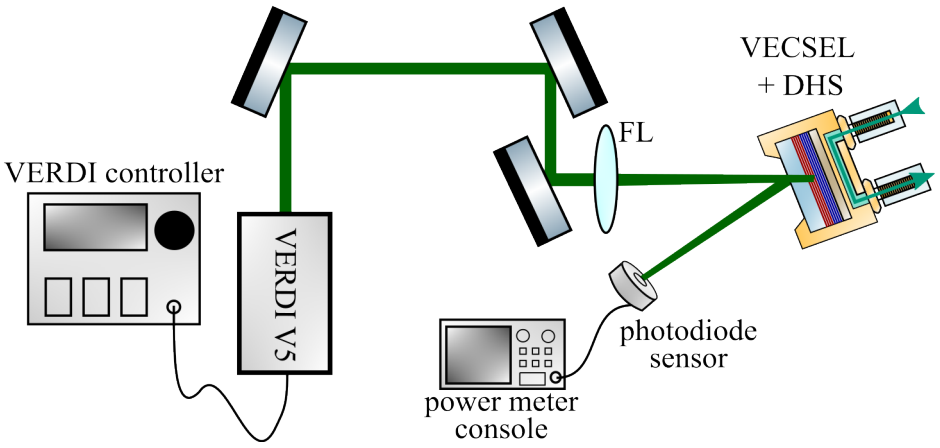


Figure 4.1: Schematic (not to scale) of the external pump laser setup. FL: focussing lens; DHS: diamond heat spreader. The pump laser operates at a wavelength of 532 nm.

minimise non-radiative losses and enhance laser efficiency, while a thin GaAs cap layer is applied to the surface to prevent oxidation associated with the aluminium content in the structure.

The VECSEL wafer was cleaved into a 4×4 mm^2 sample and bonded to a 500 µm-thick diamond heat spreader (DHS) using liquid-assisted optical contacting. Once a clean and stable contact was achieved, the diamond-bonded sample was mounted on a water-cooled brass block serving as the heatsink for the VECSEL chip. Thermal management was further enhanced by inserting a thin layer of indium foil between the base of the heatsink and the back surface of the VECSEL chip.

4.3 VECSEL pump source: Coherent Verdi V5 laser

The AlGaInP-based VECSEL was optically pumped using a commercial 5.5 W, 532 nm Coherent Verdi V5, which is a high-power, low-noise diode-pumped solid-state laser (DPSSL). As discussed in Chapter 3, achieving high beam quality, high output power, and low-threshold operation requires precise alignment to ensure optimal overlap between the intracavity VECSEL mode and the external pump beam incident on the chip surface. Based on previous studies of similar VECSEL structures [50], [135], a focussed

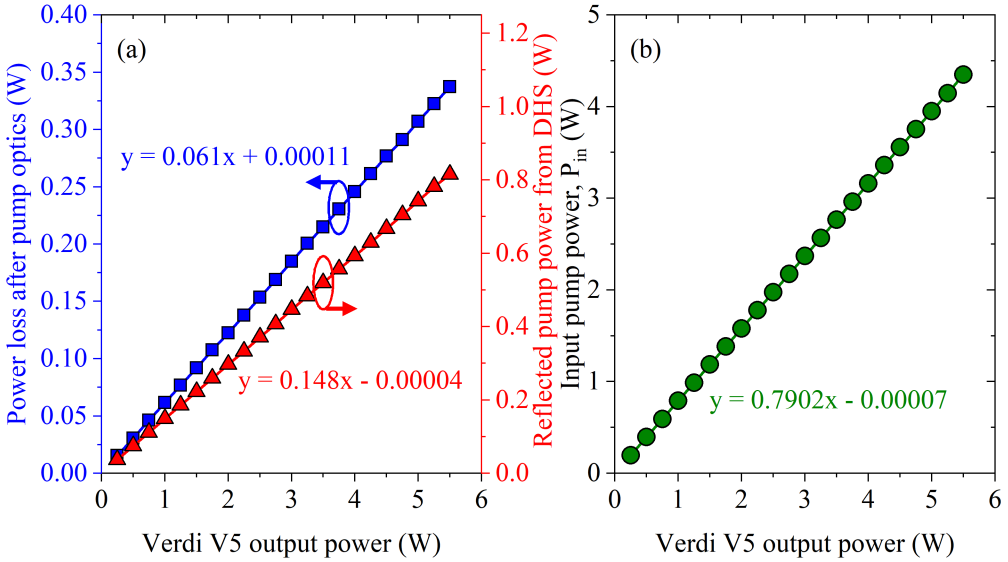


Figure 4.2: Calibration of the pump power delivered to the VECSEL gain chip. **(a)** Measured pump power losses introduced by the pump optics (blue squares) and measured power loss due to reflection from the diamond heat spreader (DHS) (red triangles). **(b)** Calibrated external pump power incident at the VECSEL chip surface, obtained by subtracting the combined losses from the pump optics and DHS reflections from the Verdi V5 output power.

pump spot of ∼90 µm in diameter was selected as an appropriate starting point, as also described in Chapter 3.

As shown in Fig. 4.1, the 532 nm pump beam was directed onto the VECSEL chip surface using a series of broadband dielectric mirrors. A 300 mm focussing lens was then introduced to reduce the size of the collimated beam to the desired spot size at the focus. The pump beam diameter was measured with a Coherent BeamMaster viewing camera equipped with an integrated seven-razor knife-edge profiler. To determine the beam focus accurately, measurements were taken at multiple positions along the optical axis. The BeamMaster camera was mounted on a 300 mm translation stage, enabling controlled translation through the focal point with minimal distortion. The resulting beam waist was measured to be (90.2 ± 0.1) µm at a distance of ∼ 300 mm from the focussing lens, in excellent agreement with our target spot size diameter of ∼90 µm.

To determine the input pump power, defined as the external pump power incident at the VECSEL chip surface, calibration of both the power transmitted through the pump optics and the power reflected from the DHS was required. The pump optics transmission losses were quantified by measuring the optical power immediately after the focussing lens and comparing it with the power emitted directly from the Verdi. The loss was then determined as the difference between these two measurements (see Fig. 4.2a, blue data points). The VECSEL chip was then positioned at the desired distance and angle relative to the focussing lens (see Fig. 3.8), and the reflected pump power was measured using the same power meter, repositioned to collect the light reflected from the DHS, as indicated by the red data points in Fig. 4.2a.

The pump power incident on the VECSEL chip surface was calibrated by accounting for the combined transmission losses of the pump optics and the Fresnel reflection loss at the air–diamond interface, which were subtracted from the measured output pump power (see Fig. 4.2b, green data points). Of the maximum available 5.5 W of external pump power, $\sim$4.35 W ($\sim$79%) was incident at the VECSEL chip surface. This level of incident pump power is sufficient to generate the intracavity VECSEL power required to reach the SRO oscillation threshold, as discussed at the end of Chapter 3.

4.4 VECSEL cavity design and characterisation

Prior to constructing the SRO resonator, the performance of the AlGaInP-based VECSEL was evaluated using a Z-shaped four-mirror cavity, as shown in Fig. 4.3. All optical components and cavity parameters were identical to those intended for the ICSRO VECSEL cavity design illustrated in Fig. 3.8, with the exception of the separation between mirrors M_3 and M_{OC} ($M_{\mathrm{OC}} = M_4$ in Fig. 3.8), which was reduced to 91.5 mm. This reduction in cavity length was implemented to compensate for the optical thickness of the 5%-MgO:PPLN crystal, thereby maintaining an identical intracavity VECSEL mode size at the chip surface once all ICSRO components were introduced. For this M_3–M_{OC}

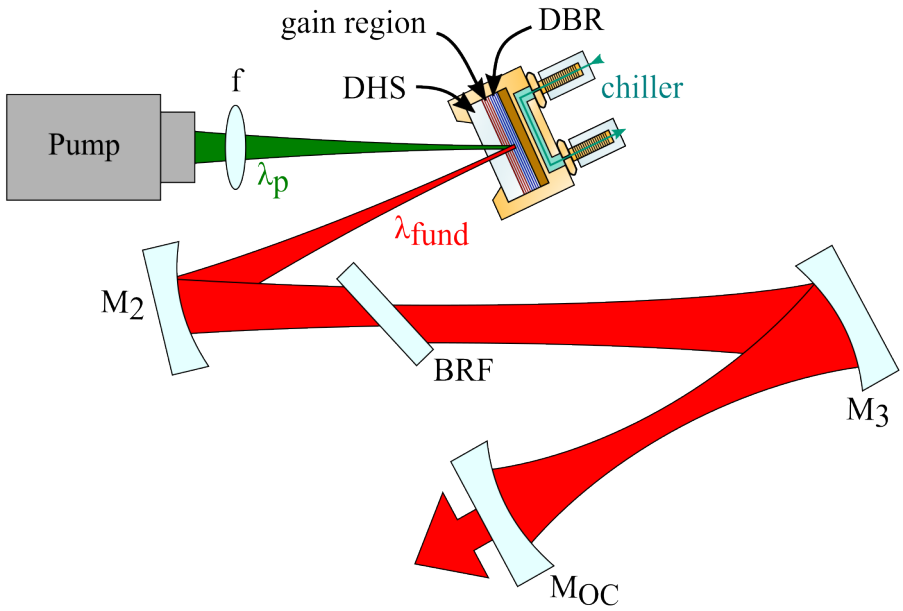


Figure 4.3: Schematic of the four-mirror 'Z-shaped' VECSEL configuration. The optical elements are indicated as follows: f: focussing lens; DHS: diamond heat spreader; DBR: distributed Bragg reflector; M_x $(x = 2, 3)$: cavity mirrors; M_{OC}: output coupling mirror; BRF: birefringent filter; λ_{p}, λ_{fund}: VECSEL pump and VECSEL fundamental wavelengths at 532 nm and 690.6 nm, respectively.

separation, the TEM_{00} cavity mode diameter at the VECSEL chip surface was calculated to be $\sim$90 µm.

With the VECSEL fundamental resonator aligned and optimised, the next step is to characterise the performance of the AlGaInP-based device. The analysis begins with measurements of output power and intracavity loss using the Caird method, followed by an evaluation of the VECSEL's spectral behaviour and tuning range.

4.4.1 Power transfer

The power transfer of the VECSEL for various OC transmissions is shown in Fig. 4.4. The inset of the figure demonstrates the power levels obtained when M_{OC} is replaced by a high-reflector (HR) mirror ($R_M > 99.99\%$). For the 3% OC, the threshold was 630 mW with a slope efficiency of 15.8% and a maximum output power of 440 mW. Figure 4.4 also shows the power transfers with 2% and 4% OC, where thresholds of 550

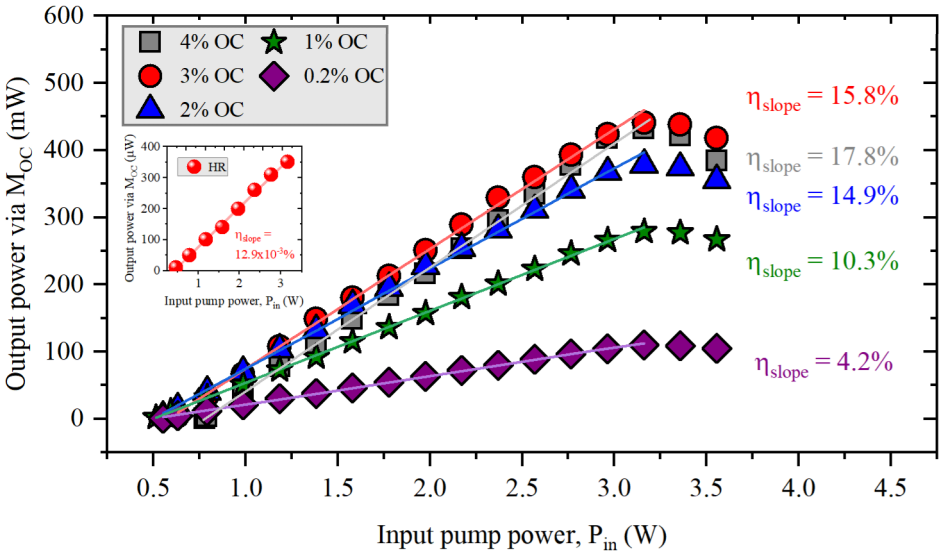


Figure 4.4: Power transfer characteristics of the VECSEL for various OC transmissions. Inset: Power transfer characteristic with M_{OC} replaced with a HR mirror. η_{slope}: slope efficiency; OC: output coupler; HR: high-reflector.

mW and 780 mW and maximum output powers of 380 mW and 430 mW were measured, respectively, corresponding to slope efficiencies of 14.9% (for the 2% OC) and 17.8% (for the 4% OC).

As shown in Fig. 4.4, pump-induced thermal rollover becomes the dominant limitation for input pump powers exceeding 3.2 W. For the VECSEL configuration presented in Fig. 4.3, the OC transmission that maximises the extractable fundamental power is identified to be $\sim 3\%$. This conclusion is based on the observation that, for incident pump powers exceeding 3.2 W, the device enters a thermally limited regime in which the available modal gain decreases with further increases in pump power. As a result, the maximum effective gain occurs at pump levels directly before the rollover point. Among the set of output couplers investigated, the 3% OC yields the highest output power at this thermally constrained operating point. This indicates that a 3% transmission provides the most favourable balance between intracavity circulating power, extraction efficiency, and thermally induced gain saturation. Therefore, the 3% OC is taken to represent the thermally limited optimum for this VECSEL configuration.

One approach to extend the onset of thermal rollover is to increase the pump spot size, thereby distributing the thermal load over a larger area. However, this would result in a commensurate increase in the intracavity mode size and, consequently, a modified cavity design. An alternative approach is to reduce the on-chip heatsink temperature to sub-zero conditions. In practice, however, laboratory temperatures below $\sim$10°C lead to condensation on the mount. Therefore, the on-chip chiller temperature was maintained at 12°C throughout the experimental investigation.

4.4.2 Caird analysis

The round-trip losses of the VECSEL cavity can be estimated from the measured power transfer characteristics. Two commonly employed methods for estimating internal laser-cavity losses are the Caird plot [183] and the Findlay–Clay analysis [184]. The Caird method determines losses from the slope efficiency as a function of output coupling, whereas the Findlay–Clay method relies on measurements of the laser threshold for different output coupling. For this investigation, where the laser is optimised for high-power operation, the Caird analysis is the preferred method, whereas the Findlay–Clay approach is more appropriate for configurations targeting low-threshold performance.

Although the Caird model was originally developed for four-level lasers [183], it can also be applied to VECSELs to estimate round-trip losses, provided that these losses are sufficiently small and pump-dependent effects can be neglected. Therefore, based on the power transfer characteristics of Fig. 4.4, only data up to an input pump power of 3.2 W is considered for analysing the slope efficiency. At higher pump powers, heating of the gain region reduces slope efficiency by increasing carrier leakage from the QWs and enhancing non-radiative recombination, which leads to an increase in the effective cavity loss. Measuring under these conditions ensures that the contributions from internal heating and pump-dependent effects remain minimal, allowing a reliable estimation of the cavity loss.

The Caird analysis is based on the assumption that the slope efficiency in a solid-state laser depends on the pump absorption efficiency (η_{abs}), the internal conversion

efficiency (η_{int}), the quantum defect (η_{quant}), the output coupling (T_{OC}), and the cavity loss ($\mathcal{L}$), expressed as:

$$\eta_{\text{eff}} = \eta_{\text{abs}}\eta_{\text{quant}}\eta_{\text{int}}\left(\frac{T_{\text{OC}}}{T_{\text{OC}}+\mathcal{L}}\right), \tag{4.1}$$

where $\eta_{\text{quant}} = \lambda_{\text{in}}^{\text{p}}/\lambda_{\text{L}}$ denotes the ratio of the external pump wavelength to the fundamental VECSEL wavelength. For the present study, $\lambda_{\text{in}}^{\text{p}} = 532$ nm and $\lambda_{\text{L}} = 690.6$ nm. Inverting Eq. (4.1) yields a linear relationship between $(\eta_{\text{eff}})^{-1}$ and $(T_{\text{OC}})^{-1}$:

$$\frac{1}{\eta_{\text{eff}}} = \frac{1}{\eta_0}\left(1+\frac{\mathcal{L}}{T_{\text{OC}}}\right). \tag{4.2}$$

where η_0 denotes the maximum achievable slope efficiency in the absence of passive loss, and is defined as:

$$\eta_0 = \eta_{\text{abs}}\eta_{\text{quant}}\eta_{\text{int}}. \tag{4.3}$$

By re-writing Eq. (4.2) as a straight line function in the form $y = a + bx$, where:

$$y = \frac{1}{\eta_{\text{eff}}}, \tag{4.4a}$$

$$x = \frac{1}{T_{\text{OC}}}, \tag{4.4b}$$

$$a = \frac{1}{\eta_0}, \tag{4.4c}$$

$$b = \frac{\mathcal{L}}{\eta_0} = a\mathcal{L}, \tag{4.4d}$$

the cavity loss ($\mathcal{L}$) can be extracted from the slope of the linear relationship between $(\eta_{\text{eff}})^{-1}$ and $(T_{\text{OC}})^{-1}$, giving:

$$\mathcal{L} = \frac{b}{a}. \tag{4.5}$$

It should be noted that the Caird analysis has certain limitations. For instance, as discussed earlier, it does not account for gain saturation or pump-dependent effects. Additionally, internal losses can only be separated from cavity losses when the total loss remains sufficiently small. In the present case, however, a reliable estimation of the cavity losses is feasible, as the internal losses are expected to be low, and slope efficiencies

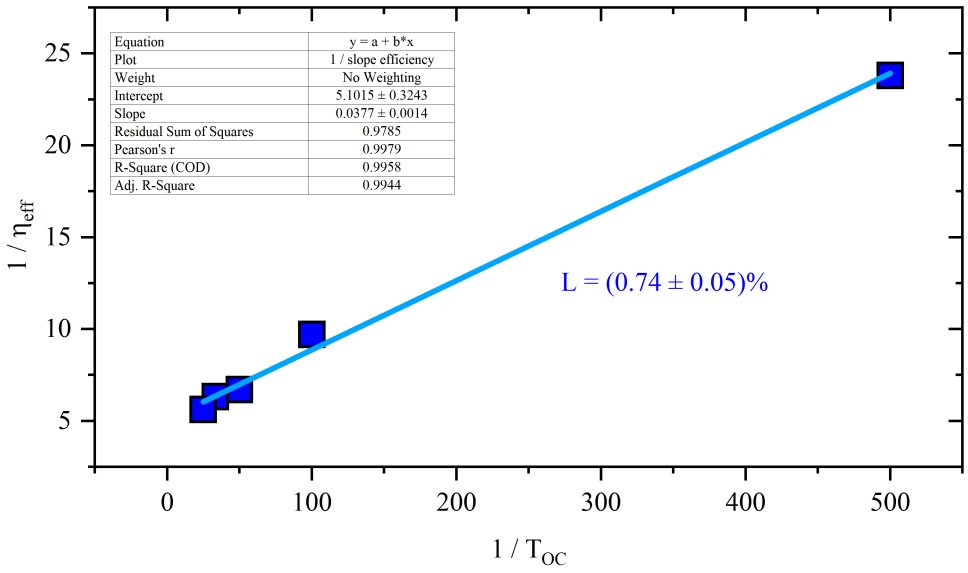


Figure 4.5: Cavity loss measurement of the AlGaInP-based VECSEL from Caird plot.

were measured at moderate output coupling prior to the onset of thermal rollover. From Fig. 4.4, the slope efficiencies for different output couplers were obtained, yielding an estimated round-trip loss of $(0.74 \pm 0.05)\%$ via the Caird plot (see Fig. 4.5).

4.4.3 Spectral performance

To mitigate the thermal load within the active region, a synthetic single-crystal diamond heat spreader was employed to minimise the temperature rise per Watt of incident pump power. The thermal performance of the diamond-bonded VECSEL sample was evaluated by monitoring the evolution of the emission spectrum up to the thermal rollover point (at an input pump power of 3.2 W) using an optical spectrum analyser (OSA; Anritsu MS9710C). As illustrated in Fig. 4.6a, the central emission wavelength shifted from 691.1 nm at a pump threshold of 800 mW (purple trace) to 694.5 nm at the maximum thermal limit of 3.2 W (red trace). The presence of the diamond heat spreader introduces a distinct sub-cavity etalon effect, modulating the broad gain envelope into a characteristic comb-like spectral profile.

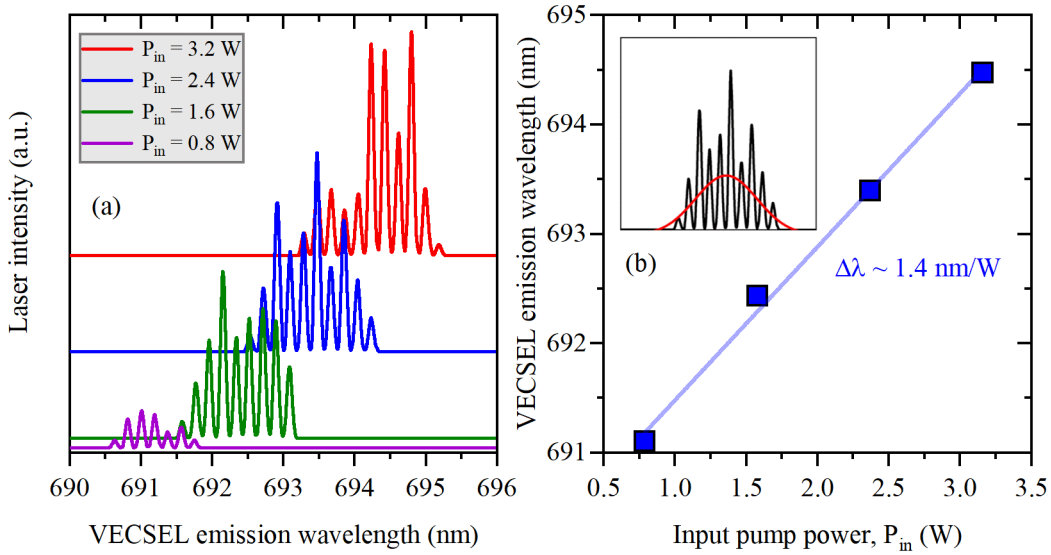


Figure 4.6: Spectral shift characteristics of the AlGaInP-based VECSEL. **(a)** Emission spectra recorded for increasing increments of input pump power, P_{in}. **(b)** Corresponding central wavelengths extracted from the spectra in (a) as a function of P_{in}. Inset: VECSEL emission spectra taken at 2.4 W of P_{in}, with a Voigt fit applied to determine the central wavelength used in (b).

The temperature rise in the gain region can be estimated by analysing the thermally induced red-shift of the VECSEL emission wavelength as the input pump power is increased. As shown in Fig. 4.6b, the AlGaInP-based VECSEL exhibits a thermal tuning rate of $\sim$1.4 nm/W, which is significantly lower than previously reported values for AlGaInP-based red-VECSELs bonded to sapphire substrates [185], confirming the superior thermal conductivity and heat-dissipation capabilities of diamond. To ensure robust spectral analysis despite the etalon-induced asymmetries, the central wavelengths were extracted using a Voigt fitting procedure, as demonstrated in the inset of Fig. 4.6b.

Integration of a quartz birefringent filter (BRF) into the resonator at Brewster's angle minimises insertion loss for *p*-polarized light while establishing a stable linear polarization state. The filter introduces a wavelength-dependent phase retardation between the orthogonal components of the intracavity field. Coarse tuning is achieved by rotating the crystal about its surface normal, which modifies the orientation of the optic axis relative to the beam's wavevector. This rotation alters the effective extraordinary refractive

index, thus shifting the transmission maxima across the gain bandwidth. Consequently, the laser operates at the wavelength of minimum transmission loss, enabling smooth, continuous tuning via a micrometre-screw mount for precise spectral adjustment.

The VECSEL fundamental wavelength was monitored by collecting a fraction of the beam reflected from the BRF using a multimode optical fibre, which delivered the signal to the same Anritsu OSA used for analysing the spectral shift pattern. Simultaneously, the output power was recorded using a thermal power meter to ensure that the spectral and power measurements were acquired under identical operating conditions. The fundamental emission of the VECSEL was characterised for BRF thicknesses of 2 mm, 4 mm, and 6 mm, with the power of each tuning curve measured at the output of a 1% OC at an input pump power of 2.4 W. The broadest tuning range, spanning approximately 12 nm ($\sim$ 685–697 nm), was achieved using the 2 mm-thick filter (see Fig. 4.7a, red data points). Conversely, the 6 mm-thick filter yielded the narrowest tuning range (see Fig. 4.7a, green data points), while the 4 mm-thick filter provided an intermediate tuning span of 9 nm, ranging from $\sim$ 686–695 nm (see Fig. 4.7a, orange data points).

Rotation of the BRF affects both its wavelength-dependent transmission and the intracavity polarization state. Each angular adjustment shifts the wavelength that experiences the lowest loss, enabling tuning, while also modifying how the polarization aligns with the gain medium and other cavity elements. Because the gain spectrum and several intracavity losses depend on polarization, the BRF angle directly influences the net round-trip gain and therefore the output power. This behaviour is also illustrated in Fig. 4.7a: for the 2 mm-thick BRF (red data points), the output power exceeds 100 mW near 685 nm, increases to a maximum of 165 mW around 690 nm, and then decreases to roughly 70 mW by 697 nm.

Increasing the BRF thickness enhances spectral selectivity by suppressing a larger number of longitudinal modes. Although this narrows the emission linewidth, it also reduces the available tuning range. Thicker filters are therefore advantageous when stable single-peak operation is required, as confirmed by the OSA measurements in Fig. 4.7b. In this figure, the 4 mm-thick BRF maintains single-peak emission across

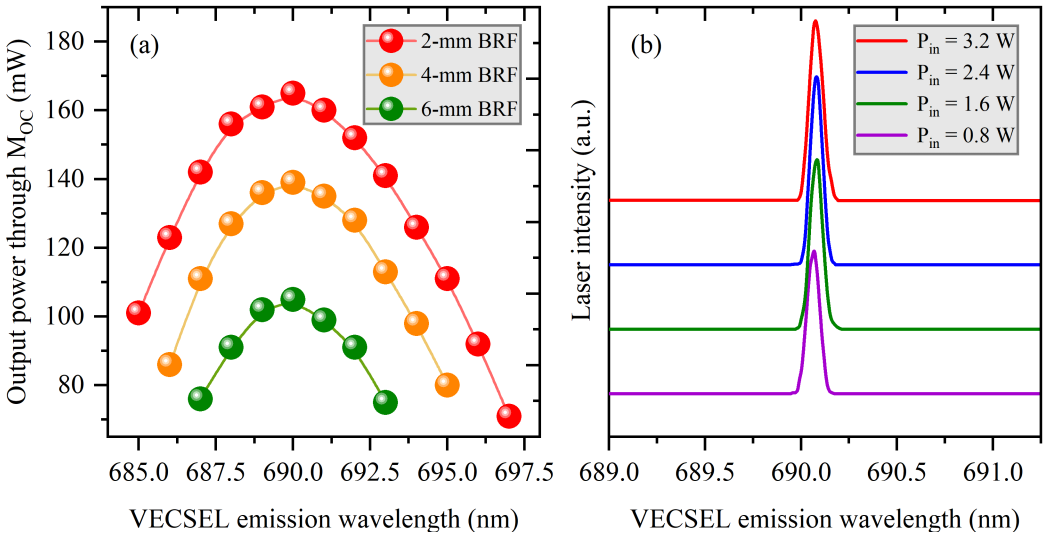


Figure 4.7: Spectral performance of the AlGaInP-based VECSEL. **(a)** Spectral tuning curves measured using a 1% OC at an input pump power of 2.4 W, obtained by rotating BRFs of different thicknesses. **(b)** Emission spectra recorded for increasing input pump powers (P_{in}) with the 4 mm-thick BRF positioned between cavity mirrors M_2 and M_3. The spectra are vertically offset for clarity and do not represent the measured intensity.

all pump powers up to 3.2 W, with the spectral width limited by the 50 pm resolution of the Anritsu MS9710C OSA. Throughout this range, the central wavelength remains stable near 690 nm, exhibiting negligible thermal red-shift. This stability arises because the BRF imposes higher loss on neighbouring longitudinal modes, ensuring that the dominant mode continues to experience the highest net gain even as the external pump power increases.

The optimal quartz thickness was identified by analysing the output spectra with the same Anritsu MS9710C OSA. The 4 mm-thick filter produced a single emission peak with a resolution-limited full-width at half-maximum (FWHM) of (97.3 ± 0.1) pm (see Fig. 4.8a). In contrast, the 2 mm-thick filter resulted in a multi-peak spectral distribution with an estimated linewidth of (366.3 ± 19.3) pm (see Fig. 4.8b). Given the acceptance bandwidth requirements for the SRO (detailed in Chapter 2), a linewidth below 126 pm is essential; consequently, the 2 mm-thick filter was rejected for exceeding this bandwidth by over a factor of three. While the 6 mm-thick filter also facilitated single-peak emission,

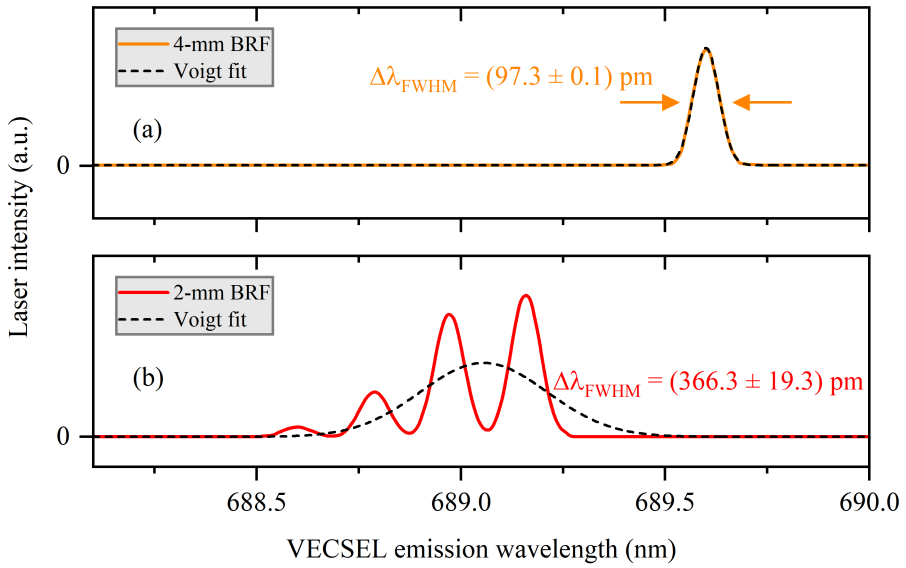


Figure 4.8: Emission spectra of the AlGaInP-based VECSEL measured with an optical spectrum analyser (OSA; Anritsu MS9710C; resolution – 0.05 nm). Data recorded for BRF thicknesses of **(a)** 4 mm and **(b)** 2 mm at an input pump power of 2.4 W.

the 4 mm-thick filter was ultimately selected for its superior efficiency, yielding > 135 mW ($M_{\mathrm{OC}} = 1\%$ OC) at 2.4 W of input pump power, compared to 105 mW for the 6 mm-thick variant under the same pumping conditions (see Fig. 4.7a).

4.5 ICSRO VECSEL cavity design and characterisation

With the full characterisation of the OPO pump laser (i.e., the VECSEL fundamental) complete, the focus now shifts to the ICSRO, where the 5%-MgO:PPLN crystal and DM are introduced to generate efficient down-converted signal and idler waves. This section begins with a description of the alignment procedure, followed by an analysis of the VECSEL spectrum to confirm that operation remains within the SRO acceptance bandwidth. The VECSEL beam quality is also evaluated to confirm its excellent transverse characteristics, which are essential for efficient spatial overlap with the fundamental resonant idler cavity mode.

4.5.1 Alignment procedure

Before aligning the SRO cavity, the four-mirror AlGaInP-based VECSEL resonator was first aligned with the 5%-MgO:PPLN crystal inserted. The introduction of the crystal initially destabilised the cavity due to the crystal's long interaction length, making this stage particularly challenging.

Alignment began by temporarily removing the cavity end mirror M_4. In this configuration, the 5%-MgO:PPLN crystal was positioned such that its geometric centre lay at the design distance of 54.3 mm from the folding mirror M_3, while it was oriented at $\theta = 90°$ with respect to the resonator axis. This orientation ensured that the horizontally polarized VECSEL mode satisfied the conditions for efficient type-0 quasi-phase matching (QPM).

Once the crystal was aligned, cavity end mirror M_4 was reinserted and its position adjusted to increase the M_3–M_4 separation from 91.5 mm (see Fig. 4.3) to 113.3 mm (see Fig. 4.9). Additionally, the cavity end mirror M_4 was positioned such that the fluorescence emerging from the crystal was centred on the mirror substrate. Since the resonator operated in a standing-wave configuration, the fluorescence reflected from M_4 retraced its path through the crystal, enabling oscillation at the VECSEL fundamental wavelength.

To suppress multi-peak emission above threshold, two fused-silica etalons of thickness 200 µm and 300 µm were inserted between mirrors M_2 and M_3. Fine angular tuning of these etalons enabled stable single-peak operation, yielding single-wavelength emission tunable over $\sim$ 686–698 nm, centred at $\lambda_L = 690.6$ nm (see Fig. 4.10a). At the peak wavelength of 690.6 nm, the measured FWHM spectral width was (73.1 ± 0.2) pm, as recorded using the Anritsu MS9710C OSA (see Fig. 4.10b), which is well within the calculated 126 pm spectral acceptance bandwidth (see Section 2.5.2).

The next stage of the alignment procedure involved confirming that the intracavity field propagated through the correct poling period of the 5%-MgO:PPLN crystal, namely $\Lambda_{\mathrm{QPM}} = 14.55$ µm. Leakage from the VECSEL fundamental output (via end mirror M_4) was fibre-coupled into an InGaAs single-photon detector (IDQ201, ID Quantique). The

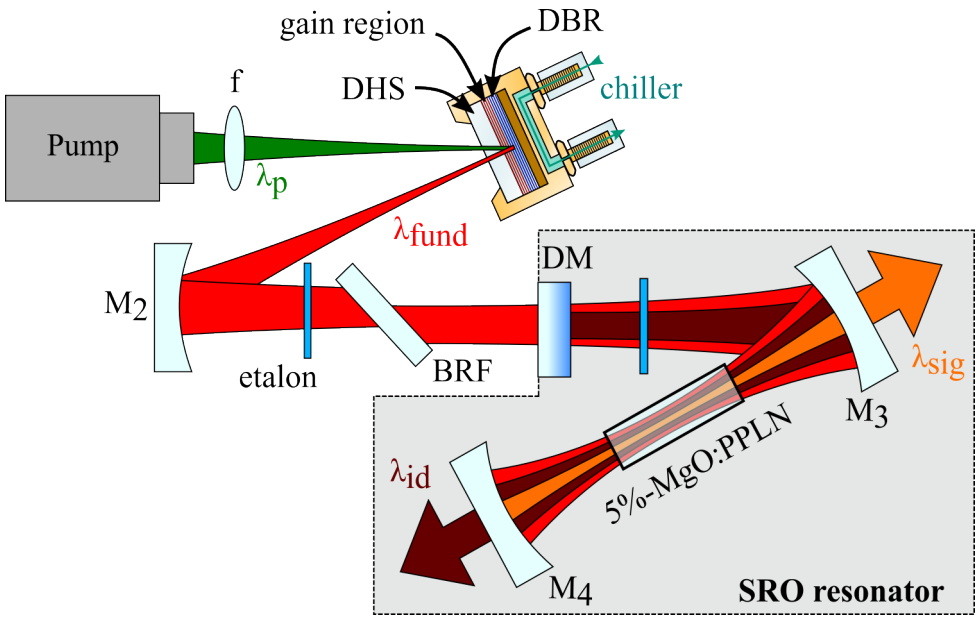


Figure 4.9: Schematic (not to scale) of the AlGaInP-based VECSEL-pumped ICSRO experimental setup, with OC for the resonant idler. The VECSEL (DBR-M_2-M_3-M_4) and the SRO resonant-idler (DM-M_3-M_4) cavities are collinear, with the latter including a 5%-mol MgO:PPLN crystal. The free spectral range (FSR) of the VECSEL and SRO cavities are 365 MHz and 565 MHz, respectively. The optical elements are indicated as follows: f: lens; DBR: distributed Bragg reflector; DHS: diamond heat spreader; DM: dichroic mirror; λ_{p}, λ_{fund}, λ_{sig}, λ_{id}: VECSEL pump, VECSEL fundamental, signal, and idler wavelengths at 532 nm, 690.6 nm, 1245.2 nm, and 1550.8 nm, respectively. Figure reproduced from Ref. [58].

detector was used as a qualitative diagnostic, as no other suitable detector was available, to identify the correct poling period by monitoring changes in the fundamental output. Although the VECSEL fundamental wavelength was outside the detector's specified wavelength range, sufficient optical filtering was introduced to reduce the incident power and prevent detector saturation and/or damage. Since the 5%-MgO:PPLN crystal was non-critically phase-matched through temperature stabilisation, the pump, signal, and idler waves all propagated collinearly, resulting in negligible spatial walk-off and reliable detection. An IR long-pass filter ($\lambda > 1500$ nm) was used to suppress residual pump photons. The crystal temperature was then stabilised at 114°C, corresponding to the theoretical QPM temperature for a 690.6 nm SRO pump source, calculated using the

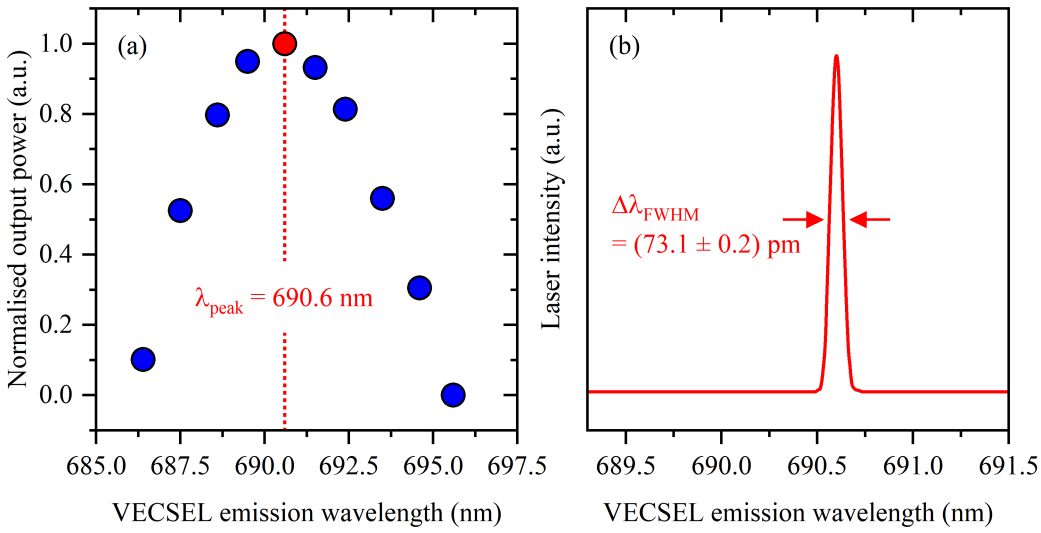


Figure 4.10: Spectral performance of the AlGaInP-based VECSEL with all intracavity components inserted. **(a)** Tunability of the VECSEL output spectrum via rotation of a 4 mm-thick quartz BRF. **(b)** Full-width at half-maximum (FWHM) linewidth measurement of the VECSEL at 690.6 nm (see red data point in (a)). Figure adapted from Ref. [58].

Sellmeier equation of Gayer *et al.* [88]. The crystal was then translated along the y-axis until a clear increase in photon counts above the dark-count level was observed. This high-count region extended over $\sim$500 µm, consistent with the thickness of a single poled domain.

With the VECSEL cavity optimised and the crystal aligned to the correct poling period, the next stage involved aligning the SRO cavity. For this alignment process, the DM was positioned at its design distance of 105 mm from folding mirror M_3 (see Table 3.4) and adjusted such that the back-reflected VECSEL beam (from the DM substrate) overlapped precisely with the intense intracavity beam visible on folding mirror M_3. Fine horizontal and vertical tilt adjustments were made until the InGaAs detector reached saturation. At this point, strong infrared fluorescence became visible on a viewing card placed behind folding mirror M_3, confirming that the SRO cavity had reached threshold and that parametric oscillation had been established.

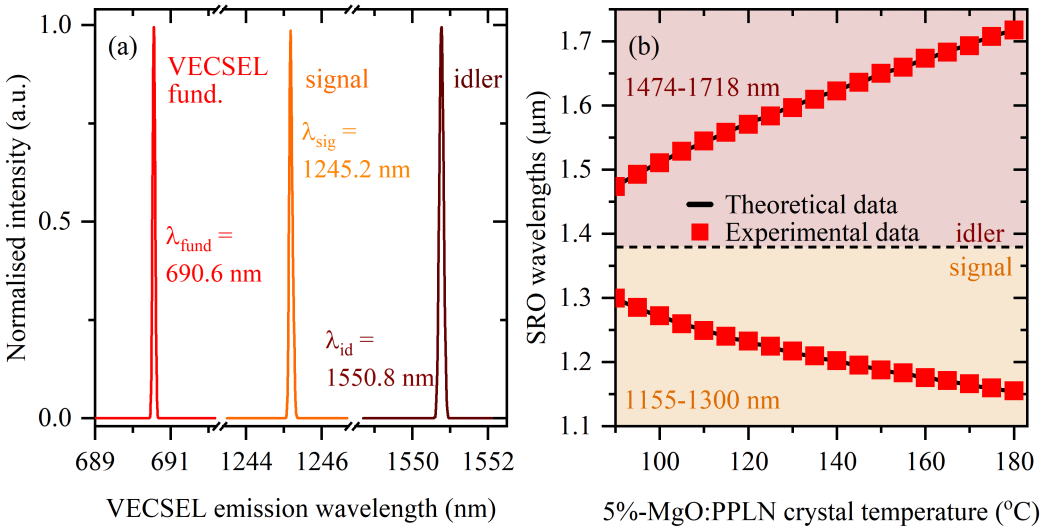


Figure 4.11: **(a)** Normalised intensity spectra of the VECSEL fundamental, signal, and idler, centred at 690.6 nm, 1245.2 nm, and 1550.8 nm, respectively, measured using an Optical Spectrum Analyser (OSA; Anritsu MS9710C; resolution – 0.05 nm). **(b)** Temperature tuning curve of the SRO, measured using the $\Lambda_{\mathrm{QPM}} = 14.55$ µm poling period of the 5%-MgO:PPLN crystal and pumped at $\lambda_{\mathrm{fund}} = 690.6$ nm. Solid curve: theoretical tuning curve calculated via Ref. [88]. Figure adapted from Ref. [58].

4.5.2 Spectral performance

The spectral emission of the VECSEL fundamental, signal, and idler were measured using the Anritsu MS9710C OSA, which exhibited a spectral resolution of 0.05 nm. As described in Chapter 2, the use of QPM eliminated spatial walk-off, thereby allowing the spectra of each ICSRO interacting wave to be measured simultaneously through the same fibre coupler. Each field was coupled into the OSA via leakage from the cavity end mirror M_4. For a fixed VECSEL fundamental wavelength of 690.6 nm, a 5%-MgO:PPLN crystal temperature of 114°C, and a fixed grating period of $\Lambda = 14.55$ µm, the corresponding signal and idler wavelengths were measured to be 1245.2 nm and 1550.8 nm, respectively, as shown in Fig. 4.11a. From this point onwards, the fundamental pump-laser wavelength is denoted by λ_{fund}, rather than λ_L, to align with the notation used in the published literature and to distinguish it from the signal and idler wavelengths, λ_s and λ_i.

Tuning of the SRO was accomplished solely by varying the temperature of the 5%-MgO:PPLN crystal. Although the temperature-stabilised oven provided an operating range from 30°C to 200°C, the practical tuning range was narrower than the theoretical predictions presented in Section 2.5.3. This limitation arose from the finite bandwidths of the dielectric coatings on the cavity mirrors, which imposed excessive loss outside their designed spectral ranges and prevented the SRO from reaching threshold. Consequently, the experimentally accessible tuning range was restricted to between 90°C and 180°C. As illustrated in Fig. 4.11b, varying the 5%-MgO:PPLN crystal temperature from 90°C to 180°C enabled signal tuning from 1300 to 1155 nm (a span of 145 nm) and idler tuning from 1474 to 1718 nm (a span of 244 nm). These correspond to tuning rates of 1.6 nm/°C for the signal and 2.7 nm/°C for the idler. A theoretical curve calculated using the temperature-dependent Sellmeier equation of Gayer *et al.* [88] is also plotted in Fig. 4.11b and shows excellent agreement with the experimental data.

4.5.3 VECSEL beam quality

Beam quality is a key parameter in laser characterisation and is essential for ensuring high stability within an optical resonator. It is quantified by the beam propagation factor M^2, which measures the deviation of a laser beam from an ideal single-mode TEM_{00} Gaussian profile. A diffraction-limited TEM_{00} beam has $M^2 = 1$, while values $M^2 > 1$ indicate the presence of higher-order transverse modes.

Experimentally, beam quality is assessed by analysing the beam after transmission through a focussing lens. In accordance with ISO 11146-1:2021 [186], the beam diameter must be measured at least five times within the first Rayleigh range and at least five times beyond two Rayleigh ranges to accurately determine the divergence. In this work, the beam radii were recorded by focussing the VECSEL output onto a CMOS camera (Thorlabs DCC1545M) equipped with a 1440×1080-pixel sensor and 3.45 µm square pixels.

Measurements were limited to the fundamental output of the VECSEL pump laser, as the CMOS camera lacked sufficient quantum efficiency at the signal and idler wave-

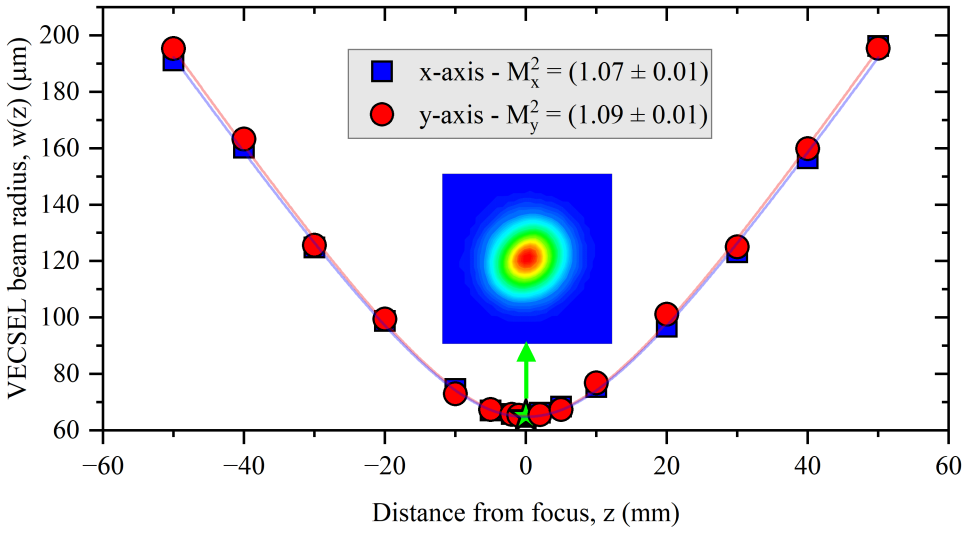


Figure 4.12: Beam quality measurement of the AlGaInP-based VECSEL. Inset: beam profile recorded at the focal point (indicated by a green star) using a commercial CMOS camera (Thorlabs DCC1545M). Inset reproduced from Ref. [58].

lengths. Nevertheless, in an ICSRO, characterising the pump beam quality remains highly informative. The spatial profile of the intracavity pump determines the transverse distribution of nonlinear gain and therefore the spatial overlap with the resonant idler mode. Since the idler is resonant in the OPO cavity, its transverse profile is largely governed by the cavity eigenmodes and is therefore less sensitive to moderate pump distortions. A distorted or multimode pump can nevertheless reduce the gain overlap, increasing the SRO oscillation threshold and reducing conversion efficiency. Under sufficiently strong spatial distortion, higher-order idler cavity modes may also acquire sufficient parametric gain to oscillate. In contrast, the non-resonant signal is generated during single-pass nonlinear mixing and is not subject to the same cavity mode selection. Its spatial profile therefore depends strongly on the pump–idler interaction, making the signal beam quality more sensitive to pump distortions and potentially less stable.

The measured beam radii were fitted to the Gaussian beam propagation equation, that is:

$$w(z) = \sqrt{w_0^2 + \theta^2 (z - z_0)^2}, \tag{4.6}$$

where w_0 is the beam waist radius at the focal point, z_0 denotes the focal position, and θ reperesents the beam divergence, defined by:

$$\theta = \frac{M^2\lambda}{\pi w_0}. \tag{4.7}$$

Using Eq. (4.6), the beam divergence and beam propagation factor for a given wavelength were extracted from the beam-radius measurements shown in Fig. 4.12. By fitting the nonlinear Eq. (4.6) to the experimental data, the propagation factors along the horizontal and vertical axes were found to be:

$$M_x^2 = (1.07 \pm 0.01), \quad M_y^2 = (1.09 \pm 0.01),$$

respectively, for the VECSEL fundamental wave (see Fig. 4.12), confirming a high-quality, diffraction-limited output beam. Correspondingly, the beam divergence of the VECSEL output along the horizontal and vertical axes were calculated to be:

$$\theta_x = (3.63 \pm 0.03) \text{ mrad}, \quad \theta_y = (3.68 \pm 0.03) \text{ mrad}.$$

With the characteristics of the VECSEL pump source now fully established, the following section presents a full characterisation of the SRO. The initial stage of this characterisation involves evaluating the output power and conversion efficiency. This characterisation is performed for two cavity configurations: one in which the cavity end mirror M_4 is highly-reflective at the idler wavelength (HR-idler configuration), and one in which M_4 is partially transmissive at the idler wavelength and acts as an output coupler (OC-idler configuration). The corresponding output powers and conversion efficiencies for each configuration are summarised in Table 4.1. In the following analysis, the pump power incident on the VECSEL chip surface from the external laser is denoted by P_{in}, the fundamental intracavity VECSEL pump power by P_{intra}, and the VECSEL output power by P_{out}^L.

4.5.4 HR-idler ICSRO power and efficiency performance

For the HR-idler configuration, the non-resonant signal exits the cavity through the end mirror M_4 ($R_{\text{sig}} < 2\%$) after a single pass through the 5%-MgO:PPLN crystal, while the idler is resonant and HR by all SRO cavity mirrors (DM, M_3, M_4, $R_{\text{id}} > 99.9\%$; see Fig. 3.8 in Chapter 3). The intracavity VECSEL power – defined as the circulating power within the ICSRO resonator – was obtained by monitoring the field leaking through the folding mirror M_3.

To obtain an accurate estimate of the intracavity circulating power, the transmission of the HR folding mirror M_3 was required. This transmission was measured using the free-running AlGaInP-based VECSEL configuration shown in Fig. 4.3. Because the coating specifications indicated an extremely low transmission at the VECSEL wavelength ($R_M > 99.99\%$), the HR mirror substrate had to be characterised under conditions where the highest possible output power could be achieved. From the power-transfer characteristics, this occurred when operating with the 3% OC (serving as the M_{OC} substrate). Accordingly, at a fundamental wavelength near 690 nm, the HR substrate was positioned a short distance after the OC, and the output power was recorded both before and after the substrate. To ensure high accuracy when measuring the weak transmission, a shielding lens tube was introduced between the HR substrate and the power meter to isolate the sensor from stray light and back-reflections. These measurements yielded an exceptionally low transmission of 0.00012%, corresponding to detected powers of 440 mW (before the substrate) and 530 nW (after the substrate).

From Fig. 4.13, the VECSEL and SRO thresholds are observed at input pump powers of 0.99 W and 1.78 W, respectively. At the SRO threshold, the intracavity VECSEL power is estimated to be 1.59 W, in excellent agreement with the threshold condition calculated in Chapter 3 ($\text{P}_{\text{th}}^{\text{SRO,intra}} = 1.54$ W) [60]. This close agreement indicates that the ICSRO resonator is both well-aligned and optimised according to the design specifications, and that the coatings of the laser cavity optics perform as expected.

Figure 4.13 further highlights the three well-defined operational regions of the ICSRO, with clear evidence of the 'pump-clamping' effect [37], [60]: below the VECSEL

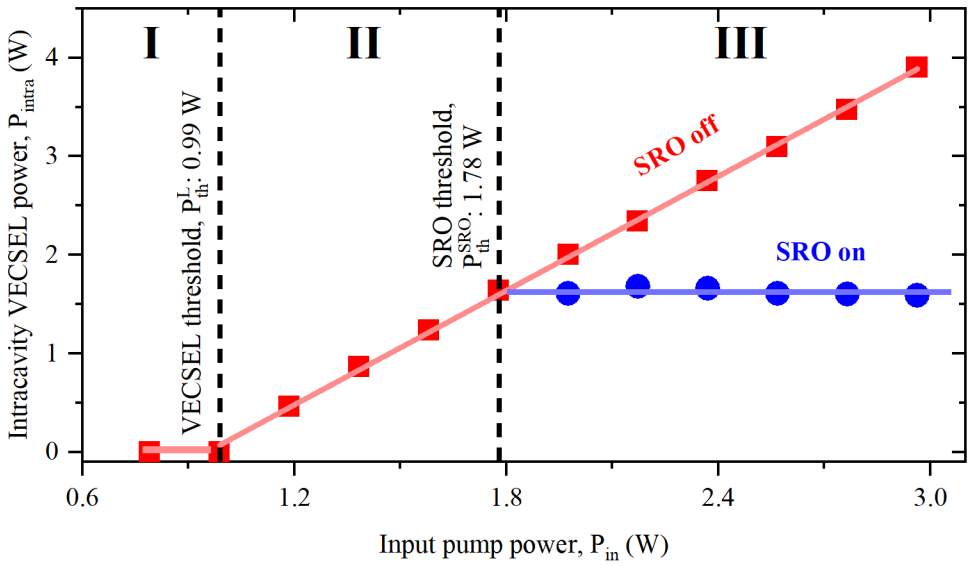


Figure 4.13: Intracavity AlGaInP-based VECSEL power as a function of input pump power, shown both in the presence (blue circles) and absence (red squares) of parametric down-conversion (PDC) for the HR-idler ICSRO regime. Regions I, II, and III correspond to "below VECSEL threshold," "between VECSEL and SRO thresholds," and "above SRO threshold," respectively. Figure reproduced from Ref. [58], with the x-axis label corrected from absorbed DPSSL power to input pump power, and the symbols P_{in} and P_{intra} added to the x- and y-axis labels, respectively.

threshold (Region I), between the VECSEL and SRO thresholds (Region II), and above the SRO threshold (Region III). This clamping behaviour is consistent with the theoretical analysis presented in Chapter 2, which illustrates that any intracavity VECSEL power exceeding 1.59 W is efficiently coupled through the PDC process and converted into signal and idler photons, provided the system operates below the optimal pump-depletion threshold. The observed linear relationship between the VECSEL intracavity field and the input pump power in the absence of PDC, along with the expected clamping behavior above the SRO threshold, demonstrates efficient mode-matching and optimal alignment within the ICSRO system.

Furthermore, Fig. 4.14 presents the extracted one-way non-resonant signal power as a function of input pump power. At the maximum input pump power of 2.96 W, just before the onset of thermal rollover, the extracted one-way signal power reached 14.2 mW.

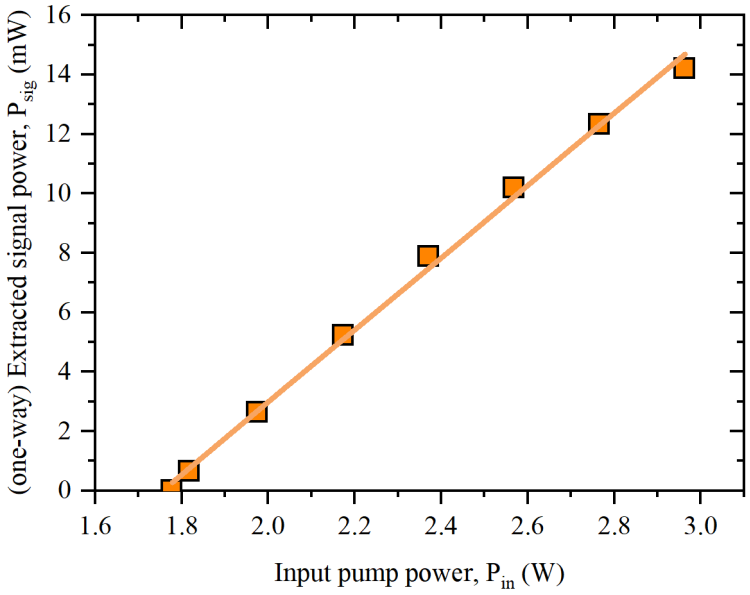


Figure 4.14: Extracted (one-way) non-resonant signal power for increasing increments of input pump power. Figure reproduced from Ref. [58], with the x-axis label corrected from absorbed DPSSL power to input pump power, and the symbols P_{in} and P_{sig} added to the x- and y-axis labels, respectively.

In this configuration, the thermal rollover point is lower than that of the free-running VECSEL cavity shown in Fig. 4.3, where only the BRF was inserted, indicating a larger temperature rise per unit pump power. This behaviour arises from the additional intracavity loss introduced by the OPO components, which increases the gain required to sustain lasing and consequently raises the carrier inversion in the quantum wells (QWs). The higher carrier inversion enhances non-radiative recombination and thermal carrier leakage, causing a greater fraction of the pump energy to be converted into heat. Consequently, the active region reaches its thermal rollover limit at a lower input pump power. The signal power was measured by placing an IR bandpass filter ($\lambda = 1250 \pm 25$ nm) behind the end mirror M_4 to block contributions from the VECSEL fundamental or resonant idler wavelengths. The bandpass filter was calibrated at the signal wavelength of 1245.2 nm by evaluating the ratio of the signal output power, extracted via mirror M_4, with and without the filter in place. Moreover, the extracted signal power exhibits a linear increase with pump power up to the thermal rollover point, with no observ-

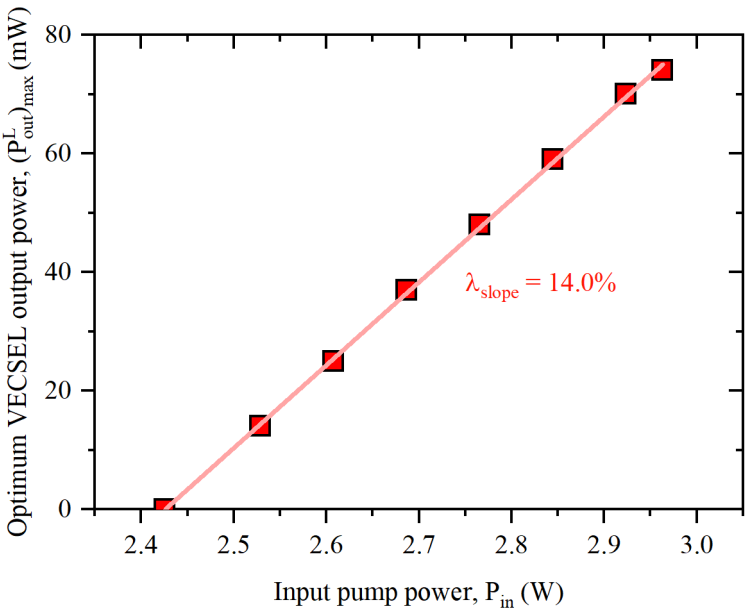


Figure 4.15: Optimum VECSEL output power measured using a 3% OC as a function of increasing input pump power, with PDC suppressed. The threshold increases from approximately 600 mW in the free-running VECSEL regime to 2.4 W following insertion of all intracavity OPO components

able evidence of optical damage, photorefractive effects, or significant thermal lensing. Thus, the current power scaling of the SRO is limited by thermal rollover rather than any apparent degradation in the nonlinear conversion process, suggesting that further power scaling may be possible if the thermal rollover limit can be extended. This can be achieved by increasing the mode-matched spot size incident on the VECSEL chip surface, which would lead to a commensurate increase of the intracavity mode size. Therefore, extending the onset of thermal rollover permits the extraction of higher signal powers; however, this is contingent upon the availability of sufficient pump power to sustain the enlarged intracavity mode and preserve high conversion efficiency.

To evaluate the overall down-conversion efficiency of the ICSRO, it was first necessary to determine the maximum extractable power at the VECSEL fundamental wavelength. In principle, this could be achieved by replacing the end mirror M_4 with a set of output couplers and, with the SRO deliberately misaligned, measuring the corresponding

maximum output power. In practice, the power-transfer behaviour shown in Fig. 4.4 indicates that the VECSEL gain medium is constrained by thermal rollover; hence, the OC transmission providing the highest output power is considered optimal. The same range of OC transmissions investigated in the free-running VECSEL regime (see Fig. 4.4) was subsequently evaluated at an input pump power of 2.96 W. The 3% OC provided the highest output power and was therefore selected for the SRO configuration. The maximum VECSEL output power through M_4 was then measured using the 3% OC, with the SRO maintained below threshold. In this configuration, M_4 was coated exclusively for the VECSEL wavelength, introducing substantial losses at the resonant idler wavelength and thereby suppressing SRO oscillation. As shown in Fig. 4.15, a maximum output of 74 mW was obtained at an input pump power of 2.96 W, corresponding to a slope efficiency of 14% (see Table 4.1). This value represents the maximum available fundamental pump power that can be usefully converted into down-converted signal and idler power within our thermally-limited AlGaInP-based VECSEL pump source.

The threshold at the VECSEL wavelength increases markedly from approximately 600 mW with only the BRF inserted (see Fig. 4.4) to 2.4 W when all intracavity components are present (see Fig. 4.15). As shown in Fig. 4.15, this rise reflects the additional round-trip losses introduced by the nonlinear crystal and intracavity etalon filters. In the free-running cavity, internal losses were minimal, so the threshold was largely determined by the gain medium and only weakly dependent on the OC transmission. With the added intracavity elements, absorption, scattering, and wavelength-selective losses significantly increase the threshold – up to 2.4 W – and enhance the sensitivity to output coupling.

The total down-converted laser power P_{DC} can be calculated from the one-way extracted signal power P_{sig} using:

$$P_{\mathrm{DC}} = \frac{2P_{\mathrm{sig}}}{\eta_{\mathrm{sig}}}\left(1 + \frac{\lambda_{\mathrm{sig}}}{\lambda_{\mathrm{id}}}\right), \tag{4.8}$$

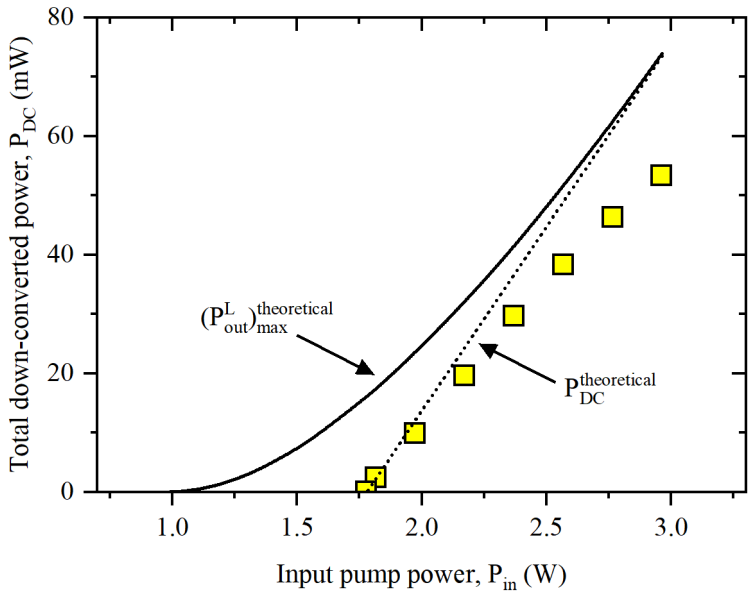


Figure 4.16: Total down-converted power of the AlGaInP-based VECSEL-pumped SRO operating in the HR-idler regime. The dotted line represents the theoretical down-converted power predicted by Eq. (2.44), while the solid line indicates the maximum theoretical VECSEL output expected in the absence of PDC, as given by Eq. (2.49).

where $\eta_{\text{sig}} \approx 0.96$ is the signal cavity-coupling efficiency, and λ_{sig} and λ_{id} are the signal and idler wavelengths, respectively. For $\lambda_{\text{sig}} = 1245.2$ nm and $\lambda_{\text{id}} = 1550.8$ nm, the maximum down-converted laser power is 53.3 mW at 2.96 W of input pump power (see Fig. 4.16).

The total down-conversion efficiency is obtained by taking the ratio of the total down-converted power to the maximum VECSEL output power in the absence of PDC, which yields a total down-conversion efficiency of 72.1% (see Table 4.1) at the maximum input pump power of 2.96 W (see Fig. 4.17).

As demonstrated in Chapter 2, 100% down-conversion efficiency is achieved when the SRO threshold $P_{\text{th}}^{\text{SRO}}$ satisfies:

$$\left(P_{\text{th}}^{\text{SRO}}\right)^2 = P_{\text{th}}^{\text{L}}\, P_{\text{in}}, \tag{4.9}$$

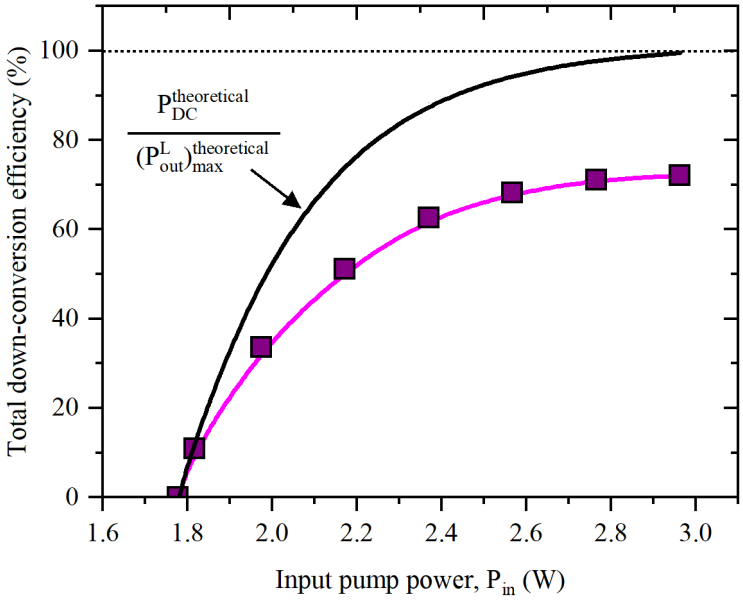


Figure 4.17: Estimated down-conversion efficiency of the AlGaInP-based VECSEL-pumped SRO operating in the HR-idler regime. The experimental data (purple squares) in this figure are reproduced from Ref. [58], with the x-axis label corrected from absorbed DPSSL pump power to input pump power, and the symbol P_{in} added to the x-axis. The solid line represents the theoretical down-conversion efficiency predicted using Eqs. (2.44) and (2.49), while the dotted line indicates the theoretical maximum down-conversion efficiency.

where P_{th}^{L} is the VECSEL threshold and P_{in} is the input pump power of the external laser. It is worth noting that both $P_{\text{th}}^{\text{SRO}}$ and P_{th}^{L} refer to threshold powers based on P_{in}. Under optimal conditions, the input pump power corresponding to maximum down-conversion efficiency is:

$$P_{\text{in}} = \frac{\left(P_{\text{th}}^{\text{SRO}}\right)^2}{P_{\text{th}}^{\text{L}}} = \frac{(1.78\ \text{W})^2}{0.99\ \text{W}} = 3.2\ \text{W}. \tag{4.10}$$

It is worth noting that the ICSRO is operating $\sim$1.7 times threshold and, by referring to Eq. (4.10), the ICSRO is also operating at only 92.5% of the optimal pumping level. Therefore, the SRO only requires operation at 1.8 times threshold to achieve near-optimal efficiency, which is significantly less than externally-pumped OPOs, which typically require 2.47 times threshold to reach optimal performance [187]. An alternative

route to improving the down-conversion efficiency is to reduce the SRO threshold. For an input pump power of 2.96 W, this requires lowering $P_{\mathrm{th}}^{\mathrm{SRO}}$ to 1.71 W, which can be achieved either by increasing the effective nonlinearity coefficient or by reducing intracavity losses in the SRO cavity. In the present HR-idler configuration, the highest available nonlinear coefficient is already utilised through type-0 QPM in the 5%-MgO:PPLN crystal. Therefore, the only remaining means of lowering the SRO threshold is to minimise losses within the SRO cavity at the idler wavelength.

Having fully characterised the power and efficiency of the HR-idler configuration, the investigation is extended to the OC-idler regime by replacing the HR end mirror M_4 with a partially-transmissive OC mirror at the idler wavelength.

4.5.5 OC-idler ICSRO power and efficiency performance

For the OC-idler configuration, the power and efficiency was characterised by introducing a partially-transmitting OC ($T_{\mathrm{OC}} = 1.7\%$) at the idler wavelength via cavity end mirror M_4. Under this configuration, the non-resonant signal wave was now HR at M_4 and exited the cavity through folding mirror M_3 after a double pass through the 5%-MgO:PPLN crystal (see Fig. 4.9). From Section 4.5.4, the HR-idler regime showed that, in the absence of an output coupler, the SRO preferentially generated infrared output at the signal wavelength and exhibited a reduced threshold due to the lower intracavity loss at the resonant idler wavelength. Transitioning to the OC-idler regime, however, enabled milliwatt-level idler output to be obtained, while also allowing independent extraction of the signal and idler waves from separate cavity mirrors.

As illustrated in Fig. 4.18, the VECSEL intracavity field experiences increased losses at the fundamental wavelength, as evidenced by the rise in the VECSEL threshold from 0.99 W to 1.87 W of input pump power. This threshold increase is attributed to the cavity reconfiguration required to optimise the OC-idler regime, which involved pumping a different region of the VECSEL gain chip. Small spatial variations in the epitaxial structure can alter the gain spectrum and sub-cavity resonance, resulting in less favourable spectral overlap with the fixed lasing wavelength and consequently increasing

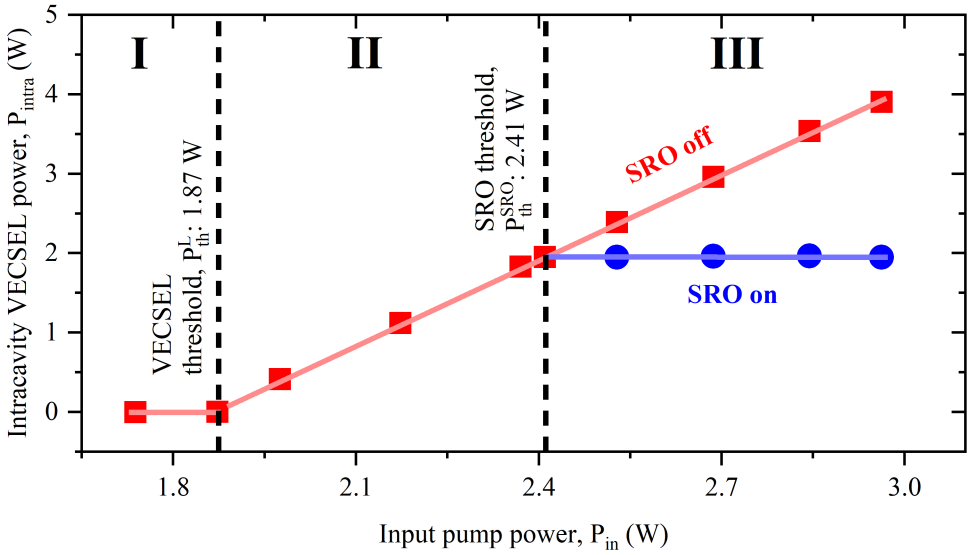


Figure 4.18: Intracavity AlGaInP-based VECSEL power as a function of input pump power, shown both in the presence (blue circles) and absence (red squares) of PDC for the OC-idler ICSRO regime. Regions I, II, and III correspond to "below VECSEL threshold," "between VECSEL and SRO thresholds," and "above SRO threshold," respectively.

the threshold. Despite this, excellent 'clamping' behavior is still observed above the SRO threshold, similar to the HR-idler regime (see Fig. 4.13), indicating that efficient mode-matching and strong optical alignment is also obtained for the OC-idler regime.

The SRO begins oscillation at a higher input pump power of 2.41 W, corresponding to 1.95 W of intracavity VECSEL power. This represents an increase of 630 mW relative to the HR-idler SRO threshold of 1.78 W (see Fig. 4.13). Nevertheless, at the maximum input pump power of 2.96 W – just below the onset of thermal rollover – the maximum intracavity VECSEL power circulating within the ICSRO cavity remains essentially identical to that observed in the HR-idler configuration ($\sim$3.9 W; see Fig. 4.13).

At the maximum input pump power of 2.96 W, the measured one-way extracted idler power is 5.6 mW at 1550.8 nm (see Fig. 4.19). In contrast, the non-resonant signal undergoes a double pass through the 5%-MgO:PPLN crystal, yielding a total signal power of 26.2 mW at 1245.2 nm, measured via the folding mirror M_3. To note, only

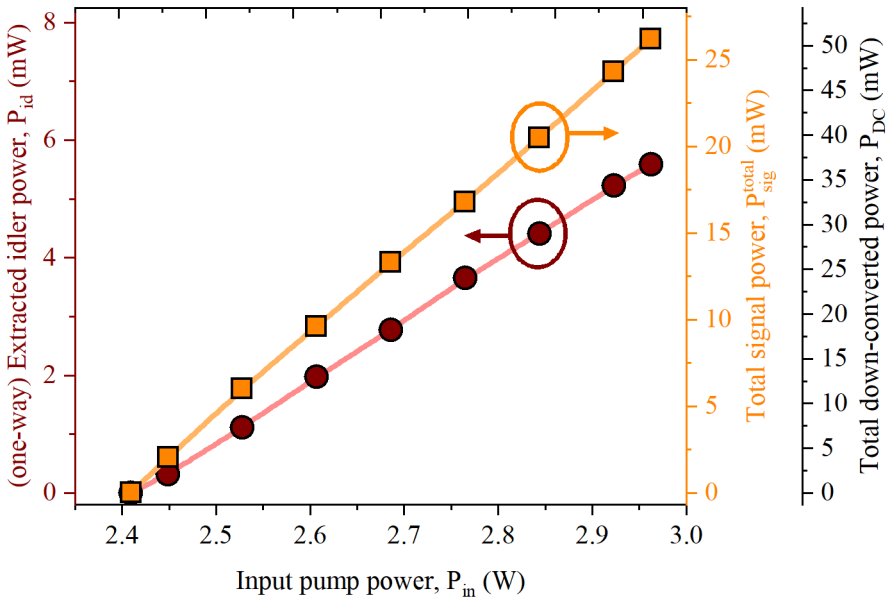


Figure 4.19: Extracted one-way idler power (brown circles), measured total signal power (orange squares), and total down-converted power (yyy-axis), calculated using Eq. (4.8), as a function of input pump power. Figure reproduced from Ref. [58], with the x-axis label corrected from absorbed DPSSL power to input pump power, and the symbols P_{in}, P_{id}, $P_{\text{sig}}^{\text{total}}$, and P_{DC} added to the x-, y-, yy- and yyy-axis labels, respectively. The yyy-axis represents the calculated total down-converted power derived from the measured total signal power shown on the yy-axis.

a single transmission through M_3 is detected because the signal field leaves the cavity before completing a round-trip.

Using a signal-coupling efficiency of $\eta_{\text{sig}} \approx 91\%$ – which accounts for transmission losses at mirrors M_3 and M_4 as well as reflection losses at the 5%-MgO:PPLN facets – the total down-converted power is calculated to be 51.9 mW using Eq. (4.8). This value is reduced by a factor of two relative to the HR-idler configuration because the non-resonant signal experiences a double pass through the nonlinear crystal and exits the cavity exclusively through M_3. Of the total down-converted power, the signal contributes 28.8 mW, while the idler contributes 23.1 mW. Given that an extracted idler power of 5.6 mW corresponds to an OC transmission of 1.7%, the implied total round-trip loss of the SRO cavity is 7.0%.

The output coupler exhibited a measured transmission of 1.7%, corresponding to an insertion loss of $(1.9 \pm 0.1)\%$. The total loss of the HR-idler SRO cavity was estimated to be $(4.7 \pm 0.3)\%$, based on the calculated mirror insertion losses and the anti-reflective (AR) coating losses at the 5%-MgO:PPLN crystal facets. This estimate does not include additional parasitic loss mechanisms that may arise within the 5%-MgO:PPLN crystal itself.

To quantify the insertion loss of each SRO cavity mirror, the mirrors were temporarily replaced with substrates from the same coating batch, ensuring that stable laser operation was maintained. The idler output power was then measured before and after each substrate, with each substrate positioned outside the resonator and oriented to match its in-cavity angle of incidence. For the DM and end mirror M_4, insertion loss was determined by measuring the reflected and transmitted power at a small tilt of approximately 1°. This tilt was sufficient to spatially separate the reflected beam from the incident beam for accurate measurement, while remaining small enough to avoid influencing the coating performance. After characterisation, each mirror was reinstalled prior to conducting the power measurements presented in this section.

Direct measurement of the AR-coating loss at 1550.8 nm for the 5%-MgO:PPLN crystal was not feasible due to the lack of a suitable light source in the absence of PDC. Nonetheless, the calculated total SRO cavity loss of 7.0% is consistent with the sum of the estimated HR-idler cavity losses $(4.7 \pm 0.3)\%$ and the output-coupler insertion loss $(1.9 \pm 0.1)\%$. The small remaining discrepancy is attributed to unquantified parasitic losses – such as absorption and scattering within the 5%-MgO:PPLN crystal – for which direct measurement was not possible.

Figure 4.20 presents the extraction efficiency of the OC-idler ICSRO system. At the maximum available pump power of 2.96 W, the measured signal and idler powers of 26.2 mW and 5.6 mW correspond to extraction efficiencies of 35.4% and 7.6%, respectively, yielding a combined extraction efficiency of 43%. These values indicate that further optimisation of the idler OC transmission could enhance the ICSRO performance even further. Also shown in Fig. 4.20 is the total down-conversion efficiency versus input

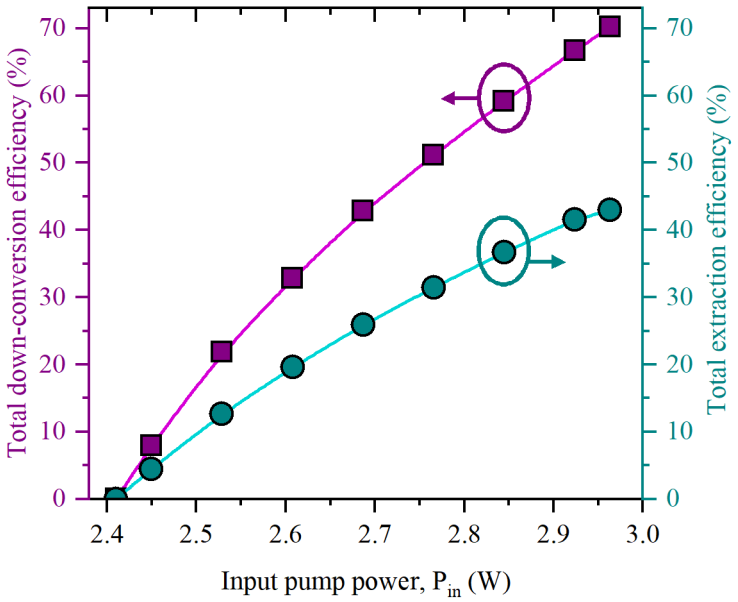


Figure 4.20: Estimated SRO down-conversion efficiency (purple squares) and total extraction efficiency (cyan circles) as a function of input pump power. Figure reproduced from Ref. [58], with the x-axis label corrected from absorbed DPSSL power to input pump power, and the symbol P_{in} added to the x-axis.

pump power for the OC-idler configuration. The total down-conversion efficiency in this regime reaches a maximum of 70.2% at 2.96 W of input pump power (see Table 4.1). Moreover, the optimal OC for the VECSEL fundamental wavelength of 690.6 nm remains $\sim 3\%$ for the OC-idler regime, since the maximum intracavity VECSEL power at 2.96 W is effectively identical to that obtained in the HR-idler configuration (see Fig. 4.13), despite the pump spot being located at a different position on the gain chip. This behaviour is expected: the maximum achievable power is ultimately limited by the thermal rollover point, which in both configurations occurs beyond 2.96 W of input pump power.

Introducing the 3% OC increases the cavity loss significantly to raise the VECSEL threshold above the thermal rollover limit (occurring beyond 2.96 W), thereby preventing laser oscillation at the fundamental wavelength and precluding direct measurement of the output power and slope efficiency. Therefore, no theoretical VECSEL curve is shown in Fig. 4.20. Instead, a maximum VECSEL output power of 74 mW (in the absence of

Table 4.1: Summary of optical power and efficiency for the ICSRO VECSEL system.

	Power (mW)	**Efficiency (%)**
Input pump	2960	–
VECSEL (max. output)	74	14
HR-idler ICSRO (total down-converted)	53.3	72.1
OC-idler ICSRO (total down-converted)	51.9	70.2

PDC) was assumed for the subsequent analysis, corresponding to the maximum output power measured in the HR-idler regime, and used to estimate the maximum PDC power achievable in the OC-idler configuration.

To determine the input pump power required for 100% down-conversion efficiency, the measured VECSEL and SRO thresholds were used in the same manner as for the HR-idler regime. Substituting the threshold powers of 1.87 W and 2.41 W (see Fig. 4.18) into Eq. (4.10) shows that an input pump power of 3.11 W is required to optimise both the non-resonant signal power and the total down-converted output. However, determining the optimal resonant idler power requires an alternative approach, which involves evaluating the SRO threshold using the following expression:

$$P_{\text{in}} = \frac{\left(P_{\text{th}}^{\text{SRO}}\right)_{\text{OC}}^{2}}{\left(P_{\text{th}}^{\text{SRO}}\right)_{\text{min}}}, \tag{4.11}$$

where $\left(P_{\text{th}}^{\text{SRO}}\right)_{\text{OC}}$ and $\left(P_{\text{th}}^{\text{SRO}}\right)_{\text{min}}$ are the input pump powers at which the SRO reaches threshold in the presence and absence of output coupling, respectively. Using Eq. (4.11) together with the measured SRO thresholds of 1.78 W (without OC present) and 2.41 W (with OC present), the input pump power required to optimise the resonant idler output is found to be 3.26 W. This highlights the critical role of the external pump power in the SRO: by adjusting the input pump power, the ICSRO system can be operated either for maximum total down-converted power (and maximum non-resonant signal power) or for maximum resonant idler power.

Although the ICSRO system is a proof-of-principle tabletop setup, the results, particularly in comparison with previously reported CW-ICSRO systems [26], [188], [189],

[190], highlight the fact that our ICSRO system is well-aligned and operating with near-optimum mode-matching. Reported efficiencies for alternative pump geometries and external ring resonators range from 66% [190] to 93% [189]. The achieved down-conversion efficiencies of 72.1% (for the HR-idler) and 70.2% (for the OC-idler) in our system are thus competitive, with the added advantage of the ultra-low noise performance from the VECSEL architecture.

Two approaches could further enhance the down-conversion efficiencies to match or exceed these benchmarks. First, operating the SRO at the theoretical optimum input pump power (3.2 W for HR-idler, 3.11 W for OC-idler) can be achieved by increasing the thermal rollover point by increasing the VECSEL pump spot size. However, as explained earlier on in this chapter, this would also lead to a commensurate increase of the intracavity mode size. Second, the ICSRO can be optimised for maximum down-conversion efficiency rather than for minimum oscillation threshold. As discussed in Chapter 3, and based on the theoretical work by Guha *et al.* [177], [178], optimal efficiency can be achieved by designing the ICSRO resonator to provide focussing parameters of $\xi^{p}_{\mathrm{foc}} = 1.0$ and $\xi^{i}_{\mathrm{foc}} = 0.9$ at the centre of the 5%-MgO:PPLN crystal for the VECSEL fundamental and resonant idler, respectively. Such optimisation may raise the ICSRO threshold, necessitating higher pump power to reach or approach the optimal pumping point.

With the power and efficiency dynamics of the ICSRO VECSEL system fully characterised in both the HR-idler and OC-idler configurations, we now turn to an investigation of the passive power stability of the ICSRO. In the OC-idler regime, we compare the short-term output-power fluctuations of the VECSEL fundamental above and below the SRO threshold, as well as the long-term amplitude fluctuations of the non-resonant signal.

4.5.6 Passive power stability characteristics of the SRO pumped in a multi-longitudinal-mode VECSEL

Figure 4.21 illustrates the short-term passive stability of the VECSEL output power, measured using a Tektronix oscilloscope and determined from the leakage through the

HR folding mirror M_3. The data is presented for two operating conditions: when the SRO is 'switched on' (blue data points) and when the SRO is 'switched off' (red data points). The 'switched off' condition is achieved by intentionally misaligning the SRO cavity via a slight tilt of the DM. This misalignment effectively disables the SRO, which can then be 'switched back on' again by reversing the misalignment, without making any further adjustments to the remaining components of the SRO resonator.

At the maximum input pump power of 2.96 W, and when the VECSEL operates on multiple longitudinal modes, the passive power stability was assessed over a timescale of 5 ms. Excellent stability is observed under both conditions, with root mean square (RMS) fluctuations of 0.86% in the absence of PDC and 0.96% in its presence (see Fig. 4.21a). The reduction in VECSEL power beyond the SRO threshold can be attributed to the pump 'clamping' effect, which mirrors the intracavity VECSEL power behavior shown in Figs. 4.13 and 4.18.

Despite demonstrating excellent short-term stability in the absence of PDC, perhaps the most notable feature is the suppression of amplitude fluctuations above the SRO threshold. This confirms that the VECSEL, and consequently the SRO, operate without the quasi-continuous bursts of relaxation oscillations typically observed in solid-state systems. In contrast, solid-state OPOs frequently exhibit such instabilities due to their long upper-state lifetimes (Class-B dynamics), whereas the rapid carrier dynamics of the semiconductor gain medium provide inherently stable operation [166]. As demonstrated throughout this investigation, the relaxation-oscillation-free behaviour of the Class-A VECSEL highlights its suitability as a pump source for OPO operation in advanced quantum technologies. This characteristic is especially advantageous for high-precision applications, such as squeezed-light generation and quantum-optics experiments, where ultra-low intensity noise is essential.

The long-term power stability of the non-resonant signal was measured over a timescale of 4000s at an input pump power of 2.69 W, through the folding mirror M_3 (see Fig. 4.21b). The input pump power was reduced to facilitate a direct comparison with the power-stability measurements obtained during single longitudinal mode operation

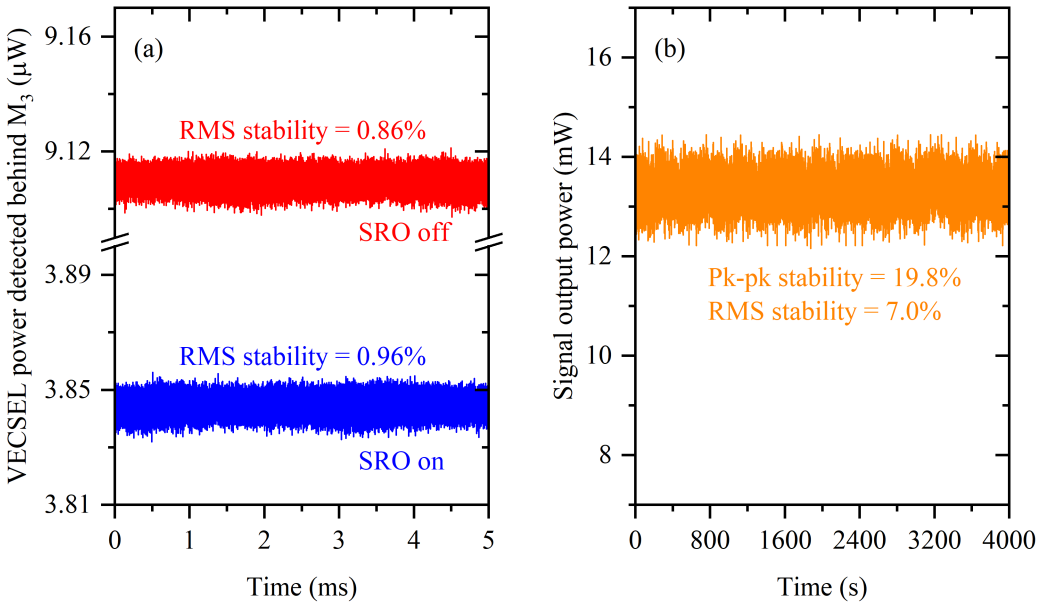


Figure 4.21: OC-idler ICSRO passive power stability analysis when the VECSEL is operating on multiple longitudinal modes. **(a)** Short-term (5 ms) VECSEL power stability, measured via leakage through HR mirror M_3, in the presence (blue data points) and absence (red data points) of PDC, at an input pump power of 2.96 W. **(b)** Long-term SRO signal power stability, measured over 4000 s via folding mirror M_3, at an input pump power of 2.69 W. Pk-pk: peak-to-peak, RMS: root-mean-square. Figure reproduced from Ref. [58].

(see Section 4.6). This adjustment ensures consistency with the specific operating point at which the single-frequency performance was optimised. The peak-to-peak (pk-pk) and RMS amplitude fluctuations were found to be no greater than 19.8% and 7.0%, respectively.

A further advantage of using a VECSEL as the SRO pump source is evident in Fig. 4.21b. Notably, none of the characteristic signatures of the inefficient self-pulsing regime – frequently observed in DPSSL ICSROs operated well above threshold [42], [43] – are present. In particular, the non-resonant signal shows no spiking behaviour or periodic amplitude modulation over the measurement timescale. Although these measurements do not capture the fast temporal dynamics required to definitively exclude high-frequency self-pulsing, no intermittent bursts or enhanced low-frequency power fluctuations are observed in the intensity noise measurements presented in Chapter 5, thus providing

strong evidence that the ICSRO operates in a stable steady-state when pumped by a VECSEL.

One promising route to further improving the passive power stability of the ICSRO system is to enforce single longitudinal mode operation of the VECSEL, a strategy that is examined in detail in the following section.

4.6 Single-frequency ICSRO VECSEL

Up to this point, the combination of the 300 µm-thick etalon in the VECSEL branch and the 200 µm-thick etalon in the SRO branch of the ICSRO cavity has provided sufficient spectral discrimination to maintain single-peak wavelength operation within the OPO pump-acceptance bandwidth. However, the measured spectral bandwidth is limited by the 50 pm resolution of the Anritsu MS9710C OSA. As a result, it cannot be conclusively determined whether this etalon combination and the 4 mm-thick BRF is sufficient to filter the VECSEL – and consequently the SRO – down to a single longitudinal mode.

The following section examines the theoretical considerations and experimental procedures employed to enforce stable single-frequency operation of the ICSRO VECSEL system, a capability that is highly advantageous for the implementation of active stabilisation techniques.

4.6.1 Confocal Fabry–Pérot interferometer

Confocal Fabry–Pérot interferometer (FPI)s are widely employed as high-resolution spectral analysers for characterising the longitudinal mode structure and linewidths of laser sources. As illustrated in Fig. 4.22, a standard confocal FPI consists of two spherical mirrors with identical radii of curvature r, separated by a distance $d = r$, thereby satisfying the confocal condition. In this configuration, and neglecting spherical aberrations, a ray entering the cavity parallel to the optical axis is focussed to a common focal point midway between the mirrors (see Fig. 4.22). After four successive traversals of the cavity, the ray retraces its original path and returns to the entrance plane.

For a confocal FPI, the free spectral range (FSR), defined as the frequency separation between adjacent longitudinal resonances, is given by:

$$\Delta\nu_{\mathrm{FSR}}^{\mathrm{FPI}} = \frac{c}{4L_{\mathrm{cav}}}, \tag{4.12}$$

where c is the speed of light in vacuum and L_{cav} is the physical mirror separation. The factor of four arises from the confocal geometry, in which the intracavity optical field reproduces itself after four cavity traversals. For an incident plane wave entering the cavity at an angle θ_{inc} relative to the optical axis, the longitudinal resonance condition may be expressed as:

$$2L_{\mathrm{cav}}\cos\theta_{\mathrm{inc}} = m\lambda, \tag{4.13}$$

where λ is the wavelength of the incident light and m is an integer. In addition, the resonance peaks in a confocal FPI occur when the total round-trip phase accumulated by the intracavity field satisfies the following condition:

$$\Phi_{\mathrm{RT}} = 2kL_{\mathrm{cav}} + \phi_{\mathrm{Gouy}} = 2\pi m, \quad m = 0, 1, 2, \ldots \tag{4.14}$$

where $k = 2\pi/\lambda$ is the wavenumber, L_{cav} is the cavity length, and ϕ_{Gouy} accounts for the transverse-mode Gouy phase shift. At these resonant frequencies, a series of partially transmitted field components resulting from multiple reflections within the confocal cavity interfere constructively at the output mirror. This constructive interference produces sharp maxima in the transmitted intensity, observed as distinct resonance peaks.

To enable spectral analysis, one of the FPI cavity mirrors – typically the rear mirror – is mounted on a piezoelectric transducer (PZT) ring actuator, providing fine, controllable adjustment of the cavity length. Varying the mirror position alters the optical path length and thus the round-trip phase accumulated by the intracavity field. By scanning the cavity length with the PZT while monitoring the transmitted power, the resonance frequencies of the interferometer are swept across the spectrum of the incident light.

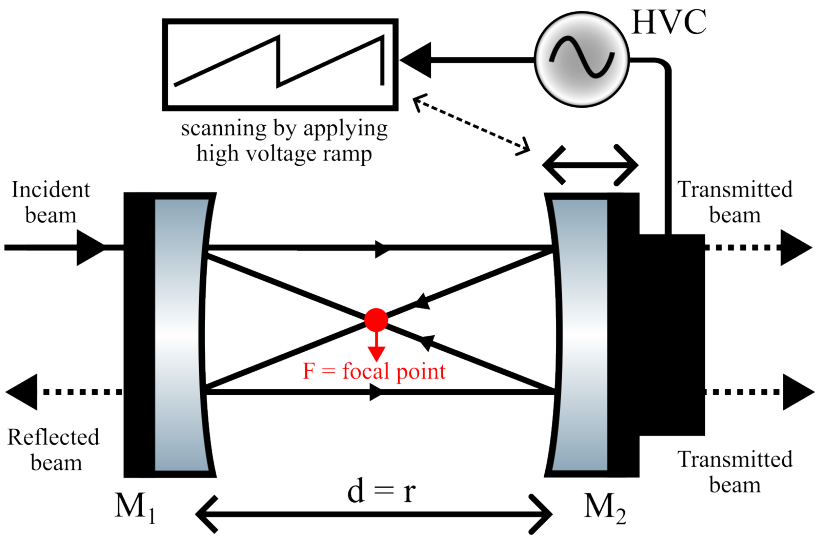


Figure 4.22: Schematic of a scanning confocal Fabry–Pérot interferometer (FPI). d: mirror separation; r: mirror radius of curvature; HVC: high-voltage controller.

Transmission maxima are therefore observed whenever a cavity resonance coincides with the optical frequency of the incoming field.

Furthermore, the performance of an optical cavity is commonly characterised by its finesse $\mathcal{F}$, which quantifies the sharpness of its resonance features and, equivalently, the ability of the cavity to store optical energy. For a symmetric FP cavity with identical mirror reflectivities R_M and negligible additional losses, the finesse is given by:

$$\mathcal{F} = \frac{\pi\sqrt{R_M}}{1 - R_M}, \tag{4.15}$$

where a higher finesse corresponds to narrower resonance linewidths and greater sensitivity of the cavity transmission to changes in optical path length. The finesse is formally defined as the ratio of the FSR to the full width at half maximum (FWHM) of an individual resonance peak. Accordingly, the spectral bandwidth $\Delta\nu_{\mathrm{FWHM}}$ associated with a single cavity resonance is given by:

$$\Delta\nu_{\mathrm{FWHM}} = \frac{\Delta\nu_{\mathrm{FSR}}}{\mathcal{F}}, \tag{4.16}$$

which directly links the cavity's spectral resolution to its optical losses. As a result, high-finesse cavities are capable of resolving closely spaced spectral features, making them particularly well suited for high-resolution laser linewidth measurements.

4.6.2 The Fabry–Pérot etalon effect

The plane-parallel intracavity diamond heat spreader bonded to the AlGaInP-based VECSEL wafer provides only limited spectral filtering. This is largely a consequence of the VECSEL's broad gain bandwidth, which supports multiple longitudinal and transverse modes and therefore produces numerous etalon resonances (see Fig. 4.23). Suppressing these resonances is essential for achieving single-mode and/or narrow-linewidth operation. In the free-running AlGaInP-based VECSEL (see Fig. 4.3), the 4 mm-thick quartz BRF is sufficiently thick to restrict the emission to a single spectral peak (see Fig. 4.10b). However, once the 5%-MgO:PPLN crystal is introduced and the SRO operates above threshold, the spectrum broadens again, necessitating additional spectral filtering.

A practical and widely adopted method for introducing spectral selectivity into a laser resonator is the insertion of one or more FP etalons within the cavity. Functionally, FP etalons are equivalent to FPIs, with the distinction that the reflective surfaces of an etalon remain rigidly fixed. The spectral interference characteristics produced by an FP etalon are governed by the physical thickness of the substrate, its refractive index, the reflectivity of the coatings, and the degree of parallelism and surface flatness achieved during fabrication. Increasing the etalon thickness reduces the spacing between successive transmission maxima while higher mirror reflectivity yields correspondingly narrower transmission peaks. Because the optical path length depends on the angle of incidence, the spectral position of the transmission resonances can be tuned slightly by tilting the etalon plate. The wavelength-dependent transmission function of an ideal etalon is given by:

$$T_E(\lambda) = \frac{(1 - R_E)^2}{1 + R_E^2 - 2R_E \cos\left(\phi_E(\lambda)\right)}, \tag{4.17}$$

where the phase accumulated during a single round trip within the etalon is:

$$\phi_E(\lambda) = \frac{4\pi n_E L_E \cos(\theta_E)}{\lambda}, \tag{4.18}$$

and R_E, n_E, L_E, and θ_E denote the surface reflectivity, refractive index, thickness, and internal angle of refraction of the etalon, respectively, while λ denotes the wavelength. The frequency separation between adjacent transmission maxima, known as the FSR, is defined as:

$$\Delta\lambda^E_{\mathrm{FSR}} = \frac{\lambda^2}{2n_E L_E \cos(\theta_E)}, \tag{4.19}$$

and, in terms of frequency, is given by:

$$\Delta\nu^E_{\mathrm{FSR}} = \frac{c}{2n_E L_E \cos(\theta_E)}. \tag{4.20}$$

To achieve stable single longitudinal mode operation, the FWHM linewidth of the intracavity etalon must be narrower than the longitudinal mode spacing of the laser resonator. As an example, a 300 µm-thick fused-silica etalon (see Fig. 4.23) provides an FSR of $\sim$345 GHz, which is several orders of magnitude larger than the AlGaInP–based VECSEL cavity mode separation of $\sim$ 360 MHz. Under these conditions, the fundamental VECSEL output would naturally be expected to oscillate on multiple longitudinal modes unless the intracavity etalon exhibited a finesse of $\sim$ 960, according to Eq. (4.16). However, the stringent requirement for low intracavity loss in VECSEL resonators restricts the use of intracavity etalons to low finesse, as higher finesse devices would significantly increase round-trip losses and raise the lasing threshold beyond practical limits. As a result, a single intracavity etalon does not provide sufficient spectral selectivity to suppress all competing longitudinal modes. To overcome this limitation, a dual-etalon configuration is employed, in which a low-finesse, large-FSR etalon provides coarse mode selection via angular rotation, while a second etalon with a smaller FSR supplies fine spectral discrimination (see Fig. 4.23). Therefore, stable, single-frequency operation is achieved when the transmission maxima of both etalons coincide with a

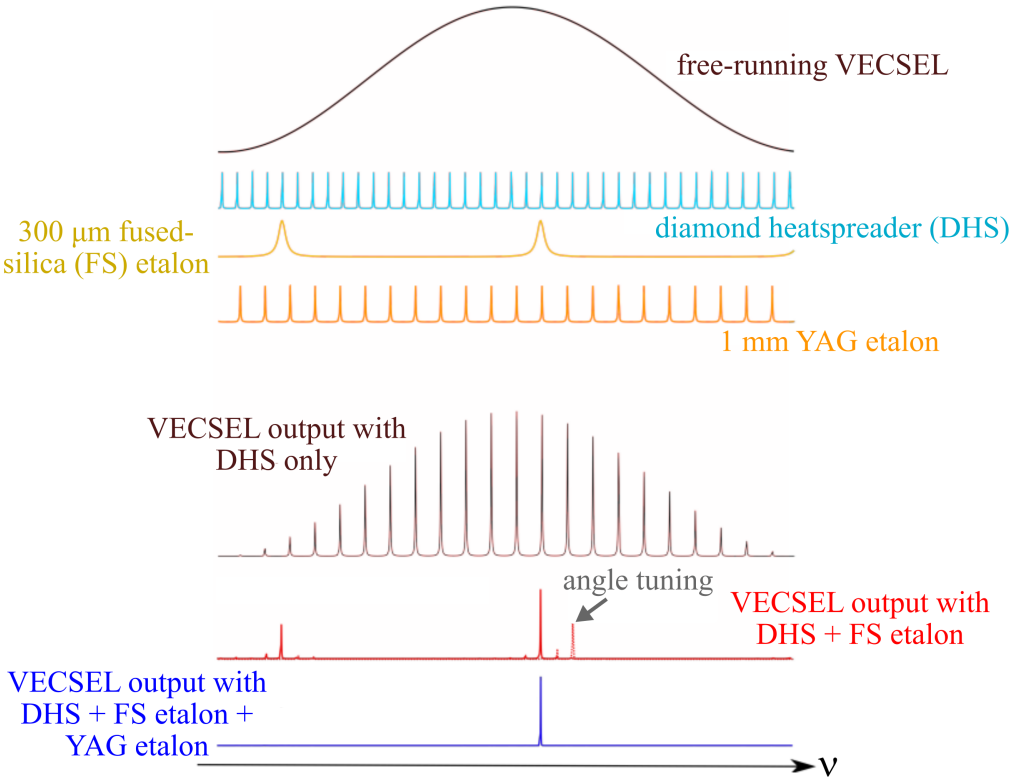


Figure 4.23: Schematic illustration of single-frequency mode selection using two intracavity etalon filters of different thicknesses: a 300 µm-thick fused-silica etalon and a 1 mm-thick YAG etalon. Coarse and fine tuning of the resonant transmission peaks are achieved via angular adjustment of the fused-silica and YAG etalons, respectively, resulting in a controlled shift of the etalon resonance frequencies. Figure adapted from Ref. [191].

single longitudinal cavity mode within the gain bandwidth, thereby ensuring effective mode suppression without incurring excessive intracavity loss.

As an initial step, and as emphasised throughout this chapter, the output power and conversion efficiency of the ICSRO were characterised using the two fused-silica etalons positioned between cavity mirrors M_2 and M_3 (see Fig. 4.9). In the subsequent section, we first justify the replacement of the 200 µm-thick etalon based on its spectral filtering limitations, and then provide a comprehensive characterisation of the single-frequency

ICSRO performance with the introduction of a 1 mm-thick yttrium aluminium garnet (YAG) filter. This analysis includes detailed spectral and passive power-stability measurements of all three ICSRO interacting waves, thereby quantifying both the frequency and amplitude stability of the ICSRO VECSEL system.

4.6.3 Experimental configuration

The schematic of the ICSRO VECSEL configuration employed to demonstrate stable single-frequency operation, including the external coupling optics, is presented in Fig. 4.24. The transmission spectra of each ICSRO interacting wave was measured by coupling each field into its corresponding scanning confocal FPI. The visible FPI had an FSR of 1 GHz and a finesse of ~ 400, while the IR FPI had an FSR of 1.5 GHz and a finesse of ~ 200. A sawtooth waveform was applied to the PZT of the infrared reference cavity via a high-voltage controller (HVC) to scan the signal and idler spectra. Synchronisation with the VECSEL fundamental was achieved using a digital trigger derived from the visible-cavity reference controller. The two FPI systems employed different cavity-scanning waveforms as a consequence of their respective electronic and PZT drive configurations. In each case, the applied waveform provided the required variation in cavity length to scan the corresponding spectral range and resolve the transmission fringes.

To select either the signal or idler for measurement with the IR FPI, a flip mirror was placed before the reference cavity. When the flip mirror was raised, the signal beam was directed into the FPI; when lowered, the corresponding idler beam was coupled instead. For the VECSEL, the fundamental light was coupled into the visible FPI using one of the intracavity BRF reflections, since all ICSRO cavity mirrors were HR at the VECSEL wavelength.

4.6.4 Spectral characteristics

The VECSEL fundamental spectrum was measured using the visible confocal FPI, positioned at the diagnostic port observing the rejected pump light from the intracavity

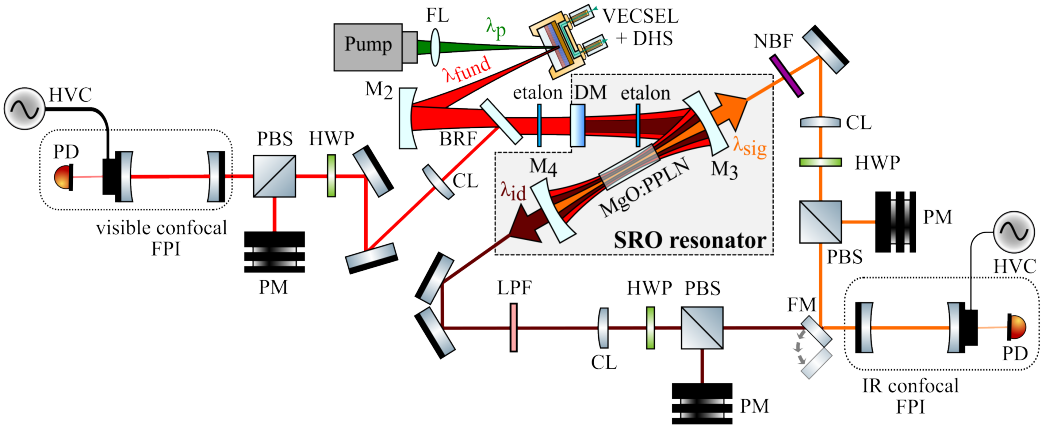


Figure 4.24: Schematic (not to scale) of the AlGaInP-based VECSEL-pumped ICSRO configuration used to achieve single-frequency operation. In this configuration, the 200 µm-thick fused-silica etalon has been replaced by a 1 mm-thick YAG etalon in the SRO branch. The optical elements are indicated as follows: FL: focussing lens; DHS: diamond heat spreader; DM: dichroic mirror; HWP: half-wave plate; PBS: polarizing beam splitter; FPI: Fabry–Pérot interferometer; PD: photodiode; HVC: high-voltage controller; LPF: long-pass filter; NBF: narrow-band filter; PM: power meter; CL: collimating lens; FM: flip mirror; λ_{p}, λ_{fund}, λ_{sig}, λ_{id}: VECSEL pump, VECSEL fundamental, signal, and idler wavelengths at 532 nm, 690.6 nm, 1245.2 nm, and 1550.8 nm, respectively. Figure adapted from Ref. [58].

BRF (see Fig. 4.24). For this baseline measurement, both fused-silica etalon filters were kept in place within the VECSEL cavity; a typical spectrum of the resulting VECSEL field is shown in Fig. 4.25. The VECSEL fundamental was found to operate in a weakly multimode regime, with one dominant longitudinal mode, two neighbouring modes of reduced intensity, and several additional modes close to the noise floor. The frequency spacing between each of the cavity modes was equal to integer multiples of $\sim$360 MHz, consistent with the FSR of the VECSEL cavity (365 MHz; see Fig. 4.9). The observed evolution of the multimode FPI spectrum is indicative of dynamical longitudinal mode behavior, which may arise from mode competition or occasional mode hopping within the cavity. These results confirm that, even with both fused-silica etalon filters introduced, the VECSEL fundamental field cannot maintain stable single-frequency operation above the SRO threshold.

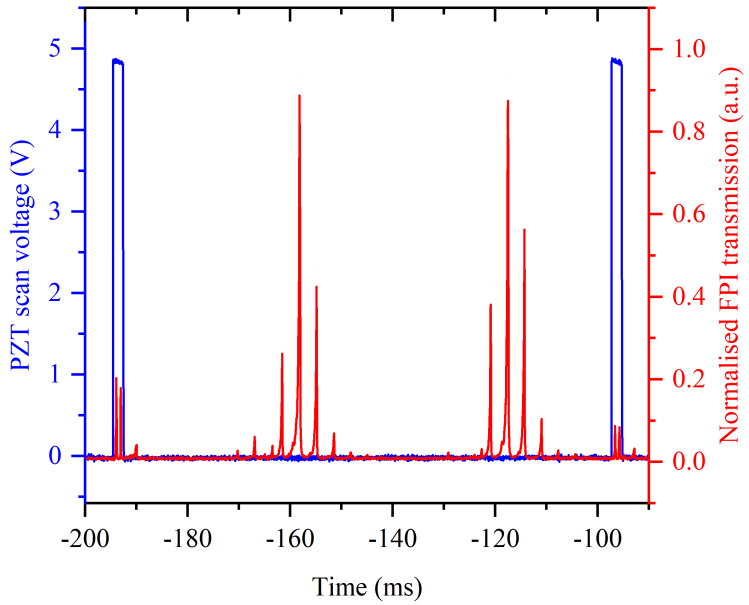


Figure 4.25: Normalised FPI transmission and reference cavity PZT scan voltage as a function of time for the VECSEL fundamental wavelength. The FSR and finesse of the visible FPI was 1 GHz and ~ 400, respectively. PZT: piezoelectric transducer; FPI: Fabry–Pérot interferometer.

Furthermore, because the 5%-MgO:PPLN crystal does not provide any mechanism for energy storage, spatial hole burning cannot occur within the SRO. Consequently, the resonant idler field naturally oscillates on a single longitudinal mode located at the peak of the phase matched gain bandwidth. To verify this behavior, the IR FPI was employed to analyse the frequency spectrum of the small fraction of idler light leaking from the cavity end mirror M_4. The resulting transmission trace, presented in Fig. 4.26, confirms that the idler field indeed operates on a single longitudinal mode.

To accurately determine the idler linewidth, the spectral width measured in the time domain on the oscilloscope must be converted to frequency units using a calibration factor. Using the oscilloscope traces of the FPI idler signal, the temporal separation between adjacent peaks was related to the known frequency interval via the following conversion factor:

$$\Delta f = \frac{\Delta\nu_{\mathrm{FSR}}^{\mathrm{FPI}}}{|t_1^{\mathrm{peak}} - t_2^{\mathrm{peak}}|}, \tag{4.21}$$

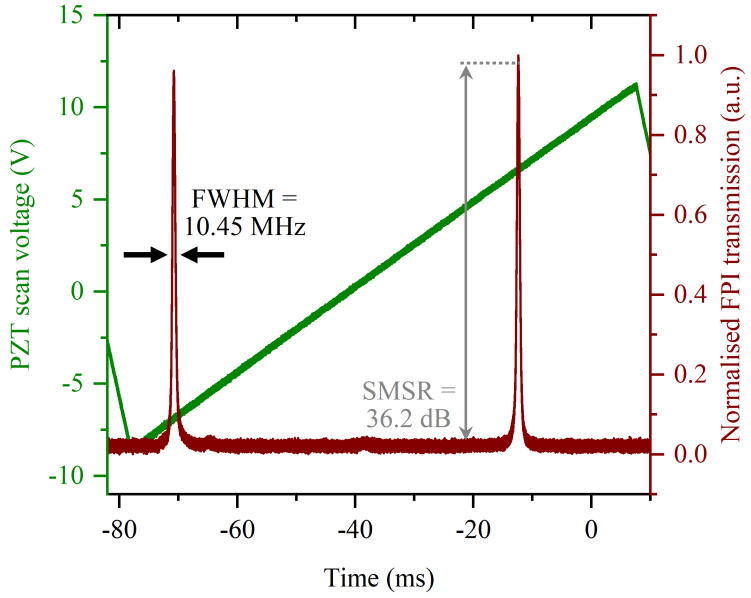


Figure 4.26: Normalised FPI transmission and reference cavity PZT scan voltage as a function of time for the resonant idler wavelength. The FSR and finesse of the IR FPI was 1.5 GHz and ~ 200, respectively. PZT: piezoelectric transducer; FPI: Fabry–Pérot interferometer; SMSR: side-mode suppression-ratio; FWHM: full-width at half-maximum. Figure adapted from Ref. [58].

where t_1^{peak} and t_2^{peak} denote the times at which consecutive resonance peaks occur on the oscilloscope, and $\Delta\nu_{\text{FSR}}^{\text{FPI}}$ is the FSR of the FPI in frequency units. Therefore, the spectral linewidth of the idler can be determined from the measured temporal width of the resonance peaks using the following relation:

$$\Delta\nu_{\text{FWHM}} = \Delta f \, \Delta t_{\text{FWHM}}, \tag{4.22}$$

where Δt_{FWHM} represents the FWHM of a resonance peak in the temporal domain, and Δf is the calibration factor defined in Eq. (4.21). Applying Eq. (4.22) with the IR FPI FSR of 1.5 GHz, the FWHM spectral linewidth of the idler wave was estimated to be 10.45 MHz (see Fig. 4.26).

Another important metric for verifying single longitudinal mode operation is the side-mode suppression-ratio (SMSR), which quantifies the relative strength of the main

oscillating mode compared to the largest side mode. For most practical applications, an SMSR exceeding 30 dB is generally regarded as sufficient to confirm that the laser is oscillating on a single-frequency mode. From the idler FPI transmission trace recorded on the oscilloscope (see Fig. 4.26), the SMSR was calculated using the following relation:

$$\mathrm{SMSR} = 10\log_{10}\left(\frac{P_{\mathrm{main}}}{P_{\mathrm{side}}}\right), \tag{4.23}$$

where P_{main} and P_{side} are the powers of the main resonance peak and the largest side-mode peak, respectively, as measured in voltage units on the oscilloscope. Applying Eq. (4.23) to the FPI oscilloscope measurements, the SMSR of the resonant idler wave was determined to be 36.2 dB. This confirms that the idler field oscillates predominantly on a single-frequency mode, with contributions from neighbouring modes being effectively negligible, as expected.

Although the multimode VECSEL spectrum lies within the OPO pump-acceptance bandwidth (see Fig. 4.10), achieving stable single-mode operation requires stronger intracavity spectral filtering. To this end, the 200 µm-thick fused-silica etalon in the SRO branch of the ICSRO cavity was replaced with a 1 mm-thick YAG etalon. The combination of the YAG material's higher refractive index and increased substrate thickness decreases the FWHM, resulting in a narrower transmission maxima. This effectively suppresses neighbouring longitudinal modes and improves the single-frequency stability of the VECSEL output, as schematically illustrated in Fig. 4.23.

Following optimisation of the alignment of both the 300 µm fused-silica and YAG etalons, the VECSEL emission spectrum was measured using the visible FPI. As shown in Fig. 4.27, the laser now operates predominantly on a single longitudinal mode. Analysis of the FPI traces using Eqs. (4.21) and (4.22) yields a FWHM VECSEL linewidth of 2.67 MHz, while the SMSR calculated from Eq. (4.23) is 38.7 dB. These results demonstrate that the initially multimode VECSEL emission is effectively suppressed, yielding stable single longitudinal mode operation through the insertion and fine-tuning of the YAG etalon.

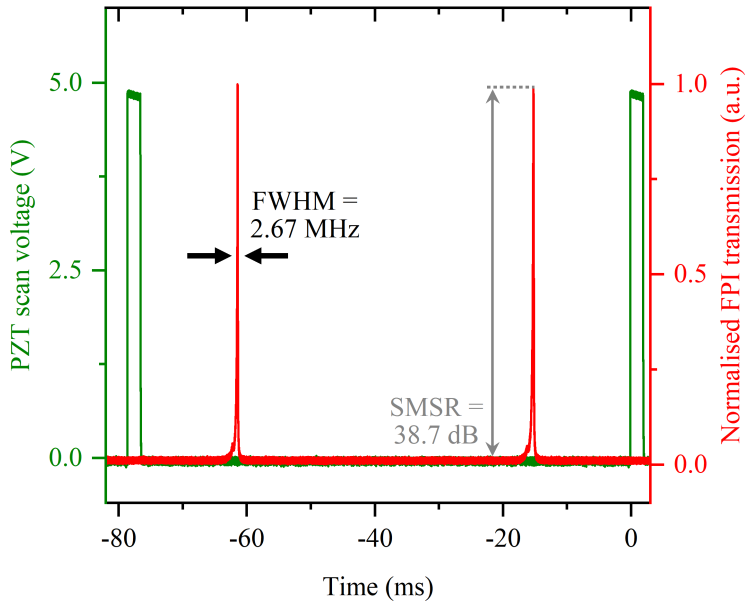


Figure 4.27: Normalised FPI transmission and reference cavity PZT scan voltage as a function of time for the VECSEL fundamental wavelength. The FSR and finesse of the visible FPI was 1 GHz and ~ 400, respectively. PZT: piezoelectric transducer; FPI: Fabry–Pérot interferometer; SMSR: side-mode suppression-ratio; FWHM: full-width at half-maximum. Figure adapted from Ref. [58].

In principle, the frequency bandwidth of the VECSEL fundamental is directly transferred to the non-resonant signal in the SRO, as the resonant idler field is constrained by the high-finesse cavity modes of the OPO resonator. Nevertheless, experimental verification is essential, as the linewidth of the non-resonant signal is a critical parameter for high-precision applications. A direct measurement of the signal linewidth was possible because the mirror coatings of the IR FPI provide sufficient transmission at both the signal wavelength ($\lambda_{\text{sig}} = 1245.2$ nm) and the idler wavelength ($\lambda_{\text{id}} = 1550.8$ nm). As shown in Fig. 4.28, the non-resonant signal exhibits stable single longitudinal mode operation, with a mode spacing of 1.5 GHz, consistent with the FSR of the IR FPI. Utilising Eqs. (4.21)–(4.23) to the measured FPI signal trace yielded a FWHM linewidth of 10.52 MHz and a SMSR of 35.4 dB. These results confirm that the non-resonant signal inherits the spectral purity of the VECSEL fundamental and, as expected, operates on a single longitudinal mode.

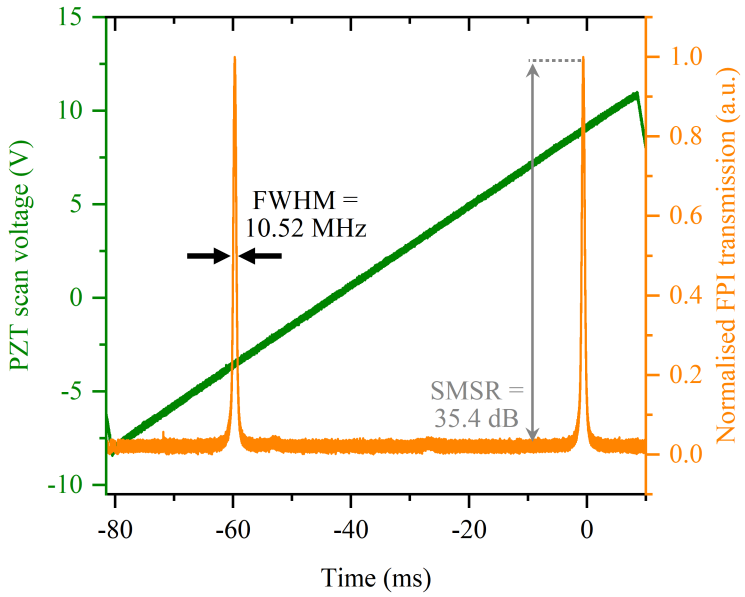


Figure 4.28: Normalised FPI transmission and reference cavity PZT scan voltage as a function of time for the non-resonant signal wavelength. The FSR and finesse of the IR FPI was 1.5 GHz and ~ 200, respectively. PZT: piezoelectric transducer; FPI: Fabry–Pérot interferometer; SMSR: side-mode suppression-ratio; FWHM: full-width at half-maximum. Figure adapted from Ref. [58].

It is important to emphasise that the measured linewidths of all three ICSRO interacting waves are constrained by the resolution limits of their respective FPIs (e.g., 2.5 MHz for the visible FPI and 7.5 MHz for the IR FPI). The critical result, however, is that each interacting wave exhibits single longitudinal mode operation. This is unequivocally confirmed by their high SMSR values, all exceeding 35 dB, which demonstrates robust suppression of adjacent cavity modes and verifies that each field oscillates on a single frequency mode. Building on previous studies of IR CW VECSEL-pumped OPOs [26], [27], [192], only the work by Hempler *et al.* [27] claims stable, single-frequency OPO operation. However, since the OPO spectra reported in their study are resolution-limited at 0.17 nm, it is reasonable to conclude that our work provides the first direct evidence of single-frequency operation within a VECSEL-pumped OPO system.

4.6.5 Passive power stability characteristics

The next stage of the investigation was to assess the duration over which single-frequency operation was maintained for in each of the ICSRO interacting waves. The most effective method for identifying mode-hopping events or the onset of multi-longitudinal-mode operation is through long-term power or frequency stability measurements. In this investigation, passive power stability measurements were performed for each ICSRO interacting wave at an input pump power of 2.69 W (see Fig. 4.29). As noted earlier, the incident pump power applied to the VECSEL chip was kept below the 2.96 W thermal rollover threshold. Operating at this reduced level limits the intracavity gain, thus minimising the impact of thermal and nonlinear effects. This attenuation of gain successfully prevents mode hopping and suppresses adjacent longitudinal mode competition, thereby enhancing the overall stability of the system. Measurements were conducted over a 500s timescale, as cavity length fluctuations induced by environmental noise, mechanical vibrations of the optical mounts, and thermal drift lead to mode hopping or temporary multimode operation over longer acquisition times.

The experimental configuration for the power stability measurements is detailed in the schematic shown in Fig. 4.24. The fundamental VECSEL output power was monitored using the same intracavity BRF reflection employed for coupling light into the visible FPI to measure the output spectrum. A combination of a half-wave plate (HWP) and polarizing beam splitter (PBS) directed the VECSEL beam such that it was simultaneously transmitted to the visible FPI for monitoring single-frequency operation and reflected towards a thermal power meter for assessing power stability. This configuration, as expected, yielded a higher average output power compared with the short-term stability measurements obtained from leakage through the HR mirror M_3 (see Fig. 4.21a). It should be noted that the BRF reflection samples only a small fraction of the total circulating intracavity power. Although this fraction is not directly proportional to the absolute intracavity power without explicit calibration, it still provides a stable and fixed coupling to the cavity field. Therefore, as the objective is not to determine the total intracavity power, the BRF reflection still serves as a reliable diagnostic for assessing the

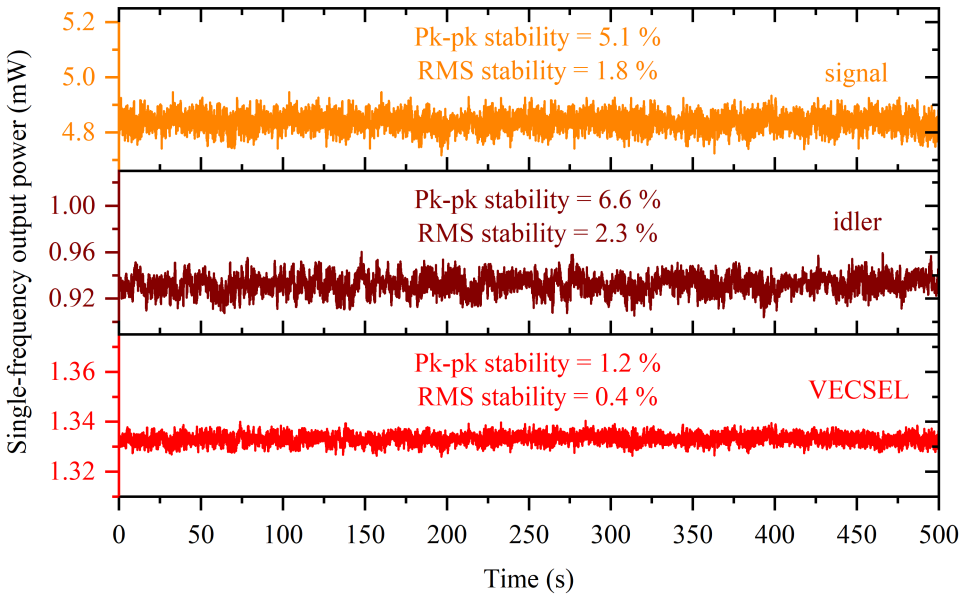


Figure 4.29: Single-frequency ICSRO passive power stability, measured over 500 s, at an input pump power of 2.69 W. The single-frequency output powers for the VECSEL fundamental, signal, and idler are measured via one of the quartz BRF reflections, and via leakage through cavity mirrors M_3 and M_4, respectively. Pk-pk: peak-to-peak, RMS: root-mean-square. Figure reproduced from Ref. [58].

passive power stability of the VECSEL field. On the other hand, the down-converted signal and idler powers were monitored via cavity mirrors M_3 and M_4, respectively.

Similarly, a HWP and PBS were incorporated into both the signal and idler beam paths, allowing simultaneous measurement of the transient behavior and long-term power stability of both beams. Excellent passive power stability was observed for all three interacting wavelengths, with RMS stabilities of 0.4%, 1.8%, and 2.3% measured for the VECSEL fundamental, signal, and idler, respectively (see Fig. 4.29). By referring to the passive power stability of the non-resonant signal field, this represents a near four-fold improvement in power stability compared to the multi-longitudinal-mode configuration (see Fig. 4.21b).

The passive power stabilities achieved in this ICSRO VECSEL system are comparable to those reported for single-frequency 1064 nm ytterbium (Yb) fibre-pumped CW-SRO systems [193], [194], and more than twice as stable as previously reported

solid-state-pumped CW-SRO systems [192], [195]. A key factor contributing to this enhanced stability is the RPG arrangement of the QWs embedded within the VECSEL active region, which allows the external cavity to be designed linearly, offering a simpler configuration while preserving the stability characteristics typically associated with ring resonators. Another significant advantage arises from the minimal thermal lensing effects inherent in the VECSEL, which is significantly lower than what you would expect to find in solid-state lasers. This reduction is attributed to the semiconductor disk architecture of the VECSEL gain medium, combined with advanced thermal management techniques. These factors synergistically minimise thermal distortions in the optical path length, ensuring that beam profile changes and distortions remain negligible.

4.7 Conclusion

In conclusion, we report the first demonstration of an intracavity OPO pumped by an AlGaInP-based VECSEL. Operating at a fundamental wavelength of 690.6 nm, the CW VECSEL pump source generated non-degenerate PDC emission at 1245.2 nm and 1550.8 nm for the non-resonant signal and resonant idler waves, respectively. Intracavity spectral filtering, implemented using a combination of a quartz BRF and fused-silica etalon filters, enabled resolution-limited VECSEL operation with a linewidth of 73 pm; well within the ICSRO pump-acceptance bandwidth of 126 pm. By selecting an appropriate 5%-MgO:PPLN poling period ($\Lambda_{\mathrm{QPM}} = 14.55$ µm), both signal and idler wavelengths were maintained within the bandwidth of the high-reflectivity dielectric coatings of the cavity mirrors, allowing continuous SRO tuning from 1155 nm to 1718 nm via adjustment of the 5%-MgO:PPLN crystal temperature between 90°C–180°C. The measured tuning characteristics are in excellent agreement with the Sellmeier equation outlined by Gayer *et al.* [88].

The HR-idler regime was the first ICSRO VECSEL configuration to be experimentally engineered and optimised. In this regime, the VECSEL and SRO thresholds were reached at external input pump powers of 0.99 W and 1.78 W, respectively. In the

absence of an idler output coupler, and at the maximum external input pump power of 2.96 W (before the onset of thermal rollover), a total down-converted power of 53.3 mW was achieved, corresponding to a total down-conversion efficiency of 72.1%. Subsequently, the HR end mirror M_4 was replaced with a partially transmitting output coupler ($T_{OC} = 1.7\%$), while folding mirror M_3 was replaced with an alternative substrate to allow the signal and idler to escape the SRO through separate cavity mirrors, thereby creating the OC-idler regime. Under these conditions, and by pumping the VECSEL on a different spot on the gain chip, a total down-converted power of 51.9 mW was measured at 2.96 W of input pump power, corresponding to an estimated total down-conversion efficiency of 70.2%. Of this total, 28.8 mW consisted of non-resonant signal power at 1245.2 nm, while 23.1 mW consisted of resonant idler power at 1550.8 nm.

The passive power stability of the ICSRO was characterised for both multimode and single-frequency VECSEL operation. In the multimode regime, the VECSEL exhibited excellent short-term amplitude stability both with and without down-conversion. Unlike conventional solid-state media, the VECSELs Class-A dynamics suppress relaxation oscillations, preventing the transfer of excess intensity noise to the signal and idler fields – a critical advantage for high-precision applications. To achieve single-frequency operation, the 200 µm-thick fused-silica etalon was replaced with a 1 mm-thick YAG etalon, yielding MHz-level linewidths and SMSRs exceeding 35 dB for all three ICSRO interacting waves. Over a 500s timescale, RMS stabilities of 0.4%, 1.8%, and 2.3% were recorded for the VECSEL fundamental, signal, and idler, respectively. This represents a near four-fold enhancement in passive stability compared to the multimode regime, providing a robust foundation for future active stabilisation schemes.

It should be noted that the ICSRO results presented here were obtained using an open tabletop system and, therefore, further improvements to the laser operation, in terms of stability and efficiency, are expected to be achieved by, for example, passive and active stabilisation techniques. Passive stabilisation techniques include enclosing the ICSRO in a sealed box to attenuate environmental noise, while operating the system at a reduced beam height could help to minimise mechanical fluctuations. Additionally,

mirror substrates can be glued directly to their respective mounts; this approach further reduces mechanical instabilities compared to conventional kinematic mounting. Further, active stabilisation techniques may involve temperature control of intracavity elements, such as the BRF and etalon filters, as well as thermo-electric cooling of the VECSEL gain region. These approaches are expected to significantly reduce thermal noise and improve long-term power and frequency stability, potentially over several hours or more.

Further optimisation of the single-frequency ICSRO VECSEL system is required, particularly through the implementation of active stabilisation schemes, to suppress intensity and quantum phase noise transferred to the signal and idler modes while simultaneously enhancing the overall system efficiency. In particular, active frequency locking of both the VECSEL fundamental and resonant idler to their respective cavities represents a significant step towards achieving this goal and constitutes the central focus of Chapter 5.

Chapter 5

Sub-kHz linewidth intracavity VECSEL-pumped OPO

5.1 Introduction

The work presented in this chapter has been published in the peer-reviewed journal APL Photonics under Ref. [59]. In this publication, the candidate was the lead contributor to the research, responsible for experimental design, implementation, data acquisition, analysis, software development, validation, visualisation, and preparation of the original manuscript. Co-authors contributed in supporting and supervisory roles, as detailed in the *Thesis Overview* section of Chapter 1.

In this chapter, we outline the techniques that were implemented to develop the single-frequency ICSRO VECSEL system of Chapter 4, demonstrating sub-kHz (sub-10 kHz) linewidth operation of the resonant idler (VECSEL fundamental and non-resonant signal), accompanied by substantial reductions in relative intensity noise (RIN) across all three ICSRO interacting wavelengths. The superior low-noise performance, both in terms of intensity and frequency, is obtained through the implementation of two separate frequency stabilisation schemes. The first scheme, where the widely-used Pound–Drever–Hall (PDH) technique is employed, permits locking of the VECSEL cavity to a

moderately-high-finesse confocal Fabry–Pérot (FP) reference cavity. The second scheme applies side-of-fringe (SOF) locking to the optical parametric oscillator (OPO) resonant idler cavity, for locking to an alternative FP reference cavity. For each interacting wave, and with both stabilisation loops switched on, RIN reductions of more than 20 dB were achieved at low Fourier frequencies compared to the free-running regime.

This chapter begins with an overview of the main noise mechanisms and coherence properties in laser systems, establishing the theoretical foundation for what follows. Building on this framework, it then examines the noise model proposed by Myara *et al.* [45], with particular focus on its applicability to vertical-external-cavity surface-emitting lasers (VECSELs). The discussion next addresses active frequency stabilisation techniques, specifically the Pound–Drever–Hall (PDH) method, including a detailed theoretical derivation of the associated error signal. The core of this chapter is devoted to the investigation of the noise dynamics of the intracavity singly-resonant optical parametric oscillator (ICSRO) VECSEL system. In this context, we provide a comprehensive characterisation of the RIN, frequency noise, and integrated linewidths associated with the VECSEL fundamental, signal, and idler fields. Finally, we compare these results to existing literature, demonstrating that our system matches the performance of the most stable externally-pumped OPOs while maintaining its inherent immunity to relaxation oscillations.

5.2 Noise and coherence properties of lasers

Like other optical instruments, lasers are subject to various types and sources of noise. A significant proportion of these disturbances can be mitigated through careful laser design and the judicious selection of materials. Broadly, noise in laser systems falls into two main categories: quantum noise and technical noise. Quantum noise arises primarily from the spontaneous emission of photons within the gain medium of the laser. In contrast, technical noise stems from imperfections and fluctuations associated with the

laser's physical construction and components, such as mirror vibrations, pump source instability, and other mechanical or electronic disturbances [196].

Fundamentally, laser noise originates from the spontaneous emission that is superimposed on the coherent stimulated emission field. Owing to its intrinsically random phase, the spontaneous emission can be represented as a phasor with uniformly distributed phase states. Therefore, the resulting optical field – comprising both stimulated and spontaneous components – exhibits temporal fluctuations in amplitude and phase, giving rise to intensity and phase noise, respectively. Temporal variations of the optical phase directly translate into frequency fluctuations through the relation:

$$\nu = \frac{1}{2\pi} \frac{d\phi(t)}{dt}. \tag{5.1}$$

For a single-frequency laser, spontaneous emission is partially filtered by the cold-cavity FP resonance that defines the oscillating laser mode. The effectiveness of this filtering process plays a central role in determining the laser's fundamental noise characteristics. For example, low-fundamental-noise operation requires FP modes with narrow cold-cavity linewidths, corresponding to long cavity photon lifetimes. Such conditions may be achieved by increasing the cavity length and/or enhancing the cavity finesse through minimisation of intracavity losses. Consequently, irrespective of the specific laser architecture, the design of compact, low-noise laser sources critically depends on achieving a high cavity Q-factor.

The preceding analysis establishes that laser noise arises from the fundamental interplay between spontaneous emission and the resonant filtering of the optical cavity. The resulting amplitude, phase, and frequency fluctuations dictate the ultimate coherence and temporal stability of the emitted field. While these stochastic processes are intrinsic to all laser oscillators, their relative magnitudes are highly sensitive to the cavity architecture, the intracavity photon lifetime, and the system's susceptibility to external perturbations. Optically-pumped external-cavity lasers (OP-ECLs) – of which VECSELs are a prominent subclass – represent a significant case study in this regard.

Their macroscopic resonators facilitate extended photon lifetimes for narrow-linewidth operation; however, this increased cavity length inherently heightens the system's sensitivity to pump-induced fluctuations, mechanical instabilities, and thermal gradients. The following subsections are therefore dedicated to a rigorous examination of the noise dynamics inherent to OP-ECL architectures.

5.2.1 Schawlow-Townes-Henry (STH) linewidth

A key consequence of phase noise in lasers is its direct role in producing a finite spectral linewidth. Although lasers are often described as 'single-frequency' sources, all such lasers exhibit a non-zero linewidth; a fundamental limitation arising from intrinsic phase fluctuations. Notably, this limitation remains even for an ideal laser, where all technical noise sources have been completely eliminated through optimised design and engineering. In this idealised scenario, the residual linewidth is caused solely by quantum phase noise, setting an irreducible limit on the spectral purity of the laser. This intrinsic contribution to the laser linewidth is quantitatively described by the Schawlow-Townes-Henry (STH) formula, which accounts for phase perturbations induced by spontaneous emission within the laser cavity [45], [197]:

$$\Delta\nu_{\mathrm{STH}} = \frac{\pi h\nu}{P_{\mathrm{out}}}\,\Delta\nu_{\mathrm{cold}}^{2}\,\xi_{\mathrm{sp}}\,(1+\alpha_{\mathrm{H}}^{2}). \tag{5.2}$$

In the STH framework (see Eq. 5.2), the parameter $\Delta\nu_{\mathrm{STH}}$ represents the fundamental quantum-limited linewidth of the laser. Here, h is Planck's constant, ν is the optical frequency of the single-mode oscillating within the laser cavity, and P_{out} is the output power of this mode. The term $\Delta\nu_{\mathrm{cold}}$ denotes the cold-cavity linewidth, characterising the cavity's intrinsic losses in the absence of gain. The factor ξ_{sp} accounts for the contribution of spontaneous emission into the laser mode, while α_{H}, known as the Henry factor, describes amplitude-to-phase coupling in the semiconductor gain medium. Finally, the term $(1+\alpha_{\mathrm{H}}^{2})$, referred to as the linewidth enhancement factor, captures the effect of this coupling on the phase noise.

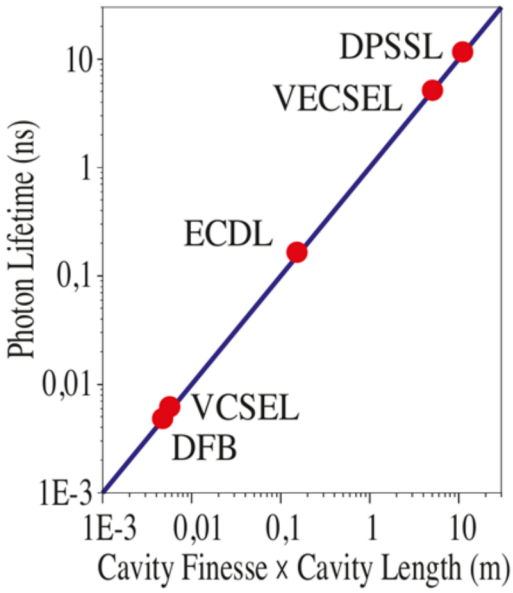


Figure 5.1: Photon lifetime for various laser technologies, including 1 cm VECSEL, 1 cm external-cavity diode laser (ECDL), 1 m Ti:Sapphire diode-pumped solid-state laser (DPSSL), 300 µm distributed feedback (DFB) laser, and microcavity VCSEL. Figure reproduced from Ref. [45].

According to Eq. (5.2), the STH linewidth can be minimised by either increasing the single-mode output power, reducing the cold-cavity linewidth, or by decreasing the linewidth enhancement factor. For example, a typical distributed feedback (DFB) laser exhibits a Schawlow–Townes-Henry (STH) linewidth on the order of MHz, whereas VECSELs achieve linewidths down to the millihertz level, while DPSSLs can reach even lower values, extending into the sub-millihertz range (see Table 5.1) [45]. As shown in Fig. 5.1, this enhanced performance arises from the intrinsically higher cavity finesse, extended external-cavity geometry, and correspondingly longer photon lifetimes than short-cavity DFB lasers.

5.2.2 Intensity noise: Class-A dynamics

The temporal dynamics of a laser system are fundamentally governed by the relationship between the gain medium's upper-state (carrier) lifetime τ_u, and the cavity photon lifetime τ_c. A long photon lifetime naturally imposes slow damping dynamics within

the resonator. Consequently, the laser intensity acts as a low-pass filter, tracking only low-frequency variations and effectively suppressing spontaneous-emission noise beyond a characteristic cutoff frequency. Above this frequency, intensity fluctuations are increasingly attenuated, and the noise rolls off towards the shot-noise-limit. In external-cavity systems such as DPSSLs and VECSELs, this limit is reached at significantly lower Fourier frequencies than in short-cavity devices such as DFB lasers (see Table 5.1).

However, this noise-suppressed regime is only accessible when the cavity dynamics dominate the overall system response. This requires the gain medium to respond quasi-instantaneously to fluctuations in the intracavity photon flux. Most conventional solid-state gain media possess long carrier lifetimes – typically on the order of milliseconds – which introduce slow intrinsic dynamics that interact with the cavity response. This coupling gives rise to the resonant behavior characteristic of Class-B lasers, which amplify spontaneous-emission noise via relaxation oscillations. In contrast, semiconductor gain media exhibit upper-state carrier lifetimes on the order of a few nanoseconds. In VECSEL systems, this lifetime is significantly shorter than the cavity photon lifetime, placing the laser firmly in the Class-A regime. As established in Chapter 3, Class-A VECSELs enable relaxation-oscillation-free operation, even when driven above the SRO threshold.

The external-cavity architecture of VECSELs provides a versatile platform for investigating these dynamical transitions, as it allows precise control over the τ_c/τ_u ratio. This was demonstrated experimentally by Baili *et al.* [198], who observed the transition from Class-B to Class-A behavior by tuning the cavity photon lifetime via adjustment of the cavity length. By adjusting τ_c relative to τ_u, they accessed both regimes: relaxation oscillation peaks near 100 MHz were observed when $\tau_u > \tau_c$, and disappeared when $\tau_u < \tau_c$, confirming the transition. These results highlight that VECSELs, owing to their fast carrier dynamics and external cavity design, can operate deeply within the Class-A regime and suppress the relaxation oscillations inherent to conventional Class-B DPSSLs and DFB lasers (see Table 5.1).

5.2.3 Photon and electron shot-noise

Photon shot noise originates from the discrete and inherently stochastic nature of photon-number fluctuations within an optical field; it is therefore an intrinsic property of the field itself, independent of the downstream detection mechanism. For a coherent optical field, such as that produced by an ideal free-running laser, the photon-number statistics follow a Poisson distribution. The probability $P_n(T)$ of finding n photons within a temporal interval T is given by:

$$P_n(T) = \frac{\bar{n}}{n!}\, e^{-\bar{n}}, \tag{5.3}$$

where $\bar{n}$ is the mean photon number within the measurement interval. For a Poisson distribution, the variance of the photon number is equal to the mean, $\mathrm{Var}(n) = \bar{n}$, indicating that the photon number exhibits intrinsic statistical fluctuations about its mean value. These fluctuations constitute an intrinsic noise source of the optical field and exist prior to detection.

Upon detection, the discrete nature of the photoelectric process gives rise to a corresponding fluctuation in the photocurrent, commonly referred to as detector shot noise or electron shot noise. For a photodetector operating under steady illumination, the one-sided power spectral density (PSD) of these current fluctuations is described by Schottky's formula [199]:

$$S_{\mathrm{SN}}(f) = 2eI_{\mathrm{DC}}, \tag{5.4}$$

where e is the elementary charge and I_{DC} is the time-averaged photocurrent. This detector shot noise arises from the discrete arrival of photoelectrons and is therefore distinct from the intrinsic photon-number fluctuations of the incident optical field. The photodetector converts fluctuations in the optical field into fluctuations in the measured photocurrent, while the detection process itself introduces an additional shot-noise contribution.

5.2.4 Relative intensity noise (RIN)

Relative intensity noise (RIN) quantifies fluctuations in a laser's optical output and is defined as the PSD of intensity variations normalised to the square of the mean optical power. This normalisation enables direct comparison between sources with different output powers and provides a consistent frequency-domain description of noise. In practice, the measured intensity noise comprises both intrinsic laser fluctuations and contributions from the photodetection process. Shot noise, which is spectrally white, sets the fundamental noise floor and is typically accounted for in measurements. RIN captures the total intensity noise in a single metric without distinguishing between individual noise sources. This provides a consistent basis for comparing the overall stability of different lasers across varying operating conditions. When the optical power is converted into an electrical current by a photodetector, the RIN of the laser can be expressed as:

$$\mathrm{RIN}(f) = \frac{S_I(f) - S_{\mathrm{SN}}(f)}{I_{\mathrm{DC}}^2} \ \mathrm{Hz}^{-1}. \tag{5.5}$$

Here, $S_I(f)$ denotes the total current PSD measured during the experiment, while $S_{\mathrm{SN}}(f)$ is the PSD of the shot-noise current, and I_{DC} is the average (DC) photocurrent. In practice, RIN is often expressed in units of dBc/Hz, providing a logarithmic measure of noise power density relative to the carrier, which facilitates straightforward comparison between different systems. The conversion to these units is given by:

$$\mathrm{RIN}\,[\mathrm{dBc/Hz}] = 10\log_{10}\left(\mathrm{RIN}(f) \ \ [\mathrm{Hz}^{-1}]\right). \tag{5.6}$$

5.2.5 Phase noise

Phase noise refers to short-term fluctuations in the phase or frequency stability of a laser. Its fundamental origin lies in quantum noise resulting from spontaneous emission within the gain medium. While stimulated emission generates photons that are coherent in phase and polarization with the existing laser field, spontaneous emission produces photons with random phase and polarization, thereby perturbing the phase stability of

the laser. Moreover, intensity fluctuations caused either by spontaneous emission or by technical sources such as pump injection can also induce phase shifts in the laser output, effectively coupling intensity noise into phase noise via the linewidth enhancement factor [197]. Dynamically, this coupling occurs because the laser's phase is highly sensitive to even small changes in the amplitude of the light inside the cavity. As first explained by Henry [197], intensity fluctuations induce transient changes in the carrier density within the active region. Since the refractive index depends on the carrier density, these perturbations translate directly into phase fluctuations, thereby converting amplitude noise into phase noise. This effect is more pronounced in semiconductor lasers, where the linewidth enhancement factor is significantly larger than in conventional solid-state gain media [200].

Experimentally, phase noise is commonly quantified using the phase noise PSD $S_\phi(f)$. To provide additional insight, the frequency noise PSD $S_\nu(f)$, is also frequently used. These two quantities are directly related by [201]:

$$S_\nu(f) = f^2 S_\phi(f), \tag{5.7}$$

where f is the noise (Fourier) frequency. This relationship reflects the fact that phase noise and frequency noise originate from the same underlying physical process. Phase noise characterises fluctuations in the phase of the optical field, whereas frequency noise corresponds to the time derivative of these phase fluctuations:

$$\phi(t) = 2\pi \int \nu(t)\, dt, \tag{5.8a}$$

$$\nu(t) = \frac{1}{2\pi} \frac{d\phi(t)}{dt}. \tag{5.8b}$$

Here, $\phi(t)$ denotes the instantaneous optical phase in radians and $\nu(t)$ denotes the instantaneous optical frequency in Hz.

Measuring laser phase noise is fundamentally more complex than measuring intensity noise, as it requires a reference signal with lower phase noise than the laser under test. In

principle, if a second laser with sufficiently low phase noise and nearly identical frequency is available, the outputs of both lasers can be mixed to produce a low-frequency beat note, from which the phase noise of the laser of interest can be extracted [202]. However, this approach is often impractical due to the difficulty of obtaining such a reference laser.

To overcome this limitation, the self-heterodyne technique is widely employed. This method enables phase noise characterisation using a single laser source by introducing a controlled delay line and frequency shift along the same optical path, allowing the phase noise information to be extracted from the resulting interference signal. The primary limitation of this technique is the requirement for a long optical fibre delay line, which can be both costly and experimentally cumbersome.

In this investigation, the coherence and frequency stability of the ICSRO VECSEL system were evaluated using the frequency noise PSD, rather than by performing direct phase noise measurements. This choice was motivated by two practical constraints: firstly, the self-heterodyne delay line required for the VECSEL would have been impractically long and, secondly, an additional laser with the necessary spectral purity and stability was unavailable. Despite these limitations, the frequency noise PSD still provides several advantages: for instance, it offers a quantitative, indirect measure of the laser's phase noise characteristics, as well as enabling a precise estimation of the laser linewidth via numerical integration techniques.

To summarise, the fundamental noise components of VECSELs remain exceptionally low compared with other laser technologies, as illustrated in Table 5.1. In practical devices, however, these intrinsic limits associated with VECSELs are still inevitably obscured by additional noise sources arising from technical constraints, including pump intensity fluctuations, thermal effects, mechanical vibrations, and environmental disturbances. These considerations motivate the following section, in which the theoretical VECSEL noise model developed by Myara *et al.* [45] is examined. This model provides a foundational framework for understanding how technical noise contributions influence the overall noise performance of practical VECSEL systems.

Table 5.1: Comparative analysis of the dynamical classification and fundamental noise limits for VECSEL, DPSSL, and DFB architectures. $\Delta\nu_{\mathrm{STH}}$: Shawlow-Townes-Henry linewidth; f_c^{laser}: laser cavity cutoff frequency.

Laser Type	**Dynamic Class**	$\boldsymbol{\Delta\nu_{\mathrm{STH}}}$	$\boldsymbol{f_c^{\mathrm{laser}}}$
VECSEL	Class-A	∼mHz	∼MHz
DPSSL	Class-B	<mHz	∼MHz
DFB	Class-B	∼MHz	∼GHz

5.3 Noise properties of VECSELs: Myara model

A comprehensive theoretical model describing the noise dynamics of optically pumped VECSEL devices was developed in 2013 by Mikhaël Myara and colleagues at the Institute of Electronics and Systems, University of Montpellier [45]. This model considers a VECSEL operating in a single longitudinal mode and incorporates the effects of pump intensity noise, thermal noise, and mechanical noise. Although the model is based on a GaAs (or GaSb) VECSEL gain structure, the fundamental concepts are directly applicable to the AlGaInP-based VECSEL gain medium used in this investigation. For the purposes of this thesis, we focus exclusively on the intensity and frequency noise properties as predicted by theoretical simulations. The derivation of the underlying VECSEL noise model is not presented here; readers interested in the complete theoretical treatment are referred to Ref. [45].

Figure 5.2 presents a numerical analysis of an optically-pumped VECSEL subjected to a single-mode pump-noise excitation. From the intensity noise model, it is clear that the VECSEL cavity acts as a low-pass filter for intensity noise (see Fig. 5.2a): both the pump-induced fluctuations and the spontaneous emission contribution roll off above the cavity cut-off frequency, f_c^{laser}. In the medium-to-high frequency range – for example, beyond ∼20 MHz in Fig. 5.2a – the VECSEL intensity noise approaches the shot-noise limit. Experimentally, this behaviour has been confirmed in both optically-pumped [203] and electrically-pumped [204] VECSEL systems, where shot-noise-limited operation is observed above 10 MHz and 2 MHz, respectively.

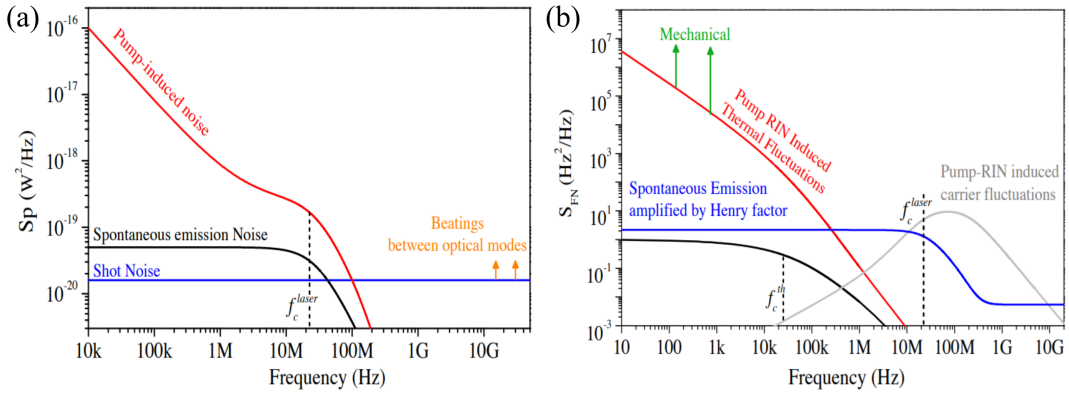


Figure 5.2: Numerical simulations of the noise model of an optically-pumped VECSEL, showing **(a)** intensity noise and **(b)** frequency noise, as reported by Myara *et al.* [45]. Here, f_c^{laser} denotes the cavity cutoff frequency, and f_c^{th} denotes the thermal cutoff frequency. Figure reproduced from Ref. [45] for illustrative purposes.

At very high frequencies (e.g., above 10 GHz), Fig. 5.2a also reveals beat notes arising from residual side modes of the laser. These features can be eliminated through improved cavity engineering that enhances the side-mode suppression ratio (SMSR), thereby ensuring stable single-frequency operation. Conversely, at low frequencies, i.e., within the VECSELs dynamical bandwidth, the intensity noise is dominated by the RIN of the external pump laser.

For the frequency-noise spectrum, the dominant contributions, as expected, originate from technical noise sources such as thermally induced pump fluctuations and mechanical vibrations, whereas the fundamental noise mechanisms are found to be almost negligible (see Fig. 5.2b). Therefore, reducing frequency noise in a VECSEL requires suppressing both mechanical and thermal fluctuations, as well as minimising pump-induced noise. Mechanical noise can be mitigated through appropriate cavity design and engineering. For example, vibration sensitivity can be reduced by minimising the beam height relative to the optical table and rigidly gluing mirror substrates to their respective mounts, rather than using standard laboratory kinematic mounts. In contrast, thermal noise can be reduced by implementing thermo-electric cooling of the VECSEL gain structure, instead of relying solely on conventional water-cooling via a chiller system. Suppress-

ing pump-induced noise is more challenging, particularly when the pump source is a sealed commercial laser with limited access to internal control parameters. Nevertheless, a promising route toward reducing pump-intensity fluctuations is the adoption of electrical pumping. However, the numerous advantages of optical pumping, as explained in Chapter 3, currently outweigh the potential benefits of electrical injection at most wavelengths. For this reason, electrical pumping is not considered beyond this point in the investigation.

Building on the theoretical understanding of noise dynamics in VECSELs, we now consider strategies for actively suppressing both intensity and frequency fluctuations in these lasers. Among the most widely implemented techniques is active stabilisation, which can significantly improve spectral purity and long-term stability. This is particularly true for VECSELs, where only low-frequency noise components – i.e., those below the cavity cutoff frequency – are relevant and can be effectively mitigated using standard electronic noise suppression techniques, as they lie within the operational bandwidth of typical control electronics. The following section therefore focuses on the two stabilisation schemes applied in this work – Pound–Drever–Hall (PDH) and side-of-fringe (SOF) stabilisation – highlighting how each method contributes to reducing noise and enhancing the overall performance of the ICSRO VECSEL system.

5.4 Frequency stabilisation

A variety of passive and active techniques have been developed to mitigate noise in laser systems. Passive methods focus on enhancing mechanical and thermal stability while minimising the fundamental STH linewidth ($\Delta\nu_{\mathrm{STH}}$; see Eq. 5.2). Specifically, this linewidth reduction can be achieved by increasing the cavity photon lifetime through appropriate cavity design, including the choice of cavity length and mirror losses. VECSELs require highly reflective dielectric coatings to reach threshold due to their relatively low gain, which inherently creates a high-finesse cavity. This configuration narrows the cold-cavity linewidth and, when paired with high single-mode output power and a very

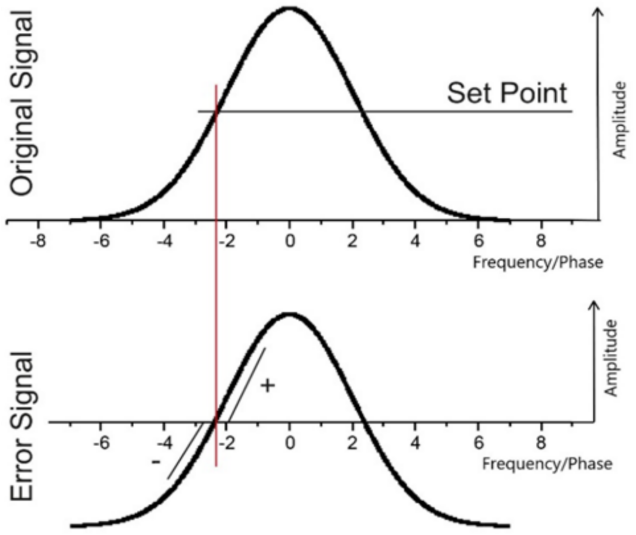


Figure 5.3: Schematic of side-of-fringe (SOF) laser stabilisation. Figure reproduced from Ref. [205].

low spontaneous emission factor, allows the fundamental STH limit to reach the millihertz regime.

Despite this low fundamental limit, the focus of this chapter remains on active stabilisation. These techniques are necessary to suppress the technical noise inherent to the open-cavity of the ICSRO VECSEL system and to ensure long-term spectral and temporal stability. Active stabilisation works by monitoring laser frequency fluctuations and applying feedback to correct them. A highly effective way to reduce linewidth – and overall noise – is to lock the laser to a stable frequency reference, such as an optical cavity or an atomic transition. The performance of this method is ultimately limited by the stability of the reference and the speed of the feedback system. In this work, commercial Fabry–Pérot interferometers (FPIs) are used as the frequency discriminators to provide this stable reference.

One of the simplest active stabilisation methods, and the approach used in this work to stabilise the OPO idler cavity, is side-of-fringe (SOF) locking. This method converts frequency fluctuations into intensity variations by operating the laser on the linear slope of a reference cavity resonance (see Fig. 5.3). While conceptually straightforward, SOF

locking has several inherent limitations. Specifically, laser amplitude noise couples directly into the error signal, making it impossible for the feedback loop to distinguish between frequency fluctuations and power variations. Additionally, the finite response time of the reference cavity limits the bandwidth over which frequency noise can be accurately detected. Finally, SOF locking offers a narrow capture range, as modest frequency drifts can move the operating point away from the linear slope, leading to a loss of lock.

The SOF locking technique is only briefly discussed here, as it is well established in the literature. In contrast, the PDH method, which is used in this work to stabilise the VECSEL fundamental cavity, relies on more complex phase-modulation dynamics. For this reason, a more detailed theoretical derivation of the PDH error signal, together with its practical implementation, is presented in the following section to provide a detailed overview of the operating principle and performance of the technique.

5.5 Pound-Drever-Hall (PDH) stabilisation: theory and implementation

The Pound–Drever–Hall (PDH) stabilisation scheme, originally introduced by Pound [206] and subsequently developed by Drever *et al.* [207], provides an intuitively simple yet highly effective method for laser frequency stabilisation. Frequency measurements are performed using a phase-sensitive detection scheme, often referred to as nulled lock-in detection. A major advantage of PDH locking is that it decouples frequency noise from intensity noise, thus having the ability to achieve frequency discrimination that is largely immune from amplitude fluctuations. Furthermore, the PDH technique circumvents the bandwidth limitations imposed by the cavity's transmission response time. Because the technique evaluates the coherent interference between the reflected carrier and sidebands, the resulting error signal tracks the instantaneous phase response of the cavity under detuning, thereby offering a capture bandwidth far exceeding the cavity's physical linewidth. In practice, the achievable feedback bandwidth is determined primarily by the

response of the detection and servo electronics, actuator dynamics, propagation delays, and the frequency-dependent response of the cavity reflection. A detailed theoretical explanation of the PDH method, including how the error signal is generated, is provided by Black [208].

Experimentally, the laser phase is modulated using an electro-optic modulator (EOM) driven by a local oscillator (LO) signal, typically a simple sine wave, before the light is directed into the reference cavity. The reflected beam from the reference cavity is extracted by a combination of a polarizing beam splitter (PBS) and a quarter-wave plate (QWP), which directs the reflected light onto a photodetector. The photodetector output is then compared with the LO signal using a frequency mixer. Conceptually, a mixer produces an output corresponding to the product of its input signals, generating components at both DC (or low frequency), and at twice the modulation frequency. The low-frequency component is of interest, as it encodes information about the dispersive phase shift of the reflected carrier relative to the sidebands, and therefore carries the detuning information required to form the PDH error signal. This component is isolated using a low-pass filter and subsequently fed through a servo controller and a high-voltage amplifier (HVA). For this investigation, the output of the HVA is applied to a piezoelectric transducer (PZT) mounted on the first folding mirror M_2. This allows for precise control over the mirror position and the total cavity length. By adjusting this mirror, the cavity resonance is therefore tuned and used as a reference to lock the laser frequency to the FP resonance.

Having established the basic principles of the PDH technique, the PDH error signal is now considered. The following subsection presents a theoretical derivation of this error signal, highlighting its antisymmetric shape around the cavity resonance, which is central to its use in precision frequency stabilisation.

5.5.1 PDH error signal

To produce an error signal that is antisymmetric with respect to the cavity resonance frequency, phase modulation is applied to the laser beam. An EOM is used to phase-

modulate the laser output, generating optical sidebands that provide the frequency reference for the derivation of the error signal. The EOM operates analogously to a variable waveplate, comprising a crystal whose refractive index varies linearly with an applied electric field. Applying a time-varying voltage thus induces a small, rapidly adjustable phase shift in the transmitted light. Considering a sinusoidal phase modulation with frequency Ω and modulation depth β, the electric field of the CW laser after passing through the EOM can be expressed using Bessel functions [208]:

$$\begin{aligned} E_{\text{inc}} &= E_0\, e^{i(\omega_e t + \beta \sin(\Omega t))} \approx E_0 \left[J_0(\beta) + 2iJ_1(\beta)\sin(\Omega t)\right] e^{i\omega_e t} \\ &= E_0\Big[J_0(\beta)e^{i\omega_e t} + J_1(\beta)e^{i(\omega_e+\Omega)t} - J_1(\beta)e^{i(\omega_e-\Omega)t}\Big]. \end{aligned} \tag{5.9}$$

Here, J_0 and J_1 denote the zeroth- and first-order Bessel functions, respectively. The final form of Eq. (5.9) demonstrates that the phase modulation introduced by the EOM generates an incident optical field comprising three distinct frequency components: the carrier at frequency ω_e and two sidebands at $\omega_e \pm \Omega$.

If $P_0 \equiv |E_0|^2$ represents the total power of the incident beam, then for low modulation depths ($\beta < 1$), most of the optical power resides in the carrier and the first-order sidebands. In this regime, the power distribution can be approximated as $P_c^{\text{PDH}} + 2P_s^{\text{PDH}} \approx P_0$, where P_c^{PDH} and P_s^{PDH} correspond to the powers in the carrier and each of the first-order sidebands, respectively. This approximation reflects the negligible contribution of higher-order sidebands at small modulation depths.

To determine the total reflected field when multiple frequency components are incident on a Fabry-Pérot (FP) cavity, each component can be treated independently as a monochromatic plane wave and multiplied by the complex cavity reflection coefficient, $F(\omega_e)$, evaluated at its respective frequency. In the PDH architecture, the incident laser field undergoes phase modulation, resulting in a spectrum that consists of a central carrier and two first-order sidebands. The total reflected electric field E_{ref} is obtained by the coherent summation of these individual spectral components:

$$E_{\text{ref}} = E_0\Big[F(\omega_e)J_0(\beta)e^{i\omega_e t} + F(\omega_e+\Omega)J_1(\beta)e^{i(\omega_e+\Omega)t} - F(\omega_e-\Omega)J_1(\beta)e^{i(\omega_e-\Omega)t}\Big], \tag{5.10}$$

where E_0 is the unmodulated field amplitude and ω_e denotes the optical carrier angular frequency. The frequency-dependent response of the symmetric reference cavity is characterised by the complex reflection coefficient:

$$F(\omega_e) = \frac{E_{\text{ref}}}{E_{\text{inc}}} = \frac{r_m \left(e^{i2\pi\nu_e/\Delta\nu_{\text{FSR}}^{\text{PDH}}} - 1 \right)}{1 - r_m^2 e^{i2\pi\nu_e/\Delta\nu_{\text{FSR}}^{\text{PDH}}}}. \tag{5.11}$$

Here, r_m refers to the amplitude reflection coefficient of each of the identical FP cavity mirrors, $\nu_e = \omega_e/2\pi$ is the cyclic carrier frequency, and $\Delta\nu_{\text{FSR}}^{\text{PDH}} = c/2L_{\text{cav}}$ denotes the FSR of the PDH reference cavity of length L_{cav}. The dimensionless ratio $2\pi\nu_e/\Delta\nu_{\text{FSR}}^{\text{PDH}}$ defines the exact round-trip optical phase shift inside the cavity. On resonance, this phase shift matches an integer multiple of 2π, driving the numerator of Eq. (5.11) to zero. This condition produces perfect destructive interference between the initial reflection off the front mirror and the field leaking out from the internal cavity mode, minimising the reflected carrier power.

Experimentally, the photodetector possesses a square-law response that monitors the time-averaged optical power of the reflected beam. By defining $P_{\text{ref}} = |E_{\text{ref}}|^2$, the total reflected power can be analytically expanded as:

$$\begin{aligned} P_{\text{ref}} = {} & P_c^{\text{PDH}} |F(\omega_e)|^2 + P_s^{\text{PDH}} \left(|F(\omega_e + \Omega)|^2 + |F(\omega_e - \Omega)|^2 \right) \\ & + 2\sqrt{P_c^{\text{PDH}} P_s^{\text{PDH}}} \Big[\text{Re}\left(F(\omega_e) F^*(\omega_e + \Omega) - F^*(\omega_e) F(\omega_e - \Omega) \right) \cos(\Omega t) \\ & + \text{Im}\left(F(\omega_e) F^*(\omega_e + \Omega) - F^*(\omega_e) F(\omega_e - \Omega) \right) \sin(\Omega t) \Big] \\ & + \mathcal{O}(2\Omega), \end{aligned} \tag{5.12}$$

where $P_c^{\text{PDH}} = P_0 J_0^2(\beta)$ and $P_s^{\text{PDH}} = P_0 J_1^2(\beta)$ represent the power distributed into the carrier and a single sideband, respectively, from the total incident power P_0.

In Eq. (5.12), the cross-interference terms oscillating at the fundamental modulation frequency Ω originate from the optical beat note between the carrier and the sidebands, whereas the higher-harmonic $\mathcal{O}(2\Omega)$ terms stem from the mutual interference between the sidebands themselves. Because the fundamental Ω terms directly probe the complex

phase of the reflected carrier relative to the unperturbed sidebands, they form the physical basis for the frequency error signal. The Ω-frequency component contains both in-phase ($\cos\Omega t$) and quadrature ($\sin\Omega t$) terms, whose relative magnitudes depend on the scale of the modulation frequency Ω relative to the cavity linewidth $\Delta\nu_{\mathrm{FWHM}} = \Delta\nu_{\mathrm{FSR}}^{\mathrm{PDH}}/\mathcal{F}$, where $\mathcal{F}$ is the cavity finesse.

At low modulation frequencies ($\Omega \ll 2\pi\Delta\nu_{\mathrm{FSR}}^{\mathrm{PDH}}/\mathcal{F}$), the internal cavity field adapts adiabatically to the frequency modulation. In this regime, both the carrier and the sidebands enter the cavity, causing the in-phase cosine component of the photodetector signal to dominate while the quadrature sine component is suppressed. Conversely, at high modulation frequencies ($\Omega \gg 2\pi\Delta\nu_{\mathrm{FSR}}^{\mathrm{PDH}}/\mathcal{F}$), the internal field cannot track the rapid phase variations. Consequently, the sidebands are strictly rejected by the cavity and act as a stable phase reference, allowing the quadrature sine component to dominate the detected signal while the cosine component becomes negligible.

To extract the phase information required for the error signal, the photodetector output (see Eq. (5.12)) is fed into an RF mixer along with a local oscillator (LO) reference signal. In the high-modulation regime, where the error signal resides entirely in the quadrature component ($\sin\Omega t$), the internal reference must be adjusted using a 90° phase shifter to align the mixer's demodulation axis with the signal phase. If Ω and Ω' represent the frequencies of the photodetector signal and the phase-shifted mixer LO input, respectively, this process can be described mathematically as follows:

$$\begin{aligned}\sin(\Omega t)\,\cos(\Omega' t - 90^\circ) &= \sin(\Omega t)\,\sin(\Omega' t)\\ &= \frac{1}{2}\Big[\cos\big((\Omega-\Omega')t\big) - \cos\big((\Omega+\Omega')t\big)\Big]\\ &\xrightarrow{\text{LPF}} \frac{1}{2}\cos\big((\Omega-\Omega')t\big).\end{aligned} \tag{5.13}$$

When the modulation frequency matches that of the local oscillator perfectly ($\Omega = \Omega'$), the time-dependent difference term evaluates to $\cos(0) = 1$. The high-frequency sum term $\cos(2\Omega t)$ is stripped away by the low-pass filter, leaving a stable, maximum static DC error voltage proportional to $\frac{1}{2}$, which is subsequently used to feed the servo loop.

Furthermore, when the carrier frequency is near the cavity resonance in this high-modulation regime, the sidebands lie completely outside the cavity's acceptance bandwidth. As the cavity rejects these off-resonant sidebands, they undergo immediate reflection at the input mirror. Far from resonance, the phase of this reflected light exhibits an asymptotic shift toward $\pm 180^\circ$ relative to the incident field. This simplifies their respective reflection coefficients to $F(\omega_e \pm \Omega) \approx -1$. Under these boundary conditions, the complex combination of the reflection coefficients yields a purely imaginary value:

$$F(\omega_e)F^*(\omega_e + \Omega) - F^*(\omega_e)F(\omega_e - \Omega) \approx -i2\,\mathrm{Im}\{F(\omega_e)\}. \tag{5.14}$$

Consequently, the cosine term in Eq. (5.12) vanishes, and the filtered PDH error signal, ϵ, simplifies to its classic anti-symmetric form:

$$\epsilon = -2\sqrt{P_c^{\mathrm{PDH}} P_s^{\mathrm{PDH}}}\,\mathrm{Im}\Big\{F(\omega_e)F^*(\omega_e + \Omega) - F^*(\omega_e)F(\omega_e - \Omega)\Big\}. \tag{5.15}$$

The PDH error signal is plotted in Fig. 5.4 as a function of the normalised frequency detuning, $\Delta\nu_{\mathrm{det}}/\Delta\nu_{\mathrm{FSR}}^{\mathrm{PDH}}$, where the vertical axis is normalised by $2\sqrt{P_c^{\mathrm{PDH}} P_s^{\mathrm{PDH}}}$ to remove dependencies on the absolute optical power incident on the photodetector. This error signal highlights a definitive advantage of the PDH technique over SOF methods: its strict anti-symmetry about the cavity resonance. When the laser frequency is swept across the resonance condition, the direction of the detuning can be unambiguously determined by the polarity of the error signal. A positive voltage indicates that the laser frequency lies on one side of the cavity resonance, while a negative voltage signifies the opposite side. The zero-crossing point corresponds precisely to the centre of the resonance, providing the electronic feedback loop with the necessary magnitude and polarity information to continuously lock the laser frequency to the reference cavity.

5.5.2 Proportional-integral-derivative (PID) controller

Having derived a well-defined PDH error signal that is linearly proportional to the frequency offset, the next step in the PDH scheme is to use this signal to actively lock the

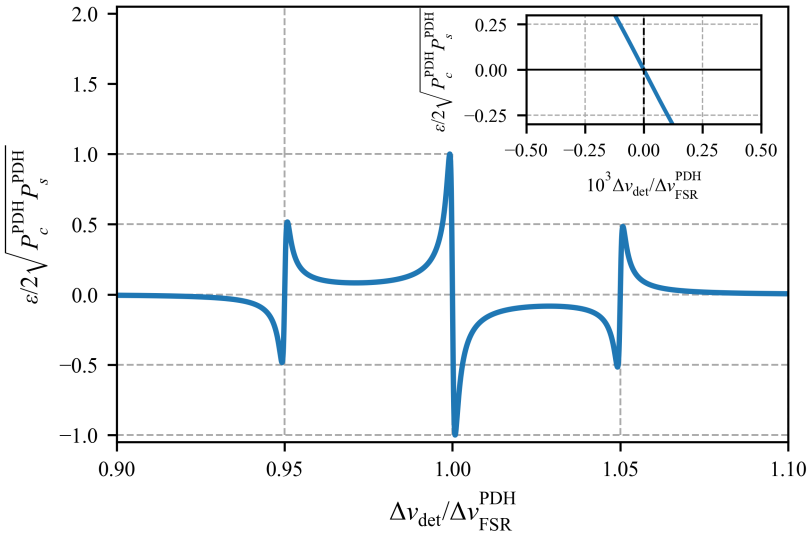


Figure 5.4: The theoretical PDH error signal ϵ (normalised by $2\sqrt{P_c^{\mathrm{PDH}}P_s^{\mathrm{PDH}}}$) plotted as a function of the normalised frequency detuning $\Delta\nu_{\mathrm{det}}/\Delta\nu_{\mathrm{FSR}}^{\mathrm{PDH}}$ for $\Omega = 50$ MHz, $\Delta\nu_{\mathrm{FSR}}^{\mathrm{PDH}} = 1$ GHz, and $r_m = 99.5\%$. The characteristic anti-symmetric dispersion profile, magnified within the inset, highlights the sharp central linear slope across the cavity resonance ($\Delta\nu_{\mathrm{det}} = 0$), which provides an unambiguous zero-crossing point for frequency stabilisation. The side peaks (extrema) located at $\Delta\nu_{\mathrm{det}} = \pm\Omega/2\pi$ arise from the coherent beating of the carrier with the phase-modulated sidebands.

laser frequency to the cavity resonance. This usually requires the use of a servo loop. A servo loop is a general class of feedback systems, typically electronic, that processes an input signal – in this case, the low-frequency (DC) error signal – and generates an output that minimises the error, ideally driving it to zero.

Among the available control techniques, proportional-integral-derivative (PID) control is the most widely employed, due to its simplicity and robust performance across a broad range of applications. The fundamental goal of the feedback loop is to suppress environmental disturbances and technical noise that could otherwise cause the laser frequency to drift away from resonance. In a PID controller, with a setpoint y_{sp}, the control signal $u(t)$ is defined as [209]:

$$u(t) = k_p e(t) + k_i \int_0^t e(\tau)\,d\tau + k_d \frac{d}{dt} e(t), \tag{5.16}$$

where $e(t) = y_{sp} - y_{pv}$ is the error signal, with y_{pv} denoting the measured process variable. The control signal is composed of three distinct terms: one that is directly proportional to the error signal, scaled by a proportional gain k_p; another that is proportional to the integral of the error signal, scaled by an integral gain k_i; and a third term that is proportional to the derivative of the error signal, scaled by a derivative gain k_d.

In the context of PID control systems, the three components – P, I, and D – can be conceptually interpreted as responses to the present, past, and anticipated future behaviour of the system, respectively, with each component fulfilling a crucial task in the control loop. The P control responds to the current error between the desired setpoint and the measured output. It provides a fast response that is directly proportional to the magnitude of the error signal. While P control is effective at mitigating disturbances and ensuring a quick response, it inherently leaves a residual steady-state error. This residual error can be reduced by increasing the proportional gain k_p, but this will increase the probability of unwanted oscillations.

To eliminate the steady-state error associated with the P control, the I control is introduced. By accumulating the error over time, the I control ensures that any persistent offset is gradually driven to zero. Increasing the integral gain k_i strengthens the influence of the I control by allowing it to correct steady-state errors more quickly. However, just like with the P control, a higher gain also makes the system more prone to oscillations and potential instability. While it is essential to increase both k_p and k_i to obtain a fast and robust feedback loop, their combined action will eventually make the system susceptible to unwanted oscillations.

The D control addresses this issue by anticipating upcoming errors and taking immediate counteraction. By responding to the rate of change of the error, the D term acts as a predictive element, damping oscillations and enhancing the system's responsiveness. When properly tuned in conjunction with the P and I components, the D control enables higher overall gains to be obtained while preserving the system stability, thus improving both the speed and robustness of the feedback loop. The main challenge with the D control is that it assumes the system's behaviour changes smoothly over time. In practice,

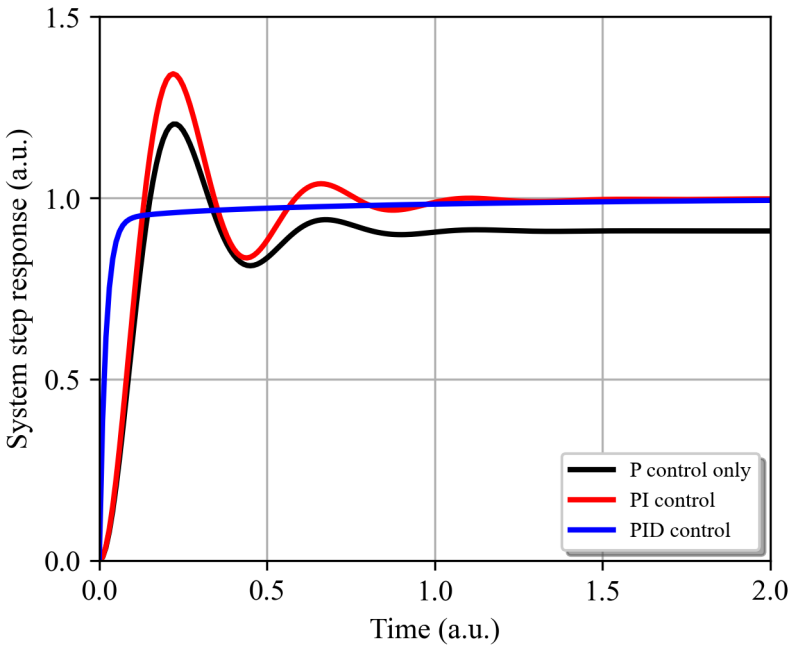


Figure 5.5: Example of a "proportional" (P, black line), "proportional-integral" (PI, red line) and "proportional-integral-derivative" (PID, blue line) feedback control system with setpoint $y_{sp} = 1$. The system response to a pure P controller is fast, but a steady-state error always exists. Adding an I control slows down the response but cancels out any residual error from the P control. Finally, introducing a D control allows for the fastest response of all three and compensates all disturbances.

however, if the system is affected by noise or random fluctuations, the D component may introduce additional noise, potentially leading to instability in the system.

Figure 5.5 shows an example of a P, PI, and PID-controlled system response and illustrates possible oscillations. The PID-controlled system, when optimally tuned, demonstrates the most rapid and stable response, effectively eliminating disturbances and allowing complete cancellation of any perturbations.

5.6 Noise dynamics in a dual-locked ICSRO VECSEL

Having reviewed the theoretical foundations of the PDH error signal and the principles governing PID-based servo loops, we now turn our attention to the practical realisation

of these concepts within the dual-locked ICSRO VECSEL system. The following section presents the motivation, experimental implementation, and detailed analysis of a dual-locking scheme in which both the VECSEL fundamental frequency and the resonant idler frequency are simultaneously stabilised to their respective FP reference cavities.

5.6.1 Motivation

As discussed in Chapter 1, a key advantage of CW OPOs lies in their suitability for quantum optics and quantum information processing, where they provide a natural platform for entanglement-based protocols and squeezed light generation through the production of signal and idler photons exhibiting strong non-classical correlations. However, the level of intensity-difference squeezing achievable in practice is often constrained by pump laser noise, particularly when relaxation oscillations introduce excess noise above the standard quantum limit. Although solid-state lasers are capable of delivering Watt-level output powers with excellent beam quality, their relatively long gain lifetimes (on the order of 100 µs to several ms) lead to quasi-continuous amplitude fluctuations above the OPO threshold, rendering them sub-optimal for squeezing applications. In contrast, VECSELs operate in a Class-A dynamical regime with effective gain lifetimes on the order of a few nanoseconds, which strongly suppresses relaxation oscillations. As demonstrated at the end of Chapter 4, this behaviour enabled RMS passive power stabilities below 2.3% for all three interacting waves of the ICSRO, without requiring additional self-pulsing suppression techniques.

Although the transient dynamics of VECSEL-pumped OPOs have already been studied both theoretically [44] and experimentally [26], the frequency and phase stability of such systems remain largely unexplored. In particular, neither the noise transfer between the signal and idler waves under active frequency stabilisation, nor a quantitative characterisation of linewidth and frequency noise has been reported to date. A single prior study has suggested that 'frequency pulling' may affect stability in regimes of strong nonlinear frequency conversion [27]; however, no systematic or quantitative analysis of the noise dynamics has been presented, to our knowledge. There are, however,

previous studies of the noise dynamics of stabilised AlGaInP-based red-VECSELs, i.e., without the intracavity OPO. For example, sub-kHz linewidths have been demonstrated in conventional two-mirror resonators, alongside RIN levels below −120 dBc/Hz (f > 1 Hz) [136] and −129 dBc/Hz (f > 100 Hz) [137] at emission wavelengths near 689 nm and 698 nm, respectively. Broader linewidths, on the order of 11.4 kHz [50] and 25 kHz [51], have also been observed in extended three- and four-mirror VECSEL configurations, respectively.

5.6.2 Experimental configuration

A schematic of the dual-locked OC-idler ICSRO VECSEL system is shown in Fig. 5.6, based on the free-running resonator architecture introduced in Chapter 4. The OC-idler ICSRO VECSEL system (highlighted in the red box of Fig. 5.6a) corresponds to the cavity configuration described in Fig. 4.9, with two notable modifications: firstly, the etalon within the VECSEL cavity has been removed, leaving just a single 1 mm-thick yttrium aluminium garnet (YAG) etalon in the OPO cavity; secondly, both the dichroic mirror (DM) and first folding mirror M_2 have been mounted on PZTs for the purpose of active frequency stabilisation. With these minor modifications, the fundamental performance of the VECSEL – including peak wavelength, tunability, intracavity power, and beam quality – along with the output power and stability of all three ICSRO interacting waves, remained comparable to those reported in Chapter 4.

Figure 5.6 also includes both frequency stabilisation loops; the first, utilises PDH-locking of the VECSEL fundamental (see Fig 5.6b; yellow box) by stabilising to a commercial air-spaced FP reference cavity (free spectral range, or FSR, of 1 GHz, finesse ≈ 400). To implement this scheme, the phase of the VECSEL beam is modulated at 74 MHz upon traversal through a resonant EOM (Qubig E0-F74L3) before reaching the FP reference cavity. Since the EOM modulation frequency is significantly higher than the linewidth of the visible FPI reference cavity, the sine term dominates the PDH error signal. The reflected signal is then captured using a high-speed photodiode (Qubig PD-AC100-VIS), where the error signal is created (within the electronics) by mixing

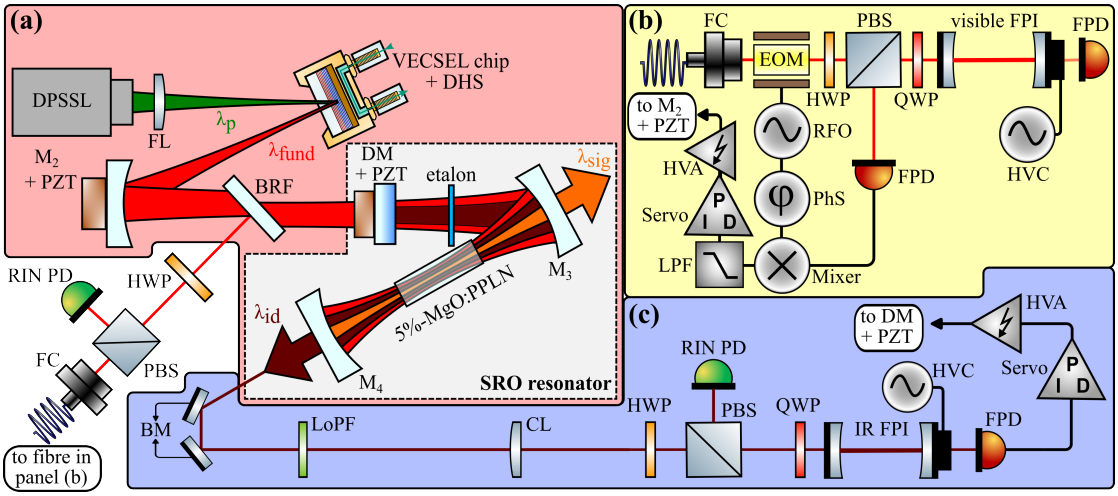


Figure 5.6: Schematic (not to scale) of the dual-locked ICSRO VECSEL setup. (a) AlGaInP-based VECSEL-pumped SRO, with OC (T_{OC} = 1.7%) for the OPO resonant idler via M_4; (b) Pound-Drever-Hall (PDH) stabilsation of the VECSEL fundamental; (c) Side-of-fringe (SOF) stabilisation of the OPO resonant idler. The optical elements are indicated as follows: FL: focussing lens; DHS: synthetic diamond heat spreader; PZT: piezoelectric transducer; BRF: birefringent filter; M_x(x = 2,3,4): cavity mirrors; DM: dichroic mirror; BM: broadband mirrors; LoPF: long-pass filter; CL: collimating lens; FC: fibre coupler; RIN PD: relative intensity noise photodetector; HWP: half-wave plate; QWP: quarter-wave plate; PBS: polarizing beam splitter; EOM: electro-optic modulator; FPD: fast photodetector; IR: infrared; FPI: Fabry–Pérot interferometer; HVC: high-voltage controller; RFO: radio frequency oscillator; PhS: phase shifter; LPF: low-pass filter; HVA: high-voltage amplifier. λ_p, λ_{fund}, λ_{sig}, and λ_{id}: VECSEL pump, VECSEL fundamental, signal and idler wavelengths at 532 nm, 690.6 nm, 1245.2 nm and 1550.8 nm, respectively. Figure adapted from Ref. [59]. The non-resonant signal-field measurement path to the IR FPI is shown separately in Fig. 4.24.

the local oscillator signal (that is driving the EOM) and the FP reflected signal via a frequency mixer. This error signal is then fed back into the VECSEL cavity through the M_2-PZT (PI P-016.10H), via a PID servo controller (New Focus LB1005) and a HVA (PI E-618), which ultimately closes the feedback loop. It is important to note that the internal electronics of the servo lock box – including the frequency mixer, low-pass filter, and PID controller – are integrated within a single unit, such that the PI gain can be optimally tuned and that the resulting error signal is generated at the servo output.

The feedback circuit for the OPO resonant idler (see Fig 5.6c; blue box), is based on the SOF technique [210], where the OPO cavity is locked to a separate air-spaced FP

cavity (FSR = 1.5 GHz, finesse ≈ 200). Here, the error signal is sent to the DM-PZT (PI P-010.00H) after being processed by a secondary PID servo (New Focus LB1005) and, subsequently, amplified by a wide-bandwidth HVA module (Piezo Drive PDm200).

Having described the experimental configuration of the dual-locked ICSRO VECSEL system, we now turn to the specific operating conditions under which frequency locking was achieved. This discussion focuses primarily on the feedback parameters and loop settings that enabled stable operation and effective suppression of both frequency and intensity noise.

5.7 Lock acquisition and operating conditions

Once the alignment of the ICSRO VECSEL system of Fig. 5.6a was optimised for single-frequency operation, the frequency discrimination within each FPI could be determined. The first trace under analysis corresponds to the PDH error signal (see Fig. 5.7a), obtained following modulation of the VECSEL fundamental beam. It is important to emphasise that both the demodulation process and the subsequent low-pass filtering are carried out by the internal electronics of the servo lock box. This integrated functionality produces the characteristic PDH error signal at the servo output, as illustrated in Fig. 5.7a. The measured error signal exhibits the opposite polarity to the theoretical response presented in Fig. 5.4, arising from the phase and sign convention of the experimental demodulation electronics relative to the theoretical reference; the polarity of the PDH error signal indicates the direction of frequency detuning relative to the cavity resonance.

This antisymmetric error signal is obtained by scanning the VECSEL cavity length using the PZT mounted on mirror M_2 while the FPI reference cavity is kept fixed. The resulting PDH error signal displays two well-resolved sidebands, each separated from the carrier by the 74 MHz modulation frequency, which are clearly distinguished in the measurement (see Fig. 5.7a). Although the FPI itself has a PZT actuator that can be

used for calibration or to record transmission traces (see Figs. 5.7b and 5.7c), its length is not varied during the locking procedure.

In addition to the PDH error signal, two identical traces corresponding to the transmission of the alternative FPI are used for SOF locking. These traces correspond to the OPO non-resonant signal (see Fig. 5.7b) and the resonant idler (see Fig. 5.7c). As the laser frequency is scanned across a cavity resonance, the transmitted intensity follows the Airy function, producing Lorentzian-shaped peaks at each resonance. By operating on the linear slope (or "side") of a transmission fringe, frequency deviations produce proportional changes in intensity, which form the error signal for the servo. For this SOF technique, the operating point is set (via adjustment of the servo trigger) at the midpoint of the FPI transmission curve, corresponding to the steepest slope of the resonance. This ensures maximum sensitivity, as deviations from the operating point produce a well-defined error signal that the servo system can use to stabilise the laser frequency. In practice, this method is simpler, though less frequency-linear, than PDH stabilisation, since the lock point is defined by the fringe slope rather than the zero-crossing point of a demodulated signal. While the SOF technique is used to stabilise the OPO resonant idler, the same reference cavity is simultaneously employed to monitor the non-resonant signal. In this case, the cavity is not locked and the servo electronics are inactive, but the signal is still measured on the cavity slope to characterise the free-running frequency noise.

Using the experimental data, the finesse of the visible and infrared FPIs at the VECSEL fundamental and OPO idler wavelengths of 690.6 nm and 1550.8 nm were determined to be 422(6) and 238.9(1), respectively, using Eq. 4.15. From these finesse values, the cavity resonance widths were calculated via Eq. 4.16 to be 2.37(3) MHz and 6.28(1) MHz. Table 5.2 summarises the detailed experimental parameters for all three ICSRO interacting fields, including frequency noise detection sensitivities and milliwatt-level output powers.

The remainder of this chapter presents a detailed analysis of the noise and stability performance of the ICSRO VECSEL system under different levels of active stabilisation.

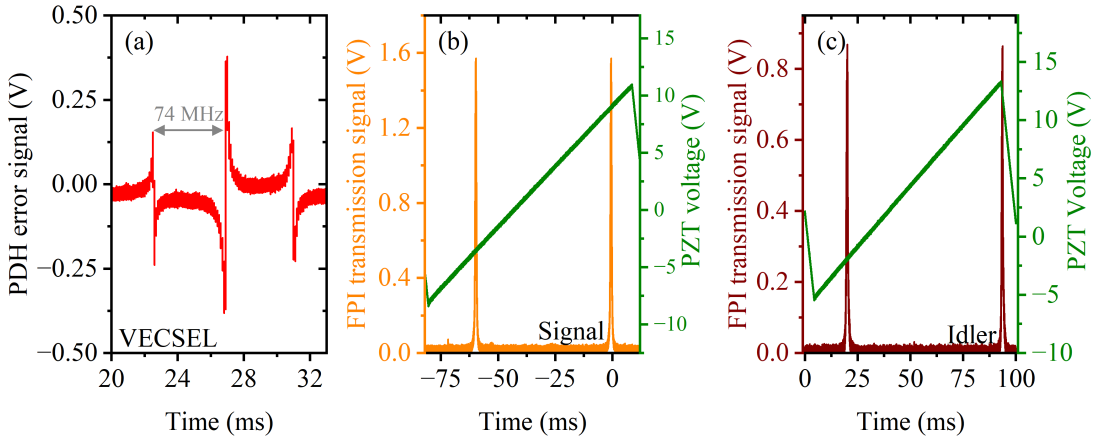


Figure 5.7: Characterisation of the ICSRO VECSEL error signals under active frequency stabilisation. **(a)** PDH error signal obtained from the PID servo controller while scanning the VECSEL cavity near resonance. **(b)** Transmission signal recorded from the infrared FPI, corresponding to the non-resonant signal wavelength at 1245.2 nm. **(c)** Transmission signal recorded from the infrared FPI, corresponding to the resonant idler wavelength at 1550.8 nm.

Table 5.2: Experimental conditions under which frequency locking was achieved. The reported optical power corresponds to the signal power measured during the locking operation. $\Delta\nu_{\mathrm{FWHM}}$: cavity resonance width. Table reproduced from Ref. [59], with $\Delta\nu_{\mathrm{cav}}$ replaced with $\Delta\nu_{\mathrm{FWHM}}$.

ICSRO wave	**Wavelength (nm)**	**Optical power (mW)**	**Output coupling**	$\Delta\nu_{\mathrm{FWHM}}$ **(MHz)**	**Frequency discriminator (mV·MHz^{-1})**
VECSEL fundamental	690.6(1)	1.33(2)	BRF reflection	2.37(3)	310(10)
OPO signal	1245.2(1)	4.8(1)	98% (via M_3)	8.73(1)	173(3)
OPO idler	1550.8(1)	0.93(3)	1.7% (via M_4)	6.28(1)	135(3)

The discussion begins with a characterisation of the RIN, followed by an examination of the relative frequency noise. The integrated linewidths of each of the three interacting waves are then analysed, providing quantitative metrics for assessing and comparing the overall noise and stability of the system. These results are directly compared with previously reported data from externally-pumped OPO systems in the literature.

5.8 Relative intensity noise characteristics of the ICSRO VECSEL

In this section, we demonstrate the RIN performance of the ICSRO VECSEL under increasing degrees of active frequency stabilisation. To perform this measurement, a bias-tee was employed to effectively separate the AC and DC components of the detected photocurrent signals. Here, the VECSEL fundamental beam was monitored using a Si-biased photodetector (Thorlabs DET10A-M), whereas the OPO signal and idler were detected using an InGaAs photodetector (Thorlabs PDA10CS-EC).

The characteristic 3-dB cutoff frequency, illustrated in all RIN spectra, was calculated via the following expression [211]:

$$f_{\text{cutoff,3dB}} = \frac{\Delta\nu_{\text{FSR}}^{\text{cav}}}{2\mathcal{F}}, \tag{5.17}$$

where $\Delta\nu_{\text{FSR}}^{\text{cav}}$ and $\mathcal{F}$ represent the cavity FSR and finesse, respectively. For the VECSEL cavity, the finesse was determined by experimentally assessing the insertion losses of each intracavity element. These measurements were then combined to obtain the total round-trip cavity loss, which was subsequently used to estimate the cavity finesse $\mathcal{F}$, following the standard finesse–loss relationship [212]. Direct characterisation of the insertion loss of the 5%-MgO:PPLN crystal in the OPO cavity was not feasible due to the absence of an auxiliary laser at the idler wavelength of 1.55 µm. To address this limitation, the manufacturer-provided anti-reflection (AR) coating specifications were incorporated into the loss calculation to account for their contribution. This methodology ensured that all significant optical losses were accounted for, enabling a reliable estimation of both the effective cavity finesse and the OPO resonator cutoff frequency.

Furthermore, the shot-noise limits that are included in each RIN spectrum are calculated using the following two-sided PSD expression:

$$\text{RIN}_{\text{shot}} = 10\log_{10}\left(\frac{2hc}{\eta_{\text{quant}}\lambda P_{\text{PD}}}\right)\ [\text{dBc/Hz}], \tag{5.18}$$

Table 5.3: Experimental conditions under which the shot-noise was calculated. R_{PD}: photodiode responsivity; η_{quant}: quantum efficiency; λ: optical wavelength; P_{PD}: optical power incident at the photodiode; $\mathrm{RIN}_{\mathrm{shot}}$: shot-noise-limited RIN.

ICSRO wave	$\boldsymbol{R_{\mathrm{PD}}}$ **(A/W)**	$\boldsymbol{\eta_{\mathrm{quant}}}$ **(%)**	$\boldsymbol{\lambda}$ **(nm)**	$\boldsymbol{P_{\mathrm{PD}}}$ **(mW)**	$\mathbf{RIN_{shot}}$ **(dBc/Hz)**
VECSEL fund.	0.43	77.4	690.6	8.30	-160.5
OPO signal	0.86	85.9	1245.2	8.25	-163.5
OPO idler	1.05	84.2	1550.8	2.15	-158.5

where c denotes the speed of light in vacuum, and λ and P_{PD} represent the optical wavelength and power incident on the photodiode, respectively. The quantum efficiency of each photodiode η_{quant} is defined as [213]:

$$\eta_{\mathrm{quant}} = \frac{R_{\mathrm{PD}} hc}{e\lambda}, \tag{5.19}$$

where R_{PD} is the responsivity of the photodiode and e is referred to as the elementary charge.

The shot-noise-level establishes the fundamental quantum-limited noise floor, originating from the intrinsic statistical fluctuations of discrete photon detection events. Experimental conditions for all three ICSRO interacting wavelengths, including the optical powers incident on each photodiode, are summarised in Table 5.3. The responsivity of each photodiode was determined from the manufacturer-provided wavelength-dependent responsivity curves, while the optical powers were recorded directly in front of each detector for each interacting wave.

In the subsections that follow, we present a systematic analysis and discussion of the RIN characteristics associated with each interacting wave in the ICSRO VECSEL system. Each contribution is examined individually in order to clearly highlight its specific role and impact on the overall noise performance of the system.

5.8.1 VECSEL fundamental

Firstly, as illustrated in Fig. 5.8, the VECSEL fundamental RIN, demonstrated for an aquisition time of 100 ms, is measured to be below -128 dBc/Hz in all scenarios for fre-

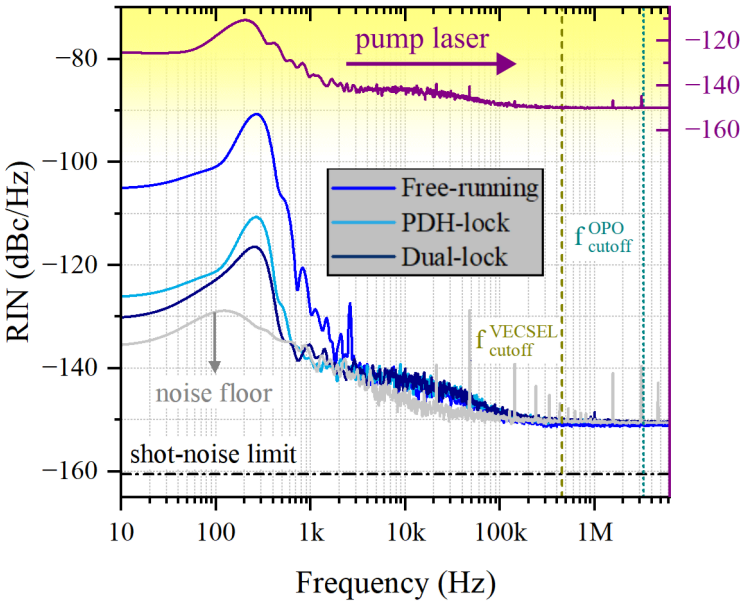


Figure 5.8: Characterisation of the relative intensity noise (RIN), measured for frequencies between 10 Hz and 6.25 MHz, for the VECSEL fundamental under all three stages of stabilisation. The black dash-dot line corresponds to the shot noise of the VECSEL fundamental. The dark yellow dashed (or turquoise dotted) line highlights the cavity cutoff frequency for the VECSEL (or OPO) cavity. For completeness, the RIN of the external pump laser is shown by the purple trace at the top of the figure. Figure adapted from Ref. [59].

quencies above 1 kHz. For frequencies above 150 kHz, the noise is predominantly limited by the noise floor of the photodetector (Thorlabs DET10A-M; also shown in Fig. 5.8; grey trace) and, therefore, we were unable to measure down to the VECSEL shot-noise-limit (−160.5 dBc/Hz, see black dash-dot line in Fig. 5.8 and also Table 5.3); the noise level that we would expect to observe above the VECSEL cavity cutoff frequency, which in this case is ∼450 kHz (see Fig. 5.8, dark-yellow dashed line). Additionally, it is assumed that the noise floor obscures any intensity noise fluctuations upto the VECSEL cavity cutoff frequency, which would otherwise lead to amplitude-to-phase coupling via the linewidth enhancement factor, according to the Myara model [45].

It is worth noting that, in the dual-locked configuration, the minor reduction in low-frequency (e.g., < 300 Hz) intensity noise of the VECSEL, relative to the PDH-locked

case, is likely due to active stabilisation of the mechanical noise of the intracavity DM during OPO cavity locking.

Furthermore, Fig. 5.8 also shows the RIN of the external pump laser (purple curve), which is lower than the VECSEL because the latter experiences resonant amplification of the technical noise by the gain–cavity dynamics. The broad excess noise near 200 Hz, recurrent in all RIN spectra albeit at slightly different frequencies, is attributed to mechanical resonances, system elevation, and servo gain necessitated by elevated environmental noise of an open tabletop system. Enhanced spectral resolution of the RIN measurements at Fourier frequencies around this broad feature could resolve discrete resonant mode contributions masked by the baseline noise, thereby enabling targeted identification and suppression through optimised cavity architecture and mechanical packaging.

5.8.2 OPO non-resonant signal

The RIN of the OPO signal, measured with and without stabilisation of the VECSEL and OPO cavities, is presented in Fig. 5.9. The signal field exhibits a RIN profile that closely follows that of the VECSEL fundamental, illustrating the strong correlation of noise between the fundamental and non-resonant fields within the ICSRO system. This correlation indicates that, at the signal wavelength, the OPO cavity provides minimal feedback or filtering, allowing fluctuations in the VECSEL to be directly transferred to the non-resonant signal field. For Fourier frequencies above 100 kHz, the RIN approaches a constant noise floor of ~ -156 dBc/Hz, corresponding to the detection-limited sensitivity of the photodetector (Thorlabs PDA10CS-EC).

Similar to the VECSEL fundamental RIN, the signal RIN measurements are limited by the detection noise floor, precluding the direct observation of quantum-limited behaviour. At an incident power of 8.25 mW, the shot-noise-limited RIN is calculated to be ~ -163.5 dBc/Hz (see Table 5.3). It is instructive to note that the non-resonant signal is expected to approach this limit at Fourier frequencies above the VECSEL cavity cutoff ($\sim$450 kHz; indicated by the dark yellow dashed line in Fig. 5.9), rather than the

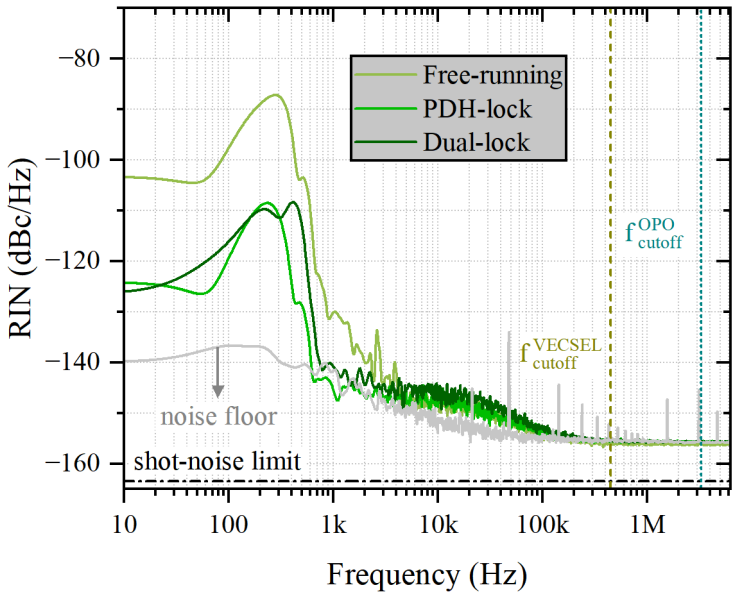


Figure 5.9: Characterisation of the relative intensity noise (RIN), measured for frequencies between 10 Hz and 6.25 MHz, for the OPO non-resonant signal, under all three stages of stabilisation. The black dash-dot line corresponds to the shot noise of the OPO non-resonant signal. The dark yellow dashed (or turquoise dotted) line highlights the cavity cutoff frequency for the VECSEL (or OPO) cavity. Figure adapted from Ref. [59].

higher OPO cavity cutoff (∼3.25 MHz; indicated by the turqoise dotted line in Fig. 5.9). Because the signal is non-resonant, it is exempt from OPO cavity filtering; its noise is instead governed by VECSEL pump fluctuations and the nonlinear interaction bandwidth. Once these pump-induced fluctuations are filtered by the VECSEL resonator, the signal should become limited by vacuum fluctuations and asymptotically approach the shot-noise floor.

5.8.3 OPO resonant idler

The RIN characteristics of the OPO idler, evaluated under the same stabilisation conditions, are presented in Fig. 5.10. In both the free-running and PDH-lock-only configurations, the idler exhibits an elevated noise level in the frequency range between 1 and 5 kHz compared to the VECSEL and non-resonant signal. This behaviour is at-

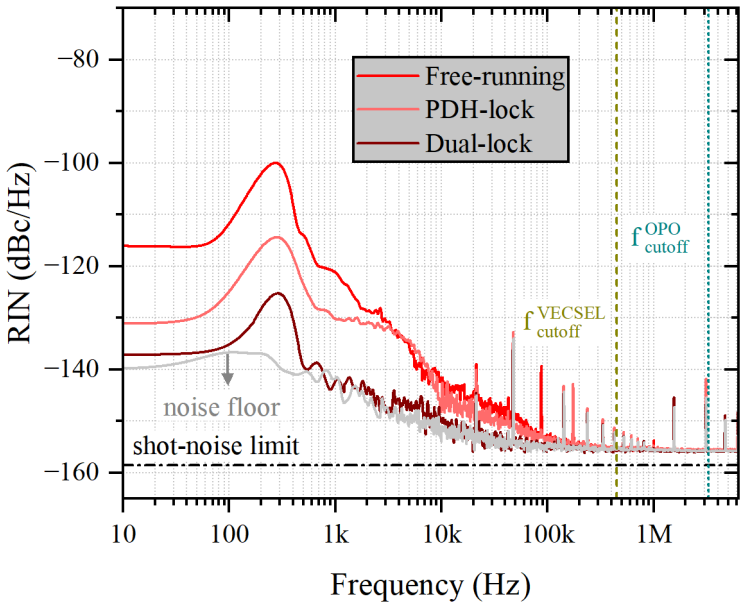


Figure 5.10: Characterisation of the relative intensity noise (RIN), measured for frequencies between 10 Hz and 6.25 MHz, for the OPO resonant idler, under all three stages of stabilisation. The black dash-dot line corresponds to the shot noise of the OPO resonant idler. The dark yellow dashed (or turquoise dotted) line highlights the cavity cutoff frequency for the VECSEL (or OPO) cavity. Figure adapted from Ref. [59].

tributed to the lower finesse of the OPO cavity and the presence of residual mechanical vibrations that are not actively compensated by the PDH servo loop. The influence of these mechanical contributions is further illustrated in the RIN spectra of the VECSEL and signal fields, where the implementation of VECSEL cavity stabilisation effectively suppresses the weaker noise bump observed over the same frequency range. Similarly, under dual-locking conditions – where both the VECSEL and OPO cavities are simultaneously stabilised – the excess idler noise is eliminated, accompanied by an overall RIN reduction of ∼21 dB at 10 Hz relative to the free-running regime. This result highlights the effectiveness of dual stabilisation in mitigating both mechanical and intensity-related noise processes within the ICSRO system.

Having examined the RIN of each ICSRO interacting wave under the various stabilisation configurations, the discussion now turns to the frequency noise dynamics. While the RIN results were organised by optical field, the frequency noise is more appropriately

compared across stabilisation regimes, since the locking architecture directly determines the coupled frequency dynamics of the system. The following section therefore presents the frequency noise behaviour for the free-running, PDH-locked, and dual-locked regimes individually.

5.9 Frequency noise characteristics of the ICSRO VECSEL

The frequency noise is characterised by recording the residual (AC) error signal from the PDH (for the VECSEL fundamental) and SOF (for the OPO signal and idler) servo controllers over a range of acquisition times. The sampling times were selected to remain consistent with prior literature and to assess stability over practically relevant timescales, particularly given that VECSEL linewidths are known to broaden over longer acquisitions times due to the cumulative effects of environmental noise. The free-running noise is recorded with the servo loop remaining open (ensuring the laser is on-resonance with the FP reference cavity), whilst the noise of the locked laser is recorded with the feedback loop closed. Here, the maximum sampling time is limited by drift in both confocal FP cavities, mode-hopping of the VECSEL and OPO cavities due to technical noise influences incident on the open cavity, and thermal fluctuations at the 5%-MgO:PPLN facets induced by the temperature difference between the crystal – stabilised at 114 °C within an oven – and the ambient room temperature environment.

The frequency noise power spectral density (FNPSD) graphs, $S_\nu(f)$ of the ICSRO fields, are derived from the noise data using the method outlined by Tröbs and Heinzel [214]. The following subsections provide a detailed examination of the FNPSD for each interacting wave in the ICSRO system. The analysis is organised by stabilisation regime to clearly illustrate how each control scheme influences the noise behaviour and overall stability of the VECSEL fundamental, signal, and idler waves. To provide a direct comparison of the frequency-noise performance before and after stabilisation,

Fig. 5.14 presents the FNPSD for the relevant interacting fields in both the unlocked and locked regimes.

5.9.1 Free-running regime

For the case of the free-running VECSEL fundamental field (see Fig. 5.11; blue trace), the low-frequency noise dominates, as expected, resulting from intensity fluctuations of the pump being injected into the VECSEL, along with mechanical, thermal and environmental disturbances concurrent within both laser cavities. Fig. 5.11 also shows the free-running FNPSD of the OPO signal, which closely matches the fundamental noise spectrum of the VECSEL in the 10 to 450 kHz range. This similarity arises from the non-resonant nature of the signal wave within the OPO cavity. This noise, which is likely generated by the intensity fluctuations of the VECSEL fundamental, which translate into frequency noise via the Henry factor [45], is transferred (partially) to the OPO signal with minimal suppression due to the lack of OPO cavity filtering and feedback. Conversely, the free-running FNPSD of the OPO idler, also illustrated in Fig. 5.11, is as much as two orders of magnitude lower, notably at frequencies below 0.5 kHz, due to the fact that the OPO cavity acts as an additional filter for noise suppression. This filtering effect, combined with the splitting of frequency noise – via the VECSEL fundamental – between the OPO signal and idler, according to the energy conservation relation, are the contributing factors. Additionally, the peaks observed between 10 and 450 kHz for all three ICSRO interacting waves originate from noise transferred from the green pump laser that is not adequately filtered out by the VECSEL cavity ($f_{\text{cutoff}}^{\text{VECSEL}} \sim 450$ kHz; see Fig. 5.11; dark yellow dashed line), inducing temperature-dependent refractive index changes and, hence, cavity length fluctuations that are directly transferred to the VECSEL fundamental frequency.

Also plotted in Fig. 5.11 is the β-separation line [215], defined as $S_\beta(f) = (8\pi^{-2}\ln 2)f$, where f is the Fourier frequency. This line divides the FNPSD spectrum into two distinct regions: the first, delimited by $S_\beta(f) \leq S_\nu(f)$, represents frequency fluctuations that predominantly affect the Gaussian 'core' of the laser line shape and allow deter-

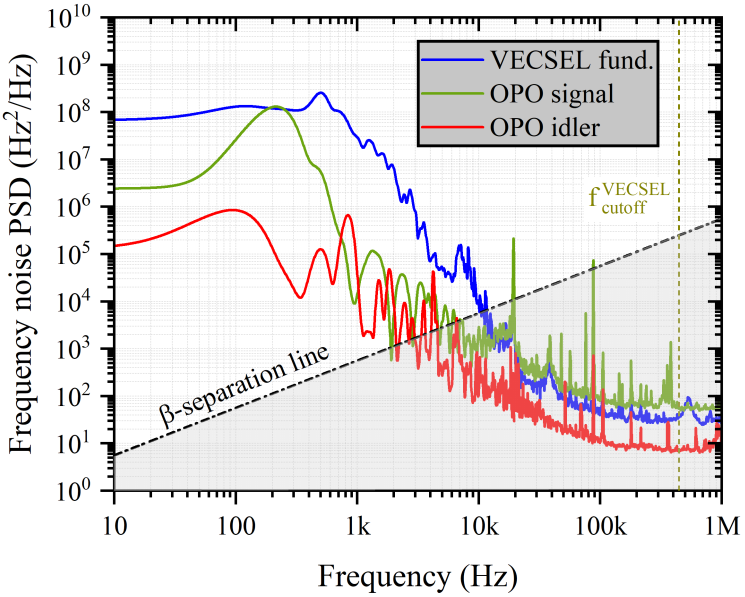


Figure 5.11: Characterisation of the frequency noise power spectral density (FNPSD) of the ICSRO VECSEL in the free-running regime. The dark yellow dashed line indicates the cavity cutoff frequency for the VECSEL cavity. The black dash-dot line is the β-separation line. Figure adapted from Ref. [59].

mination of the laser linewidth; the second, bound by $S_\beta(f) \geq S_\nu(f)$, corresponds to fast frequency fluctuations that do not alter the linewidth but instead contribute to the Lorentzian pedestal of the laser line shape.

5.9.2 PDH-lock-only regime

For the PDH-locked configuration, Fig. 5.12 shows the FNPSD of the VECSEL fundamental, OPO signal and OPO idler. When the servo loop is closed, it can be clearly seen that, particularly for the VECSEL and non-resonant signal waves, the relative frequency noise is reduced by over three orders of magnitude at low Fourier frequencies (e.g., < 10 Hz). Despite this, the noise band below 1 kHz still retains significant contributions from pure mechanical and thermal noise, as well as pump laser noise not perfectly compensated by the servo loop, with peaks at 50 Hz and 150 Hz related to the mains electricity frequency and harmonics. Additionally, for both the VECSEL and non-resonant signal waves, there is a broad resonance near 5 kHz, which is likely at-

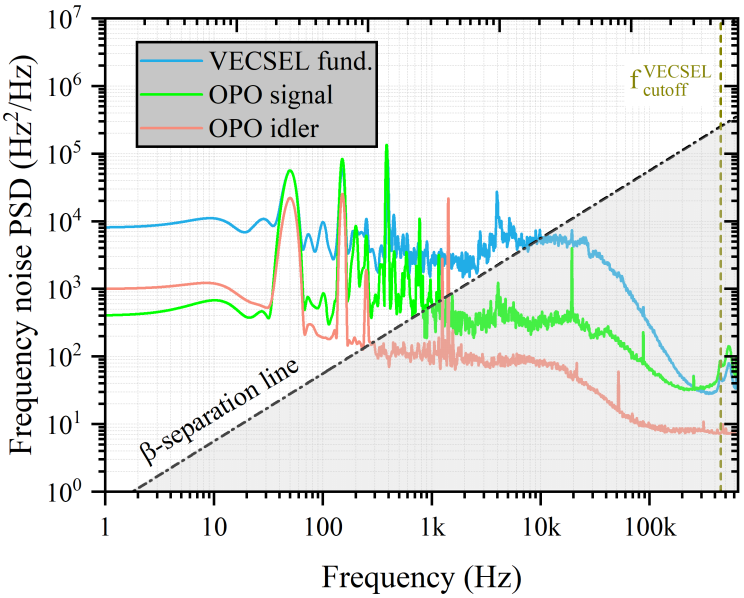


Figure 5.12: Characterisation of the frequency noise power spectral density (FNPSD) of the ICSRO VECSEL in the PDH-locked-only regime. The dark yellow dashed line indicates the cavity cutoff frequency for the VECSEL cavity. The black dash-dot line is the β-separation line. Figure adapted from Ref. [59].

tributed to a mechanical resonance of the PZT and mirror mount (mounted 10 cm from the optical table) or the PZT's limited response near the upper end of its frequency range. Likewise, in the case of the OPO idler wave (also shown in Fig. 5.12), the broad peaks that are located between 1 and 2 kHz are most likely a consequence of one of the mechanical resonances of the OPO cavity, which includes the DM.

5.9.3 Dual-lock regime

Fig. 5.13 shows the FNPSD of the VECSEL fundamental and OPO idler under dual-locking conditions. It can be seen that the frequency noise behaviour of the VECSEL fundamental is similar to the spectrum obtained under PDH-locking (see Fig. 5.12), with a small increase at very low frequencies (up to 10 Hz), likely attributable to the extended measurement duration (from 1 to 4s), which exaggerates the influence of thermal and mechanical drifts. On the other hand, the frequency noise of the OPO idler is reduced to such an extent that it now exhibits a quasi-white spectrum, except for a few reso-

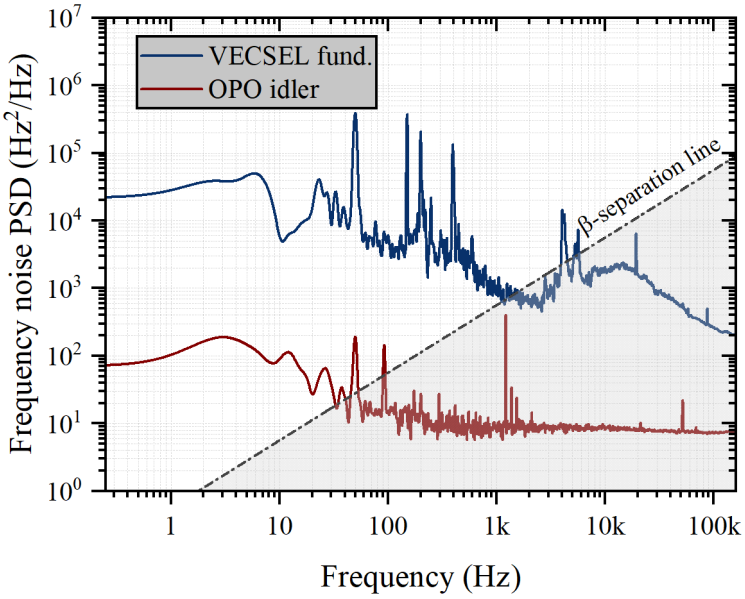


Figure 5.13: Characterisation of the frequency noise power spectral density (FNPSD) of the ICSRO VECSEL in the dual-lock regime. The black dash-dot line is the β-separation line. Figure adapted from Ref. [59].

nances, particularly between 1 and 2 kHz, that were unable to be suppressed by either stabilisation scheme.

This experiment provides a clear demonstration of frequency noise transfer from the fundamental VECSEL pump beam to the non-resonant signal. Comparison of the dual-locked PSD spectra in Fig. 5.13 shows that the frequency noise of the resonant idler is suppressed relative to the VECSEL fundamental by at least two orders of magnitude when both cavities are simultaneously stabilised. Given that the parametric process must satisfy the energy conservation relation $\omega_p = \omega_s + \omega_i$, where ω_p, ω_s, and ω_i are the angular frequencies of the pump, signal, and idler beams, respectively, the VECSEL fundamental frequency noise that is absent from the idler must be transferred to the non-resonant signal [216]. Although we could not directly verify the corresponding increase in frequency noise of the OPO signal due to the absence of an additional FPI reference, we again note the corresponding increase in the signal intensity noise shown in Fig. 5.9.

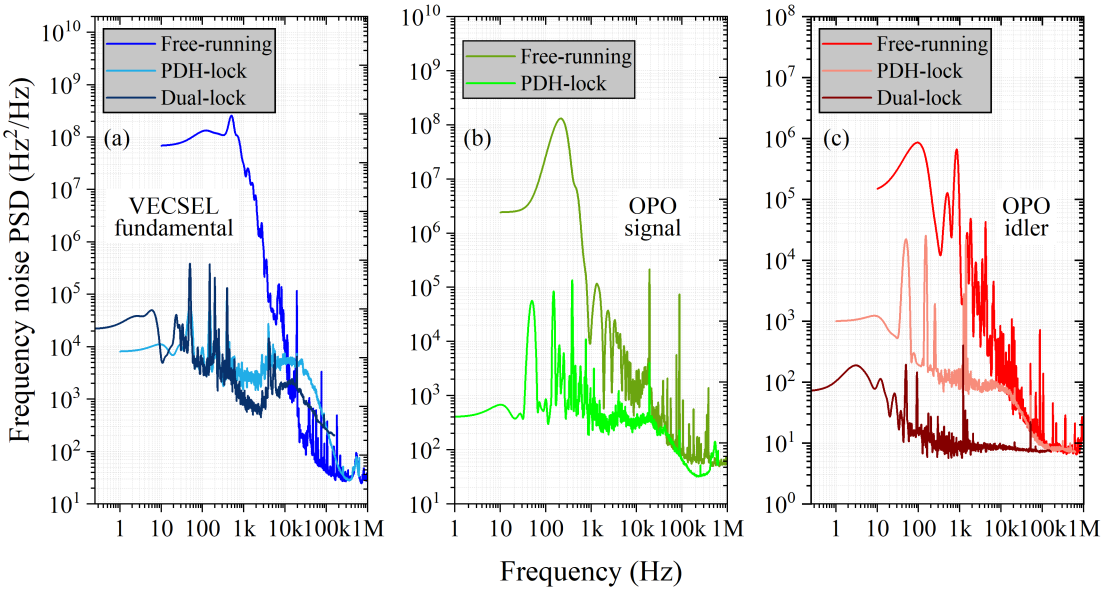


Figure 5.14: Comparison of the frequency noise power spectral density (FNPSD) for the interacting fields in the unlocked and locked regimes: (a) VECSEL fundamental, (b) OPO signal, and (c) OPO idler.

To synthesize the preceding analysis, Fig. 5.14 provides a direct comparison of the frequency-noise performance across all three interacting fields in both the unlocked and locked regimes. This unified view underscores the effectiveness of the active stabilisation schemes in suppressing low-frequency acoustic noise, mechanical vibrations, and thermal drift. This tightly constrains phase fluctuations across the VECSEL fundamental, signal, and idler waves, thereby narrowing their effective linewidths. Note that the differing Fourier frequency spans across the spectra reflect the tailored sampling rates and acquisition times used for each field's measurement.

With the system's RIN and FNPSD dynamics fully established under each control scheme, the analysis moves to quantifying the resulting phase coherence. The following section evaluates the spectral linewidths of the VECSEL fundamental, signal, and idler fields using numerical integration techniques.

5.10 Spectral linewidth characteristics of the ICSRO VECSEL

The spectral linewidths of the VECSEL fundamental, signal, and idler were obtained from the FNPSD data (see Section 5.9). In this section, we begin by examining the free-running linewidths of the ICSRO using three independent analysis methods. For the PDH-locked and dual-locked regimes, the full-width at half-maximum (FWHM) linewidths of each interacting wave were determined by reconstructing each optical field via autocorrelation and subsequently analysing the resulting autocorrelation function via the Wiener–Khinchine theorem [215]. This approach allows a direct comparison of the spectral coherence and phase stability of each wave under different stabilisation schemes.

5.10.1 Free-running regime

We begin by examining the free-running linewidth of the VECSEL fundamental, illustrated by the blue Gaussian-like curve in Fig. 5.15. A straightforward method to estimate this linewidth is by calculating the RMS value of the measured frequency fluctuations. This RMS linewidth, denoted as $\Delta\nu_{\mathrm{RMS}}$, represents the standard deviation of the instantaneous frequency variation from its mean value. Using the experimentally recorded frequency noise data, we obtain an RMS linewidth of:

$$\Delta\nu_{\mathrm{RMS}} = 364.5 \text{ kHz}. \tag{5.20}$$

Assuming that the laser output exhibits a Gaussian spectral profile, the corresponding FWHM linewidth can be related to the RMS value through the well-known relation [217]:

$$\Delta\nu_{\mathrm{FWHM}} = 2\sqrt{2\ln(2)}\,\Delta\nu_{\mathrm{RMS}}. \tag{5.21}$$

This relation arises from the definition of a Gaussian function, where the FWHM is linked to the standard deviation by a constant factor of $2\sqrt{2\ln(2)} \approx 2.355$. Hence, for

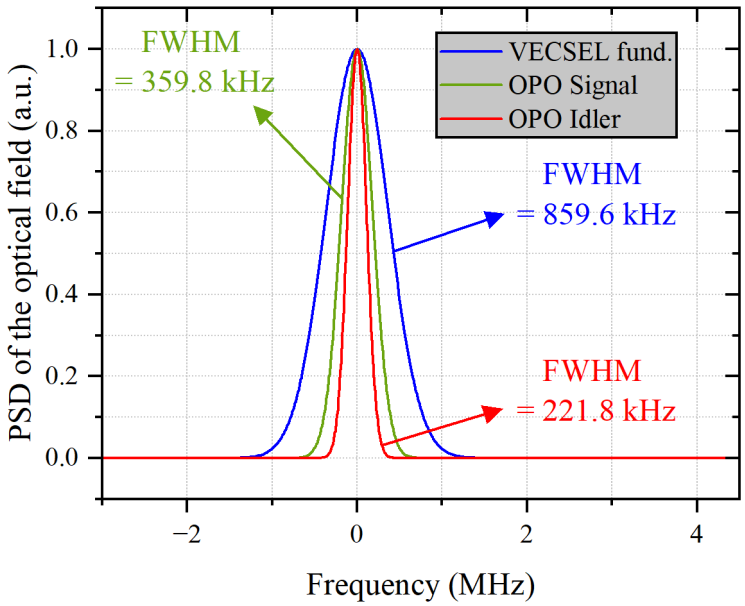


Figure 5.15: Characterisation of the spectral linewidth of the ICSRO VECSEL, via autocorrelation and the Weiner-Khintchine theorem, under free-running conditions. Figure adapted from Ref. [59].

the measured $\Delta\nu_{\mathrm{RMS}} = 364.5$ kHz, the corresponding Gaussian linewidth is calculated to be:

$$\Delta\nu_{\mathrm{FWHM}} \approx 2.355 \times 364.5 \text{ kHz} \approx 857.6 \text{ kHz}. \tag{5.22}$$

To further characterise the laser linewidth, we analyse the FNPSD, $S_\nu(f)$, using the method introduced by Di Domenico *et al.* [215]. This technique involves plotting the so-called β-separation line, which serves as a reference boundary for distinguishing between frequency noise components that contribute to linewidth broadening and those that do not. This β-separation line, denoted as $S_\beta(f)$, which is illustrated in all FNPSD plots (see Figs. 5.11–5.13), is defined as [215]:

$$S_\beta(f) = \frac{8\ln(2)}{\pi^2} f, \tag{5.23}$$

where f represents the Fourier frequency. This function splits the FNPSD spectrum into two regions: the portion of $S_\nu(f)$ that lies above $S_\beta(f)$ corresponds to frequency

fluctuations that directly broaden the laser linewidth (the so-called "Gaussian" region), while components lying below $S_\beta(f)$ contribute mainly to the Lorentzian wings of the spectral line shape. Using this approach, the FWHM linewidth of the laser can be estimated from the following expression [215]:

$$\Delta\nu_{\text{FWHM}} = \sqrt{8A\ln(2)}, \tag{5.24}$$

where the parameter A is defined as:

$$A = \int_{f_1}^{f_2} H\left[S_\nu(f) - S_\beta(f)\right] S_\nu(f)\, df. \tag{5.25}$$

Here, $H(x)$ denotes the Heaviside unit step function, defined as $H(x) = 1$ for $x \geq 0$ and $H(x) = 0$ otherwise. The inclusion of this function ensures that only those frequency noise components for which $S_\nu(f) > S_\beta(f)$ (i.e., the dominant contributors to linewidth broadening) are included in the integration.

Applying Eqs. (5.24) and (5.25) to the free-running VECSEL FNPSD curve of Fig. 5.11 (blue trace), with integration limits of $f_1 = 10$ Hz and $f_2 = 10$ kHz, yields a FWHM linewidth of:

$$\Delta\nu_{\text{FWHM}} = 857.5 \text{ kHz}, \tag{5.26}$$

which is in excellent agreement with the theoretical estimate obtained using Eq. (5.22).

Furthermore, it is also possible to use the FNPSD data of the free-running VECSEL to reconstruct its corresponding optical spectrum by first computing the autocorrelation function of the electric field $E(t)$. The temporal autocorrelation function $R_E(\tau)$, as derived in Ref. [217], is given by:

$$R_E(\tau) \propto \exp\left[-\int_{-\infty}^{\infty} S_\nu(f)\, \frac{1-\cos(2\pi f\tau)}{f^2}\, df\right], \tag{5.27}$$

where τ is the time delay and f denotes the Fourier frequency. In practice, the integration is carried out over a finite frequency range determined by the available experimental data. In our case, the integral is evaluated over the range [10 Hz, 1 MHz].

According to the Wiener–Khintchine theorem [217], the PSD of the optical field can be obtained by taking the Fourier transform of the autocorrelation function $R_E(\tau)$. This approach allows for the reconstruction of the laser's optical spectrum directly from its measured frequency noise characteristics. Applying this technique to the free-running VECSEL yields the optical spectrum shown in Fig. 5.15 (blue trace). The resulting profile exhibits a Gaussian-like shape with a FWHM linewidth of:

$$\Delta\nu_{\mathrm{FWHM}} = 859.6 \text{ kHz}, \tag{5.28}$$

over the specified frequency range of [10 Hz, 1 MHz]. This integrated linewidth is in excellent agreement with both RMS (see Eq. 5.22) and β-separation line (see Eq. 5.26) theoretical methods, further validating the consistency between the frequency-domain analysis and the reconstructed optical spectrum. This analytical approach was applied to all subsequent measurements, motivated by prior work from our group at the Institute of Photonics, University of Strathclyde, where Moriya *et al.* [135] validated this method for a two-mirror AlGaInP-based red-VECSEL. In this study, linewidths determined via autocorrelation and the Wiener–Khinchine theorem were confirmed against optical beat-note measurements using a commercial system locked to an ultra-stable, high-finesse cavity via PDH stabilisation. The close agreement between theory and experiment demonstrated that the Wiener–Khinchine approach provides a reliable estimate of spectral linewidths, especially when direct self-heterodyne measurements are impractical.

Extending this analysis to the free-running OPO down-converted fields, FWHM spectral linewidths of 359.8 kHz and 221.8 kHz were calculated (also using the autocorrelation and Weiner-Khintchine method) for an averaging time of 100 ms, for the OPO signal and idler, respectively (see Fig. 5.15). Here, the narrower free-running linewidths of the OPO down-converted waves (compared to the VECSEL fundamental) can be attributed to the splitting of the VECSEL frequency noise between the OPO signal and idler frequencies; a phenomenon that arises as a result of energy conservation inherent within

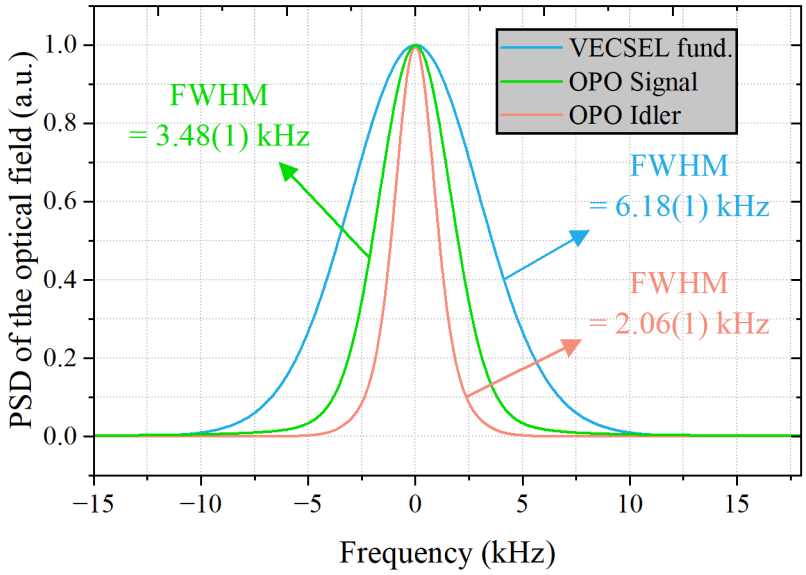


Figure 5.16: Characterisation of the spectral linewidth of the ICSRO VECSEL, via auto-correlation and the Weiner-Khintchine theorem, under the configuration where only the PDH servo loop was switched on (PDH-locked regime). Figure adapted from Ref. [59].

the down-conversion process. Further, the idler linewidth is narrower than the signal due to resonant enhancement of the OPO cavity which provides stronger feedback and filtering to the idler field.

5.10.2 PDH-lock-only regime

For the PDH-locked configuration (see Fig. 5.16), under an acquisition time of 1s, the spectral linewidths were again determined using the Wiener–Khinchine method [217]. From the resulting spectral profiles, a Voigt fitting function was applied to the PSD data, and the integrated linewidths were extracted by isolating the Gaussian contribution of the nonlinear fit. In this regime, the VECSEL fundamental linewidth was calculated to be 6.18(1) kHz, representing a reduction of two orders of magnitude compared to the free-running case. Significant narrowing of the linewidth is attributed to the fast and robust PDH-locking mechanism, which actively suppresses phase and frequency fluctuations of the VECSEL, particularly at low Fourier frequencies above the β-separation line. Here, the suppression of frequency noise increases the laser's coherence time, resulting in a

narrower and more well-defined optical spectrum. The OPO signal and idler linewidths, measured at 3.48(1) kHz and 2.06(1) kHz, respectively, show a similar narrowing effect, as expected. This stability is a direct result of the locked VECSEL pump field, as its reduced frequency noise is transferred to the down-converted signal and idler waves. Due to energy conservation within the PDC process, the frequency fluctuations of the OPO signal and idler are tightly constrained, leading to correlated linewidth narrowing.

5.10.3 Dual-lock regime

Lastly, for the dual-locked configuration (see Fig. 5.17), with a sampling time of 4s, the spectral line shape of the OPO idler is no longer Gaussian but instead more Lorentzian, which is consistent with the quasi-white spectrum obtained in Fig. 5.13. Upon reconstructing the optical field and applying the Wiener–Khinchine technique [217], a sub-kHz linewidth of 151(1) Hz was obtained by taking the dominant Lorentzian contribution from the Voigt fit. This result implies that the technical noise fluctuations associated with the idler field have been suppressed to such an extent that the intrinsic field noise is primarily governed by the quantum noise inherent to the PDC process, though the observed floor remains bounded by the shot-noise limit of the photocurrent and the electronic noise of the detection system.

Under this dual-locking configuration, the VECSEL fundamental linewidth was calculated to be 6.21(1) kHz (see Fig. 5.17), nearly identical to the linewidth obtained under PDH-locking (see Fig. 5.16). This outcome results from two competing effects: first, the longer sampling time in the dual-locking configuration increases the contribution of $1/f$ noise at low Fourier frequencies, which tends to broaden the measured linewidth relative to the case where only the PDH servo loop is switched on. Second, this broadening effect is partially offset by a likely reduction of mechanical noise from the DM, which is the only intracavity element separating the VECSEL and OPO cavities. The interplay of these opposing factors produces a linewidth comparable to that achieved under PDH-locking alone.

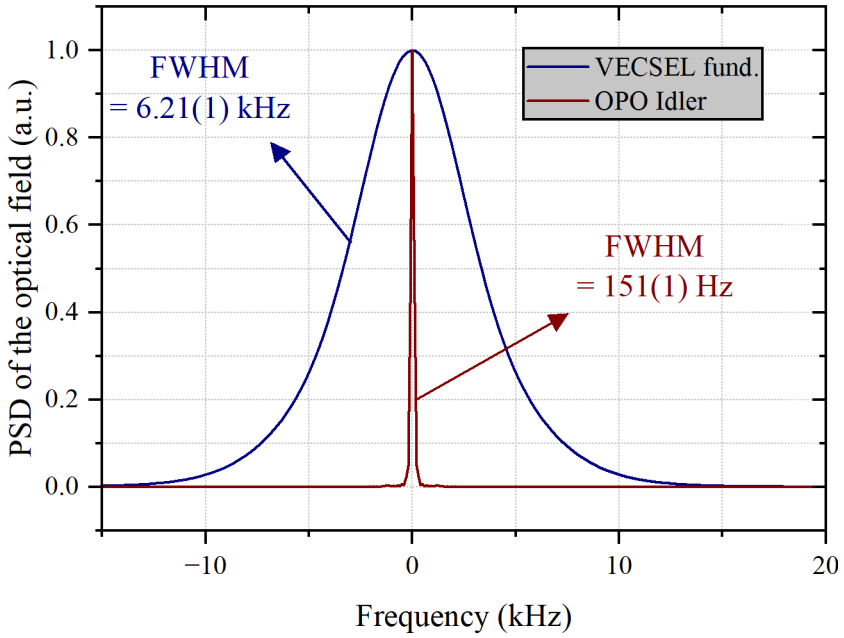


Figure 5.17: Characterisation of the spectral linewidth of the ICSRO VECSEL, via autocorrelation and the Weiner-Khintchine theorem, for the configuration where both PDH and SOF servo loops are switched on simultaneously (dual-locked regime). Figure adapted from Ref. [59].

The demonstrated linewidth narrowing underscores the utility of the dual-locked ICSRO VECSEL system for high-precision quantum optics applications, notably two-color continuous-variable (CV) entanglement [3]. In this regime, the OPO signal and idler exhibit exceptional phase stability, with linewidths below 10 kHz and 1 kHz, respectively. This performance arises from the intrinsically low-noise VECSEL architecture, combined with the flexibility of its external cavity, which allows straightforward integration of cavity PZTs for simultaneous stabilisation of the ICSRO VECSEL cavities.

Having quantified the frequency stability of the ICSRO VECSEL system through linewidth analysis across different stabilisation regimes, the discussion now turns to a broader comparison. The following section compares these results with externally-pumped OPOs found in the literature. This allows us to place the performance of the current ICSRO approach into a broader context.

5.10.4 Comparative analysis of frequency stability with externally-pumped OPOs

To the best of our knowledge, there are currently no reported approaches for active noise suppression in CW ICSRO systems in the literature. Previous investigations into noise suppression in solid-state-pumped systems have primarily focused on pulsed operation or self-pulsing damping strategies (e.g., SHG- or Raman-based damping) [42], [43]. These approaches differ fundamentally from the CW, single-frequency driven regime investigated in this work. For this reason, we have compared our results with externally-pumped OPO (ECOPO) systems, where active stabilisation techniques have been implemented, as summarised in Table 5.4. As shown, significant advancements have been made in stabilising externally-pumped singly-resonant OPO (SRO) devices, achieving narrow linewidths through locking to high-finesse FP cavities using PDH [216], [218], SOF [52], [53], [219] or peak-of-fringe (POF) [220] techniques. These locking methods have significantly improved the stability of both resonant [220] and non-resonant waves [53], [218], [219], as well as the second-harmonic (2ω) of the resonant wave [52], [216], in SRO laser systems. Notably, Ly *et al.* [219] reported a linewidth of 30 Hz (2s sampling time) for a 1 W CW ring-cavity SRO operating at 1.65 µm (see Table 5.4). In comparison, our ICSRO VECSEL system exhibited an integrated linewidth of 151(1) Hz for the resonant idler over an acquisition time of 4s. These results demonstrate that excellent frequency stability, similar to the most stable externally-pumped SROs, can be achieved even with an intracavity-pumped SRO in a linear standing-wave cavity, due to the ultra-low noise of the VECSEL architecture. The observed linewidths can be attributed to the implementation of dual-locking, in combination with the resonant periodic gain (RPG) quantum well (QW) arrangement and the minimal thermal lensing inherent to the VECSEL technology. While excellent frequency stability has been demonstrated, further improvements, such as implementing a more robust mechanism for the OPO cavity (e.g., PDH-locking instead of SOF-locking) and locking both VECSEL and OPO resonators to higher finesse FP reference cavities, could lead to further

Table 5.4: Comparison of frequency-stabilised OPO systems reported in the literature. 2ω = second-harmonic; λ = optical wavelength; λ_{lock} = locked wavelength; R = resonant; NR = non-resonant; Δv_{FWHM} = integrated linewidth; POF: peak-of-fringe; MgO:PPSLT: magnesium-oxide-doped periodically-poled stoichiometric lithium tantalate. Table adapted from Ref. [59], where λ_{lock} and Δv_{FWHM} replaces λ_L and $\Delta\nu$, respectively, for consistency with the thesis notation.

Pump Laser		**OPO crystal**	**Frequency stabilisation**				**Ref.**
Type	λ **(nm)**		**SRO wave**	λ_{lock} **(nm)**	$\Delta\nu_{\text{FWHM}}$ **(kHz)**	**Method**	
Nd:YVO_4	532 (2ω)	MgO:PPSLT (30 mm)	(2ω) Idler (R)	604	0.7	PDH	[216]
Nd:YAG	1064	MgO:PPLN (50 mm)	Idler (NR)	3390	4.6	PDH	[218]
Nd:YVO_4	532 (2ω)	MgO:PPSLT (30 mm)	(2ω) Idler (R)	602	4	SOF	[52]
Nd:YVO_4	532 (2ω)	MgO:PPSLT (30 mm)	Signal (NR)	947	13	SOF	[53]
Nd:YVO_4	532 (2ω)	MgO:PPSLT (30 mm)	Idler (NR)	1646	0.03	SOF	[219]
Yb-fibre amplifier	1064	MgO:PPLN (50 mm)	Signal (R)	1547	4	POF	[220]
PDH-locked VECSEL	690	MgO:PPLN (40 mm)	Idler (R)	1550	0.151	SOF	This work

noise reduction in order to target even narrower linewidths than the 30 Hz reported in Ref. [219].

5.11 Conclusion

In conclusion, this work has presented, to the best of our knowledge, the first study of the noise dynamics, including both frequency and intensity noise, within a ICSRO VECSEL system. The ICSRO VECSEL results presented here were obtained using an open tabletop system, and further improvements to laser stability and noise performance, particularly at low Fourier frequencies, are expected through passive stabilisation techniques, such as implementing a box enclosure to reduce the impact of environmental instabilities. Additional enhancements could be achieved through active stabilisation of intracavity elements (e.g., the quartz BRF and/or YAG etalon) and thermo-electric cool-

ing of the AlGaInP-based VECSEL gain region, which would reduce thermal fluctuations and improve noise reduction, particularly at low noise frequencies.

Despite this, the results – demonstrating RIN reductions of > 20 dB for all three ICSRO interacting waves – along with relaxation-oscillation-free ICSRO operation (due to the so-called Class-A dynamics of the VECSEL [166], [221]), position our dual-locked ICSRO VECSEL system to target intensity-difference squeezing in the near future. Compared with a recent study in which temporal instabilities in a CW ytterbium-doped potassium yttrium tungstate (Yb:KYW) ICSRO were suppressed via a two-photon absorption (TPA) mechanism [222], the free-running VECSEL fundamental demonstrated in this work exhibits superior performance. In particular, RIN levels > 40 dB lower are achieved at Fourier frequencies above 100 Hz. These findings underscore the distinct advantages of employing VECSEL gain media as OPO pump sources, achieving intensity noise suppression unattainable with conventional solid-state architectures. Moreover, we note that the sub-Poissonian intensity correlations and squeezing levels observed in below-threshold SROs are comparable to those of doubly-resonant OPOs [223], while offering a more straightforward experimental set-up. Therefore, the current VECSEL-pumped OPO system also represents a promising approach for high-precision applications, such as quantum sensing [48], [49], [224]. Furthermore, the open-cavity design, combined with the high down-conversion efficiency – exceeding 70% – already demonstrated in our ICSRO VECSEL system [58] (see Chapter 4), should enable power scaling from the current mW-level.

From a frequency-stability perspective, the ICSRO VECSEL system demonstrates sub-10 kHz integrated linewidths for the VECSEL fundamental and OPO signal (non-resonant) waves and, notably, sub-kHz linewidth for the OPO idler (resonant) wave. Analysis of the FNPSD data indicates that the singly resonant architecture enables the resonant idler to be stabilised well below the frequency noise level of the VECSEL fundamental, effectively redistributing excess pump noise into the non-resonant signal. While direct verification of this noise transfer was not possible in the present work due to the absence of an additional FPI reference for the signal, the observed suppression

of idler noise to levels significantly below that of the VECSEL strongly supports this interpretation.

While the current ICSRO VECSEL system demonstrates strong noise suppression, there remains scope for further optimisation. One clear improvement is the replacement of the SOF locking scheme with the more robust PDH technique for OPO cavity stabilisation. By referencing the phase of the reflected field, the PDH method effectively decouples frequency and intensity noise, producing an error signal largely insensitive to pump-induced amplitude fluctuations. In addition, locking both the VECSEL and OPO cavities to higher-finesse reference cavities would enhance frequency discrimination, helping to overcome limitations set by the detector noise floor. Together, these refinements could enable linewidths well below the current sub-10 kHz level, further establishing the ICSRO VECSEL as a stable and coherent platform for quantum optics experiments and for potential squeezed-light generation.

This chapter concludes the presentation and analysis of the experimental results contained in this thesis. Through these investigations, the implementation, optimisation, and development of a low-noise, compact laser source has been successfully demonstrated, highlighting its suitability for integration into future quantum experiments and related applications. The final chapter will synthesise the key concepts and findings presented throughout the thesis and draw the overall conclusions of this work.

Chapter 6

Conclusions

6.1 Introduction

In this thesis, we have presented the development and characterisation of low-noise optical parametric oscillators (OPOs), with particular emphasis on intracavity singly resonant OPOs (ICSROs) driven under continuous-wave (CW) pumping. Notably, we report the first direct evidence of single-frequency operation within an OPO pumped by a vertical-external-cavity surface-emitting laser (VECSEL). In addition, we present what is, to the best of our knowledge, the first detailed characterisation of the noise dynamics, including intensity and frequency noise, in a VECSEL-pumped OPO system. These results provide new insights into both the coherence properties and the amplitude stability of the ICSRO VECSEL system, underscoring its suitability as a coherent light source for high-precision applications.

The following chapter summarises the principal results and conclusions of this thesis. It also outlines potential avenues for future research, including both experimental optimisations and the development of an alternative theoretical cavity design. These developments are expected to enhance the performance of the current ICSRO VECSEL system, thereby making it well suited for applications such as intensity-difference squeezed light generation.

6.2 Summary of experimental results and conclusions

In the introductory chapter, four distinct operational configurations of the OPO were identified: the singly resonant OPO (SRO), the doubly resonant OPO (DRO), the triply resonant OPO (TRO), and the pump-enhanced OPO (PE-OPO). While the DRO, TRO, and PE-OPO benefit from notably low oscillation thresholds, their practical implementation as tunable, low-noise, and highly stable laser sources is significantly constrained by stringent requirements on cavity length and pump laser frequency control [12], [13], [16]. In contrast, the SRO imposes no such constraints, offering greater operational robustness; however, this comes at the cost of a substantially higher oscillation threshold [11].

To address this limitation, we proposed to use the intracavity OPO approach that exploits the high circulating power available within the pump laser cavity. This approach – referred to as the intracavity singly resonant OPO (ICSRO) – allows the OPO threshold to be reached with relatively modest external pump powers, thereby retaining the advantages of the SRO configuration while mitigating its primary drawback.

The concept of quasi-phase matching (QPM) [225] was reviewed as a method for precisely tailoring the phase matching condition of the OPO while utilising the material's highest nonlinearity coefficient. Among the well-developed nonlinear crystals suitable for QPM, magnesium-oxide-doped periodically-poled $LiNbO_3$ (MgO:PPLN) was selected as the optimal (nonlinear) gain medium for the ICSRO. This choice was motivated by its high effective nonlinearity coefficient, which reduces the power required to reach the SRO oscillation threshold. Furthermore, the addition of a small fraction of MgO improves thermal stability, enabling efficient operation at lower temperatures. An overview of the MgO:PPLN crystal was presented in Chapter 3.

Furthermore, the VECSEL was identified as an ideal pump source for driving the ICSRO. While solid-state lasers are strong candidates for OPO pumping – owing to their ability to deliver Watt-level powers with excellent beam quality – they are fundamentally limited in applications requiring low-noise operation, such as amplitude-squeezing

experiments. This constraint stems fundamentally from the Class-B dynamical behavior exhibited by these systems above the OPO threshold [26], which is characterised by quasi-continuous bursts of relaxation oscillations. Conversely, VECSELs operate within the Class-A dynamical regime, a consequence of their intrinsically short upper-state carrier lifetimes relative to the long cavity photon lifetimes. The inherent absence of relaxation oscillations ensures low-noise operation, which, when combined with the favorable size, weight, power and cost (SWaP-C) metrics of the VECSEL architecture, positions it as an optimal pump source for ICSROs in noise-sensitive quantum technologies. A brief literature review of VECSELs was later provided in Chapter 3.

Chapter 2 presented the fundamental theory of nonlinear optics as it pertains to OPO technology. In media lacking inversion symmetry, a diverse repertoire of nonlinear optical phenomena manifests, wherein the efficiency of coherent energy transfer among interacting electromagnetic fields is strictly governed by the fulfillment of the phase matching condition. By engineering this condition – such as through QPM in periodically-poled materials – desired nonlinear interactions can be selectively optimised. Expanding upon the earlier discussion of QPM, it was shown that phase matching can be tuned by varying either the pump frequency, grating period, or crystal temperature. The first two parameters enable coarse tuning, while varying the crystal temperature provides fine tuning, allowing the OPO output to access the telecom O-band (1.3 µm) and C-band (1.55 µm) for the signal and idler, respectively.

Chapter 2 also introduced a theoretical model developed by Stothard [60], aimed at identifying and quantifying the key parameters governing threshold reduction under practical operating conditions. The model highlights the importance of employing sufficiently long nonlinear crystals with high effective nonlinear coefficients, together with low-loss, high-reflectivity (HR) dielectric mirrors, to minimise round-trip cavity losses.

Chapter 3 detailed the design of the ICSRO, based on a 40-mm-long 5%-MgO:PPLN crystal incorporating nine grating periods (Λ_{QPM} = 13.83–17.10 µm). The crystal was incorporated into an AlGaInP-based red-VECSEL system utilising a four-mirror linear standing-wave configuration. Precise wavelength tunability and single-frequency oper-

ation were achieved via the implementation of intracavity spectral filtering elements, specifically a quartz birefringent filter (BRF) and fused silica etalons. The OPO was incorporated directly into the VECSEL cavity via a dichroic mirror (DM), forming a nested three-mirror ICSRO resonator. To facilitate efficient type-0 QPM, the 5%-MgO:PPLN crystal was aligned orthogonally ($\sim 90°$) relative to the resonator axis. The crystal was enclosed within a temperature-controlled oven operating across a range of 30–200°C, thereby enabling precise thermal optimisation and tuning of the phase matching condition.

Numerical cavity simulations, performed using the *Rezonator* software package, optimised the spatial overlap among all three ICSRO interacting waves. The final design produced confocally focussed beam waists for both the VECSEL fundamental and resonant idler at the centre of the 5%-MgO:PPLN crystal, with focussing parameters of $\xi^{p}_{\mathrm{foc}} = 1.09$ (VECSEL fundamental) and $\xi^{i}_{\mathrm{foc}} = 0.99$ (resonant idler) – values near the theoretical optimum for minimising the CW SRO threshold [177], [178]. A minor design compromise was necessary, as the mode-matching conditions at the centre of the 5%-MgO:PPLN crystal and at the VECSEL gain chip could not be simultaneously optimised. The cavity geometry was therefore selected to provide the best overall compromise between the two conditions.

Using the theoretical model developed by Stothard [60], in conjunction with the measured dielectric mirror characteristics and an estimated intracavity parasitic loss of $\sim$2%, the minimum intracavity VECSEL power required to reach ICSRO oscillation threshold was predicted to be 1.54 W. This value was later confirmed experimentally in Chapter 4.

Chapter 4 provided a comprehensive characterisation of the CW VECSEL-pumped OPO. The system operated at signal and idler wavelengths of 1245.2 nm and 1550.8 nm, respectively, corresponding to a fixed VECSEL wavelength of 690.6 nm, a 5%-MgO:PPLN grating period of 14.55 µm, and a stabilised crystal temperature of 114°C. The measured spectral width of 73 pm was well within the predicted pump acceptance bandwidth of 126 pm.

In the HR-idler regime, threshold pump powers of 0.99 W (for the VECSEL cavity) and 1.78 W (for the OPO cavity) were obtained, with the latter corresponding to an intracavity threshold of 1.59 W, in excellent agreement with theoretical predictions. Utilising the external pump laser at an input power of 2.96 W, a one-way signal output of 14.2 mW was measured, resulting in a total down-converted power of 53.3 mW and a corresponding down-conversion efficiency of 72.1%. Extrapolation indicates that, in the absence of thermal effects, optimal pump depletion – corresponding to 100% down-conversion efficiency – would occur at an input pump power of $\sim$3.2 W. Relative to the measured OPO threshold, this corresponds to only 1.8$\times$ threshold, which is significantly lower than the optimal operating conditions typically reported for externally-pumped OPOs ($\sim$2.5$\times$ threshold [187]).

In the output-coupled (OC) idler regime, the ICSRO threshold increased to 1.87 W. This increase is attributed to spatial variations in the gain characteristics across the VECSEL wafer structure, as the pump spot was translated to a different lateral position on the chip. At an input pump power of 2.96 W, the resonant idler and non-resonant signal outputs were measured to be 5.6 mW and 26.2 mW, respectively, corresponding to a total down-converted power of 51.9 mW. Moreover, in terms of efficiency, this corresponded to a total down-conversion efficiency of 70.2% and a total extraction efficiency of 43%. Given an OC transmission of 1.7%, the inferred total round-trip loss was $\sim$7%, in good agreement with independent estimates of (4.7 ± 0.3)% intracavity loss and (1.9 ± 0.1)% OC mirror insertion loss.

Temperature tuning of the 5%-MgO:PPLN crystal over a range of 90–180°C, under fixed pump conditions, yielded signal and idler tunabilities of 1.6 nm°C^{-1} and 2.7 nm°C^{-1}, respectively. This corresponded to tuning spans of 145 nm (1155–1300 nm) for the signal and 244 nm (1474–1718 nm) for the idler.

Moreover, passive power stability measurements were performed under single frequency and multimode pumping to verify the amplitude stability of the ICSRO VECSEL system. For above-threshold SRO operation, RMS fluctuations of 0.96% were observed, while below-threshold operation yielded 0.86%. These results confirm the excellent am-

plitude stability of the VECSEL pump source, even when operating above the OPO threshold. Furthermore, no measurable amplitude instability was observed over the short acquisition interval (i.e., 5 ms), supporting relaxation-oscillation-free operation of the VECSEL above OPO threshold. Under single-frequency operation, RMS fluctuations of 0.4%, 1.8%, and 2.3% were recorded for the VECSEL fundamental, non-resonant signal, and resonant idler, respectively, representing an approximately fourfold improvement compared to the multimode regime. These values are comparable to those reported for CW single-frequency Yb-fibre-pumped SROs [193], [194] and are nearly twice as stable as previously reported solid-state-pumped CW SROs [192], [195].

Building on the achievement of single-frequency operation, Chapter 5 focussed on the implementation of active frequency stabilisation for both the VECSEL fundamental and the OPO resonant idler cavities. Two independent feedback loops were deployed: the Pound–Drever–Hall (PDH) technique [207], [208] for VECSEL cavity locking, and the side-of-fringe (SOF) method [210] for OPO idler stabilisation. Despite the open tabletop configuration, simultaneous activation of both locks achieved strong noise suppression, with relative intensity noise (RIN) reductions exceeding 20 dB (at low Fourier frequencies) across all three ICSRO interacting waves compared to the free-running regime. This demonstrates the effectiveness of dual stabilisation in enhancing amplitude stability. Combined with the VECSELs Class-A dynamics, the dual-locked ICSRO VECSEL system is potentially suitable for intensity-difference squeezing experiments where ultra-low intensity noise is critical.

Chapter 5 also examined the relative frequency noise and integrated linewidths within the ICSRO VECSEL system. Under dual-locking conditions, all three ICSRO interacting waves exhibited sub-10 kHz integrated linewidths, determined by reconstructing the optical field via autocorrelation and using the Wiener–Khinchine theorem [217]. Most notably, the resonant idler linewidth narrowed to < 200 Hz – a reduction of more than three orders of magnitude from the free-running case (~ 220 kHz). The frequency-noise power spectral density (FNPSD) showed significant flattening under stabilisation, producing a quasi-white spectrum across a wide Fourier range. This behaviour highlights

the conservation of energy in the ICSRO: residual pump-frequency noise is transferred primarily to the non-resonant signal, while the resonant idler inherits the high spectral purity of its locking reference.

The results of Chapter 5 demonstrate that the ICSRO can achieve frequency stability comparable to the most stable externally-pumped SRO systems reported to date [52], [53], [216], [218], [219], [220]. Crucially, the ICSRO VECSEL architecture uniquely enables simultaneous stabilisation of both the VECSEL fundamental and OPO resonant idler cavities, thereby achieving excellent frequency stability even for the non-resonant signal wave. While the achievable degree of intensity-difference squeezing is theoretically independent of quantum phase noise, the simultaneous suppression of intensity and frequency noise across both down-converted fields uniquely positions the dual-locked ICSRO VECSEL system as a versatile platform for precision sensing [46], quantum information processing [54], and quantum-enhanced imaging [57].

6.3 Future work

In order to establish a viable strategy for the continued development of this research, we consider its prospective applications. As extensively discussed throughout this thesis, one of the potential applications of VECSEL-pumped OPOs lies in the generation of quantum states of light, with particular emphasis on achieving intensity-difference squeezing. Within the ICSRO VECSEL system, several approaches can be employed to enhance the degree of squeezing, thus optimising the system for applications in, for example, high-sensitivity spectroscopy [49]. These approaches, which primarily focus on design and engineering improvements, are discussed in the following paragraphs.

It is important to note that the ICSRO VECSEL results presented in this thesis were obtained using an open tabletop setup. As such, further improvements in laser performance – particularly in terms of stability and efficiency – are anticipated through the implementation of passive stabilisation techniques, including enhanced laser cavity design and improved system packaging. For instance, enclosing the ICSRO VECSEL

system within a protective housing can effectively suppress air currents and mitigate environmental noise. Additionally, lowering the beam height relative to the optical table (for example, from 10 cm to 5 cm) can further enhance the mechanical stability of the system. Further improvements can also be achieved through active stabilisation of the intracavity components, such as the quartz BRF and/or the YAG etalon. Moreover, implementing thermo-electric cooling of the AlGaInP-based VECSEL gain region can reduce thermal fluctuations, resulting in enhanced noise suppression, particularly in the low-frequency regime.

With respect to efficiency, two direct methods can be implemented to further enhance the down-conversion efficiency of the ICSRO VECSEL system. The first involves operating the SRO at its theoretically optimal pumping point, which may be achieved by extending the point of thermal rollover. The thermal load within the gain medium can be mitigated by expanding the pump spot area to decrease the localised pump power density; however, this scaling induces a commensurate expansion of the fundamental intracavity mode at the VECSEL chip surface, thereby necessitating a systematic re-evaluation of the cavity mode-matching conditions. In addition, the ICSRO should be re-optimised specifically for high down-conversion efficiency rather than for low-oscillation threshold. The initial focus on minimising the oscillation threshold stemmed from a conservative design approach, necessitated by the limited external pump power available during the experiments. As demonstrated by Guha *et al.* [177], [178], improved efficiency can be realised by re-designing the ICSRO resonator to achieve optimal focussing conditions, specifically targeting focussing parameters of $\xi^{p}_{\mathrm{foc}} = 1.0$ for the VECSEL fundamental and $\xi^{i}_{\mathrm{foc}} = 0.9$ for the resonant idler at the centre of the 5%-MgO:PPLN crystal.

While excellent stability has been achieved in both intensity and phase, further enhancements remain possible to suppress intensity and frequency noise and to attain even narrower spectral linewidths. One such enhancement involves implementing a more robust cavity-locking scheme for the OPO – specifically, replacing the SOF technique with the PDH method. The PDH scheme provides superior lock stability by using phase

modulation and coherent demodulation to generate a high-bandwidth, zero-crossing error signal. This signal is inherently immune to laser intensity noise and significantly less sensitive to environmental disturbances, thereby enabling precise, long-term resonance locking. Furthermore, locking the VECSEL and OPO to higher-finesse reference cavities would enhance frequency discrimination sensitivity, improving the signal-to-noise ratio of the lock and mitigating the impact of dark and shot noise on overall stability.

Although the dual-locked ICSRO VECSEL system shows promise for achieving intensity difference squeezing above OPO threshold, a key limitation remains in reaching the optimal degree of squeezing: namely, the imbalance between the energy decay rates, or cavity photon lifetimes, of the OPO signal and idler modes. This imbalance results in varying photocurrents when measured at the photodetectors. Consequently, technical noise from the VECSEL fundamental leaks into the intensity-difference spectrum, elevating the overall measurement noise floor. Three potential solutions exist to address this photocurrent imbalance. The first involves externally attenuating the photocurrent of the resonant idler, potentially using an electronic attenuator as demonstrated by Nie *et al.* [49]; however, this approach introduces uncorrelated electronic noise to both down-converted modes. The second option involves externally reducing the non-resonant signal photocurrent by incorporating a partially reflective mirror, though this also degrades the squeezing level by introducing vacuum fluctuations into the intensity-difference noise spectrum. Therefore, the most viable solution appears to be a complete redesign of the current experimental configuration to implement a dual-cavity intracavity DRO (ICDRO) system, as illustrated in Fig. 6.1. In such a configuration, the OPO signal and idler beams are internally separated and circulate within two distinct cavities, with both the signal and idler being resonant. This architecture allows both down-converted beams to exit through separate OC mirrors, offering the potential to achieve near-perfect photocurrent balance without introducing additional losses or unwanted noise from outside the OPO VECSEL cavity.

In contrast to dual-cavity OPO configurations presented in the literature [226], [227], where the pump frequency serves as one of the resonant fields, the design proposed here

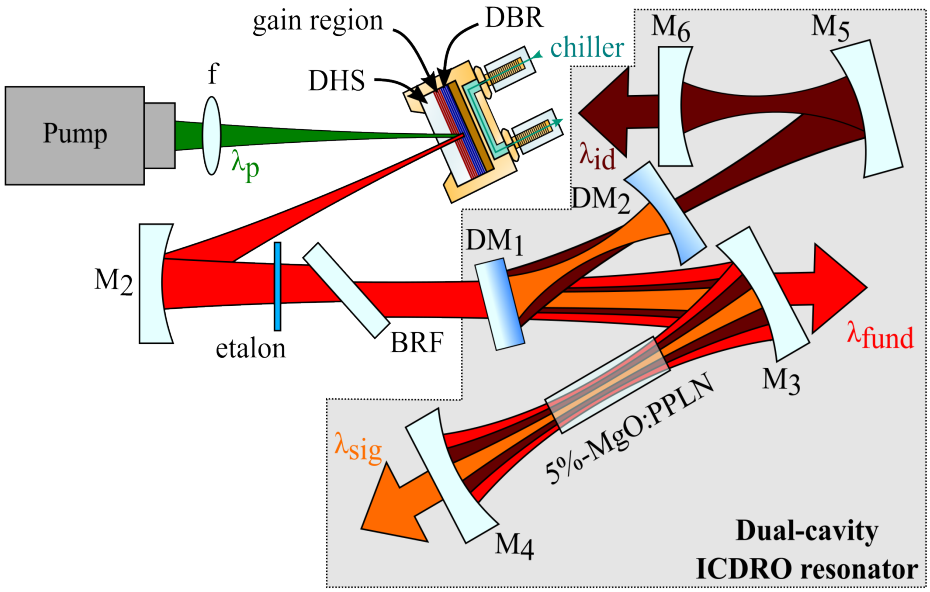


Figure 6.1: Schematic (not to scale) of the dual-cavity ICDRO VECSEL system, where both down-converted signal and idler frequencies are made resonant and internally separated. The VECSEL (DBR-M2-M3-M4), signal (DM2-DM1-M3-M4) and idler (M6-M5-DM1-M3-M4) cavities are collinear, with all three interacting waves escaping via different output-coupling mirrors. The optical elements are indicated as follows: f: lens; DBR: distributed Bragg reflector; DHS: diamond heat spreader; DM_x (x = 1,2): dichroic mirrors; M_x (x = 1,2...6): cavity mirrors; λ_p, λ_{fund}, λ_{sig}, λ_{id}: VECSEL pump, VECSEL fundamental, signal and idler wavelengths.

exclusively resonates the signal and idler frequencies. This approach effectively decouples all three interacting waves, allowing for independent output coupling through separate cavity mirrors. As a result, a similar level of tunability and stability can be obtained while providing the added benefit of further reducing the oscillation threshold compared to the conventional ICSRO configuration.

The primary application of the ICSRO VECSEL system is the generation of intensity-difference squeezed light. Of the principal factors limiting the achievable squeezing, pump intensity noise and photodetector quantum efficiency are not expected to be significant constraints for the present system, owing to the Class-A dynamics of the VECSEL and the availability of high-efficiency balanced detectors. Likewise, photocurrent imbalance between the signal and idler can be mitigated through appropriate cavity design (see

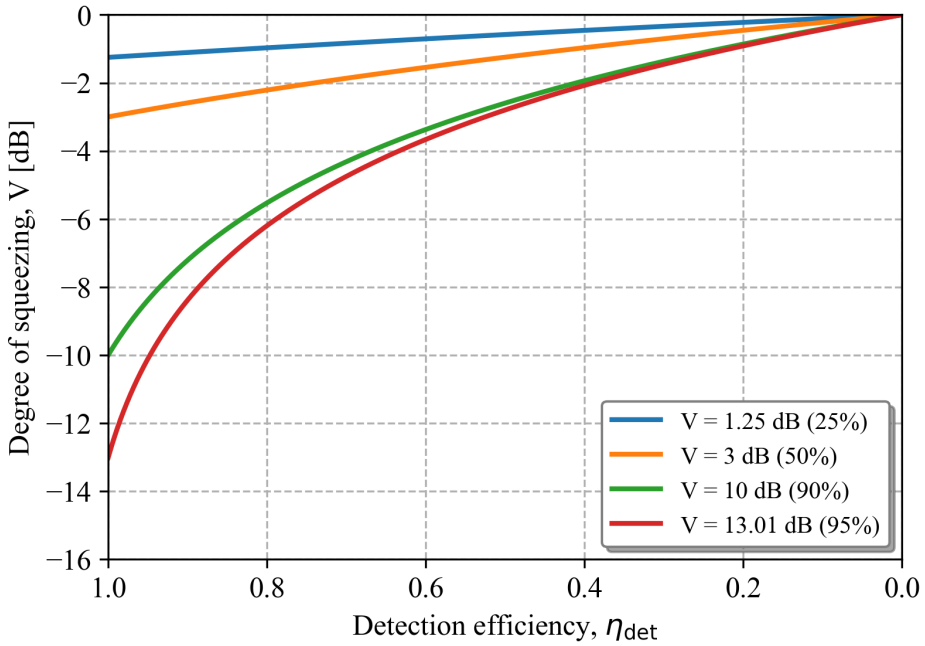


Figure 6.2: Degree of squeezing as a function of decreasing detection efficiency, illustrated for various initial squeezing levels (1.25 dB – 13.01 dB).

Fig 6.1). As a result, the dominant limitation in the current ICSRO, and in the newly designed dual-cavity ICDRO system, arises from intracavity losses in the OPO, which introduce uncorrelated vacuum fluctuations and reduce the achievable squeezing level. The following paragraph therefore models the sensitivity of the squeezing performance to optical loss.

In classical optical experiments, optical loss can often be compensated by increasing the optical power; however, this strategy is no longer valid for squeezed-light generation, where any loss irreversibly degrades the degree of squeezing. The variance of a squeezed state after optical loss V, is related to the pre-loss variance V_0 according to [228]:

$$V\ [\mathrm{dB}] = -10\log_{10}\left(\eta\, 10^{V_0\ [\mathrm{dB}]/10} + (1-\eta_{\mathrm{det}})\right), \tag{6.1}$$

where η_{det} denotes the total detection efficiency.

The impact of optical loss is illustrated in Fig. 6.2, which shows that higher initial squeezing levels experience more severe degradation for weaker detection efficiencies. Equation 6.1 further indicates that even in the limit of infinite initial squeezing, an intracavity loss of 10% limits the detectable degree of squeezing to 10 dB, while a loss of 50% restricts it to 3 dB. Consequently, the open VECSEL cavity design, which enables direct access to intracavity components and dielectric mirrors, offers a practical advantage by facilitating flexible optimisation towards low optical loss. This design approach can enable highly efficient operation, comparable to other well-optimised solid-state laser architectures, while benefiting from the inherently low-loss nature of the VECSEL configuration.

6.4 Conclusion

In this work, we present, to the best of our knowledge, the first realisation of an OPO pumped by a visible VECSEL system, specifically operating in the red spectral region via an AlGaInP-based gain structure. This system achieves CW single-frequency emission near the telecommunications O- and C-bands (1.3 µm and 1.55 µm, respectively). Of particular significance for applications in high-precision measurements – such as quantum optics experiments and the generation of squeezed states of light – we also report the first realisation of a dual-locked ICSRO VECSEL system. The system exhibits remarkably low intensity noise, alongside excellent frequency stability. The integrated spectral linewidth of the resonant idler is measured to be < 200 Hz, while the VECSEL fundamental and non-resonant signal exhibit integrated linewidths below 10 kHz.

Building on these results, future work will focus on the development of a dual-cavity ICDRO architecture. This next-generation system is expected to mitigate photocurrent imbalance issues inherent in singly-resonant designs, while preserving the low-noise characteristics of the VECSEL pump laser. Coupled with active frequency stabilisation techniques, this approach is anticipated to provide optimal squeezed light generation, particularly in regimes above the OPO threshold.

Bibliography

[1] A. K. Y. Ngai et al., "Continuous wave optical parametric oscillator for quartz-enhanced photoacoustic trace gas sensing," *Appl. Phys. B*, vol. 89, pp. 123–128, 2007.

[2] I. Ricciardi et al., "A narrow-linewidth optical parametric oscillator for mid-infrared high-resolution spectroscopy," *Mol. Phys.*, vol. 110, no. 17, pp. 2103–2109, 2012.

[3] A. S. Villar, M. Martinelli, and P. Nussenzveig, "Testing the entanglement of intense beams produced by a non-degenerate optical parametric oscillator," *Opt. Commun.*, vol. 242, pp. 551–563, 2004.

[4] A. S. Villar, L. S. Cruz, K. N. Cassemiro, M. Martinelli, and P. Nussenzveig, "Generation of bright two-color continuous variable entanglement," *Phys. Rev. Lett.*, vol. 95, 243603, 2005.

[5] A. S. Villar, K. N. Cassemiro, K. Dechoum, A. Z. Khoury, M. Martinelli, and P. Nussenzveig, "Entanglement in the above-threshold optical parametric oscillator," *J. Opt. Soc. Am. B*, vol. 24, no. 2, pp. 249–256, 2007.

[6] D. F. Walls, "Squeezed states of light," *Nature*, vol. 306, pp. 141–146, 1983.

[7] L.-A. Wu, H. J. Kimble, J. L. Hall, and H. Wu, "Generation of squeezed states by parametric down conversion," *Phys. Rev. Lett.*, vol. 57, no. 20, pp. 2520–2523, 1986.

[8] U. L. Andersen, T. Gehring, C. Marquardt, and G. Leuchs, "30 years of squeezed light generation," *Phys. Scr.*, vol. 91, no. 053001, pp. 1–11, 2016.

[9] C. Fabre, E. Giacobino, A. Heidmann, and S. Reynaud, "Noise characteristics of a non degenerate optical parametric oscillator - Application to quantum noise reduction," *J. Phys.*, vol. 50, pp. 1209–1225, 1989.

[10] W. R. Bosenberg, A. Drobshoff, J. I. Alexander, L. E. Myers, and R. L. Byer, "Continuous-wave singly resonant optical parametric oscillator based on periodically poled $LiNbO_3$," *Opt. Lett.*, vol. 21, no. 10, pp. 713–715, 1996.

[11] W. R. Bosenberg, A. Drobshoff, J. I. Alexander, L. E. Myers, and R. L. Byer, "93% pump depletion, 3.5-W continuous-wave, singly resonant optical parametric oscillator," *Opt. Lett.*, vol. 21, no. 17, pp. 1336–1338, 1996.

[12] F. G. Colville, A. J. Henderson, M. J. Padgett, J. Zhang, and M. H. Dunn, "Continuous-wave parametric oscillation in lithium triborate," *Opt. Lett.*, vol. 18, no. 3, pp. 205–207, 1993.

[13] R. G. Smith, J. E. Geusic, H. J. Levinstein, J. J. Rubin, S. Singh, and L. G. Van Uitert, "Continuous optical parametric oscillaiton in $Ba_2NaNb_5O_{15}$," *Appl. Phys. Lett.*, vol. 12, no. 9, pp. 308–310, 1968.

[14] R. C. Eckardt, C. D. Nabors, W. J. Kozlovsky, and R. L. Byer, "Optical parametric oscillator frequency tuning and control," *J. Opt. Soc. Am. B*, vol. 8, no. 3, pp. 646–667, 1991.

[15] A. J. Henderson, M. J. Padgett, F. G. Colville, J. Zhang, and M. H. Dunn, "Doubly-resonant optical parametric oscillators: Tuning behaviour and stability requirements," *Opt. Commun.*, vol. 119, pp. 256–264, 1995.

[16] G. Robertson, M. J. Padgett, and M. H. Dunn, "Continuous-wave singly resonant pump-enhanced type II LiB_3O_5 optical parametric oscillator," *Opt. Lett.*, vol. 19, no. 21, pp. 1735–1737, 1994.

[17] J. E. Hastie et al., "0.5-W single transverse-mode operation of an 850-nm diode-pumped surface-emitting semiconductor laser," *IEEE Photon. Tech. Lett.*, vol. 15, no. 7, pp. 894–896, 2003.

[18] J. E. Hastie et al., "High power CW red VECSEL with linearly polarized TEM_{00} output beam," *Opt. Express*, vol. 13, no. 1, pp. 77–81, 2005.

[19] M. A. Holm, D. Burns, A. I. Ferguson, and M. D. Dawson, "Actively stabilized single-frequency vertical-external-cavity AlGaAs laser," *IEEE Photon. Tech. Lett.*, vol. 11, no. 12, pp. 1551–1555, 1999.

[20] J. M. Rodríguez-García, D. Pabœuf, and J. E. Hastie, "Tunable, CW laser emission at 225 nm via intracavity frequency tripling in a semiconductor disk laser," *IEEE J. Sel. Top. Quantum Electron.*, vol. 23, no. 6, pp. 1–8, 2017.

[21] A. Khiar, M. Rahim, M. Fill, F. Felder, F. Hobrecker, and H. Zogg, "Continuously tunable monomode mid-infrared vertical external cavity surface emitting laser on Si," *Appl. Phys. Lett.*, vol. 97, 151104, 2010.

[22] J. E. Hastie, L. G. Morton, A. J. Kemp, M. D. Dawson, A. B. Krysa, and J. S. Roberts, "Tunable ultraviolet output from an intracavity frequency-doubled red vertical-external-cavity surface-emitting laser," *Appl. Phys. Lett.*, vol. 89, 061114, 2006.

[23] R. Casula, J.-P. Penttinen, A. J. Kemp, M. Guina, and J. E. Hastie, "1.4 µm continuous-wave diamond Raman laser," *Opt. Express*, vol. 25, no. 25, pp. 31 377–31 383, 2017.

[24] R. Casula, J.-P. Penttinen, M. Guina, A. J. Kemp, and J. E. Hastie, "Cascaded crystalline Raman lasers for extended wavelength coverage: Continuous-wave, third-Stokes operation," *Optica*, vol. 5, no. 11, pp. 1406–1413, 2018.

[25] M. Ebrahim-Zadeh, "Continuous-wave optical parametric oscillators," in *Handbook of Optics, Volume IV: Optical Properties of Materials, Nonlinear Optics, Quantum Optics*, M. Bass, Ed., 3rd, vol. 4, McGraw-Hill, 2010, pp. 1–33.

[26] D. J. M. Stothard, J.-M. Hopkins, D. Burns, and M. H. Dunn, "Stable, continuous-wave, intracavity, optical parametric oscillator pumped by a semiconductor disk laser (VECSEL).," *Opt. Express*, vol. 17, no. 13, pp. 10 648–10 658, 2009.

[27] N. Hempler, G. Robertson, C. Hamilton, G. T. Maker, and G. P. A. Malcolm, "Advances in narrow-linewidth, continuous-wave, semiconductor disk laser pumped optical parametric oscillators," in *Vertical External Cavity Surface Emitting Lasers (VECSELs) II, Proc. SPIE*, Vol. 8242, San Francisco, California, United States: SPIE, 2012, 82420J.

[28] S.-L. Tsai and C.-Y. Cho, "Generating dual-wavelength VECSEL by selecting birefringence filter material and the application toward mid-infrared region via intracavity OPO," *Opt. Express*, vol. 31, no. 15, pp. 24 555–24 565, 2023.

[29] F. Zernike and J. E. Midwinter, *Applied Nonlinear Optics*. New York, USA: John Wiley & Sons, 1973.

[30] G. A. Turnbull, M. H. Dunn, and M. Ebrahimzadeh, "Continuous-wave, intracavity optical parametric oscillators: An analysis of power characteristics," *Appl. Phys. B*, vol. 66, pp. 701–710, 1998.

[31] J. A. Giordmaine and R. C. Miller, "Tunable coherent parametric oscillation in $LiNbO_3$ at optical frequencies," *Phys. Rev. Lett.*, vol. 14, no. 24, pp. 973–976, 1965.

[32] O. G. Peterson, S. A. Tuccio, and B. B. Snavely, "CW operation of an organic dye solution laser," *Appl. Phys. Lett.*, vol. 17, no. 6, pp. 245–247, 1970.

[33] R. G. Smith, "A study of factors affecting the performance of a continuously pumped doubly resonant optical parametric oscillator," *IEEE J. Quantum Electron.*, vol. 9, no. 5, pp. 530–541, 1973.

[34] C. D. Nabors, R. C. Eckardt, W. J. Kozlovsky, and R. L. Byer, "Efficient, single-axial-mode operation of a monolithic MgO:$LiNbO_3$ optical parametric oscillator," *Opt. Lett.*, vol. 14, no. 20, pp. 1134–1136, 1989.

[35] C. D. Nabors, S. T. Yang, T. Day, and R. L. Byer, "Coherence properties of a doubly resonant monolithic optical parametric oscillator," *J. Opt. Soc. Am. B*, vol. 7, no. 5, pp. 815–820, 1990.

[36] J. A. Armstrong, N. Bloembergen, J. Ducuing, and P. S. Pershan, "Interactions between light waves in a nonlinear dielectric," *Phys. Rev.*, vol. 127, no. 6, pp. 1918–1939, 1962.

[37] F. G. Colville, M. H. Dunn, and M. Ebrahimzadeh, "Continuous-wave, singly-resonant, intracavity parametric oscillator," *Opt. Lett.*, vol. 22, no. 2, pp. 75–77, 1997.

[38] G. A. Turnbull, D. J. M. Stothard, M. Ebrahimzadeh, and M. H. Dunn, "Transient dynamics of cw intracavity singly resonant optical parametric oscillators," *IEEE J. Quantum Electron.*, vol. 35, no. 11, pp. 1666–1672, 1999.

[39] Y. Bai, J. Yu, N. P. Barnes, M. Petros, and S. Chen, "Compact intracavity pumped continuous-wave singly resonant PPLN OPO," in *Proc. CLEO/IQEC*, Technical Digest (CD), Optica Publishing Group, 2004, Paper CMI2.

[40] D. J. M. Stothard, M. Ebrahimzadeh, and M. H. Dunn, "Low-pump-threshold continuous-wave singly resonant optical parametric oscillator," *Opt. Lett.*, vol. 23, no. 24, pp. 1895–1897, 1998.

[41] D. J. M. Stothard, P.-Y. Fortin, A. Carleton, M. Ebrahimzadeh, and M. H. Dunn, "Comparison of continuous-wave optical parametric oscillators based on periodically poled $LiNbO_3$ and periodically poled $RbTiOAsO_4$ pumped internal to a high-power Nd:YVO_4 laser," *J. Opt. Soc. Am. B*, vol. 20, no. 10, pp. 2102–2108, 2003.

[42] D. J. M. Stothard and M. H. Dunn, "Relaxation oscillation suppression in continuous wave intracavity optical parametric oscillators," *Opt. Express*, vol. 18, no. 2, pp. 1336–1348, 2010.

[43] C.-Y. Cho and B.-T. Chen, "Exploring the criterion for the self-pulsing suppression of mid-IR intracavity OPO with self-Raman scattering," *Opt. Lett.*, vol. 49, no. 21, pp. 6253–6256, 2024.

[44] Y. A. Morozov, "Transient power characteristics of a compact singly resonant intracavity optical parametric oscillator pumped by a semiconductor disk laser," *J. Opt. Soc. Am. B*, vol. 33, no. 7, pp. 1470–1475, 2016.

[45] M. Myara, M. Sellahi, A. Laurain, A. Michon, I. Sagnes, and A. Garnache, "Noise Properties of NIR and MIR VECSELs," in *Proc. SPIE*, A. C. Tropper, Ed., Vol. 8606, SPIE, 2013, 86060Q.

[46] B. J. Lawrie, P. D. Lett, A. M. Marino, and R. C. Pooser, "Quantum sensing and squeezed light," *ACS Photonics*, vol. 6, pp. 1307–1318, 2019.

[47] C. Lindner, J. Kunz, S. J. Herr, J. Kießling, S. Wolf, and F. Kühnemann, "High-sensitivity quantum sensing with pump-enhanced spontaneous parametric down-conversion," *APL Photonics*, vol. 8, no. 5, 051301, 2023.

[48] P. H. Souto Ribeiro, C. Schwob, A. Maître, and C. Fabre, "Sub-shot-noise high-sensitivity spectroscopy with optical parametric oscillator twin beams," *Opt. Lett.*, vol. 22, no. 24, pp. 1893–1895, 1997.

[49] D. Nie, J. Feng, Y. Li, and K. Zhang, "Two-color quantum correlation between down-conversion beams at 1.5 and 3.3 µm from a singly resonant optical parametric oscillator," *Appl. Sci.*, vol. 10, 2698, 2020.

[50] D. Pabœuf and J. E. Hastie, "Tunable narrow linewidth AlGaInP semiconductor disk laser for Sr atom cooling applications," *Appl. Opt.*, vol. 55, no. 19, pp. 4980–4984, 2016.

[51] D. Pabœuf, P. J. Schlosser, and J. E. Hastie, "Frequency stabilization of an ultraviolet semiconductor disk laser," *Opt. Lett.*, vol. 38, no. 10, pp. 1736–1738, 2013.

[52] O. Mhibik, T.-H. My, D. Pabœuf, F. Bretenaker, and C. Drag, "Frequency stabilization at the kilohertz level of a continuous intracavity frequency-doubled singly resonant optical parametric oscillator," *Opt. Lett.*, vol. 35, no. 14, pp. 2364–2366, 2010.

[53] A. Ly, B. Szymanski, and F. Bretenaker, "Frequency stabilization of the non-resonant wave of a continuous-wave singly resonant optical parametric oscillator," *Appl. Phys. B*, vol. 120, pp. 201–205, 2015.

[54] T. D. Ladd, F. Jelezko, R. Laflamme, Y. Nakamura, C. Monroe, and J. L. O'Brien, "Quantum computers," *Nature*, vol. 464, pp. 45–53, 2010.

[55] P. Kómár et al., "A quantum network of clocks," *Appl. Phys. Express*, vol. 11, no. 4, 042801, 2018.

[56] K. Niizeki et al., "Ultrabright narrow-band telecom two-photon source for long-distance quantum communication," *Appl. Phys. Express*, vol. 11, no. 4, 042801, 2018.

[57] M. I. Kolobov, Ed., *Quantum Imaging*, 1st. New York, NY, USA: Springer-Verlag, 2007, ISBN: 978-0-387-33818-7.

[58] S. Anderson, P. H. Moriya, L. Caspani, and J. E. Hastie, "Single-frequency optical parametric oscillator intracavity-pumped by a visible VECSEL for low-noise down-conversion to 1.55 µm," *Opt. Express*, vol. 32, no. 3, pp. 4254–4266, 2024.

[59] S. Anderson, P. H. Moriya, L. Caspani, and J. E. Hastie, "Sub-kHz linewidth intracavity VECSEL-pumped OPO," *APL Photonics*, vol. 11, no. 2, 026112, 2026.

[60] D. J. M. Stothard, "Practical Continuous-Wave Intracavity Optical Parametric Oscillators," in *Advances in Optical and Photonic Devices*, K. Y. Kim, Ed., Rijeka, Croatia: InTech, 2010, pp. 293–328, ISBN: 978-953-7619-76-3.

[61] F. Pockels, *Lehrbuch der Kristalloptik*. Leipzig, Germany: B. G. Teubner, 1906, pp. 289–290.

[62] I. P. Kaminow and E. H. Turner, "Electrooptic light modulators," *Appl. Opt.*, vol. 5, no. 10, pp. 1612–1628, 1966.

[63] P. A. Franken, A. E. Hill, C. W. Peters, and G. Weinreich, "Generation of optical harmonics," *Phys. Rev. Lett.*, vol. 7, no. 4, pp. 118–119, 1961.

[64] R. W. Terhune, P. D. Maker, and C. M. Savage, "Observation of saturation effects in optical harmonic generation," *Appl. Phys. Lett.*, vol. 2, no. 3, pp. 54–55, 1963.

[65] R. W. Boyd, *Nonlinear Optics*, 4th. San Diego, CA, USA: Academic Press, 2020, ISBN: 978-0-323-85057-5.

[66] P. S. Pershan, "Nonlinear optical properties of solids: Energy considerations," *Phys. Rev.*, vol. 130, no. 3, pp. 919–929, 1963.

[67] N. Bloembergen, "Wave propagation in nonlinear electro-magnetic media," *Proc. IEEE*, vol. 51, no. 1, pp. 124–131, 1963.

[68] J. H. Hunt, P. Guyot-Sionnest, and Y. R. Shen, "Observation of C-H stretch vibrations of monolayers of molecules optical sum-frequency generation," *Chem. Phys. Lett.*, vol. 133, no. 3, pp. 189–192, 1987.

[69] Y. R. Shen, "Revisiting the basic theory of sum-frequency generation," *J. Chem. Phys.*, vol. 153, 180901, 2020.

[70] A. W. Smith and N. Braslau, "Observation of an optical difference frequency," *J. Appl. Phys.*, vol. 34, pp. 2105–2106, 1963.

[71] J. A. Giordmaine and R. C. Miller, "Optical parametric oscillator in the visible spectrum," *Appl. Phys. Lett.*, vol. 9, no. 8, pp. 298–300, 1966.

[72] B. R. Mollow and R. J. Glauber, "Quantum theory of parametric amplification," *Phys. Rev.*, vol. 160, no. 5, pp. 1076–1096, 1967.

[73] M. Bass, P. A. Franken, and J. F. Ward, "Optical rectification," *Phys. Rev.*, vol. 138, no. 2A, pp. 534–542, 1965.

[74] D. H. Auston, K. P. Cheung, J. A. Valdmanis, and D. A. Kleinman, "Cherenkov radiation from femtosecond optical pulses in electro-optic media," *Phys. Rev. Lett.*, vol. 53, no. 16, pp. 1555–1558, 1984.

[75] R. H. Stolen and A. Ashkin, "Optical Kerr effect in glass waveguide," *Appl. Phys. Lett.*, vol. 22, no. 6, pp. 294–296, 1973.

[76] Y. R. Shen and N. Bloembergen, "Theory of stimulated Brillouin and Raman scattering," *Phys. Rev.*, vol. 137, no. 6A, pp. 1787–1805, 1965.

[77] D. A. Kleinman, "Theory of second harmonic generation of light," *Phys. Rev.*, vol. 128, no. 4, pp. 1761–1775, 1962.

[78] T. Jungk, Á. Hoffmann, and E. Soergel, "New Insights into Ferroelectric Domain Imaging with Piezoresponse Force Microscopy," in *Ferroelectric Crystals for Photonic Applications: Including Nanoscale Fabrication and Characterization Techniques*, P. Ferraro, S. Grilli, and P. De Natale, Eds., Berlin, Heidelberg, Germany: Springer-Verlag, 2009, pp. 209–228, ISBN: 978-3-540-77963-6.

[79] D. Bonaccini and R. N. Smartt, "Lithium niobate double channel Fabry–Pérot interferometer for solar corona uses," *Appl. Opt.*, vol. 27, no. 24, pp. 5095–5102, 1988.

[80] I. Shoji, T. Kondo, A. Kitamoto, M. Shirane, and R. Ito, "Absolute scale of second-order nonlinear-optical coefficients," *J. Opt. Soc. Am. B*, vol. 14, no. 9, pp. 2268–2294, 1997.

[81] D. A. Roberts, "Simplified characterization of uniaxial and biaxial nonlinear optical crystals: A plea for standardization of nomenclature and conventions," *IEEE J. Quantum Electron.*, vol. 28, no. 10, pp. 2057–2074, 1992.

[82] P. D. Maker, R. W. Terhune, M. Nisenoff, and C. M. Savage, "Effects of dispersion and focusing on the production of optical harmonics," *Phys. Rev. Lett.*, vol. 8, no. 1, pp. 21–22, 1962.

[83] J. A. Giordmaine, "Mixing of light beams in crystals," *Phys. Rev. Lett.*, vol. 8, no. 1, pp. 19–20, 1962.

[84] M. Yamada, N. Nada, M. Saitoh, and K. Watanabe, "First-order quasi-phase matched $LiNbO_3$ waveguide periodically poled by applying an external field for efficient blue second-harmonic generation," *Appl. Phys. Lett.*, vol. 62, no. 5, pp. 435–436, 1993.

[85] X. P. Hu, P. Xu, and S. N. Zhu, "Engineered quasi-phase-matching for laser techniques," *Photon. Res.*, vol. 1, no. 4, pp. 171–185, 2013.

[86] M. M. Fejer, G. A. Magel, D. H. Jundt, and R. L. Byer, "Quasi-phase-matched second harmonic generation: Tuning and tolerances," *IEEE J. Quantum Electron.*, vol. 28, no. 11, pp. 2631–2654, 1992.

[87] N. P. Barnes and V. J. Corcoran, "Parametric generation processes: Spectral bandwidth and acceptance angles," *Appl. Opt.*, vol. 15, no. 3, pp. 696–699, 1976.

[88] O. Gayer, Z. Sacks, E. Galun, and A. Arie, "Temperature and wavelength dependant refractive index equations for MgO-doped congruent and stoichiometric $LiNbO_3$," *Appl. Phys. B*, vol. 91, pp. 343–348, 2008.

[89] D. J. M. Stothard, "Continuous-wave, singly resonant optical parametric oscillators pumped internal to Nd:YVO_4 lasers," Ph.D. dissertation, University of St Andrews, St Andrews, Scotland, UK, 2002.

[90] L. Moretti, M. Iodice, F. G. D. Corte, and I. Rendina, "Temperature dependance of the thermo-optic coefficient of lithium niobate, from 300 to 515 K in the visible and infrared regions," *J. Appl. Phys.*, vol. 98, 036101, 2005.

[91] A. V. Smith, "SNLO nonlinear optics code," *AS-Photonics, Albuquerque, NM*, 2024.

[92] T. Debuisschert, J. Raffy, J.-P. Pocholle, and M. Papuchon, "Intracavity optical parametric oscillator: Study of the dynamics in pulsed regime," *J. Opt. Soc. Am. B*, vol. 13, no. 7, pp. 1569–1587, 1996.

[93] G. A. Turnbull, "Continuous-wave intracavity optical parametric oscillators," Ph.D. dissertation, University of St Andrews, St Andrews, Scotland, UK, 1999.

[94] T. J. Edwards, "Continuous-wave, singly resonant optical parametric oscillation internal to the Ti:sapphire laser," Ph.D. dissertation, University of St Andrews, St Andrews, Scotland, UK, 2000.

[95] A. E. Seigman, "Nonlinear optical effects: An optical power limiter," *Appl. Opt.*, vol. 1, pp. 127–132, 1962.

[96] Tran-Ba-Chu and M. Broyer, "Intracavity single resonance optical parametric oscillator (I.S.R.O)," *J. Physique*, vol. 45, no. 10, pp. 1599–1606, 1984.

[97] O. G. Okhotnikov, *Semiconductor Disk Lasers: Physics and Technology*. Weinheim, Germany: Wiley-VCH, 2010, ISBN: 978-3-527-40933-4.

[98] M. Guina, A. Rantamäki, and A. Härkönen, "Optically pumped VECSELs: Review of technology and progress," *J. Phys. D: Appl. Phys.*, vol. 50, no. 383001, pp. 1–37, 2017.

[99] W. B. Jiang, S. R. Friberg, H. Iwamura, and Y. Yamamoto, "High powers and subpicosecond pulses from an external-cavity surface-emtting InGaAs/InP mulitple quantum well laser," *Appl. Phys. Lett.*, vol. 58, no. 8, pp. 807–809, 1991.

[100] M. Kuznetsov, F. Hakimi, R. Sprague, and A. Mooradian, "High-power (> 0.5-W CW) diode-pumped vertical-external-cavity surface-emitting semiconductor lasers with circular TEM_{00} beams," *IEEE Photon. Tech. Lett.*, vol. 9, no. 8, pp. 1063–1065, 1997.

[101] M. Kuznetsov, F. Hakimi, R. Sprague, and A. Mooradian, "Design and characteristics of high-power (>0.5-W CW) diode-pumped vertical-external-cavity surface-emitting lasers with circular TEM_{00} beams," *IEEE J. Sel. Top. Quantum Electron*, vol. 5, no. 3, pp. 561–573, 1999.

[102] D. I. Babic and S. W. Corzine, "Analytic expressions for the reflection delay, penetration depth, and absorptance of quarter-wave dielectric mirrors," *IEEE J. Quantum Electron*, vol. 28, no. 2, pp. 514–524, 1992.

[103] W. H. Bragg and W. L. Bragg, "The reflection of X-rays by crystals," *Proc. R. Soc. Lond. A*, vol. 88, pp. 428–438, 1913.

[104] E. Schrödinger, "An undulator theory of the mechanics of atoms and molecules," *Phys. Rev.*, vol. 28, no. 6, pp. 1049–1070, 1926.

[105] M. Y. A. Raja et al., "Resonant periodic gain surface-emitting semiconductor lasers," *IEEE J. Quantum Electron*, vol. 25, no. 6, pp. 1500–1512, 1989.

[106] A. Garnache, A. A. Kachanov, F. Stoeckel, and R. Houdré, "Diode-pumped broadband vertical-external-cavity surface-emitting semiconductor laser applied to high-sensitivity intracavity absorption spectroscopy," *J. Opt. Soc. Am. B*, vol. 17, no. 9, pp. 1589–1598, 2000.

[107] N. J. Ekins-Daukes, K. Kawaguchi, and J. Zhang, "Strain-balanced criteria for multiple quantum well structures and its signature in X-ray rocking curves," *Cryst. Growth Des.*, vol. 2, no. 4, pp. 287–292, 2002.

[108] Novalux Inc., *Technology*, `http://www.novalux.com`, 2003.

[109] S. Calvez, J. E. Hastie, M. Guina, O. G. Okhotnikov, and M. D. Dawson, "Semiconductor disk lasers for the generation of visible and ultraviolet radiation," *Laser & Photon. Rev.*, vol. 3, no. 5, pp. 407–434, 2009.

[110] S.-S. Beyertt et al., "Efficient gallium-arsenide disk laser," *IEEE J. Quantum Electron*, vol. 43, no. 10, pp. 869–875, 2007.

[111] F. Demaria et al., "Design of highly efficient high-power optically pumped semiconductor disk lasers," *IEEE J. Sel. Top. Quantum Electron*, vol. 15, no. 3, pp. 973–977, 2009.

[112] C. M. N. Mateo et al., "2.5 W continuous wave output at 665 nm from a multipass and quantum-well-pumped AlGaInP vertical-external-cavity surface emitting laser," *Opt. Lett.*, vol. 41, no. 6, pp. 1245–1248, 2016.

[113] J. W. Scott, R. S. Geels, S. W. Corzine, and L. A. Coldren, "Modeling temperature effects and spatial hole burning to optimize vertical-cavity surface-emitting laser performance," *IEEE J. Quantum Electron.*, vol. 29, no. 5, pp. 1295–1308, 1993.

[114] M. A. Holm, D. Burns, P. Cusumano, A. I. Ferguson, and M. D. Dawson, "High-power diode-pumped AlGaAs surface-emitting laser," *Appl. Opt.*, vol. 38, no. 27, pp. 5781–5784, 1999.

[115] A. C. Tropper and S. Hoogland, "Extended cavity surface-emitting semiconductor lasers," *Prog. Quantum. Electron.*, vol. 30, pp. 1–43, 2006.

[116] W. J. Alford et al., "Optically pumped semiconductor lasers for precision spectroscopic applications," *IEEE J. Quantum Electron*, vol. 49, no. 8, pp. 719–727, 2013.

[117] A. J. Kemp et al., "Thermal management in 2.3-µm semiconductor disk lasers: A finite element analysis," *IEEE J. Quantum Electron.*, vol. 44, no. 2, pp. 125–135, 2008.

[118] S. V. Kidalov and F. M. Shakhov, "Thermal conductivity of diamond composites," *Materials*, vol. 2, pp. 2467–2495, 2009.

[119] Y. Goldberg, M. E. Levinshtein, and S. Rumyantsev, "Silicon carbide (SiC)," in *Properties of Advanced Semiconductor Materials: GaN, AlN, InN, BN, SiC, SiGe*, M. E. Levinshtein, S. L. Rumyantsev, and M. S. Shur, Eds., New York, USA: John Wiley & Sons, 2001, pp. 93–147, ISBN: 978-0-471-35827-5.

[120] W. J. Alford, T. D. Raymond, and A. A. Allerman, "High power and good beam quality at 980 nm from a vertical external-cavity surface-emitting laser," *J. Opt. Soc. Am. B*, vol. 19, no. 4, pp. 663–666, 2002.

[121] J. Chilla, Q.-Z. Shu, H. Zhou, E. Weiss, M. Reed, and L. Spinelli, "Recent advances in optically pumped semiconductor lasers," in *Proc. SPIE*, Vol. 6451, San Jose, California, United States: SPIE, 2007, 645109.

[122] L. Fan et al., "Highly strained InGaAs/GaAs multiwatt vertical-external-cavity surface-emitting laser emitting around 1170 nm," *Appl. Phys. Lett.*, vol. 91, 131114, 2007.

[123] B. Heinen et al., "106 W continuous-wave output power from vertical-external-cavity surface-emitting laser," *Electron. lett.*, vol. 48, no. 9, pp. 516–517, 2012.

[124] S. Ranta, M. Tavast, T. Leinonen, N. van Lieu, G. Fetzer, and M. Guina, "1180 nm VECSEL with output power beyond 20 W," *Electron. lett.*, vol. 49, no. 1, pp. 59–60, 2013.

[125] M. Lukowski, C. Hessenius, and M. Fallahi, "Widely tunable high-power two-color VECSELs for new wavelength generation," *IEEE J. Quantum Electron*, vol. 21, no. 1, pp. 432–439, 2015.

[126] J. Chilla et al., "High-power optically pumped semiconductor lasers," in *Proc. SPIE*, Vol. 5332, San Jose, California, United States: SPIE, 2004, pp. 143–150.

[127] J.-H. Lee, S.-M. Lee, T. Kim, and Y.-J. Park, "7 W high-efficiency continuous-wave green light generation by intracavity frequency doubling of an end-pumped vertical external-cavity surface emitting semiconductor laser," *Appl. Phys. Lett.*, vol. 89, 241107, 2006.

[128] E. Kantola, T. Leinonen, S. Ranta, M. Tavast, and M. Guina, "High-efficiency 20 W yellow VECSEL," *Opt. Express*, vol. 22, no. 6, pp. 6372–6380, 2014.

[129] Y. Kaneda et al., "Continuous-wave, single-frequency 229 nm laser source for laser cooling of cadmium atoms," *Opt. Lett.*, vol. 41, no. 4, pp. 705–708, 2016.

[130] S. C. Burd et al., "VECSEL systems for quantum information processing with trapped beryllium ions," *J. Opt. Soc. Am. B*, vol. 40, no. 4, pp. 773–781, 2023.

[131] J. Lin, H. M. Pask, D. J. Spence, C. J. Hamilton, and G. P. A. Malcolm, "Continuous-wave VECSEL Raman laser with tunable lime-yellow-orange output," *Opt. Express*, vol. 20, no. 5, pp. 5219–5224, 2012.

[132] D. C. Parrotta, A. J. Kemp, M. D. Dawson, and J. E. Hastie, "Multiwatt, continuous-wave, tunable diamond Raman laser with intracavity frequency doubling to the visible region," *IEEE J. Quantum Electron*, vol. 19, no. 4, 1400108, 2013.

[133] D. C. Parrotta et al., "InGaAs-QW VECSEL emitting > 1300-nm via intracavity Raman conversion," in *Proc. SPIE*, Vol. 9734, San Francisco, California, United States: SPIE, 2016, 97340O.

[134] T. Schwarzbäck, M. Eichfelder, W.-M. Schulz, R. Roßbach, M. Jetter, and P. Michler, "Short wavelength red-emitting AlGaInP-VECSEL exceeds 1.2 W continuous wave output power," *Appl. Phys. B*, vol. 102, pp. 789–794, 2011.

[135] P. H. Moriya, Y. Singh, K. Bongs, and J. E. Hastie, "Sub-kHz-linewidth VECSELs for cold atom experiments," *Opt. Express*, vol. 28, no. 11, pp. 15 943–15 953, 2020.

[136] P. H. Moriya et al., "InGaN-diode-pumped AlGaInP VECSEL with sub-kHz linewidth at 689 nm," *Opt. Express*, vol. 29, no. 3, pp. 3258–3268, 2021.

[137] P. H. Moriya, M. Lee, and J. E. Hastie, "Low phase noise operation of a cavity-stabilized 698 nm AlGaInP-based VECSEL," *Opt. Express*, vol. 31, no. 17, pp. 28 018–28 025, 2023.

[138] M. Lee, P. H. Moriya, and J. E. Hastie, "Monolithic VECSEL for stable kHz linewidth," *Opt. Express*, vol. 31, no. 23, pp. 38 786–38 797, 2023.

[139] L. G. Morton, J. E. Hastie, M. D. Dawson, A. B. Krysa, and J. S. Roberts, "1W CW red VECSEL frequency-doubled to generate 60mW in the ultraviolet," in *Proc. CLEO/QELS*, Technical Digest, Long Beach, California, United States: Optica Publishing Group, 2006, Paper JWB16.

[140] H. Kahle, T. Schwarzbäck, M. Eichfelder, R. Roßbach, M. Jetter, and P. Michler, "UV laser emission around 330 nm via intracavity frequency doubling of a tunable red AlGaInP-VECSEL," in *Proc. SPIE*, Vol. 8242, San Francisco, California, United States: SPIE, 2012, 824206.

[141] T. Schwarzbäck, H. Kahle, M. Jetter, and P. Michler, "Frequency doubled AlGaInP-VECSEL with high output power at 331 nm and a large wavelength tuning range in the UV," in *Proc. SPIE*, Vol. 8432, Brussels, Belgium: SPIE, 2012, 84320W.

[142] S. A. Smith et al., "A diamond-microchip GaInNAs VECSEL operating at 1315 nm," in *Proc. LEOS*, Vol. 1, Rio Grande, Puerto Rico: IEEE, 2004, pp. 330–331.

[143] J.-M. Hopkins et al., "0.6 W CW GaInNAs vertical external-cavity surface emitting laser operating at 1.32 µm," *Electron. lett.*, vol. 40, no. 1, pp. 40–41, 2004.

[144] A. Härkönen et al., "High power frequency doubled GaInNAs semiconductor disk laser emitting at 615 nm," *Opt. Express*, vol. 15, no. 6, pp. 3224–3229, 2007.

[145] V.-M. Korpijärvi et al., "MBE growth GaInNAs-based multi-watt disk lasers," *J. Cryst. Growth*, vol. 311, pp. 1868–1871, 2009.

[146] J. Rautiainen et al., "Wafer fused optically-pumped semiconductor disk laser operating at 1220 nm," in *Proc. CLEO/Europe–EQEC*, Conference Digest, Munich, Germany: Optica Publishing Group, 2009, Paper CB5.3.

[147] J. Lyytikäinen et al., "High-Power 1.48-µm wafer-fused optically pumped semiconductor disk laser," *IEEE Photon. Tech. Lett.*, vol. 23, no. 13, pp. 917–919, 2011.

[148] A. Rantamäki et al., "1 W at 785 nm from a frequency-doubled wafer-fused semiconductor disk laser," *Opt. Express*, vol. 20, no. 8, pp. 9046–9051, 2012.

[149] T. Leinonen, V. Iakovlev, A. Sirbu, E. Kapon, and M. Guina, "33 W continuous output power semiconductor disk laser emitting at 1275 nm," *Opt. Express*, vol. 25, no. 6, pp. 7008–7013, 2017.

[150] P. J. Schlosser, J. E. Hastie, S. Calvez, A. B. Krysa, and M. D. Dawson, "InP/AlGaInP quantum dot semiconductor disk lasers for CW TEM_{00} emission at 716-755 nm," *Opt. Express*, vol. 17, no. 24, pp. 21 782–21 787, 2009.

[151] A. Härkönen et al., "Tunable self-seeded semiconductor disk laser operating at 2 µm," *Electron. lett.*, vol. 43, no. 8, pp. 457–458, 2007.

[152] N. Schulz et al., "Effect of the cavity resonance-gain offset on the output power characteristics of GaSb-based VECSELs," *IEEE Photon. Tech. Lett.*, vol. 19, no. 21, pp. 1741–1743, 2007.

[153] B. Rösener, N. Schulz, M. Rattunde, C. Manz, K. Köhler, and J. Wagner, "High-power high-brightness operation of a 2.25-µm (AlGaIn)(AsSb) based barrier-pumped vertical external cavity surface emitting laser," *IEEE Photon. Tech. Lett.*, vol. 20, no. 7, pp. 502–504, 2008.

[154] T. Töpper et al., "High-power 2.0 µm semiconductor disk laser - influence of lateral lasing," *Appl. Phys. Lett.*, vol. 100, 192107, 2012.

[155] M. Rahim, A. Khiar, M. Fill, F. Felder, and H. Zogg, "Continuously tunable singlemode VECSEL at 3.3 mm wavelength for spectroscopy," *Electron. lett.*, vol. 47, no. 18, pp. 1037–1039, 2011.

[156] M. Fill, A. Khiar, M. Rahim, F. Felder, and H. Zogg, "PbSe quantum well mid-infrared vertical external cavity surface emitting laser on Si-substrates," *J. Appl. Phys.*, vol. 109, 093101, 2011.

[157] A. Garnache, A. A. Kachanov, F. Stoeckel, and R. Planel, "High-sensitivity intracavity laser absorption spectroscopy with vertical-external-cavity surface-emitting semiconductor lasers," *Opt. Lett.*, vol. 24, no. 12, pp. 826–828, 1999.

[158] E. Bertseva and A. Campargue, "Spectral condensation near molecular transitions in intracavity laser spectroscopy with vertical external cavity surface emitting lasers," *Opt. Commun.*, vol. 232, pp. 251–261, 2004.

[159] O. Naumenko, O. Leshchishina, and A. Campargue, "High sensitivity absorption spectroscopy of HDO by ICLAS-VeCSEL between 9100 and 9640 cm^{-1}," *J. Mol. Spectrosc.*, vol. 236, pp. 58–69, 2006.

[160] L. Brancaleon and H. Moseley, "Laser and non-laser light sources for photodynamic therapy," *Lasers Med. Sci.*, vol. 17, pp. 173–186, 2002.

[161] M. Vilera et al., "2.7 W diffraction-limited yellow lasers by efficient frequency doubling of high-brightness tapered diode lasers," *Opt. Commun.*, vol. 435, pp. 145–149, 2019.

[162] E. Kantola et al., "Clinical study for assessing the use of a compact VECSEL-based yellow (590 nm) laser system in the treatment of vascular lesions," in *Proc. CLEO/Europe–EQEC*, Conference Digest, Munich, Germany: Optica Publishing Group, 2019, Paper CL_1_6.

[163] G. J. Fetzer et al., "Development and demonstration of a VECSEL based sodium guidestar system," in *Proc. SPIE*, C. Lei and L. A. Graham, Eds., Vol. 13911, San Francisco, California, United States: SPIE, 2026, 1391104.

[164] Coherent Inc., *Verdi*, `https://www.coherent.com/lasers/cw-solid-state/verdi`, 2026.

[165] Coherent Inc., "Introducing the Verdi G10: Technology proven in the most noise-sensitive applications," Coherent Inc., Tech. Rep., 2011, White Paper. [Online]. Available: `https://www.coherent.com/resources/tech-notes/lasers/Verdi-G-Series-Lasers-Technology-Proven-in-the-Most-Noise-Sensitive-Applications.pdf`

[166] F. T. Arecchi, G. L. Lippi, G. P. Puccioni, and J. R. Tredicce, "Deterministic chaos in laser with injected signal," *Opt. Commun.*, vol. 51, no. 5, pp. 308–314, 1984.

[167] A. G. White, T. C. Ralph, and H.-A. Bachor, "Active versus passive squeezing by second-harmonic generation," *J. Opt. Soc. Am. B*, vol. 13, no. 7, pp. 1337–1346, 1996.

[168] J. R. Thornton, W. D. Fountain, G. W. Flint, and T. G. Crow, "Properties of neodymium laser materials," *Appl. Opt.*, vol. 8, no. 6, pp. 1087–1102, 1969.

[169] A. A. Ballman, "Growth of piezoelectric and ferroelectric materials by the Czochralski technique," *J. Am. Ceram. Soc.*, vol. 48, pp. 112–113, 1965.

[170] D. Zhu et al., "Integrated photonics on thin-film lithium niobate," *Adv. Opt. Photon.*, vol. 13, no. 2, pp. 242–352, 2021.

[171] P. Loza-Alvarez, C. T. A. Brown, D. T. Reid, W. Sibbett, and M. Missey, "High-repetition-rate ultrashort-pulse optical parametric oscillator continuously tunable from 2.8 to 6.8 µm," *Opt. Lett.*, vol. 24, no. 21, pp. 1523–1525, 1999.

[172] J. F. A. Rida, "A survey of the mechanisms impairing optical fiber communications performance," *J. Electr. Syst.*, vol. 20, pp. 2192–2215, 2024.

[173] S. Wehner, D. Elkouss, and R. Hanson, "Quantum internet: A vision for the road ahead," *Science*, vol. 362, pp. 1–9, 2018.

[174] P. H. Moriya, M. Lee, and J. E. Hastie, "Sub-kilohertz linewidth free-running monolithic cavity VECSEL with 10^{-12} stability," *Appl. Phys. Lett.*, vol. 125, p. 021 101, 2024.

[175] H. Kogelnik and T. Li, "Laser Beams and Resonators," *Appl. Opt.*, vol. 5, no. 10, pp. 1550–1567, 1966.

[176] G. D. Boyd and D. A. Kleinman, "Parametric interaction of focused Gaussian light beams," *J. Appl. Phys.*, vol. 39, no. 8, pp. 3597–3639, 1968.

[177] S. Guha, F.-J. Wu, and J. Falk, "The effects of focusing on parametric oscillation," *IEEE J. Quantum Electron*, vol. 18, no. 5, pp. 907–912, 1982.

[178] S. Guha, "Focusing dependence of the efficiency of a singly resonant optical parametric oscillator," *Appl. Phys. B*, vol. 66, pp. 663–675, 1998.

[179] T. J. Kane and R. L. Byer, "Monolithic, unidirectional single-mode Nd:YAG ring laser," *Opt. Lett.*, vol. 10, no. 2, pp. 65–67, 1985.

[180] A. E. Siegman, *Lasers*. Mill Valley, CA, USA: University Science Books, 1986, ISBN: 978-0-935702-11-8.

[181] O. Svelto, *Principles of Lasers*, 5th. New York, NY, USA: Springer, 2010, ISBN: 978-1-4419-1301-2.

[182] U. Levy, Y. Silberberg, and N. Davidson, "Mathematics of vectorial Gaussian beams," *Adv. Opt. Photon.*, vol. 11, no. 4, pp. 828–891, 2019.

[183] J. A. Caird, S. A. Payne, P. R. Staver, A. J. Ramponi, L. L. Chase, and W. F. Krupke, "Quantum electronic properties of the $Na_3Ga_2Li_3F_{12}$:Cr^{3+} laser," *IEEE J. Quantum Electron.*, vol. 24, no. 6, pp. 1077–1099, 1988.

[184] D. Findlay and R. A. Clay, "The measurement of internal losses in 4-level lasers," *Phys. Lett.*, vol. 20, no. 3, pp. 277–278, 1966.

[185] J. E. Hastie, "High Power Surface Emitting Semiconductor Lasers," Ph.D. dissertation, University of Strathclyde, Glasgow, Scotland, UK, 2004.

[186] International Organization for Standardization. "Lasers and laser-related equipment — test methods for laser beam widths, divergence angles, and beam propagation ratios — part 1: Stigmatic and simple astigmatic beams." ISO 11146-1:2021. [Online]. Available: `https://www.iso.org/standard/77769.html`

[187] M. Ebrahimzadeh and M. H. Dunn, "Optical Parametric Oscillators," in *Handbook of Optics, Volume IV: Fiber Optics & Nonlinear Optics*, M. Bass, Ed., 2nd, New York, NY, USA: McGraw-Hill, 2001, pp. 22.1–22.71, ISBN: 978-0-07-136456-0.

[188] T. J. Edwards, G. A. Turnbull, M. H. Dunn, and M. Ebrahimzadeh, "Continuous-wave, singly-resonant, optical parametric oscillator based on periodically poled $KTiOPO_4$," *Opt. Express*, vol. 6, no. 3, pp. 58–63, 2000.

[189] Y. Yu et al., "Continuous-wave intracavity multiple optical parametric oscillator using an aperiodically poled lithium niobate around 1.57 and 3.84 µm," *IEEE Photon. J.*, vol. 9, no. 2, pp. 1–8, 2017.

[190] Y. Li, Z. Ding, P. Liu, G. Chen, and Z. Zhang, "Widely tunable, continuous-wave, intra-cavity optical parametric oscillator based on an Yb-doped fiber laser," *Opt. Lett.*, vol. 43, no. 21, pp. 5391–5394, 2018.

[191] R. Casula, "Broadly tunable VECSEL-pumped crystalline Raman laser," Ph.D. dissertation, University of Strathclyde, Glasgow, Scotland, UK, 2019.

[192] M. Ebrahimzadeh, G. A. Turnbull, T. J. Edwards, D. J. M. Stothard, I. D. Lindsay, and M. H. Dunn, "Intracavity continuous-wave singly resonant optical parametric oscillators," *J. Opt. Soc. Am. B*, vol. 16, no. 9, pp. 1499–1511, 1999.

[193] K. Devi, S. C. Kumar, and M. Ebrahim-Zadeh, "High-power, continuous-wave, single-frequency, all-periodically-poled, near-infrared source," *Opt. Lett.*, vol. 37, no. 24, pp. 5049–5051, 2012.

[194] M. K. Shukla and R. Das, "High-power single-frequency source in the mid-infrared using a singly resonant optical parametric oscillator pumped by a Yb-fiber laser," *IEEE J. Sel. Top. Quantum. Electron*, vol. 24, no. 5, pp. 1–6, 2018.

[195] G. K. Samanta, G. R. Fayaz, and M. Ebrahim-Zadeh, "1.59 W, single-frequency, continuous-wave optical parametric oscillator based on MgO:sPPLT," *Opt. Lett.*, vol. 32, no. 17, pp. 2623–2625, 2007.

[196] R. Paschotta, "Laser noise," *Encyclopedia of Laser Physics and Technology*, 2025.

[197] C. H. Henry, "Theory of the linewidth of semiconductior lasers," *IEEE J. Quantum Electron.*, vol. 18, no. 2, pp. 259–264, 1982.

[198] G. Baili, M. A. T. Malherbe, D. Dolfi, I. Sagnes, and F. Bretenaker, "Direct observation of the Class-B to Class-A transition in the dynamical behavior of a semiconductor laser," *EPL*, vol. 87, 44005, 2009.

[199] A. Yariv and P. Yeh, *Photonics: Optical Electronics in Modern Communications*, 6th. New York, NY, USA: Oxford University Press, 2007, ISBN: 978-0-19-517946-0.

[200] S. Valling, T. Fordell, and A. M. Lindberg, "Maps of the dynamics of an optically injected solid-state laser," *Phys. Rev. A*, vol. 72, 033810, 2005.

[201] R. Paschotta, "Frequency noise," *Encyclopedia of Laser Physics and Technology*, 2025.

[202] R. Paschotta, "Noise in laser technology (Part 1): Intensity and phase Noise," *Optik & Photonik*, vol. 4, pp. 48–50, 2009.

[203] S. Pes et al., "Class-A operation of an optically-pumped 1.6 µm-emitting quantum dash-based vertical-external-cavity surface-emitting laser on InP," *Opt. Express*, vol. 25, no. 10, pp. 11 760–11 766, 2017.

[204] A. Kerchaoui et al., "Electrically pumped shot-noise limited Class A VECSEL at telecom wavelength," *Opt. Lett.*, vol. 46, no. 10, pp. 2465–2468, 2021.

[205] TOPTICA Photonics SE, "Phase and frequency locking of diode lasers," TOPTICA Photonics SE, Application Note. [Online]. Available: `https://www.toptica.com/`

[206] R. V. Pound, "Electronic frequency stabilization of microwave oscillators," *Rev. Sci. Instrum.*, vol. 17, no. 11, pp. 490–505, 1946.

[207] R. W. P. Drever et al., "Laser phase and frequency stabilization using an optical resonator," *Appl. Phys. B*, vol. 31, pp. 97–105, 1983.

[208] E. D. Black, "An introduction to Pound-Drever-Hall laser frequency stabilization," *Am. J. Phys.*, vol. 69, no. 1, pp. 79–87, 2001.

[209] G. C. Goodwin, S. F. Graebe, and M. E. Salgado, *Control System Design*. Upper Saddle River, NJ, USA: Prentice Hall, 2001, ISBN: 978-0-13-958653-8.

[210] R. L. Barger, M. S. Sorem, and J. L. Hall, "Frequency stabilization of a cw dye laser," *Appl. Phys. Lett.*, vol. 22, no. 11, pp. 573–575, 1973.

[211] N. Uehara and K. Ueda, "Accurate measurement of ultralow loss in a high-finesse Fabry–Pérot interferometer using the frequency response functions," *Appl. Phys. B*, vol. 61, pp. 9–15, 1995.

[212] R. Paschotta, "Finesse," *Encyclopedia of Laser Physics and Technology*, 2025.

[213] R. Paschotta, "Shot noise," *Encyclopedia of Laser Physics and Technology*, 2025.

[214] M. Tröbs and G. Heinzel, "Improved spectrum estimation from digitized time series on a logarithmic frequency axis," *Measurement*, vol. 39, pp. 120–129, 2006.

[215] D. Di Domenico, S. Schilt, and P. Thomann, "Simple approach to the relation between laser frequency noise and laser line shape," *Appl. Opt.*, vol. 49, no. 25, pp. 4801–4807, 2010.

[216] O. Mhibik, D. Pabœuf, C. Drag, and F. Bretenaker, "Sub-kHz-level relative stabilization of an intracavity doubled continuous-wave optical parametric oscillator using Pound-Drever-Hall scheme," *Opt. Express*, vol. 19, no. 19, pp. 18 049–18 057, 2011.

[217] D. S. Elliott, R. Roy, and S. J. Smith, "Extracavity laser band-shape and bandwidth modification," *Phys. Rev. A*, vol. 26, no. 1, pp. 12–18, 1982.

[218] I. Ricciardi et al., "Sub-kilohertz linewidth narrowing of a mid-infrared optical parametric oscillator idler frequency by direct cavity stabilization," *Opt. Lett.*, vol. 40, no. 20, pp. 4743–4746, 2015.

[219] A. Ly, C. Siour, and F. Bretenaker, "30-Hz relative linewidth watt output power 1.65 µm continuous-wave singly resonant optical parametric oscillator," *Opt. Express*, vol. 25, no. 8, pp. 9049–9060, 2017.

[220] E. Andrieux, T. Zanon, M. Cadoret, A. Rihan, and J.-J. Zondy, "500 GHz mode-hop-free idler tuning range with a frequency-stabilized singly resonant optical parametric oscillator," *Opt. Lett.*, vol. 36, no. 7, pp. 1212–1214, 2011.

[221] G. Baili, M. Alouini, D. Dolfi, F. Bretenaker, I. Sagnes, and A. Garnache, "Shot-noise-limited operation of a monomode high-cavity-finesse semiconductor laser for microwave photonics applications," *Opt. Lett.*, vol. 32, no. 6, pp. 650–652, 2007.

[222] D. Gao, Z. Ding, and Z. Zhang, "Suppression of relaxation-oscillations in intracavity optical parametric oscillators by two-photon absorption," *Opt. Lett.*, vol. 45, no. 21, pp. 5954–5957, 2020.

[223] D. Cuozzo and G.-L. Oppo, "Two-color continuous-variable quantum entanglement in a singly resonant optical parametric oscillator," *Phys. Rev. A*, vol. 84, 043810, 2011.

[224] E. Knyazev, F. Y. Khalili, and M. V. Chekhova, "Overcoming inefficient detection in sub-shot-noise absoprtion measurement and imaging," *Opt. Express*, vol. 27, no. 6, pp. 7868–7885, 2019.

[225] L. E. Myers and W. R. Bosenberg, "Periodically poled lithium niobate and quasi-phase-matched optical parametric oscillators," *IEEE J. Quantum Electron.*, vol. 33, no. 10, pp. 1663–1672, 1997.

[226] F. G. Colville, M. J. Padgett, and M. H. Dunn, "Continuous-wave, dual-cavity, doubly resonant, optical parametric oscillator," *Appl. Phys. Lett.*, vol. 64, no. 12, pp. 1490–1492, 1994.

[227] G. A. Turnbull, D. McGloin, I. D. Lindsay, M. Ebrahimzadeh, and M. H. Dunn, "Extended mode-hop-free tuning by use of a dual-cavity, pump-enhanced optical parametric oscillator," *Opt. Lett.*, vol. 25, no. 5, pp. 341–343, 2000.

[228] A. Khalaidovski, "Beyond the Quantum Limit – A Squeezed-Light Laser in GEO 600," Ph.D. dissertation, Leibniz University Hannover, Hannover, Germany, 2011.

List of Publications

Journal Articles

- S. Anderson, P. H. Moriya, L. Caspani and J. E. Hastie, "Single-frequency optical parametric oscillator intracavity-pumped by a visible VECSEL for low-noise down-conversion to 1.55 µm," *Opt. Express*, vol. 17, no. 3, 4254–4266, 2024. DOI: 10.1364/OE.510807

- S. Anderson, P. H. Moriya, L. Caspani and J. E. Hastie, "Sub-kHz linewidth intracavity VECSEL-pumped OPO," *APL Photonics*, vol. 11, 026112, 2026. DOI: 10.1063/5.0308873

Conference Proceedings

- S. Anderson, P. H. Moriya, L. Caspani and J. E. Hastie, "Intra-cavity singly-resonant OPO pumped by a visible VECSEL for low-noise down-conversion to 1.55 µm," *Laser Congress 2023 (ASSL, LAC)*, Technical Digest Series (Optica Publishing Group, 2023), Paper AW5A.3. DOI: 10.1364/ASSL.2023.AW5A.3

Conference Talks

- S. Anderson, P. H. Moriya, L. Caspani and J. E. Hastie, "Intra-cavity singly-resonant OPO pumped by a visible VECSEL for low-noise down-conversion to 1.55 µm," *Laser Congress 2023 (ASSL, LAC)*, Technical Digest Series (Optica Publish-

ing Group, 2023), Paper AW5A.3. DOI: 10.1364/ASSL.2023.AW5A.3 (**contributed oral presentation of published work**).

- S. Anderson, P. H. Moriya, L. Caspani and J. E. Hastie, "Sub-kHz linewidths of a dual-locked ICSRO VECSEL," presented at *SPIE Photonics West: VECSELs XIV*, San Francisco, USA, 2025. (**contributed oral presentation**).

  The associated SPIE proceedings paper was withdrawn prior to publication to enable submission of an extended version to a higher-impact peer-reviewed journal.

Appendix A: Python script for calculating RIN PSD

```
"""
This Python script calculates the Relative Intensity Noise (RIN) Power
Spectral Density (PSD). It first computes the Logarithmic PSD (LPSD)
following the implementation described in references [1] and [2].
Variable names correspond closely to those in the reference papers, and
equation numbers from the publications are included in the comments.

References:
 [1] Michael Trobs and Gerhard Heinzel, "Improved spectrum estimation
 from digitized time series on a logarithmic frequency axis,"
 Measurement, vol. 39 (2006), pp. 120  129  . DOI: 10.1016/j.measurement
     .2005.10.010

 [2] Michael Trobs and Gerhard Heinzel, "Corrigendum to 'Improved
 spectrum estimation from digitized time series on a logarithmic
 frequency axis.'"
"""

# Import necessary libraries
import numpy as np
import pandas as pd
import matplotlib.pyplot as plt
from matplotlib.ticker import EngFormatter
from scipy.signal import windows
import time
```

```
25
26
27  # Define physical constants
28  R_load = 50                # Load resistance [Ohm]
29  e = 1.60217662E-19         # Electron charge [C]
30  k = 1.380E-23              # Boltzmann constant [J/K]
31  t = 293                    # Room temperature [K]
32
33  """
34  Define the LPSD function. This function computes the power spectral
35  density using logarithmic frequency scaling, which provides better
36  resolution across multiple frequency decades.
37  """
38
39  def lpsd(x, windowfcn, fmin, fmax, Jdes, Kdes, Kmin, fs, xi):
40
41  """
42  Parameters:
43      x : ndarray
44          Input time series.
45      windowfcn : function
46          Function that returns a window of a given length.
47      fmin : float
48          Minimum frequency to estimate.
49      fmax : float
50          Maximum frequency to estimate.
51      Jdes : int
52          Desired number of Fourier frequencies.
53      Kdes : int
54          Desired number of averages.
55      Kmin : int
56          Minimum number of averages.
57      fs : float
58          Sampling frequency.
59      xi : float
60          Fractional overlap between segments (0 <= xi < 1).
```

```
61
62  Returns:
63      Pxx : ndarray
64          Power spectrum estimates (uncalibrated).
65      f : ndarray
66          Frequencies corresponding to Pxx.
67      C : dict
68          Calibration factors: 'PS' for power spectrum and 'PSD' for power
                spectral density.
69  """
70
71      assert callable(windowfcn)
72      assert fmax > fmin
73      assert Jdes > 0
74      assert Kdes > 0
75      assert Kmin > 0
76      assert fs > 0
77      assert 0 <= xi < 1
78
79      N = len(x)
80      jj = np.arange(Jdes)
81
82      assert fmin >= fs / N
83      assert fmax <= fs / 2
84
85      g = np.log(fmax) - np.log(fmin)      # Eqn (12)
86      f = fmin * np.exp(jj * g / (Jdes - 1))       # Eqn (13)
87      rp = fmin * np.exp(jj * g / (Jdes - 1)) * (np.exp(g / (Jdes - 1)) -
            1)     # Eqn (15)
88
89      ravg = (fs / N) * (1 + (1 - xi) * (Kdes - 1))        # Eqn (16)
90      rmin = (fs / N) * (1 + (1 - xi) * (Kmin - 1))        # Eqn (17)
91
92      case1 = rp >= ravg
93      case2 = (rp < ravg) & (np.sqrt(ravg * rp) > rmin)
94      case3 = ~(case1 | case2)         # Case 3 True if Cases 1 and 2 False
```

```
95
96      rpp = np.zeros(Jdes)
97      rpp[case1] = rp[case1]
98      rpp[case2] = np.sqrt(ravg * rp[case2])
99      rpp[case3] = rmin
100
101     L = np.round(fs / rpp).astype(int)      # Eqn (19)
102     r = fs / L      # Eqn (20)
103     m = f / r       # Eqn (7)
104
105     Pxx = np.full(Jdes, np.nan)
106     S1 = np.full(Jdes, np.nan)
107     S2 = np.full(Jdes, np.nan)
108
109     for jj in range(Jdes):
110         D = int(round((1 - xi) * L[jj]))        # Eqn (2)
111         K = int(np.floor((N - L[jj]) / D + 1))      # Eqn (3)
112
113         if K <= 0 or L[jj] <= 0:
114             continue        # skip invalid parameters
115
116         indices = np.arange(L[jj])[:, None] + D * np.arange(K) # Eqn (5)
117
118         if indices.max() >= N:
119             continue
120
121         data = x[indices]
122         data = data - np.mean(data, axis=0)     # Eqn (4)
123
124         window = windowfcn(L[jj])
125         sinusoid = np.exp(-2j * np.pi * np.arange(L[jj]) * m[jj] / L[jj])
126         windowed_data = data * (window[:, None] * sinusoid[:, None])
                  # Eqn (6)
127
128         Pxx[jj] = np.mean(np.abs(np.sum(windowed_data, axis=0)) ** 2)
                  # Eqn (8)
```

```
        S1[jj] = np.sum(window)      # Eqn (23)
        S2[jj] = np.sum(window ** 2)         # Eqn (24)

    C = {'PS': 2 / S1**2,        # Eqn (28)
    'PSD': 2 / (fs * S2)}        # Eqn (29)

    return Pxx, f, C

"""
Since LPSD function is now defined, we now use this function to
plot (and extract) the RIN PSD from the oscilloscope data
"""

# Import oscilloscope data
filename = 'Insert file name.csv'  # Insert file name

# Read data from where dataset begins
data = pd.read_csv(filename, skiprows=2, names=["TIME", "CH1", "CH2"])

T = data["TIME"].values[:1250000]          # T corresponds to time data
ACsignal = data["CH1"].values[:1250000]  # CH1 corresponds to AC data
DCsignal = data["CH2"].values[:1250000]  # CH2 corresponds to DC data

T = T - T[0]
L = len(T)
dt = T[7] - T[6]          # dt defines the time step
fs = 1 / dt               # Sampling frequency

Mean_DC = np.mean(DCsignal)      # determines mean of DC data
Mean_AC = np.mean(ACsignal)      # determines mean of AC data

# Define LPSD parameters
N = L
X = ACsignal
fmin = fs / N
fmax = fs / 2
```

```
Jdes = 2000
Kdes = 30
Kmin = 15
xi = 0.4
window_function = windows.hann      # Hanning window function chosen

print("Computing LPSD...")
start = time.time()
Pxx, f, C = lpsd(X, window_function, fmin, fmax, Jdes, Kdes, Kmin, fs, xi
    )
end = time.time()
print(f"LPSD computed in {end - start:.3f} seconds")

# Convert the result to RIN PSD
S_voltage = Pxx * C["LPSD"]
S_current = S_voltage / (R_load**2)
S_shot = 2*e*Mean_DC / R_load       # Shot-noise
RIN_current = (S_current - S_shot ) / (Mean_DC / R_load)**2
log_RIN = 10 * np.log10(RIN_current)

# Plot the RIN PSD
plt.semilogx(f, log_RIN, color=(1, 0, 0), linewidth=3)
plt.title("RIN PSD")
plt.xlabel("Frequency [Hz]")
plt.ylabel("RIN [dBc/Hz]")
plt.xlim(10, 6.25e6)    # Defines x-axis from 10 Hz to 6.25 MHz
plt.ylim(-160, -80)     # Defines y-axis from -160 to -80 dBc/Hz

formatter = EngFormatter(unit='')       # No 'Hz' suffix on tick labels
plt.gca().xaxis.set_major_formatter(formatter)
ax = plt.gca()
ax.grid(True, which='both', linestyle=':', linewidth=0.8, color='grey',
    alpha=0.6)

plt.tight_layout()
plt.show()
```

```
199
200 # RIN PSD data exported to csv file format
201 np.savetxt('freq.csv', f, delimiter=",", fmt='%.12e')
202 np.savetxt('RIN_PSD.csv', log_RIN, delimiter=",", fmt='%.12e')
```

Appendix B: Python script for calculating frequency noise PSD

```
"""
This Python script calculates the frequency noise PSD using the same
LPSD function as in Appendix A. Detailed descriptions and comments
for defining the LPSD function are provided in Appendix A, so they
are omitted here.
"""

import numpy as np
import pandas as pd
import matplotlib.pyplot as plt
from matplotlib.ticker import EngFormatter, LogFormatterSciNotation
from scipy.signal import windows
import time

# --- Define the lpsd function ---
def lpsd(x, windowfcn, fmin, fmax, Jdes, Kdes, Kmin, fs, xi):

    assert callable(windowfcn)
    assert fmax > fmin
    assert Jdes > 0
    assert Kdes > 0
    assert Kmin > 0
    assert fs > 0
    assert 0 <= xi < 1

```

```
    N = len(x)
    jj = np.arange(Jdes)

    assert fmin >= fs / N
    assert fmax <= fs / 2

    g = np.log(fmax) - np.log(fmin)
    f = fmin * np.exp(jj * g / (Jdes - 1))
    rp = fmin * np.exp(jj * g / (Jdes - 1)) * (np.exp(g / (Jdes - 1)) -
        1)

    ravg = (fs / N) * (1 + (1 - xi) * (Kdes - 1))
    rmin = (fs / N) * (1 + (1 - xi) * (Kmin - 1))

    case1 = rp >= ravg
    case2 = (rp < ravg) & (np.sqrt(ravg * rp) > rmin)
    case3 = ~(case1 | case2)

    rpp = np.zeros(Jdes)
    rpp[case1] = rp[case1]
    rpp[case2] = np.sqrt(ravg * rp[case2])
    rpp[case3] = rmin

    L = np.round(fs / rpp).astype(int)
    r = fs / L
    m = f / r

    Pxx = np.full(Jdes, np.nan)
    S1 = np.full(Jdes, np.nan)
    S2 = np.full(Jdes, np.nan)

    for jj in range(Jdes):
        D = int(round((1 - xi) * L[jj]))
        K = int(np.floor((N - L[jj]) / D + 1))
        if K <= 0 or L[jj] <= 0:
            continue
```

```
61
62          indices = np.arange(L[jj])[:, None] + D * np.arange(K)
63          if indices.max() >= N:
64              continue
65
66          data = x[indices]
67          data = data - np.mean(data, axis=0)
68
69          window = windowfcn(L[jj])
70          sinusoid = np.exp(-2j * np.pi * np.arange(L[jj]) * m[jj] / L[jj])
71          windowed_data = data * (window[:, None] * sinusoid[:, None])
72
73          Pxx[jj] = np.mean(np.abs(np.sum(windowed_data, axis=0)) ** 2)
74          S1[jj] = np.sum(window)
75          S2[jj] = np.sum(window ** 2)
76
77      C = {'PS': 2 / S1**2, 'PSD': 2 / (fs * S2)}
78      return Pxx, f, C
79
80  """
81  Since LPSD function is now defined, we now use this function to
82  plot (and extract) the frequency noise PSD from the oscilloscope data
83  """
84
85  # --- Frequency Discrimination Constants ---
86  """
87  Measured constants used to convert photodetector voltage fluctuations
88  into equivalent laser frequency fluctuations.
89  """
90
91  FSR = "Insert FSR of Fabry-Perot (FP) reference cavity"
92  Finesse = "Insert finesse of FP reference cavity"
93  Signal_PP = "Insert peak-to-peak voltage of error signal"
94
95  # Import oscillscope data
96  filename = "Insert file name.csv"      # Insert file name
```

```
97
98  # Read data from where dataset begins
99  data = pd.read_csv(filename, skiprows=2, header=None, names=["TIME", "CH1
        "])
100
101 T = data["TIME"].values[:1250000]        # T corresponds to time data
102 V_error = data["CH1"].values[:1250000]   # V_error corresponds to the
        error signal voltage data
103
104 # --- Time preprocessing ---
105 T = T - T[0]
106 L = len(T)
107 dt = T[7]-T[6]
108 fs = 1 / dt
109
110 # --- Frequency noise conversion ---
111 """
112 For frequency conversion equation below, the factor of 2 accounts for
113 side-of-fringe locking (signal + idler); this is omitted for PDH
114 locking due to VECSEL peak-to-peak voltage measurement method.
115 """
116
117 freq_noise = 2 * (FSR / Finesse) * (1 / Signal_PP) * V_error
118
119 # --- LPSD parameters ---
120 N = L
121 X = freq_noise - np.mean(freq_noise)
122 Jdes = 2000
123 Kdes = 30
124 Kmin = 15
125 xi = 0.4
126 fmin = fs / N
127 fmax = fs / 2
128 window_function = windows.hann
129
130 # --- Compute LPSD ---
```

```
print("Computing LPSD...")
start = time.time()
Pxx, f, C = lpsd(X, window_function, fmin, fmax, Jdes, Kdes, Kmin, fs, xi)
end = time.time()
print(f"LPSD computed in {end - start:.3f} seconds")

# --- Calibrate PSD ---
FNPSD = Pxx * C['PSD']

# --- Plot PSD ---
plt.figure()
plt.loglog(f, FNPSD, color='red', linewidth=2)
plt.title("Frequency Noise PSD")
plt.xlabel("Frequency [Hz]")
plt.ylabel("Frequency noise PSD [Hz$^2$/Hz]")
plt.xlim(10, 1e6)    # Defines x-axis from 10 Hz to 1 MHz
plt.ylim(1, 1e10)    # Defines y-axis in units of Hz**2/Hz

# --- Engineering notation on x-axis ---
formatter = EngFormatter(unit='')  # No 'Hz' suffix on tick labels
plt.gca().xaxis.set_major_formatter(formatter)

# --- Scientific notation on y-axis ---
plt.gca().yaxis.set_major_formatter(LogFormatterSciNotation(base=10, labelOnlyBase=True))  # Defines y-axis in scientific notation

# --- Grid and layout ---
ax = plt.gca()
ax.grid(True, which='both', linestyle=':', linewidth=0.8, color='grey', alpha=0.6)

plt.tight_layout()
plt.show()

# --- Export data to CSV ---
```

```
164 np.savetxt("FNPSD.csv", FNPSD, fmt='%.6e')
165 np.savetxt("freq.csv", f, fmt='%.6e')
```